An Experimental and Theoretical Study of the ECR Plasma Engine

Dissertation by

Joel Christopher Sercel

In Partial Fulfillment of the Requirements

for the Degree of

Doctor of Philosophy

California Institute of Technology

Pasadena, California

1993

(Submitted April 26, 1993)

The effort described in the pages that follow is dedicated to

the memory of my father, Major John Sercel;

to my partner in life, Cynthia Ann Sercel;

and to the future - Alexander John Sercel.

ACKNOWLEDGMENT

I believe that both personal and professional acknowledgments are appropriate in a Ph.D. thesis because it is an accomplishment with both personal and professional aspects. With this in mind, these acknowledgments start with the professional and move to the personal.

On the professional side, the two primary sponsors of work reported in this document were the Air Force Office of Scientific Research (AFOSR) under grant AFOSR-87-0205 and the Office of Aeronautics and Space Technology (OAST) at the National Aeronautics and Space Administration (NASA). The program managers responsible for the support of this work for four years at the AFOSR included first Dr. Robert Vondra and then Dr. Mitat Birkan. The NASA-OAST managers who provided support for this program under the Advanced Propulsion Concepts effort at the Jet Propulsion Laboratory (JPL) included Mr. Marcus Watkins, Dr. Gary Bennett, and Mr. Earl Van Landingham.

I would like to thank my management at JPL for, among other things, providing a unique environment that has allowed me to work almost full time managing the Advanced Propulsion Concepts effort while pursuing my graduate studies at Caltech. This experience has allowed me to develop my professional and academic talents in parallel at an accelerated rate that would not have been otherwise possible. The first two people I must mention in this regard are Dr. Duane (Dip) Dipprey and Mr. John (Jack) Stocky who persuaded me to apply to Caltech. My supervisors at JPL have contributed to this dissertation, each in their own way. These individuals, including Mr. Philip Garrision, Mr. James Kelley, Dr. Mack Dowdy, Mr. David Maynard and Dr. James Cutts, deserve my thanks. I trust that the large number of supervisors I have had while doing this work is not a reflection of the difficulty of managing a certain JPL employee who happened to have spent some time as a graduate student at Caltech.

Several Caltech faculty and students contributed to this project. In only having room to name a few, I pick the following three. Thank you to my advisor, Professor F. E. C. (Fred) Culick, for his support of my admission to Caltech and my candidacy and for his technical contributions and guidance in this project. An acknowledgment is also owed to Professor David Goodwin, who provided additional guidance for this work and whose insights and technical knowledge of the relevant physics were part of the success of the

project. Finally, thanks are due to David Kaufman for his valuable assistance in several areas of experimental work and for his review of portions of this document.

Several of my working colleagues at JPL have contributed significantly. Foremost I must thank Dr. Dennis Fitzgerald who accomplished much of the detailed design and assembly of the plasma diagnostics we developed here and with whom I worked shoulder to shoulder in the laboratory collecting the data that is presented in this thesis. Another major contributor in the laboratory was Ms. Stephanie Leifer, who helped much in developing diagnostics and taking data. I am also happy to acknowledge Dr. David King (then of JPL) with whom I discussed plasma physics and the theory of the ECR plasma accelerator. Insights gained in my conversations with Dr. King have made their way into the pages of this document. Finally, I thank Dr. Donald Rapp, JPL Technologist extraordinare, for an early reading of a rough draft and for words of encouragement about the doctoral process. I don't have the space to detail the contributions of several other JPL people who contributed to this project, but I hope the members of the Electric Propulsion Technology and Advanced Propulsion Systems group will accept my genuine appreciation. It has been a pleasure working with you all.

To the personnel friends and family who provided moral support and encouragement - my thanks!

ABSTRACT

The process of Electron-Cyclotron-Resonance (ECR) plasma acceleration has several potential applications including use as a new type of electric space propulsion device designated the ECR plasma engine. The ECR plasma engine is interesting due to its theoretical promise to deliver a combination of improved efficiency, specific impulse, power-handling capability, length of life, or operational flexibility relative to other electric propulsion devices now being developed. Besides its possible application in electric propulsion, the ECR plasma engine might be useful for beamed-energy propulsion or fusion propulsion. Related devices are used in the semiconductors field for plasma etching.

This study includes theoretical modeling and a series of experimental measurements. The theoretical work was focused in two areas. The first area involved the development of a collisionless, steady-state, axisymmetric model of a cold flowing plasma separating from a diverging magnetic field. This model suggests that beam divergence can be an important loss mechanism for plasma propulsion devices that use magnetic nozzles, but that the use of optimized field geometries can reduce divergence losses to acceptable levels. We suggest that future research be directed at confirming theoretical predictions made using the axisymmetric model of beam separation.

The second area of theoretical investigation involved the development of a steady-state, quasi-one-dimensional model that provides theoretical predictions of plasma density, electron temperature, plasma potential, ion energy, engine specific impulse, efficiency, and thrust. The quasi-one-dimensional model consists of a system of five first-order, non-linear, ordinary differential equations. The boundary conditions required to solve the system of equations are relationships between the ambient neutral gas density, the plasma density, the two components of the electron temperature, and the position at which the plasma passes through the ion-acoustic Mach number 1. The model was used to solve two classes of problems that are thought to bound the conditions under which the ECR plasma accelerator operates. The first class of problem is based on the assumption of negligible conductive heat flow within the plasma. The second class of problem is based on the assumption that electron thermal transport along magnetic field lines is so large that the component of the electron temperature along magnetic field lines is isothermal. The model can be used to simulate accelerator operation in space or in the presence of a vacuum

system with finite tank pressure. Measurements of plasma conditions in a working research device confirm the general features of the quasi-one-dimensional theory.

The experimental apparatus constructed to study ECR plasma acceleration consists of a vacuum facility, a 20-kW microwave power supply, and an ECR plasma accelerator. In tests of the facility we have measured microwave input power, reflected power, propellant flow rate, and vacuum-tank static pressure. The working ECR plasma research device uses argon propellant gas with 2.12-GHz microwave radiation at power levels of up to a few kilowatts. Among the plasma diagnostics employed in this research are a gridded energy analyzer, a Faraday cup beam-density analyzer, Langmuir probes, emissive probes, and a diamagnetic loop. With these diagnostics, we have measured plasma potentials of up to 70 eV and electron temperatures of up to 35 eV. Measurements of accelerated-ion kinetic energy show a direct relationship between ion energy and peak plasma potential, as predicted by theory. Indirect measurements indicate that the plasma density in the existing accelerator is on the order of 10^{17} m^{-3}.

We now understand previously unexplained losses in converting microwave power to jet power by ECR plasma acceleration as the result of diffusion of energized plasma to the metallic walls of the accelerator. Our theory suggests that future researchers should attempt to reduce the influence of these diffusion losses by increasing the cross-sectional area of the accelerator. It may be possible to reduce line radiation losses due to electron-ion and electron-atom inelastic collisions below levels estimated by past researchers through careful accelerator design. Minimizing inelastic collision losses will place a limit on the maximum thrust density that can be achieved using argon and other non-hydrogenic propellant materials. High thrust density may be achievable using propellants that are isotopes of hydrogen because once ionized, these species exhibit negligible inelastic collision effects. Deuterium is arguably the best candidate for achieving both high efficiency and high thrust, but will only be effective at specific impulses of over about 10,000 lbf•s/lbm.

We expect that efficient ECR plasma engines can be designed for use in high specific impulse spacecraft propulsion at power levels ranging from a few kilowatts to tens of megawatts. The maximum theoretical efficiency of converting applied microwave power to directed jet power in this device can be more than 60 percent. The achievable total efficiency of converting direct-current electric power to jet power in a propulsion system based on the ECR plasma engine will probably be considerably less.

TABLE OF CONTENTS

LIST OF ILLUSTRATIONS

LIST OF TABLES

NOMENCLATURE

Acronyms and Abbreviations

$D\text{-}He^3$	Deuterium Helium-Three
ECR	Electron-Cyclotron-Resonance
GE	General Electric
JPL	Jet Propulsion Laboratory
LeRC	Lewis Research Center
NASA	National Aeronautics and Space Administration
TE	Transverse-Electric

Symbols

A	=	area of accelerator through which plasma and gas flow
a	=	radius of current loop
B	=	magnetic induction vector, T
B	=	magnitude of the magnetic field vector, T
D	=	diffusion coefficient, m^2/s
e	=	electron charge,1.602×10^{-19} c
E	=	energy, J or eV
E	=	local electric field vector, V/m
$\mathbf{F}_\mu$	=	dipole-moment force per particle, N
I	=	integer number of outer shell electrons in Gryzinski theory
J	=	electric current vector, Am^{-2}
k	=	Boltzmann's constant, J/K
m	=	electron mass, kg
n	=	plasma density, $\#/m^3$
n_a	=	atom density, $\#/m^3$
p	=	pressure, Pa or torr
P_{ecr}	=	power gained per unit volume due to ECR heating, W/m^3
P_{el}	=	power lost from electron perpendicular energy due to elastic collisions, W/m^3
P_{ina}	=	power lost due to inelastic collisions of electrons with atoms, W/m^3
P_{ini}	=	power lost due to inelastic collisions of electrons with ions, W/m^3
Q_{a+}	=	Maxwellian electron-rate factor for ionization of atoms, $s^{-1}m^{-2}$
Q_{a++}	=	Maxwellian electron-rate factor for double ionization of atoms, $s^{-1}m^{-2}$
Q_{i++}	=	Maxwellian electron-rate factor for double ionization of single ions, $s^{-1}m^{-2}$

r = cross-sectional radius of plasma, m

$\mathbf{R}$ = position vector, m

S_p = volumetric production rate for plasma particles, $m^{-3}s^{-1}$

$T_\perp$ = electron temperature parallel to magnetic field lines, eV

u = average stream-wise component of plasma velocity, m/s

u_a = average stream-wise component of atom velocity, m/s

U_{ex} = lumped excitation energy, eV

U_+ = ionization energy, eV

U_j = excitation energy of jth excited state, eV

U_1 = lowest excitation energy, eV

v_e = electron speed, m/s

W_{tot} = average total thermal energy of electrons, eV

$W_{//}$ = average energy of electrons parallel to magnetic field lines, eV

$W_\perp$ = average energy of electrons perpendicular to magnetic field lines, eV

z = stream-wise displacement, m

σ_{ea} = electron-atom-scattering cross section, m^2

σ_{ei} = electron-ion-scattering cross section, m^2

σ_i = ionization cross-section for electron-atom collisions, m^2

σ_{ix} = ion-atom-scattering cross section, m^2

σ_{ex} = lumped-excitation collision-cross-section for electron-atom collisions, m^2

σ_{exi} = lumped-excitation collision-cross-section for electron-ion collisions, m^2

$< >$ = average over the electron-speed distribution function, $s^{-1}m^{-2}$

T	=	total
w	=	waveguide

Greek

μ	=	magnetic dipole moment, J/T
Γ	=	flux of plasma, #/m^2/s
σ	=	reaction cross section, m^2
τ	=	time constant, s

Subscripts

A	=	acceleration
ael	=	atom-elastic
B	=	Bohm
e	=	electron
ex	=	atom excitation
exi	=	ion excitation
gc	=	guiding center
i	=	ionization
iel	=	ion-elastic
j	=	summation variable
l	=	lowest energy level
//	=	parallel
$\perp$	=	perpendicular
r	=	relative
sp	=	space-charge induced

FOREWORD

This dissertation is written in seven chapters with five appendices. The introductory chapter provides an entree to the topic by describing the concept of the ECR plasma accelerator, potential applications of the device, a description of the potential benefits the device may offer to the field of space propulsion, and a description of related research.

The technical discussion of the physics of ECR plasma acceleration begins in Chapter 2, which is organized in three major sections. Section 2.1 Simplified Analysis, covers several different aspects of the physics of the device. A piecemeal discussion of the physics of the device is presented to provide a framework in which each individual phenomenon can be understood in isolation without the complicating effects of coupling to other phenomena. The second section of Chapter 2 explores the important question of how a collisionless plasma can separate from a magnetic nozzle. This section presents a somewhat idealized, but none-the-less useful, approach to modeling a counter-intuitive process. The second section of Chapter 2 was required because the bulwark of this theoretical work, the quasi-one-dimensional model of Section 2.3, was not intended to address the issue of collisionless flow across magnetic field lines.

The quasi-one-dimensional model does address, simultaneously and self consistently, all of the other loss processes that we consider important to study in a steady-state model. The loss processes addressed collectively by the model include those treated piecemeal in Section 2.1, plus certain dynamic effects for which a flow model is required. The derivation of the quasi-one-dimensional model is included in Appendices B and C because the continuum mechanics approach that we used, in which a (plasma) fluid is tracked through a postulated control volume, is fairly standard and many readers may want to skip the derivation or refer to those parts of it that are of special interest.

Chapter 3 describes the apparatus we developed to conduct experimental studies. Chapter 4 describes the approach used to conduct numerical calculations using the quasi-one-dimensional model of Chapter 2 and it presents a summary of the results of our calculations. For a detailed listing of the computer program, refer to Appendix E. For a detailed presentation of our computational results, refer to Appendix F.

In Chapter 5 we compare the results of calculations with the results of experimental measurements. In Chapter 6 we provide an interpretation of these results, outline our conclusions, and discuss possible future work that could usefully follow this study.

This dissertation does not include a tutorial discussion of the fundamentals of rocket propulsion because such tutorials can be found elsewhere. For a particularly good treatment of the subject we recommend Fujio Iinoya's recent publication (1993).

The units used in this document are somewhat inconsistent and may be confusing to some. The reason for this inconsistency is that this document describes both experimental and theoretical work and the language of experimentalists who work in propulsion technology is very different from the language of theorists who publish their work in plasma physics journals. To a theorist the unit of 'sccm' seems ungainly and inconvenient but to the experimentalist it is a quantity that can be easily measured with a stop watch, graduated cylinder, and soap bubble.*

Finally, a few words on the author's decision to use the first person pronoun. In the *old school* of technical writing the first person pronoun was considered bad form. Many professionals, especially engineers, still consider the first person to be inappropriate in technical writing because they think that it sounds pompous or self-aggrandizing. In recent years, however, the technical community has begun to join the rest of the literate world in accepting composition in the first person as preferable because it allows the author to eliminate ambiguity and write in the active voice. Some technical conferences now request that papers be prepared using the first person. We use the plural as a reminder that this work could not have been completed without the aid of those mentioned in the acknowledgments.

---

* We did use the somewhat more sophisticated Hastings flow meter to measure flow rates in this work, but we checked the calibration with the kitchen physics approach.

Chapter 1

INTRODUCTION

1.1 Concept of ECR Plasma Acceleration

We examine Electron-Cyclotron-Resonance (ECR) plasma acceleration with an eye to its potential application in high specific impulse spacecraft propulsion systems. This electrodeless process promises to use microwave-frequency electromagnetic radiation to efficiently accelerate propellant. The advantages of high specific impulse propulsion include reduced trip time, reduced propellant consumption, and the ability to accomplish high-energy missions that are not feasible using existing thermal propulsion technology. Electric propulsion represents the most-likely near-term option for achieving high specific impulse. More exotic options, such as beamed-energy propulsion or fusion propulsion, are further in the future. ECR plasma acceleration may have applications in all of these areas.

Figure 1.1 depicts a schematic of an ECR plasma accelerator. Major components of this axisymmetric device include a waveguide, a dielectric window, a solenoid coil, and a gas-injection system. A waveguide channels microwave power into the device through the dielectric window. The purpose of the window is to separate the neutral gas region, where microwave breakdown occurs, from the region upstream of the window, where the use of a higher or lower gas pressure suppresses breakdown. A large vacuum system holds the neutral gas region to pressures of about 10^{-4} torr. In an actual space application, the vacuum of space would provide the required gas pumping. The solenoid coil in an ECR accelerator must be designed to produce a magnetic field that diverges to the right, as shown in the figure. The strength of the magnetic field produced by the solenoid is selected so that the cyclotron frequency of electrons, orbiting field lines in the desired ECR heating region, is equal to the frequency of the applied microwave radiation.

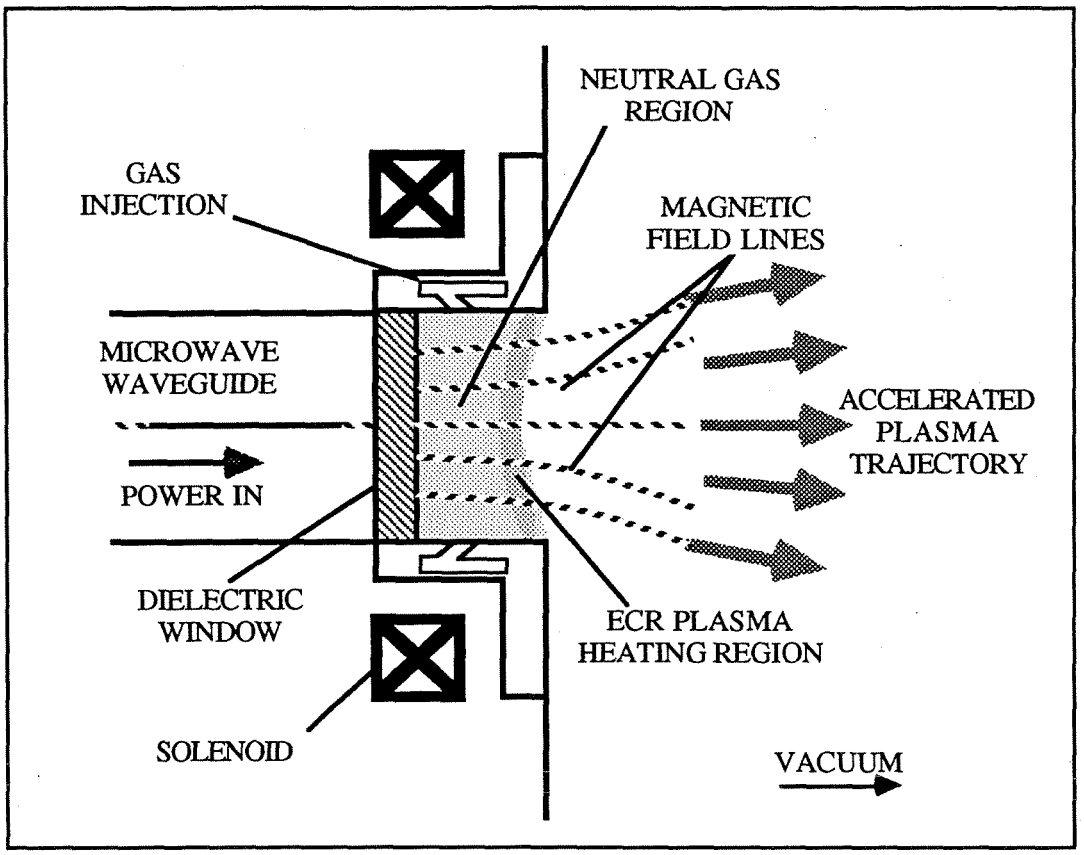

Fig. 1.1 Schematic of ECR plasma accelerator

The gas-injection system provides a steady flow of propellant into the neutral gas region. The propellant subsequently diffuses by free molecular flow into the ECR heating region. After the gas-injection system establishes a steady gas stream, a microwave generator supplies ECR power and a direct-current power supply provides current to activate the solenoid coil. Free electrons present in the ECR heating region gain kinetic energy in the combined presence of the microwave radiation and the magnetic field. These energetic electrons undergo collisions with neutral gas atoms, thereby ionizing the gas and producing more free electrons in an avalanche process. In steady-state operation, the gas-injection system constantly replenishes the neutral gas region, which acts as a source for the plasma flow.

Each of the free electrons orbiting about magnetic field lines in the plasma has a magnetic dipole moment. The axes of the magnetic dipoles associated with these free electrons naturally align themselves opposite to the axis of the magnetic field of the solenoid. This opposition between the electron-cyclotron magnetic dipoles and the applied diverging solenoid field results in a net force on the electrons that is initially directed primarily in the

axial (downstream) direction. Because the Debye length in this plasma is small compared to the dimensions of the device, the net force on the electrons does not produce a macroscopic charge separation. Also, the force on the electrons does not result in a net current flow because the accelerator is conductively isolated. Instead, an electrostatic field couples the bulk ion motion to the bulk electron motion and the plasma accelerates downstream as a quasi-neutral fluid. The electric field responsible for accelerating the ions is interchangeably referred to as a *microscopic polarization field* or as an *ambipolar electric field.*

The combined effect of the electrostatic coupling of plasma species and the divergence of the magnetic field causes the accelerated plasma beam to diverge during separation from the magnetic field. We have analyzed this exhaust plume divergence and found that it is responsible for a loss in engine efficiency (see Section 2.2). Other losses that are present in the conversion of microwave power to jet power include: i) imperfect coupling of the applied microwave power, ii) electron thermal energy used to ionize the propellant atoms, iii) ion-electron recombination effects, iv) the effects of incomplete propellant ionization, v) plasma interactions with the walls of the accelerator, and vi) radiation from the plasma. Section 2.3 and Chapter 4 treat these loss mechanisms.

Table 1-1 includes a listing of the loss mechanisms we have estimated. The second column in the table is an estimate of the loss associated with each of these mechanisms for the experimental apparatus we have tested. Our analysis of losses in a hypothetical, optimized ECR plasma accelerator that uses argon propellant gas at a specific impulse of 3,000 lbf•s/lbm is the basis for the third column in the table. Actual efficiencies can be somewhat higher at higher specific impulse, lower at lower specific impulse, and significantly different for other propellants. We discuss projections of maximum achievable efficiency more fully in Section 4.3.7. From the data of Table 1-1, we conclude that the present device is highly inefficient. However, we do suggest that within the context of the existing theory considerable room still exists for improvement.

Table 1-1 Estimated Jet-Power Losses for Existing Device and an Optimized ECR Plasma Accelerator

Loss Mechanism	Estimate for Present Device (%)	Estimate for Optimized Device (%)
Plume Divergence	7	7
Reflection of Applied Power	5	1
Transmission of Applied Power	5	1
Propellant Ionization	30	9
Recombination	7	2
Propellant Utilization	14	9
Wall Effects	30	3
Total Losses	98	32
Estimated Efficiency (microwave to jet power)	2	64

1.2 Potential Applications and Benefits

Any suitable microwave source can act as the power supply when ECR plasma engines are used for spacecraft propulsion. As such, this plasma acceleration mechanism promises potential benefits for electric propulsion, beamed-energy propulsion, or fusion propulsion. The following discussion briefly describes these potential applications of ECR plasma acceleration

Electric propulsion is the application for which ECR plasma engines have the most promise in the relatively near future (i.e., less than a few decades). Desirable attributes of an effective electric propulsion technology include i) thrust efficiency greater than about 50 percent; ii) flexibility to operate throughout a specific impulse range of about 1,000 lbf•s/lbm to about 20,000 lbf•s/lbm; iii) unit-power-handling capability well matched to useful power supplies (kilowatts to megawatts); iv) simplicity; v) reliability; vi) engine lifetimes of up to several thousand hours; and vii) flexibility to use propellant fluids that are inexpensive, easily stored, readily available, and safe. All existing electric propulsion technologies require some compromises on these attributes. For example, electrostatic ion

thrusters promise long life and high efficiency, but are not well suited to operation at the relatively low specific impulse appropriate to Earth-orbital missions. By contrast, electrothermal arcjets can operate effectively at lower specific impulses and with less exotic propellants, but suffer from relatively low thrust efficiency and limited life.

Electric propulsion based on ECR plasma acceleration may avoid some of the performance compromises which limit existing electric propulsion technology. We believe that if the propulsion community fully develops ECR plasma engines, these devices may someday operate at thrust efficiencies comparable to those of electrostatic ion thrusters and throughout a range of specific impulses that encompass the traditional domains of both thermal and electrostatic devices. Because ECR thrusters are electrodeless, they may possess an inherently long life and be capable of processing a wide variety of propellant fluids. On the basis of on our present understanding, minimum power-handling may be as low as a few hundred watts. In principle, the only limit to maximum unit power-handling capability is the practical limit on available microwave power. At the high end of the scale, Minovitch (1983) has developed a conceptual design for an ECR device to operate at power levels as high as several gigawatts.

An important component of an electric propulsion system based on ECR plasma acceleration is the required microwave source. In the 1960s researchers (e.g., Crimi 1967) viewed limitations on the efficiency and specific-mass performance of magnetron or klystron microwave supplies as a significant problem for ECR propulsion. Technological advancements since the 1960s suggest that microwave sources for electric propulsion may deliver electric-to-microwave power conversion efficiencies of 85 to 90 percent, operational lifetimes of several years, and specific masses of less than about 0.5 kg/kW (e.g., Brown 1987, Brown 1984, Brown 1981). These performance parameters for state-of-the-art microwave generators give good promise for the future of high-performance propulsion systems that use primarily microwave power.

A complete propulsion-system design must be produced before ECR plasma acceleration can become practical for application to electric propulsion. In such a design, the efficiencies of both the microwave source and the engine are important, as are the total propulsion-system mass and the power required by the solenoid coils. Superconducting coils will require refrigeration systems, while normal conducting coils will require dedicated direct-current electric power. Chapter 7 presents a first approximation to such an ECR-propulsion-system design.

Figure 1.2 is a conceptual schematic that shows an ECR plasma engine for beamed-energy propulsion based on past studies by Minovitch (1983) and by Sercel (1987). In this application, a remotely located transmitter would launch a microwave beam toward the spacecraft. On the spacecraft, a parabolic antenna would focus the microwave power into the engine. This arrangement will free the spacecraft from carrying an expensive or massive onboard power supply with a propulsion system that operates at specific impulses previously achievable only by electric propulsion. Because the collector would have to be large to intercept a microwave beam transmitted over useful distances, the area mass density of this antenna will have to be quite low. One very lightweight design uses an inflated antenna* to receive the incoming microwave radiation, as shown in Fig. 1-2.

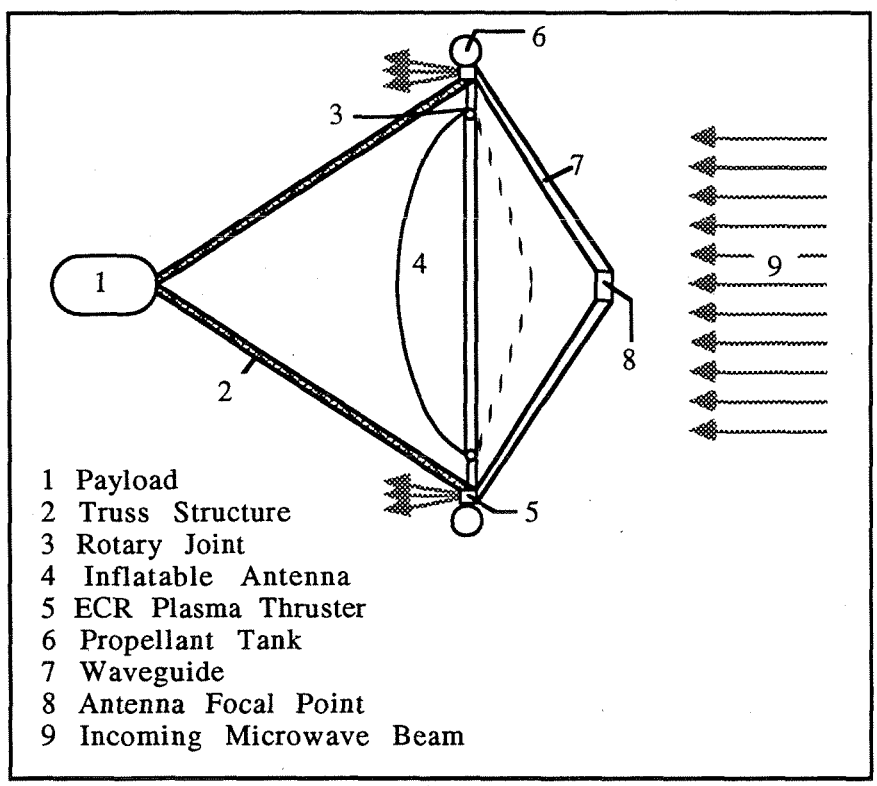

Fig. 1.2 ECR plasma engine in beamed-energy propulsion

The transmitter in such a beamed energy propulsion system could be located on the ground or in orbit. If a ground based transmitter is used, relay antennas would be required in space to deliver the beam to the spacecraft when the spacecraft is beyond the horizon.

* Inflatable antennas are an advanced technology that are scheduled to be flown by NASA in 1995.

Such relay antennas might still be needed in a scenario based on orbiting transmitters depending on the details of the mission requirements. These systems-level issues have been addressed by Brown (1985) and by Sercel (1987). A fundamental limitation to the application of beamed energy propulsion is the divergence of the power beam due to diffraction. The effect of diffraction in beamed energy propulsion is to limit the maximum transmission efficiency for a given antenna size. For the 2 GHz microwave frequency of the device studied in the present work, equal sized transmitter and receiver apertures of 100 m diameter will provide over 90 percent efficient transmission to distances up to 100 km, a range close to the requirement for ground to low Earth orbit perigee maneuvers. By increasing the microwave frequency to 22 GHz, the transmission range could be increased to 1000 km, useful for a variety of orbital maneuvers.

The most ambitious advanced application of ECR plasma acceleration that we have envisioned is its potential use as an engine for a propulsion system based on magnetic-confinement nuclear-fusion. Logan (1986) has proposed harnessing the microwave synchrotron radiation that magnetic confinement fusion reactors would produce. His analysis suggests that up to two-thirds of the fusion power output of a D-He^3 reactor can be extracted in the form of microwave radiation. We suggest the possibility that low-loss waveguides can couple this microwave power out of the fusion reactor cavity. If microwave power can be extracted from a fusion reactor in this manner, it is reasonable to speculate that it could then be delivered directly to an ECR plasma accelerator to provide power for an extremely high-performance spacecraft propulsion system. To date, no detailed systems analysis of this idea has been conducted.

1.3 History and Related Research

In the 1960s, three groups of researchers first investigated ECR plasma acceleration for its potential application to spacecraft propulsion. Included among these early groups were General Electric Company (e.g., Miller et al. 1965 and Crimi 1967), NASA LeRC (Kosmahl 1967), and the University of Tokyo (Nagatomo 1967). These groups accomplished enough research to verify some important features of ECR plasma acceleration. At the time of the investigation, however, microwave sources were quite massive and inefficient. Meanwhile, the propulsion research community was making significant progress on direct-current electric propulsion devices that showed promise of acceptable performance using the technology and analysis tools of the day (e.g., Jahn 1968). By the middle of the

1960s, these factors had led to a hiatus in research on ECR plasma acceleration that lasted about twenty years.

The Space Sciences Laboratory of the General Electric Company (GE) conducted the majority of the early experimental work on this type of plasma accelerator. In this experimental effort, several different ECR plasma thrusters were tested. Various arrangements of gas-injection schemes, waveguide designs, and window materials were evaluated. Thrust was measured for a variety of configurations at power levels of up to a few kilowatts using various propellants. The GE group was the first to make the important observation that the ECR phenomenon couples over 95 percent of the incident microwave power into the plasma stream.

At specific impulses of a few thousand seconds, Miller et al. (1965) reported a maximum efficiency of 40 percent for conversion of microwave power to jet power. However, the GE researchers later called into question the validity of many of their early thrust measurements (e.g., Crimi, Eckert, and Miller 1967). They suggested that the entrainment of gas from the vacuum chamber into the plasma heating region was increasing the effective mass flow rate and producing erroneously high thrust. In measurements not subject to concern over gas entrainment, thrust efficiency was only about 10 percent, and specific impulse was less than 2000 lbf•s/lbm. Electron temperature measurements in the plasma heating region suggested that the acceleration mechanism effectively converted the flux of electron thermal energy into jet power. The GE group concluded that an unknown mechanism prevented optimal accelerator performance by robbing the electrons of their thermal energy before this energy could contribute to plasma acceleration.

Crimi (1967) suggested that the unknown loss mechanism was line radiation caused by electron-atom inelastic collisions. However, our analysis (see Sections 2.1.3 and 4.3) concludes that line radiation could not have been responsible for the magnitude of the observed energy loss. We now understand that plasma in the GE experiments was diffusing to the walls of the accelerator across magnetic field lines. This radial motion was probably responsible for the measured low thrust efficiencies. It may now be possible to limit this loss mechanism through careful accelerator design using the theory developed in this thesis (see Section 2.1.4 and Chapter 4).

Kosmahl (1967) at Lewis Research Center (LeRC) published the first theoretical analysis of ECR plasma acceleration several years after the initiation of experimental work

at GE. In his work, Kosmahl assumed conservation of the electron-cyclotron dipole moment, zero collisions, and axisymmetric steady-state magnetic fields. A significant conclusion of Kosmahl's analysis was that the plasma trajectories cross the magnetic field lines, even without particle collisions, and that the plasma can emerge as a well-defined beam.

Kosmahl defined a propulsive efficiency to account for thrust lost due to radial acceleration of the plasma that can take place during separation from the magnetic field. He found that this propulsive efficiency depends primarily on the solenoid geometry and the position of the ionization region. His results suggest that propulsive efficiency losses from beam divergence can be as low as a few percent. We have modified and extended Kosmahl's dipole-moment calculation (see Section 2.2).

A review of the experimental work on ECR plasma acceleration, published by Nagatomo (1967) at the University of Tokyo, indicates that the research performed by the Japanese was directed at experimentally obtaining a fundamental understanding of the nature of the acceleration mechanism. Nagatomo developed several useful measuring techniques that gave accurate information on the basic physics of this process. Specifically, Nagatomo used i) small, sensitive electromagnetic probes to measure microwave field strength within the accelerator without disturbing the plasma; ii) emissive probes to measure the electrostatic potential of the accelerating plasma; and iii) a simple thrust balance to provide a direct measurement of the propulsive force between the plasma and the solenoid coil. Scientific results of Nagatomo's work were inconclusive as to the feasibility of ECR plasma acceleration for spacecraft propulsion.

Although not directed specifically at a propulsion application, a research program conducted in France in the 1960s on an ECR plasma accelerator is relevant to the present work. The Pleiade accelerator demonstrated that a diverging-field ECR device could deliver a well-collimated beam of argon ions at an energy level of 30 keV (Bardet et al. 1964). This energy level corresponds to a specific impulse of over 35,000 lbf•s/lbm. Post (1989), of Lawrence Livermore National Laboratory, has recently proposed a theory to explain how the Pleiade accelerator could have delivered such a high-energy beam of ions. The French experiments, together with Post's theoretical work, show that ECR plasma engines will not be specific impulse limited. Rather, the important question to be resolved is, "At what efficiency and at what power level can these devices be made to work for propulsion applications?"

Bornatici et al. (1983) have summarized the modern theory of the absorption of microwave radiation into a plasma by ECR. Most of the work on which they report is motivated by the need for plasma heating in magnetic-confinement fusion research. A few key differences exist between the application of ECR theory to fusion research and the application of this process to spacecraft propulsion. First, the fusion community is interested in much higher temperatures, typically several keV. Second, in the fusion application the transfer of electron thermal energy to ion thermal motion is desirable. In the propulsion application plasma dynamic effects must transfer electron thermal energy to the directed kinetic energy of the flowing plasma. Finally, the high magnetic fields associated with magnetic-confinement fusion research mandate radiation frequencies one to two orders of magnitude higher than those required for the propulsion application. In summary, it is much more difficult to apply ECR heating to fusion research than to plasma acceleration for spacecraft propulsion. It is worth noting that interest in high-power, high-frequency, microwave sources for fusion research has been an important factor in the recent development of high-power microwave sources, some of which might be useful for ECR propulsion systems.

One final area in which research relevant to the present effort is being conducted is in the development of ECR plasma sources for semiconductor etching. Groups in Japan (Tobinaga et al. 1988) have conducted the majority of this work, which has the goal of obtaining accelerated ions with energies ranging from a few volts to a few tens of volts. An important difference between the plasma-etching application and the propulsion application of ECR plasma acceleration is that efficiency is not a prime concern in plasma etching. Therefore, the observation that ECR plasma etchers work at the appropriate energy levels is sufficient knowledge, and semiconductor researchers have not conducted significant research to uncover the details of the plasma-acceleration mechanism. We hope that the work reported here will show how to improve ECR plasma accelerators for the etching application, as well as for the propulsion application.

After reviewing the preceding discussion of the history of research on ECR plasma acceleration, it is natural to wonder why we have chosen to resurrect this concept for detailed feasibility study. Our motivation is three-fold: i) advancements in superconductor technology since the 1960s and especially recent work in high-temperature superconductors suggest that the mass and power consumption of solenoid coils for practical ECR plasma engines may be acceptably low; ii) advancements in microwave generator technology suggest that the mass of the microwave-power subsystem will be low and power-efficiency

will be high if state-of-the-art technology is used; and iii) advancements in the science of plasma physics and the application of plasma physics to electric propulsion technology now make it reasonable to expect that a quantitative scientific understanding of ECR plasma acceleration can be used to design optimized devices with efficiency and specific impulse performance higher than demonstrated in the 1960s. In particular, we are optimistic that the models developed in the present research effort provide an understanding that will guide future researchers to the design of efficient ECR accelerators.

Chapter 2

THEORY OF ECR PLASMA ACCELERATION

2.1 Simplified Analysis

A comprehensive model of flow processes associated with ECR plasma acceleration is reported in Section 2.3. However, before describing this analysis several important phenomena should be discussed separately. These phenomena include i) the coupling of microwave power to plasma at electron-cyclotron-resonance; ii) elastic-scattering effects; iii) inelastic-collision losses; iv) diffusion of plasma across and along magnetic field lines; and v) the conversion of kinetic energy of electron-cyclotron motion into directed kinetic energy of the flowing plasma by expansion through a diverging magnetic field. To provide a quantitative backdrop for this discussion Table 2.1 lists order-of-magnitude characteristics and operating parameters of the ECR plasma device used in our experimental work. The values given are approximate for typical conditions. More precise reporting of data describing the research device is included in Chapter 5. The calculations included in Sections 2.1.1 through 2.1.4 and Section 2.2 are based on many simplifying assumptions that are removed in Section 2.3. An important simplification of Section 2.1 is the neglect of axial heat transport by electron motion, as discussed in Section 2.3 and the Appendix.

2.1.1 Coupling Microwave Power to Electron Motion

For the acceleration mechanism studied in this research to be useful, the gas atoms must be ionized and energy must be added to the electron orbital motion. We accomplish this by coupling microwave radiation to electron motion in an ECR heating region in which the waveguide forces the radiation to propagate parallel to magnetic field lines. Textbooks frequently address the coupling problem by treating the plasma as a continuum medium with an index of refraction having both real and imaginary parts (Chen 1984). This treatment gives well-known results that can be outlined in a few sentences. The propagating radiation displays one cutoff and one resonance. The resonance occurs at the electron-cyclotron orbital frequency, which is the lower of the two frequencies. Below resonance, propagation occurs in what is commonly referred to as the *whistler mode*, with some attenuation of the microwave power resulting from electron collisions within the plasma. At resonance, ideal theory suggests that no propagation will occur; the plasma either absorbs or reflects all the electromagnetic radiation.

Table 2.1 Order-of-Magnitude
Operating Parameters of Existing ECR Research Device

Category	Parameter	Value
Device Characteristics	R-F Power Level	1 to 7 kW
	Microwave Frequency	2.115 GHz
	Accelerator Area	0.013 m^2
	Peak Magnetic Field On Axis	0.09 T
	Solenoid Diameter	0.4 m
	Vacuum in Tank While Operating	10^{-5} torr
	Working Fluid	Argon
	Mass Flow Rate	10^{-6} kg/s
	Atom Flow Rate	10^{19} s^{-1}
Plasma Parameters	Mean Electron Thermal Energy	10^{2} eV
	Mean Ion Thermal Energy	10^{-1} eV
	Electron-Cyclotron Radius	10^{-4} m
	Ion-Cyclotron Radius	10^{-3} m
	Peak Atom Density	10^{18} m^{-3}
	Peak Plasma Density	10^{17} m^{-3}
	Debye Length*	10^{-4} m

In ECR plasma acceleration, damping due to Doppler broadening associated with electron motion (an effect quite similar to Landau damping) has a favorable impact on the reflection and attenuation characteristics of the plasma. Specifically, the resonance effect occurs over a frequency band with a width corresponding to an appreciable fraction of the field frequency (Ben Daniel 1963). Furthermore, particles being carried downstream from their point of origin produce a gradual plasma boundary. This gradual transition from gas to plasma further reduces reflection of the microwave radiation (Crimi 1967).

Crimi (1967) experimentally observed that these effects reduce reflection to negligible levels, resulting in over 95 percent of the applied microwave power being absorbed into the

* The Debye length in this device is small compared to the linear dimensions of the plasma. This allows the plasma to be treated as quasi-neutral.

plasma at electron densities appropriate to ECR acceleration. We have confirmed that the majority of the microwave power is coupled into the plasma. Our measurements suggest that under certain operating conditions less than 10 percent of the microwave power is lost to reflection from the plasma or transmission through the plasma. Crimi observed the thickness of the heating region in his experiments to be a few centimeters. He concluded that the thickness of the coupling region was relatively insensitive to experimental conditions but was determined by electron damping and the magnitude of the magnetic-field divergence.

The observation that the ECR heating region has a well-defined, small thickness allows a simplification of the analysis of this device. Specifically, one can treat the ECR heating process by assuming that the microwave power couples to the electron orbital energy in a known region with an assumed variation of coupled power per unit volume. We assume that the microwave power couples to the plasma in a volume extending 2 cm upstream and 2 cm downstream of the theoretical plane of resonance (i.e., the plane at which the ECR condition is met). The assumed dimensions of the coupling region were based on the magnitude of the magnetic field gradient and on measurements of the electron temperature.

2.1.2 Elastic-Scattering Effects

Elastic scattering of electrons has two important effects on the process of ECR plasma acceleration. The first of these effects is dynamical friction on the electron motion. This process tends to heat the electrons and can reduce the total energy available for plasma acceleration. Second, the scattering of electrons upstream from the heating region into the neutral gas region results in the presence of ions in the neutral gas region. These ions may be produced by ionizing collisions between electrons and atoms or they can be carried there by ambipolar diffusion. Excessive upstream flow of plasma can lead to large wall losses or cause damaging sputtering of the dielectric window.

For the conditions given in Table 2.1, the characteristic time for electron-atom elastic-scattering collisions is estimated to be of the order 10^{-6} s. We base this estimate on an assumed elastic-scattering cross section of 5×10^{-20} m^2 (see for example Jahn 1968). The characteristic time for electron-electron-scattering collisions is ten to one-hundred times larger than for electron-atom scattering because the Coulomb-scattering cross section at the energy levels of interest is smaller than the electron-atom scattering cross section. The

electron-ion-scattering period is on the same order as the electron-atom-scattering period because the electron-ion-scattering cross section is on the same order as the electron-atom-scattering cross section. The mean electron velocity in the stream-wise direction (the convective velocity) in the heating region is the same as the mean ion (convective) velocity, and both are of order 10^3 m/s (based on the numerical solution of the dipole-moment problem as presented in Section 2.2). Therefore, one can estimate that on the average, the plasma will flow $\approx 10^{-3}$ m between electron-scattering events in the heating region.

Because electrons in the ECR heating region move an average distance of only $\approx 10^{-3}$ m before undergoing scattering collisions, these collisions can affect the distribution of thermal energy among the three translational degrees of freedom. As the plasma begins to accelerate and the kinetic energy associated with the electron transverse motion converts to directed motion of the plasma, further elastic scattering returns some of the energy in longitudinal electron motion to transverse motion. This transfer of energy continues until the plasma becomes essentially collisionless, approximately halfway through the acceleration process. The electron thermal energy remaining in motion parallel to the magnetic field lines contributes to propulsive thrust and enhances efficiency by producing ambipolar diffusion in the direction of the plasma flow. The analysis given in Section 2.3 treats these effects.

Elastic scattering may direct some electrons upstream from the heating region into the neutral gas region. These electrons will not travel upstream at their thermal diffusion velocity, but will move by ambipolar diffusion. In other words, it is possible that a local ambipolar electric field can retard the upstream migration of electrons while accelerating the upstream migration of ions. The mean migration velocity of the two charged species in ambipolar diffusion can not exceed the ion acoustic velocity (as described in text books such as Chen 1984). Based on the plasma parameters of Table 2.1, the ion acoustic velocity is of order 10^4 m/s.

If we assume that the plasma diffusing upstream into the window moves at the ion acoustic velocity, electrons in the diffusing plasma will travel a mean distance of about 1 cm before undergoing scattering collisions with atoms in the neutral gas region. Because the total electron-atom inelastic-scattering cross section is similar to the elastic scattering cross section, these electrons travel approximately the same mean distance before they undergo inelastic collisions with the atoms in the neutral gas region. The inelastic collisions damp the motion of the electrons through ionization and excitation of the neutral gas atoms.

Recombination reactions are less likely. Electron-atom collisions can ionize atoms several centimeters upstream of the heating region.

If the distance between the heating region and the window is too small, plasma can touch the dielectric window, causing sputtering and an important loss of jet power. Window losses in this device may be reducible by increasing the ratio of the magnetic field strength at the window to the field strength in the ECR heating region, thus mirroring the plasma downstream from the window.

2.1.3 Inelastic-Collision Losses

The most important inelastic-collision processes to consider in analyzing the ECR plasma accelerator are electron-atom collisions that cause ionization and atomic line radiation. A simple analysis neglecting double ionization can provide information about the magnitude of inelastic-collision effects. We assume that power lost per unit volume of plasma due to ionization and excitation collisions can be expressed by the following empirical relationship:

$$P_{ina} = n_e n_a \left(\langle \sigma_i v_r \rangle U_i + \sum_j \langle \sigma_j v_r \rangle U_j\right) \tag{2.1}$$

where U_i is the ionization energy, σ_i is the ionization cross section for electron-atom collisions and v_r is the electron speed relative to the atoms. The summation over j refers to the jth excitation reaction resulting from electron-atom collisions in which U_j refers to energy level and σ_j refers to the collision cross section to produce that excited state. The notation $\langle \sigma v_r \rangle$ represents the product of a reaction cross section and the electron velocity averaged over the electron velocity distribution.

Dugan and Sovie (1964 and 1967) and later Brophy (1984) demonstrated that the term under the summation sign in Eq. (2.1) can be approximated by considering a single equivalent, lumped excited state characterized by a total-excitation-collision cross section, σ_{ex}, and a lumped excitation energy, U_{ex}. Dugan and Sovie also showed that U_{ex} may be approximated by

$$U_{ex} = (U_l + U_i)/2 \tag{2.2}$$

where U_l is the lowest excitation energy level. Using this lumped excitation approximation, Eq. (2.1) becomes

$$P_{ina} = n_e n_a (<\sigma_i v_r> U_i + <\sigma_{ex} v_r> U_{ex}). \quad (2.3)$$

For atomic argon, U_l is 11.55 eV and U_i is 15.76 eV. Because the two averaged products in Eq. (2.3) are approximately equal* for argon at the energy level of interest, one might expect that the minimum energy cost of producing ions through inelastic-collision processes in this device would be approximately 30 eV. If such an *ion production cost* could be achieved in ECR plasma acceleration, we could expect very efficient accelerator operation. Although there were some reports of such high efficiency reported in the experimental work of the 1960s, these reports were later shown to be the result of erroneous measurements made in the presence of excessively high vacuum system back pressure (Crimi 1967). Therefore, inelastic-collision processes alone cannot account for the low thrust efficiencies measured. The following is a qualitative discussion of how to optimize ionization process in an ECR plasma accelerator to produce the low ion production cost alluded to in the preceding paragraph.

The results presented in Section 4.3 support the central points of this qualitative discussion. For this discourse, the *ionization region*, refers loosely to a volume of plasma near the ECR heating region in which the plasma density and electron temperature are high and the mean stream-wise velocity is low. This terminology is useful because the combination of high electron temperature and high plasma density result in high rates at which electrons produce ions by impact with atoms. Because of the high densities and temperatures, significant line radiation must emerge from the ionization region.

By the time it reaches a distance significantly downstream of the ionization region, the plasma will have accelerated to a velocity about one order of magnitude higher than the velocity within the ionization region. From the continuity and state equations for a plasma, we know that the plasma density and the electron temperature will have dropped considerably at this velocity. Therefore, significantly downstream of the ionization and heating regions, the volumetric rate of ionization and radiation lost from the plasma will be relatively low.

---

* The values of these averaged products, also called rate coefficients, are calculated in Appendix A based on measured collision cross sections and theoretical models of electron-atom-collision cross sections for argon.

Upstream of the ionization region, near the gas-injection ports, the fractional ionization is much lower than downstream of, or in the ionization region. We refer to this area of relatively low ionization as the *neutral gas region.* We recognize that even in the neutral gas region, some ionization is likely to occur. The rate at which atoms diffuse out of the neutral gas region into the ionization region is a function of the conditions in the neutral gas region. For a specified mass flow rate and cross-sectional area, the continuity equation suggests that the mean density of gas atoms entering the ionization region varies inversely with the mean thermal diffusion velocity. Because the thermal diffusion velocity is proportional to the square root of the gas temperature, one way to control the mean thermal diffusion velocity of gas atoms, and hence the atom number density, is to control the gas-injection temperature. For a fixed mass flow rate, another way to control the number density is to control the cross-sectional area of the accelerator.

The magnitude of the gas density entering the ionization region is important in determining the rate of production of ions because the electron-atom collision frequency depends directly on gas density. Hence, we can expect the plasma density in the ionization region to increase with increasing gas density. To optimize ion production in an ECR plasma engine, it is desirable to control the plasma conditions in the ionization region to ensure that the mean free path through which an atom will drift downstream before being ionized by electron impact is approximately equal to the thickness of the ionization region. In this way, the vast majority of atoms are singly ionized in the ionization region with a minimum of excess inelastic electron-atom collisions. If the mean free path for ionization is significantly smaller than the thickness of the ionization region, excessive electron-heavy collisions will take place, robbing thermal energy from the electrons in the plasma and reducing efficiency. If the mean free path for ionization is much larger than the thickness of the ionization region, a significant fraction of gas atoms will pass through the ionization region as neutral particles and engine efficiency will suffer due to poor propellant utilization.

Either electron-atom or electron-ion collisions can produce double ions in ECR plasma acceleration. The rate coefficient for double ionization of argon in electron-atom reactions at temperatures of interest for propulsion is less than one-tenth as large as the rate coefficient for single ionization (see Appendix A). The product of the densities of ions and electrons in the ionization region of the accelerator can be expected to be less than one-tenth of the product of the densities of atoms and electrons (as shown in Section 4.2). The rate

coefficient for electron-ion double-ion production is similar to the rate coefficient for electron-atom ionization at relevant temperatures (see Appendix A). Therefore, we expect electron-ion double-ion production to take place at or below the rate at which electron-atom double-ion production occurs. Double-ion production should account for no more than ten to twenty percent of the propellant mass flow in an optimized ECR plasma engine using argon propellant.

From the preceding discussion, we see that the requirements imposed by a desire to minimize losses due to inelastic-collision processes will place severe limits on the plasma density, and hence, the thrust density of a practical ECR plasma engine. This will be especially true of ECR engines made to work using propellants, such as argon, that have large cross sections for inelastic collisions. Probably the only way that ECR plasma engines can be made to operate at both high thrust efficiency and high thrust density is to use deuterium as a propellant. The advantage of deuterium over other possible propellants is that after deuterium is ionized, no additional inelastic collisions can take place between plasma electrons and the ions. As such, a high-density ECR plasma engine using deuterium propellant could operate at high efficiency even if the mean free path for an atom to be ionized is a small fraction of the thickness of the ionization region.

The low atomic mass of deuterium requires that deuterium-based ECR plasma engines be designed to operate only at very high specific impulse. For example, at a specific impulse of 3000 lbf•s/lbm, deuterium ions exiting an ECR engine would have a directed kinetic energy of only about 9 eV. In this case, if the ion production cost of deuterium ions was 30 eV, the maximum theoretical efficiency of the engine, accounting for ion production losses only, would be 23 percent: too low to be of interest. If the specific impulse of the system is 15,000 lbf•s/lbm, the ions will have a kinetic energy of about 230 eV, and the corresponding maximum theoretical efficiency would be about 88 percent. Including other practical loss mechanisms, a deuterium-based ECR plasma engine might have a microwave-to-jet power efficiency of as high as 80 percent, more than high enough to be of interest.

We presented the qualitative discussion of the effects of inelastic-collision losses in the ECR plasma engine because inelastic collisions profoundly affect the applicability of this device. ECR engines using argon and other propellants that have large cross sections for inelastic electron-ion collisions will be limited to low thrust density operation because of

losses associated with inelastic collisions.* These devices may, however, have the promise of delivering high efficiency throughout a wide specific impulse range, although this promise is yet to be proven. To obtain high thrust density, ECR engines will have to use deuterium propellant and only at high specific impulses (greater than about 10,000 lbf•s/lbm).

2.1.4 Cross-Field Diffusion

An additional loss mechanism to be considered in an accurate description of ECR plasma acceleration is the power lost to the walls of the accelerator due to diffusion of charged, energized species across magnetic field lines. To analyze this loss mechanism to a first approximation, it is useful to compare the characteristic time required for diffusion to the walls with the time required for plasma to move through the accelerator due to the dipole-moment body force. The ratio of these two quantities illustrates the relative significance of cross-field diffusion in ECR plasma acceleration.

The *Bohm time* is the time constant for diffusion across magnetic field lines in a cylindrical geometry such as the ECR plasma accelerator. It can be estimated (Chen 1984) by :

$$\tau_B \approx 8eBR^2/kT_e \tag{2.4}$$

where B is the magnetic field strength, R is the radius of the accelerator, and T_e is the electron temperature. Equation (2.4) is derived using the empirical Bohm (1949) formula based on Fick's diffusion law. A physical interpretation of the Bohm time is simply the time period over which a significant fraction of the plasma would diffuse across field lines due to Bohm diffusion in the absence of other effects.

The diffusion coefficient found using the Bohm formula is about 10^2 m^2/s, several orders of magnitude higher than the diffusion coefficient of 10^{-3} m^2/s predicted by the classical diffusion equation. If the 1960's work on ECR plasma acceleration was based on the assumption of classical diffusion, this would explain why the effects of the diffusion losses were not appreciated. We have not found any reference to theoretical consideration of wall losses in our review of the literature of the 1960's work. The reason for the departure from classical theory to Bohm diffusion is still not well understood, but some

---

* As discussed in Chapter 6, charge exchange losses may limit efficiency even at low plasma density.

researchers (e.g., Schmidt 1979, Longhurst 1978, or Kaufman 1962) have suggested that the process is related to plasma instabilities or **ExB** drifts. Because Bohm diffusion gives good results over a wide variety of plasma conditions (Chen 1984), we assume that it is sufficiently accurate to model the transport of plasma across the magnetic field in ECR plasma acceleration. We also make this assumption in the analysis presented in Section 2.3 in a manner consistent with assumptions made in the theory of electrostatic ion propulsion (Longhurst 1978).

The time required for the plasma to accelerate downstream in ECR plasma acceleration depends on the average connective velocity of the plasma, v_{av}, and the characteristic distance, L, over which the plasma accelerates:

$$\tau_A \approx L/v_{av} \ . \tag{2.5}$$

The average connective velocity of the plasma is related to the electron energy and the atomic mass of the ions according to the approximate expression

$$v_{av} \approx [kT_e/(2M)]^{1/2} \tag{2.6}$$

where M is the ion mass. Equation (2.6) is simply a mathematical statement of our assumption that the plasma is accelerated to a kinetic energy (per ion) that is of the same order as the initial electron thermal energy. Combining terms,

$$\tau_A \approx L[(2M)/kT_e]^{1/2}. \tag{2.7}$$

If L is approximately twice the radius of the accelerator (an assumption consistent with previous accelerator designs), the ratio of the characteristic time for diffusion to the characteristic time for acceleration is given by:

$$\tau_B/\tau_A \approx 2.8eRB/(kMT_e)^{1/2}. \tag{2.8}$$

For effective operation of this device, it is desirable to have $\tau_B/\tau_A > 1$. If this condition is not met, radial diffusion could cause a significant fraction of the plasma energy to be lost to the accelerator wall.

The ECR plasma accelerators that were tested in the 1960s operated at $\tau_B/\tau_A < 1$. Hence, the present estimate suggests that early ECR accelerators could not have yielded high efficiency. A significant fraction of the plasma diffused across field lines to heat the wall of the accelerator almost as fast as the ionization process produced the plasma and before the ions could accelerate significantly down-stream. Therefore, a large fraction of the ionization and excitation energy required to produce the plasma was lost to the accelerator wall, along with any useful kinetic energy or electron thermal energy the plasma had acquired. This may explain why most of the measured thrust efficiencies of the early devices were well below the desired 50 percent.

2.2 Calculation of Plasma Streamlines in a Diverging Magnetic Field

The plasma physics community often reacts with doubt regarding the effective separation of the plasma from the magnetic field in the ECR plasma engine. This doubt sometimes extends to or other space propulsion devices that use similar magnetic nozzle configurations. The doubt stems from familiarity with results obtained from standard magnetohydrodynamic (MHD) plasma models that are useful in many situations. Standard MHD models treat the plasma as a single fluid with either a finite electrical resistivity or a zero resistivity (e.g., Thompson 1962 or Gerwin 1990).

In the MHD case of zero resistivity one typically sets all electric fields in the plasma to zero based on the assumption that charge carriers will move to cancel the electric fields in a period short compared to the other relevant time constants of the problem. This assumption automatically precludes the possibility of plasma motion across field lines because any cross-field motion would induce, by Faraday's law of induction, an electric field within the plasma. Such an electric field would produce infinite eddy currents that would act to prevent motion across field lines.

In using MHD models for finite resistivity, the researcher usually calculates the electrical resistivity of the plasma using particle-collision frequencies and then assumes that currents flow instantaneously in response to electric fields with magnitude and direction given by Ohm's law. In this case, plasma motion across field lines causes ohmic dissipation within the plasma. The application of either of these MHD models to problems of field separation in the ECR plasma engine would lead to erroneous results because these MHD models ignore the inertial properties of the electrons in the plasma.

The inertia of electrons in a plasma ensures that the response of the plasma to an electric field cannot be instantaneous. Even in the case of a completely collisionless plasma the current that flows in response to an applied electric field is not infinite and all such fields are not immediately screened out. In the ECR plasma engine particle inertia can allow significant separation of the plasma from the applied magnetic field, producing a well-defined but diverging beam of plasma that is accelerated to infinity to produce thrust. Another way of saying this is that the inertia of the plasma is large enough that azimuthal (Faraday induction) currents are not large enough to force the plasma to stay on field lines as it would if electron inertia were neglected. To illustrate this point, we have created a very simple dynamic model of the ECR plasma engine to calculate the shape of streamlines without complicating factors that may tend to obscure the issues.

2.2.1 Assumptions

We have used a collisionless, steady-state, cold plasma model to calculate the shape of the plasma streamlines in the ECR plasma engine. Our model, which is an extension of Kosmahl's model (1967), allows us to calculate the angle by which the plasma diverges during separation from the magnetic field. This divergence angle is important because the fraction of the momentum of the flowing plasma that is useful for thrust varies as the cosine of the divergence angle. Before presenting the details of the model, it will be useful to discuss the assumptions we have made.

This problem involves the acceleration of a plasma that is initially at a specified velocity and position in a cylindrical coordinate system. An applied, diverging magnetic field emanates from a collection of one or more current loops located parallel to the plane of the r-axis (radial) of the coordinate system and centered on the z-axis (axial). Although we neglect random thermal energy effects in the cold plasma approximation, we do include the effects of electron-cyclotron motion perpendicular to magnetic field lines in the present model. This electron-cyclotron motion results in the plasma having a finite diamagnetism. By symmetry the azimuthal components of the magnetic field of a current loop, or a collection of radially concentric current loops, is zero and the gradient of such a field has only radial and axial components. Therefore, the grad-**B** drift motion places a requirement on the initial conditions that an azimuthal electron current be present.

The only forces initially available to accelerate the plasma are the **J**x**B** (Lorentz) body force associated with the azimuthal grad•**B** current and the diamagnetic body force as-

sociated with the interaction of the plasma diamagnetism with the applied, diverging magnetic field. The azimuthal component of each of these body forces is zero. The plasma therefore accelerates only radially and axially.* Thermodynamic pressure gradient forces are neglected in our cold plasma approximation. No mechanism is available to apply an external torque to the plasma. Radial and axial plasma velocity can induce azimuthal currents. As stated above, azimuthal current in this arrangement induces radial and axial forces. Because no mechanism is present to provide net azimuthal body forces and associated azimuthal plasma velocity, there is no induced radial or axial current. The absence of radial and axial currents significantly simplifies this analysis.

2.2.2 Analysis

We use a Lagrangian* formulation to describe an electron fluid and an ion fluid that interact through an induced ambipolar electric field. The electron fluid equation of motion in the Lagrangian formulation under the assumptions described above must account for forces acting on the fluid due to i) the interaction of the volumetric magnetic dipole moment with the applied magnetic field, ii) the ambipolar electric field, and iii) the Lorentz force interaction between the electron guiding centers and the applied magnetic field. To develop an equation that can describe the electron fluid motion and account for these effects we call upon guiding center theory. The equation of motion for guiding center particles that can be used to calculate the motion of the electrons is:

$$\ddot{\mathbf{R}}_{gc} = \frac{\mathbf{F}_{\mu}}{m_s} + \frac{q}{m_s}(\dot{\mathbf{R}}_{gc} \times \mathbf{B} + \mathbf{E}_{sp}), \tag{2.9}$$

where $\mathbf{R}_{gc}$ is the position vector of the guiding center of the particle's motion. Equation (2.9) is derived in Appendix D based on guiding center theory as described by Northrop (1963). We now recall that for a cold plasma (ie., a plasma fluid in which thermal effects are negligible with respect to other energy-related effects such as magnetic field pressure), the fluid equation of motion in the Lagrangian formulation has the same form as the equation used to model particle motion. In the present case, the dipole-moment force term in the guiding center equation is included in the fluid equation of motion as a body force term. The Lagrangian form of the electron fluid equation of motion therefore becomes:

---

* This observation has recently been addressed analytically by Hooper (1991).

* The term Lagrangian here refers to the use of a control volume that moves with the fluid in contrast to the usual Eulerian approach in which the fluid moves through a fixed control volume.

$$\ddot{\mathbf{R}}_e = \frac{\mathbf{F}_\mu}{m} + \frac{q}{m}(\dot{\mathbf{R}}_e \times \mathbf{B} + \mathbf{E}_{sp}), \tag{2.10}$$

For the ion fluid, the equation of motion does not have to include a dipole-moment force because we neglect the initial perpendicular motion of the ions in this model and we can therefore use :

$$\ddot{\mathbf{R}}_i = \frac{e}{M}(\dot{\mathbf{R}}_i \times \mathbf{B} + \mathbf{E}_{sp}) \tag{2.11}$$

$\mathbf{E}_{sp}$ is the ambipolar electric field, $\mathbf{R}$ is the position vector associated with an infinitesimal fluid element, and m and M are the electron and ion mass, respectively. Notice that the Lorentz force terms in Eqs. (2.10) and (2.11) could also have been written as electric-field terms using Faraday's law of induction. Faraday's law suggests that the Lorentz force terms in Eqs. (2.10) and (2.11) have the same effect as if an azimuthal electric were present in the flow. $\mathbf{F}_\mu$ is the mean force acting on electrons due to the interaction of the electron-cyclotron magnetic dipole and the applied diverging magnetic field. The magnetic-dipole moment of electrons is an effect of their Larmor motion around the lines of the applied magnetic field.

The force on such a dipole in a diverging field is well known and given by

$$\mathbf{F}_\mu = \nabla(\mu \cdot \mathbf{B}) \, . \tag{2.12}$$

Because the dipole-moment vector of gyrating electrons is always anti-parallel to the local magnetic field vector and is invariant in a slowly changing magnetic field*, Eq. (2.12) reduces to

$$\mathbf{F}_\mu = -\mu \nabla \mathrm{B} . \tag{2.13}$$

For the case of a cylindrically symmetrical magnetic field, such as that produced by a collection of current loops arranged on the z-axis of a cylindrical coordinate system, the components ($\hat{r}$, $\hat{\theta}$, and $\hat{z}$) of $\mathbf{F}_\mu$ are

$$F_\mu = -\mu \frac{\partial B}{\partial r}, \quad F_\theta = 0, \quad F_z = -\mu \frac{\partial B}{\partial z}. \tag{2.14}$$

---

* The validity of the assumption of adiabatic invariance of μ in the context of the ECR plasma engine is addressed by Kosmahl (1967).

The magnitude of the dipole moment of a spiraling charged particle depends only on the kinetic energy associated with the particle's cyclotron motion and the magnitude of the magnetic field. The initial thermal energy of the plasma is treated in this model through the dipole-moment accelerating force in Eq. (2.14). As the plasma accelerates under the influence of $\mathbf{F}_\mu$, the kinetic energy of the electron's cyclotron motion is converted to directed kinetic energy of both ions and electrons.

The condition of quasi-neutrality is valid throughout the region of interest in this device, so the ion plasma density can be assumed equal to the electron plasma density. Because no radial or axial electric current is induced, we can assume that the radial and axial coordinates of the position vectors for the ion and electron fluid elements are the same ($r_i = r_e \equiv r$ and $z_i = z_e \equiv z$). We specify the azimuthal coordinates for the ion and electron fluid elements individually because azimuthal electrical current may flow. By specifying the $\hat{\theta}$ component of Eq. (2.11), the equation of motion for the azimuthal coordinate of the ion fluid can be written as

$$\ddot{\theta}_i = \frac{e}{rM}(B_r\dot{z} - B_z\dot{r}) - \frac{2\dot{r}\dot{\theta}_i}{r}. \tag{2.15}$$

Notice that the $\hat{\theta}$ component of electric field is always zero due to cylindrical symmetry. The corresponding equation for the electron motion can be written in an analogous way, using Eq. (2.10). Because no net torque is applied to the plasma

$$\ddot{\theta}_e = \frac{e}{rm}(B_z\dot{r} - B_r\dot{z}) - \frac{2r\dot{\theta}_e}{r}. \tag{2.16}$$

It is useful to add Eq. (2.10) to Eq. (2.11). Because the ambipolar electric field drops out, one obtains

$$m\ddot{\mathbf{R}}_e + M\ddot{\mathbf{R}}_i = \mathbf{F}_\mu + e\{\dot{\mathbf{R}}_i \times \mathbf{B} - \dot{\mathbf{R}}_e \times \mathbf{B}\}. \tag{2.17}$$

Using Eqs. (2.14) and (2.16) with ($r_i = r_e \equiv r$), the $\hat{r}$ component of Eq. (2.17) is

$$\ddot{r} = \frac{erB_Z(\dot{\theta}_i - \dot{\theta}_e) - \mu\frac{\partial B}{\partial r} + r(m\dot{\theta}_e^2 + M\dot{\theta}_i^2)}{m+M}. \tag{2.18a}$$

Similarly, the $\hat{z}$ component of Eq. (2.17) is

$$\ddot{z} = \frac{erB_r(\dot{\theta}_e - \dot{\theta}_i) - \mu\frac{\partial B}{\partial z}}{m+M} \quad . \tag{2.18b}$$

Equations (2.15), (2.16), (2.18a) and (2.18b) can be expressed as a set of eight first-order, ordinary differential equations. We solved these equations numerically given initial values for r, z, $\dot{r}$, $\dot{z}$, θ_e, θ_i, $\dot{\theta}e$, and $\dot{\theta}i$. Due to symmetry, initial values of θ_e and θ_i can be set to zero by properly arranging the coordinate system. In most cases of interest, $\dot{\theta}i$ will have an initial value of zero and the grad•B drift will determine the initial value of $\dot{\theta}e$.

2.2.3 Calculated Results

We have used this set of equations to predict the shape of the plasma streamlines for the ECR device developed and tested in this research program. For the present calculation, we approximate the magnet coil as a single-turn current loop. To calculate the components and derivatives of the magnetic induction field needed in Eqs. (2.15), (2.16), (2.18a) and (2.18b) one can apply the Biot-Savart law to a simple current loop to obtain the well known results

$$B_r = \frac{\mu_o Ia}{2\pi}\int_0^{\pi} \frac{z\cos\phi'}{(a^2+z^2+r^2+2ar\cos\phi')}d\phi'$$

and (2.19)

$$B_z = \frac{\mu_o Ia}{2p}\int_0^{\pi} \frac{a-r\cos\phi'}{(a^2+z^2+r^2+2ar\cos\phi')}d\phi' \quad .$$

We take the radius of the current loop, a, to be 0.2 m and the total current in the solenoid, I, to be 2.5 x 10^4 A. We differentiated Eq. (2.19) analytically to allow application of the chain rule in numerically calculating the partial derivatives of the magnetic field components in Eq. (2.17) and Eq. (2.18). Equations (2.15), (2.16), and (2.18) were integrated using a differential equation package developed by Lawrence Livermore National Laboratory (Hindmarsh, 1982). We used a third-order (Simpson's rule) method to numerically integrate Eqs. (2.19) and the equations for the derivatives of the magnetic field.

We calculated streamlines for plasma elements starting at eleven initial radial locations. For each of the eleven cases, the initial value of z was specified to be 0.05 m. Initial values of r were varied between r=0.005 m and r=0.05 m, inclusive. The initial value of $\dot{r}$ was

taken to be zero, while the initial value of $\dot{z}$ was taken to be 100 m/s. The atomic mass of the ions was 40 amu, representative of argon. We calculated the magnetic moment of the spiraling electrons based on an assumed mean energy per electron of 200 eV. We chose this energy level to yield a specific impulse of approximately 3000 lbf•s/lbm (30,000 N•m/s).

Figures 2.1 and 2.2 show the results of these calculations. Figure 2.1 depicts the calculated streamlines with radial position as a function of axial position for plasma elements initiating from eleven different locations. Calculated magnetic field lines are shown as dotted lines, and there are clear indications that the plasma crosses the magnetic field lines at a large angle. The plasma divergence for the specific configuration studied here is very large, and most of the separation from the magnetic field occurs two to five meters from the accelerator. From conservation of mass, one can show that near where separation takes place, the plasma density has dropped by four to five orders of magnitude relative to the plasma density at the source of the plasma flow. This result suggests that effective performance testing of ECR plasma engines may require the use of vacuum facilities with very large pumping capacities and radii of up to five meters.

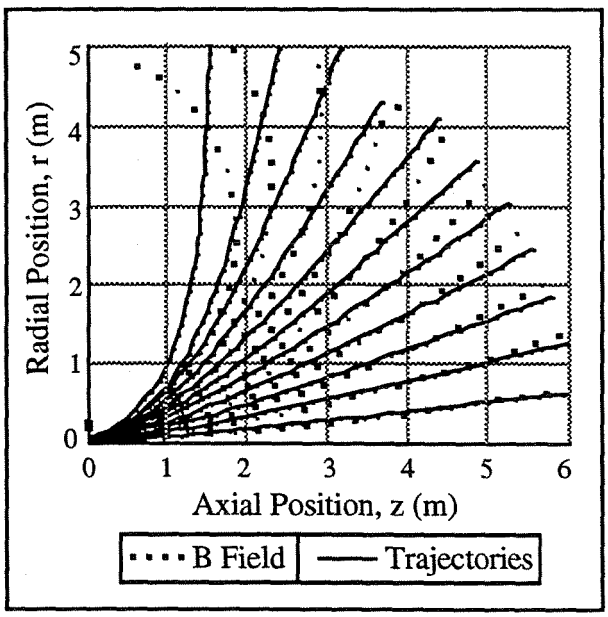

Fig. 2.1 Calculated streamlines for eleven initial plasma positions.

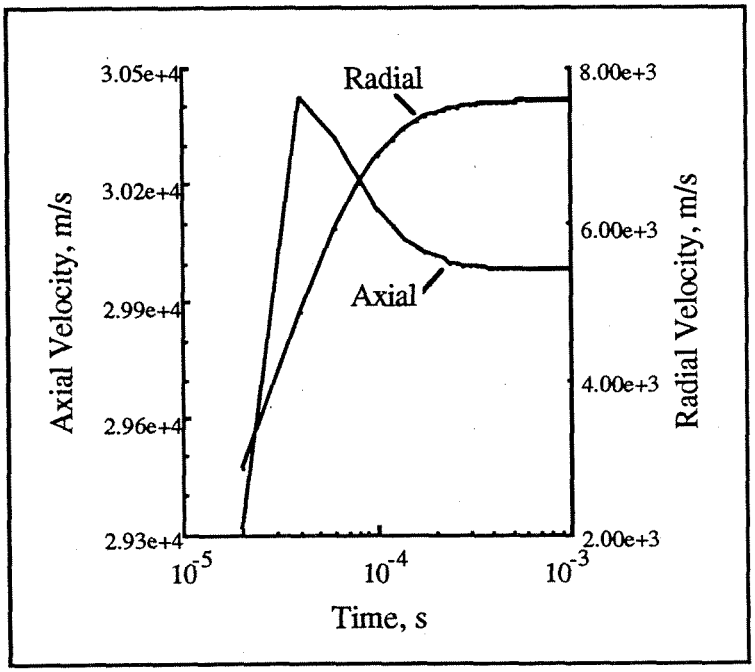

Fig. 2.2a Axial and radial plasma velocity as a function of time for a plasma element with initial radial position 0.5 cm from the accelerator axis and an initial axial position 5.0 cm from the centerline of the magnet coil.

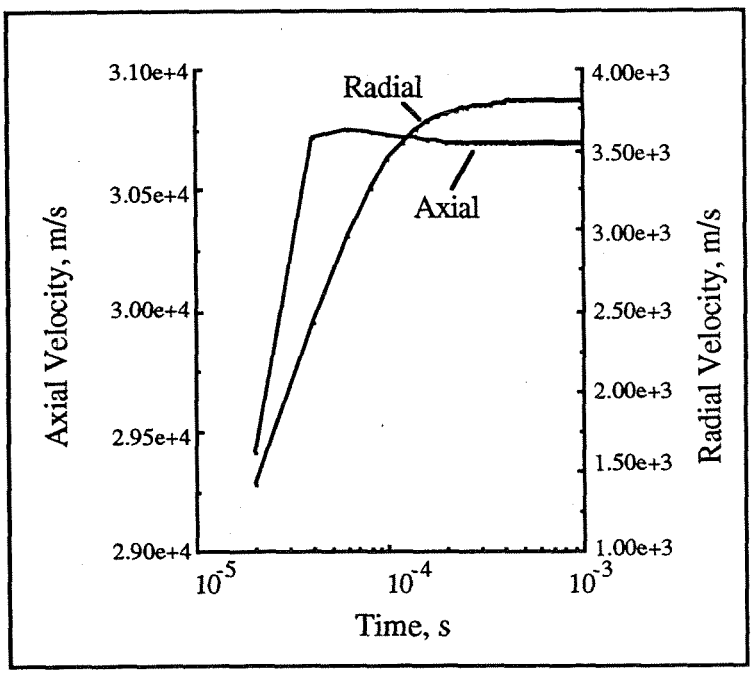

Fig. 2.2b Axial and radial plasma velocity as a function of time for a plasma element with initial radial position 1.0 cm from the accelerator axis and an initial axial position 5.0 cm from the centerline of the magnet coil.

Figure 2.2 shows the time variation of the radial and axial components of the plasma velocity for two specific initial positions. In Fig. 2.2a, the plasma element has an initial radial coordinate of r=0.005m. In Fig. 2.2b, the plasma element has an initial radial coordinate of r=0.01m. Figures 2.2a and 2.2b both show that the radial and axial components of the plasma velocities approach a constant value in less than about 10^{-3} s. This asymptotic behavior of the plasma velocity further supports the conclusion that the plasma completely separates from the field of the magnetic nozzle.

In both Figs. 2.2a and 2.2b, the initial rate of acceleration of the plasma is approximately 1.5×10^9 m/s, corresponding to a space-charge induced ambipolar electric field of about 625 V/m. For the conditions of Figs. 2.2a and 2.2b, the axial component of the plasma velocity is always much larger than the radial component of the plasma velocity. However, we do not always find this to be true. For example, several cases depicted in Fig. 2.1 display radial velocity components greater than axial velocity components after separation from the magnetic field. Calculated energy loss due to azimuthal motion of ions and electrons is less than 2 percent in all cases studied. Our calculations support Kosmahl's observation that the plasma divergence angle (and hence the divergence loss) depends strongly on the ratio of the radius of the magnet coil to the initial radial location of the plasma element.

These calculations also show that where the plasma separates from the magnetic field, the majority of the electron-cyclotron energy has been converted to ion kinetic energy. This suggests that the beam divergence may be somewhat independent of the plasma acceleration mechanism. As such, these calculations may provide information regarding the field-separation issues associated with other types of plasma engines that make use of magnetic nozzles.

Because it may be impractical to design high-current magnet coils with radii much larger than the plasma engine radii, it is desirable to find a way to reduce beam divergence without excessively increasing the radii of the primary coil used to produce the field in the magnetic nozzle. An approach suggested by this research is that of the *plasma lens*. The idea of the plasma lens is similar to that of the magnetic lenses used to focus charged particles in high-energy physics, with the difference that the plasma lens works with a quasi-neutral beam of plasma possessing collective effects.

We have analyzed the theoretical feasibility of the plasma lens in reducing the divergence of the plasma beam produced by an ECR plasma engine. To do this, we have conducted calculations similar to those used to produce Fig. 2.1 and Fig. 2.2, but we assumed that four low-current, large-radius current loops exist along with the single-turn current loop. We specified the radius of these additional current loops to be 0.6 m and the current level in the loops to be 200 A each. The direction of the current was taken to be opposite to the direction of the current in the primary coil. We did this to produce a more abrupt divergence of the magnetic field downstream of the primary coil to force a more abrupt separation of the plasma from the field. The axial locations of the four loops were 0.4, 0.525, 0.65, and 0.775 m downstream.

Fig. 2.3 shows the calculated effects of adding this magnetic lens to the magnetic nozzle. In Fig. 2.3 the dotted lines are the first seven streamlines from Fig. 2.1. The solid lines in Fig. 2.3 are the streamlines with the added magnet coils. Because the field of the plasma lens coil opposes the field of the primary magnet, the plasma trajectories initially diverge more rapidly with the lens than without it. However, in the process of completely separating from the magnetic nozzle, the calculated streamlines eventually bend back toward the centerline and divergence is less with the lens than without it. The four black squares displayed in Fig. 2.3 show the radii and axial locations of the lens coils.

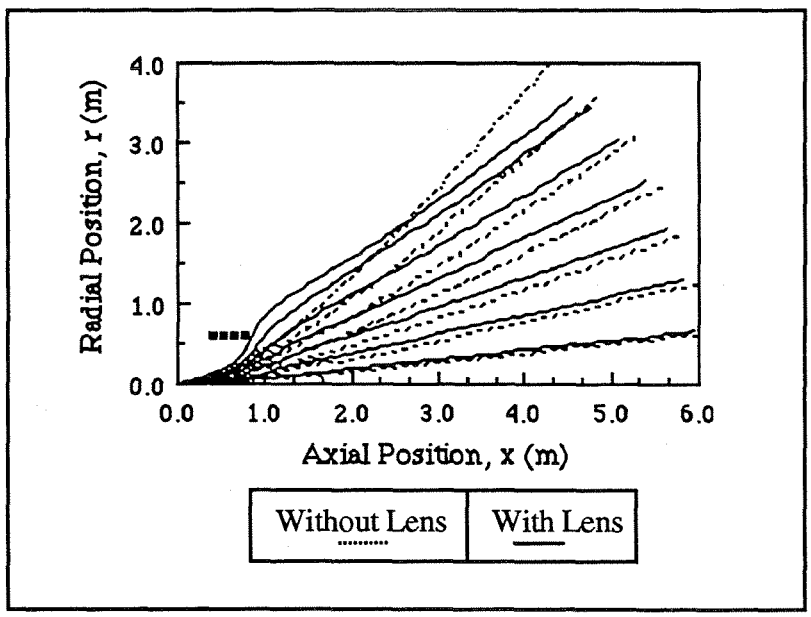

Fig. 2.3 Calculated streamlines with and without a plasma lens added to the magnetic nozzle. Solid lines are streamlines with the plasma lens; dotted lines are streamlines without.

Given that the ultimate purpose of the ECR plasma accelerator is to generate thrust for space propulsion, it is necessary that we translate these calculations of plasma trajectories into quantitative estimates of the impact that beam divergence will have on the efficiency of an ECR plasma propulsion device. To do this we define the nozzle efficiency as the ratio of the jet power* that the device generates, including the effect of beam divergence, to the jet power that the device would generate if the flow were perfectly collimated. To accomplishing this estimate, it is necessary to integrate the axial component of the momentum flux of the moving plasma from the center of the beam to the outer edge of the beam.

In the process of calculating this integral we had to make an assumption regarding the radial distribution of the plasma density. We chose to take that the radial distribution of plasma density is uniform at z=0. This assumption is conservative because we expect the actual plasma density to be peaked near the centerline where the divergence angle is small. We calculate that the nozzle efficiency corresponding to the conditions of Fig. 2.1 is 0.24 and the nozzle efficiency corresponding to the conditions of Fig. 2.3 is 0.89. Beam divergence losses can therefore be expected to be large for a device like the one tested in our experiments, but controllable to tolerable levels of about 10 percent if beam collimating techniques such as the plasma lens are successfully developed and implemented.

2.2.4 Related Work

The work reported in Section 2.2 of this thesis is directly related to at least three other studies that sought to investigate the problem of the detachment of a plasma from a magnetic nozzle. Our analysis is most similar to the analysis of Kosmahl (1967) in that the assumptions regarding negligible terms are the same in the two approaches. All of the same physical effects addressed by Kosmahl are addressed in the present work. However, our analysis is simpler than Kosmahl's approach and should, therefore, be easier to apply to a wider array of important problems. It should be noted that whereas Kosmahl assumed a priori that the electron trajectories will move in accordance with Busch's Theorem,** the results of our calculations confirm the assumption that canonical angular momentum is conserved for both the ion and the electron fluids.

---

* For a definition of jet power, see Chapter 6.

** Busch's Theorem can be shown to be equivalent to the conservation of canonical angular momentum.

Hooper (1991) published an analysis of the plasma detachment problem that provides insights into why the plasma detaches from the field. Specifically, he showed that detachment takes place due to the finite inertia of the electrons and shows that detachment appears to be related to a dimensionless parameter defined by the square root of the product of the mass of the electron and the ion, the ion velocity, and the initial radial displacement. Recently, Goodwin (1992) extended Hooper's analysis to show more clearly the role of the dimensionless parameter in predicting if plasma detachment takes place. In other related work, Gerwin (1990) addressed the detachment problem using an MHD model. He chose to neglect the effects of electron inertia in his calculation of azimuthal electric currents. Without these inertial effects, Gerwin predicted no separation. Gerwin's result is, in a sense, in agreement with Hooper's treatment and the present work because it confirms that plasma separation takes place only in the presence of finite electron inertia. We therefore suggest that future MHD-type models should include the electron inertial effects in a manner consistent with the treatment presented here.

2.2.5 Conclusions

This theoretical study provides a simple technique for predicting the shape of the plume of an ECR plasma accelerator. We predict that the ECR plasma accelerator can produce an accelerated plasma beam that detaches from the field of the magnetic nozzle without collision-induced diffusion and without significant ohmic heating of the plasma. Furthermore, controlling the field-shape of the magnetic nozzle can limit the magnitude of the beam divergence. We introduced the idea of a plasma lens as a way to control beam divergence. Calculations suggest that a plasma lens can reduce beam divergence losses by almost a factor of seven without increasing the diameter of the primary coil used in the magnetic nozzle. However, even with a magnetic lens, plume divergence can be a significant loss mechanism for ECR plasma engines. Practical ECR-plasma-engine design must include a global optimization process in which magnet mass and power requirements are traded against plume divergence losses.

2.3 Quasi-One-Dimensional Model

We have formulated a steady-state, non-equilibrium, axial-flow model of the ECR plasma acceleration process to estimate the effects of the following physical processes i) upstream ambipolar diffusion; ii) cross-field radial diffusion; iii) various elastic-scattering phenomena; iv) inelastic-collision effects; and v) the dipole-moment, grad•B accelerating force. The magnitude of the applied magnetic field, the spatial derivative of the applied magnetic field, and the spatial power density of the coupled microwave radiation are assumed to be constant in time with a specified axial variation. Appendix B includes a derivation of the equations that comprise the model, including a plasma continuity equation, an atom continuity equation, a plasma momentum equation, and two energy equations. Appendix B, also presents the equations rewritten in the *explicit form* as they were used in the numerical work described in Chapter 4.

The plasma continuity equation written in the usual form for steady quasi-one-dimensional flow is

$$\frac{d(nuA)}{dz} = A(S_i + S_d) \tag{2.20}$$

where n is the number density of electrons or ions, u is the plasma velocity, and z is the axial coordinate. The source terms in Eq. (2.20) for the present model are given by

$$S_i = nn_a\langle\sigma_i v_e\rangle \tag{2.21a}$$

$$S_d = \frac{-nKT_e}{8eBr} \tag{2.21b}$$

where the brackets $\langle\ \rangle$ represent the average over the electron speed distribution. S_i is the ionization source term and S_d is the diffusions source term. In Eq. (2.21a), σ_i refers to the cross section for ionization of atoms by electron impact and v_e represents the electron speed. Equation (2.21b) is based on the assumption of Bohm diffusion, as discussed in Section 2.1.4.

In Appendix B we derive the momentum equation using a control volume analysis for a quasi-neutral fluid. In writing the momentum equation we found it convenient to neglect

some terms of order m/M with respect to those of order unity. Likewise, terms containing $M \pm m$ are approximated as M, for simplicity, producing:

$$\frac{M}{A}\left(\frac{d(nu^2A)}{dz}\right) = F_\mu + F_{drag} - \frac{dP_{//}}{dz} + M(uS_d + u_aS_i) \tag{2.22}$$

where F_μ is the volumetric dipole-moment force, F_{drag} is the drag term that accounts for the exchange of momentum due to the motion of the plasma relative to the neutral gas, u_a is the gas velocity, and $P_{//}$ is the component of the electron pressure parallel to the magnetic field lines. The volumetric dipole moment force is the product of the plasma number density and the average force on the electrons caused by their magnetic dipole interaction with the applied magnetic field:

$$F_\mu = -\frac{nW_\perp}{B}\frac{dB}{dz}, \tag{2.23}$$

where $W_\perp$ is the component of the electron thermal energy perpendicular to the field lines* and B is the local magnetic flux density. We derived Eq. (2.23) by multiplying the z-component of Eq. (2.13) times the plasma number density and substituting $W_\perp/B$ for μ.

The drag term is a function of the number densities and velocities of the plasma and the neutral gas as well as the electron thermal velocity and the rate coefficients for momentum exchange:

$$F_{drag} = nn_a(u_a - u)(M\sigma_{ia}|u_a - u| + m < \sigma_{ea}v_e >). \tag{2.24}$$

In Eq. (2.24) n_a is the gas number density, σ_{ia} is the cross section for ion-atom momentum exchange, and σ_{ea} is the cross section for electron-atom momentum exchange. The rate coefficient for momentum exchange between the ions and the atoms is approximated in this analysis by the product of the ion-atom momentum exchange cross section and the absolute value of the difference between the plasma velocity and the gas velocity because we neglect the thermal velocity of both of these species throughout this analysis.

---

* Thermal energy is not a vector quantity, so the use of the term *component* is may seem inappropriate to the reader who is unfamiliar with the lexicon of plasma physics. However, in describing a plasma species with different temperatures perpendicular and parallel to field lines, this terminology is conventional and is used throughout this document.

The term in Eq. (2.22) for the component of the plasma pressure gradient along the magnetic field lines originates from the equation of state for a plasma with an anisotropic temperature (see Chen 1984) and is written:

$$\frac{dP_{//}}{dz} = 2(n\frac{dW_{//}}{dz} + W_{//}\frac{dn}{dz}), \tag{2.25}$$

where $W_{//}$ is the component of the electron thermal energy perpendicular to the field lines.

The third governing equation we derive in Appendix B is the conservation equation associated with electron dipole moment energy,

$$\frac{1}{A}\frac{d(nuAW_{\perp})}{dz} = Q_{\perp} - uF_{\mu} + W_{\perp}S_d. \tag{2.26}$$

In Eq. (2.26) $Q_{\perp}$ represent the net flux of thermal energy flowing into the perpendicular component of the electron thermal motion. This term accounts for conversion into electron thermal energy of microwave energy near electron cyclotron resonance, the loss of electron thermal energy due to inelastic collisions with ions and atoms, and the exchange of energy between the perpendicular and the parallel components of the electron motion due to scattering collisions. An analogous expression, $Q_{//}$, is used to describe the flow of energy into the parallel component of the electron thermal motion and is used in the conservation equations for the parallel component of the electron thermal energy and total energy.

Mathematical expressions for $Q_{\perp}$ and $Q_{//}$ are:

$$\begin{aligned} Q_{\perp} &= P_{ECR} - \frac{F_{in}W_{\perp}}{W} + F_{el} \\ Q_{\perp} &= -\frac{F_{in}W_{//}}{W} - F_{el}, \end{aligned} \tag{2.27}$$

where P_{ecr} is the volumetric power density (energy per unit time per unit volume) at which microwave energy is converted to the thermal kinetic energy of electrons. The other two new terms in Eq. (2.27), F_{in} and F_{el}, describe electron thermal energy source/sink terms

associated with elastic and inelastic collisions, respectively. The equations for these collision-induced energy-source/sink terms are

$$F_{el} = \frac{n}{2}(W_{//} - \frac{W_{\perp}}{2})[n(\langle \sigma_{ei} v_e \rangle + \langle \sigma_{ee} v_e \rangle) + n_a \langle \sigma_{ea} v_e \rangle]$$

and (2.28)

$$F_{in} = n[n_a(U_i \langle \sigma_i v_e \rangle + U_{xa} \langle \sigma_{xa} v_e \rangle) + n U_{xi} \langle \sigma_{xi} v_e \rangle],$$

where U indicates the energy lost by electrons undergoing inelastic collisions. Subscripts in the top equation, which refers to electron elastic scattering phenomena, have the following definitions: *ie* for scattering off of ions, *ee* for scattering with other electrons, and *ea* for scattering off of atoms. Subscripts in the bottom equation, which refers to inelastic collision effects, have the following meanings *i* for ionization of atoms, *xa* for inelastic excitation of atoms, and *xi* for inelastic excitation of ions. A single excitation energy for ions and different single excitation energy for atoms each with an associated rate coefficient appear in Eq. (2.28) to account for the loss of electron energy due to inelastic, line-radiation-producing collisions. Section 2.1.3 and Appendix A both include discussions of this lumped approximation for the excitation process.

The second term of the right-hand side of Eq. (2.26) represents the loss of dipole moment energy due to the work done on the plasma by the interaction between the electron-cyclotron magnetic dipoles and the applied magnetic field. The last term on the right-hand side of Eq. (2.26) accounts for the loss of dipole moment energy due to diffusion of plasma to the walls of the accelerator. This term is a result of the assumption that any electron making contact with the walls of the accelerator losses all of its thermal energy.

The last of the governing equations that describe plasma flow processes in our model is the energy equation for the parallel component of the electron thermal energy. It is derived in Appendix B by multiplying the plasma momentum equation (Eq. (2.22)) by u and subtracting the result and Eq. (2.26) from the plasma energy equation. It takes the form:

$$\frac{1}{A}\frac{d(nuAW_{//})}{dz} = Q_{//} - 2nW_{//}(\frac{u}{A}\frac{dA}{dz} + \frac{du}{dz}) + W_{//}S_d + MS_i(\frac{u^2}{2} + u_a u) \qquad (2.29)$$

A calculation of thermal conduction along the magnetic field lines due to electron heat transport will show that the assumption of zero axial heat conduction that has been implicit in this discussion is not perfectly valid. In fact, use of the Spitzer-Harm heat conduction formula (Spitzer and Harm, 1953) shows that the characteristic time required for the axial flow of thermal energy due to electron heat transport in this plasma can be a few orders-of-magnitude less than the characteristic time for the axial flow of energy due to convection.

However, it is well known that several types of instabilities that can be present in a plasma such as this one can reduce the effective thermal conductivity to well below the value calculated by the Spitzer-Harm formula. Further, the introduction of detailed calculations of axial heat transport into the model increases the order of the system by two, and we have been unable to identify and justify two additional boundary conditions. For this reason, and because the stiffness of the system increased considerably when we attempted calculations including axial heat transport, we have been unable to obtain results for the case of finite axial heat conduction. Also, in the present problem the two components of electron temperature are not necessarily in equilibrium, so the Spitzer-Harm formulation of thermal conductivity is not strictly valid.

We have therefore bound the problem using the extreme assumptions of zero axial heat conduction (already discussed) and of perfect axial heat conduction (isothermal conditions) for the parallel component of the electron energy. In the case of perfect axial heat conduction for the parallel component of the electron energy, the perpendicular component of the electron temperature was not explicitly assumed to be effected by axial heat conduction. However, the perpendicular component of the electron thermal energy was assumed to be coupled to the parallel component of the electron temperature via electron scattering effects in the same manner the two components of the electron temperature are coupled in the equations described above. The changes needed in the boundary conditions and the derivations of the equations used to model the plasma for the case we refer-to as quasi-isothermal conditions are described in Appendixes B and C.

Equation (2.22) does not change for the quasi-isothermal case because is does not explicitly include an dependency on the gradient of $W_{//}$. The momentum equation (Eq. (2.22)) does change in the quasi-isothermal case because the gradient in the parallel component of the electron temperature is contained in the pressure gradient term. The quasi-isothermal version of Eq. (2.22) is

$$\frac{M}{A}\left(\frac{d(nu^2A)}{dz}\right) = F_\mu + F_{drag} - 2W_{//}\frac{dn}{dz} + M(uS_d + u_aS_i). \tag{2.30}$$

The conservation equation associate with the electron dipole moment energy, Eq. (2.26), does not change for the quasi-isothermal case because it includes no specific dependency on $W_{//}$. The most significant change in the model that one encounters in considering the quasi-isothermal case is the elimination of the equation for the conservation of the parallel component of the electron thermal energy. This equation is not part of the model in the quasi-isothermal case because, by definition we assume

$$dW_{//}/dz = 0.$$

To be useful as a predictive tool the model comprised of Eqs. (2.20), (2.22) or (2.30), (2.26), and (2.29) must also include a set of boundary conditions so that we can solve the equations. The boundary conditions developed for this analysis are derived and presented in Appendix C. Another differential equation describing the rarefied flow of the neutral atoms, which we assume to be in thermal equilibrium with the walls of the accelerator, is also needed for these calculations and is described in the Appendix B. With the additional equation for the neutral gas, the model becomes a fifth order system. It is a fourth order system when we assume quasi-isothermal flow. The purpose of the model is to provide predictions of measurable plasma parameters and the performance of the ECR accelerator. The model can predict parameters such as plasma density, neutral gas density, the two components of the electron temperature, plasma potential, and ion velocity. Chapter 4 describes these predictions while Chapters 6 and 7 outline a comparison between these predictions and our experimental measurements.

Chapter 3

EXPERIMENTAL APPARATUS AND PROCEDURES

3.1 Apparatus

Figure 3.1 shows the major features of the apparatus used in this research including the vacuum system and the microwave power system. Key to the microwave power system is the transmitter, similar to the type used in JPL's deep space spacecraft-tracking network. The transmitter uses a 20-kW-output, water-cooled, klystron amplifier-tube, that is powered by a direct-current power supply which runs off of a three-phase, 400-Hz motor-generator set. A 1-W solid-state, signal generator provides microwave input to the amplifier. The transmitter output is stable, single-mode, microwave power at a frequency of 2.115 ± 0.05 GHz, adjustable through power levels between 20 W and 20 kW. The transmitter provides output to a rectangular waveguide in a linearly polarized, transverse-electric mode.

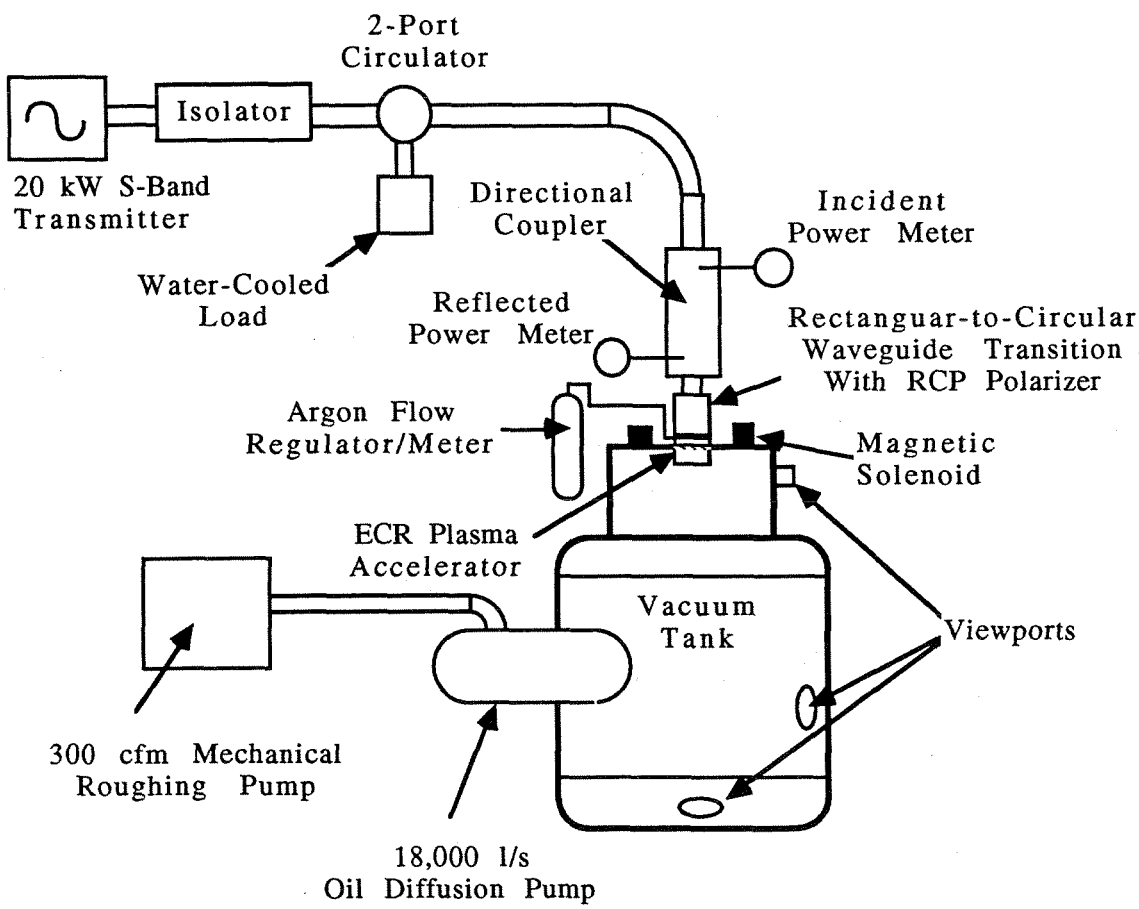

Fig. 3.1 Experimental apparatus for ECR-plasma engine research.

A water-cooled isolator protects the transmitter from damage by any unexpected reflection of the microwave power. The 2-port circulator shown in the figure is a safety device that switches the microwave power into a water-cooled load in case the transmitter is inadvertently turned on when the apparatus is not correctly configured. The directional coupler is a waveguide structure that is attached to microwave power meters that measure both incident and reflected power. By measuring incident and reflected power, we obtain an indication of how much microwave power is coupled into the plasma. The rectangular-to-circular waveguide transition with a Right Circular Polar (RCP) polarizer provides the desired RCP microwave power to the accelerator. The circular waveguide that delivers this radiation to the engine has an inner diameter of 5.04 in (12.8 cm).

We use the argon flow meter and regulator to control the flow of argon propellant into the accelerator at flow rates varying from 5 to 100 standard cubic centimeters per minute (sccm). The magnetic solenoid is a water-cooled copper coil with approximately 150 turns and a diameter of approximately 30 cm. To achieve a resonance field of 0.075 T in the diverging region of the field, the solenoid requires a steady current of 160 A at about 25 V. A shunt diode is provided as a safety measure in case of a power system failure. The steady-state operating temperature of the solenoid coil in this apparatus is between 150° F and 160° F using room-temperature inlet cooling water supplied through a pressure differential of about 30 psi..

The vacuum system in this apparatus consists of a stainless-steel, cylindrical, vacuum tank with dimensions of approximately 2m x 2m. An 18,000-l/s (22 inch diameter) oil diffusion pump backed up by a 300-cfm mechanical roughing pump provides pumping of propellant gases. Entrainment of diffusion-pump oil into the vacuum tank is limited by a baffle system that is cooled by a refrigerated, convective, liquid-alcohol cooling loop. The best vacuum achieved by this system as measured by an ionization gauge is $1x10^{-7}$ torr. At typical operating flow rates of 5 to 10 sccm of argon, the tank pressure is in the range of $2x10^{-5}$ to $4x10^{-5}$ torr, as measured by an ionization gauge.

The vacuum tank has four plate-glass view ports with diameters ranging from 5 in to 12 in. To prevent microwave leakage through these windows, fine-mesh stainless-steel screens have been spot-welded over each window on the inside of the tank. Similarly, to prevent unwanted arcing in the diffusion pump, or microwave leakage to the mechanical roughing pump, screens have been spot-welded in the tank over orifices to these devices inside the tank.

3.2 Accelerator Design and Operating Procedure

Figure 3.2 shows the ECR plasma accelerator tested in this research. Noteworthy features of this design include the double-window configuration, the conductive isolation scheme, and the twenty-hole gas-injector system.

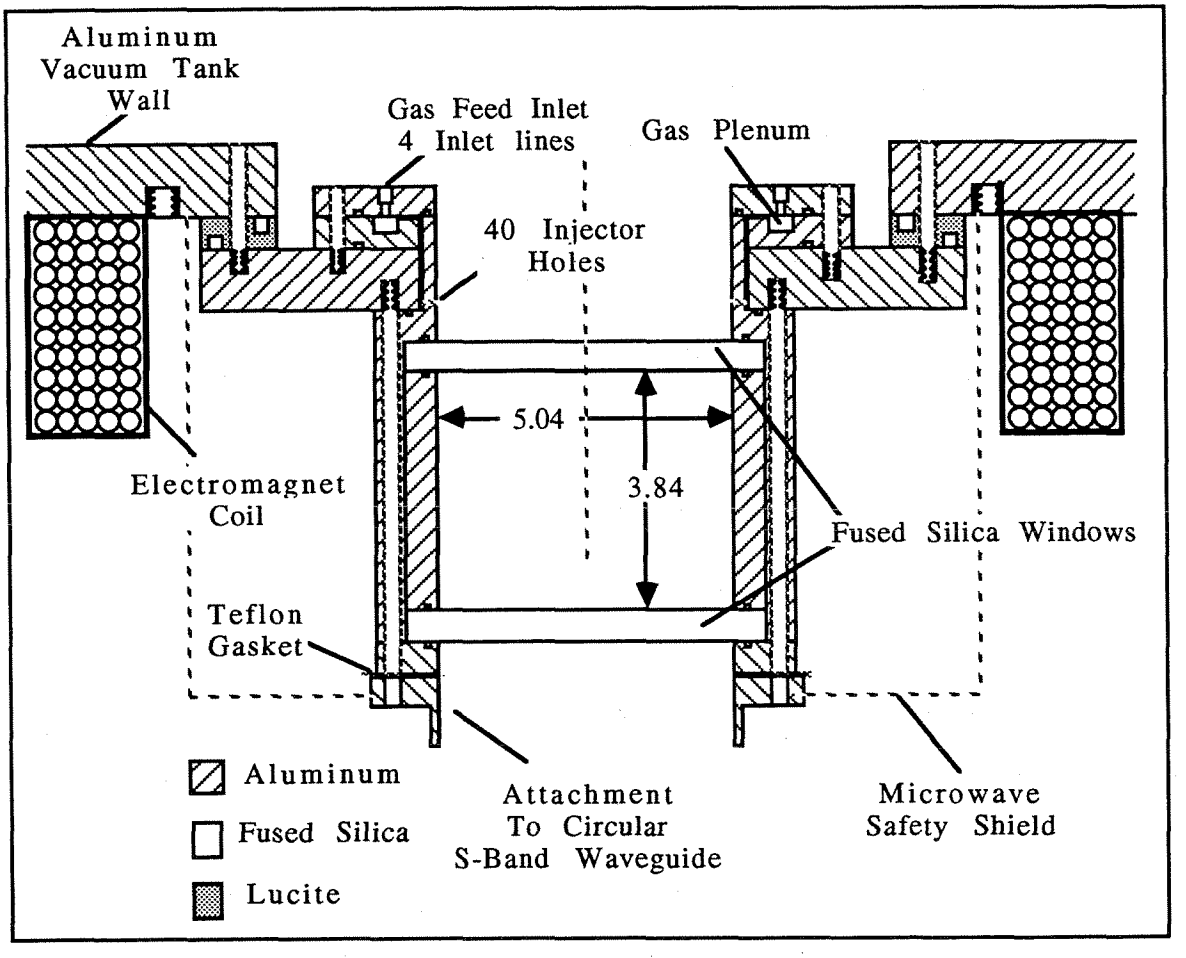

Fig. 3.2 Schematic of ECR plasma test device.

Two fused-silica windows separate the vacuum from the atmosphere and to allow microwave power into the accelerator. We included two windows in this design instead of a single window to i) ensure redundancy for safety purposes in case of a window failure, and ii) to reduce window reflective losses. This window design was accomplished with the aid of an existing numerical model which suggested that at a separation distance of 3.84 in, reflection from the first window would cancel reflection from the second window to enable maximum microwave power transmission. We measured the actual reflective losses to

be 4 percent for this window configuration at the design operating frequency of 2.115 GHz. At a slightly off-design frequency, we found the reflection to be 0.2 percent, suggesting a small error in either the assumed dielectric properties of fused silica or the computing package that was used in the calculation.

This accelerator is electrically isolated to insure that the plasma accelerating potential is not grounded. A conductive circuit to ground could occur in at least three ways: through the waveguide, through the vacuum tank walls, or through the gas-feed lines. To prevent conduction of electric current through the waveguide or the vacuum tank wall, we place a Teflon gasket between the engine and the waveguide and we place a Lucite ring between the vacuum tank wall and the engine, as shown in Fig. 3.2. Insulating nylon bolts connect the engine to the vacuum tank wall through the Lucite ring. Ceramic tubing connects the engine to the gas-feed system. Because this arrangement of conductive isolation allows for the possibility of microwave power leaking through the Teflon gasket, an aluminum microwave shield must be placed between the waveguide and the wall of the vacuum tank, as depicted in the figure.

A manifold system delivers gas to the system without violating the electrical isolation of the device. The manifold includes four six-inch-long, quarter-inch-outer-diameter ceramic tubes attached to the engine by way of four quarter-inch aluminum tubes that have been arc-welded in-place. The gas passes from the inlet lines into an annular plenum, then through a 0.02-in annular feed path to the 40 injector holes. The injector hole diameters are 0.04 in.

We have tested this accelerator using argon propellant at gas flow rates from 5 to 20 sccm and at input microwave power levels from 0.4 to 7.0 kW. Visual observation of the emitted radiation reveal some interesting effects: i) the plasma trajectory appears to have the predicted shape, ii) the plasma is stable and easy to reproduce, and iii) the plasma reflects only a few percent of the applied microwave power. Figures 3.3a and 3.3b are photographs of the ECR plasma accelerator in operation. In Fig. 3.3a, the divergence angle appears somewhat exaggerated due to the viewing angle. The observed divergence half-angle is approximately 22 degrees, 20 cm downstream of the ECR heating region, as numerically predicted for the existing coil configuration. The regular pattern observable in both photographs is due to the presence of the microwave safety screen.

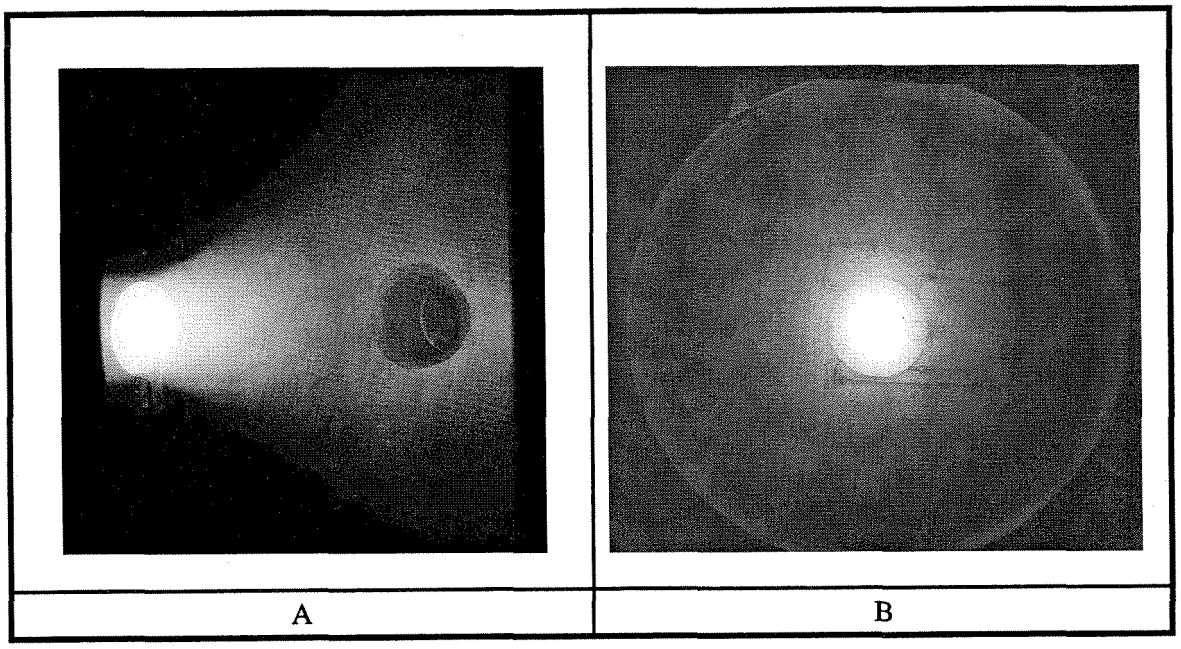

Figs. 3.3a and 3.3b Photographs of the ECR plasma plume.

The procedure used to ignite the ECR plasma consists of the following steps: i) pump down the vacuum system, ii) establish the desired propellant flow rate, iii) adjust the solenoid current to approximately 160 A, and iv) turn-on the microwave transmitter. At microwave power levels greater than about 500 W the plasma appears spontaneously. At power levels between 300 and 500 watts we have found that we can start the plasma by modulating the current level in the solenoid. The plasma is then stable as long as we maintain the solenoid current close to the optimum value of about 160 A. Microwave power levels below about 30 are not sufficient to maintain the plasma discharge bright enough to be observed visually.

When we adjust the solenoid current to levels significantly above the optimum value, over about 200 A, the plasma appears to lose its well-defined shape and essentially fills the front end of the vacuum chamber. The most likely explanation is that the resonance region is being moved downstream of the engine exit, and coupling of microwave power to the plasma is occurring downstream of the engine in the vacuum tank. Similarly, when we turn the solenoid current down to less than about 155 A, but more that 150 A, we see bright spots over each injector hole. We think this happens because the resonance region is being moved over the injector holes where the gas density is highest We have not been able to observe any plasma ignition at solenoid current levels of less than 150 A, corre-

sponding to sub-resonant magnetic field strength. The color of the plasma changes as a function of gas flow rate and microwave power level. At a flow rate of 10 sccm of argon, the plasma has a reddish tint at power levels below 500 W. The predominant color of the plasma is blue at power levels between 500 W and about 1kW. Above 1kW, the plasma is noticeably brighter and appears white in color.

3.3 Diagnostics

We have designed and used the following instruments to characterize the ECR plasma produced in this research effort: i) an electrostatic energy-analyzer, ii) a beam-density analyzer, iii) Langmuir probes for measuring electron temperature, iv) emissive probes for measuring plasma potential, and v) a diamagnetic loop.* We used each of these diagnostics to differing degrees of success in this experimental program. A brief description of the design, operating procedure, and the motivation for developing each of these devices follows. Chapter 5 of this dissertation presents quantified results of measurements that we made with these diagnostics and a comparison of these results with the results of theoretical calculations.

3.3.1 Electrostatic Energy-Analyzer

The electrostatic energy-analyzer is a device used to measure one spatial component of the ion energy distribution in a relatively low density plasma such as we encountered in this research. This device was important to our effort because it provided measurements of the directed energy of the ions as a function of spatial location. These measurements gave an indication of the effectiveness of the ECR plasma acceleration process in producing accelerated ions. Also, this diagnostic provides a measurement of the ion energy distribution, a key indicator of energy lost due to collision processes that thermalize the ions in the plasma.

The specific type of electrostatic energy analyzer that we used is sometimes referred-to in the literature as a retarding potential analyzer (Manos 1985) or a gridded energy analyzer (Haug, Felden, and Schirmann 1968). As described by Hutchinson (1987) this class of diagnostic probe represents an extension of Langmuir probe methods. The general concept of the gridded probe is to sweep the electrostatic potential of a grid through which the

---

* These diagnostics were developed in close collaboration with Dr. Dennis Fitzgerald who is acknowledged for his valuable contributions in the areas of instrument design, troubleshooting, fabrication, and data collection.

plasma ions are directed to flow. By measuring the ion current that flows through this deflector grid and differentiating the resulting voltage-current curve, one obtains a measurement of the ion energy distribution. The electrostatic energy-analyzer that we designed for this research uses a four grid configuration as depicted in Fig. 3.4. Figure 3.5a is a photograph of the device fully assembled. Figure 3.5b is a photograph of the device partially unassembled to show the plates that hold the grids in place and the insulator structure.

The first grid is electrostatically grounded and serves to separate the internal structure of the device and laboratory electronics from the electromagnetic noise produced by the plasma. The second grid is an electron repeller. A direct current power supply maintains the electron repeller at a negative potential to remove the electrons from the plasma stream. We found that it was necessary to hold the second grid at a potential of between two hundred and three hundred volts below ground potential to effectively strip off the plasma electrons. The third grid is the ion-repeller screen whose potential is varied from zero to some positive value to obtain information regarding the ion energy distribution. The fourth grid is the electron suppresser, which forces secondary electrons back into the collector plate. The suppression of secondary electrons is necessary because as the ions, which are at energy levels as high as a few hundred electron volts, hit the ion collecting surface, or any of the grids, they produce copious secondary electrons that can cause spurious currents to be detected on the ion collecting surface. The fourth grid is conductively tied to the second grid and therefore is also at a negative potential of two to three hundred volts below ground. All four of the grids are composed of stainless steel screen material with an open-hole fraction of the about 15 percent and a mesh size of about 0.1 mm.

A non-ferrous, sheet metal beam-attenuator is attached to the structure of the probe upstream of the first grid. The attenuator has a hole in it on centerline to let only a relatively narrow plasma beam into the screen area. The hole's diameter is approximately 5 mm. A thin titanium foil with 100 micron openings in it and an open fraction of about 10 percent is spot welded over the hole in the attenuator to reduce beam density. We added the attenuator system to the probe after initial tests indicating that the plasma electrons were not adequately attenuated by the electron repel grid. Another addition that we made to the probe after its initial design was to use a battery system to control the potential of the ion current collecting surface to approximately -20 volts. We found that this affected improved ion collection and thereby reduced noise in the collected current signal.

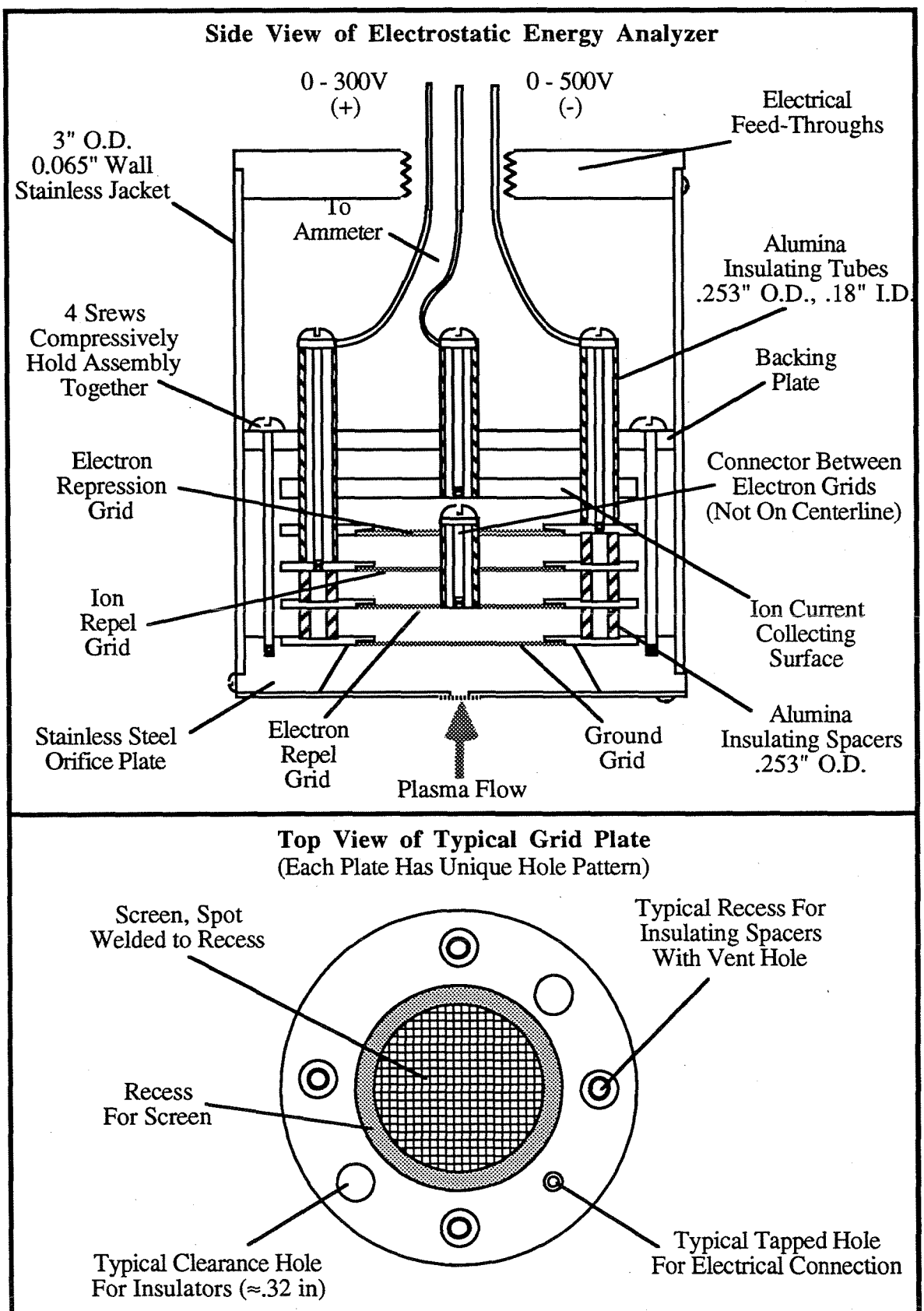

Fig. 3.4 Approximate Full-Scale Drawing of Electrostaic Energy Analyzer

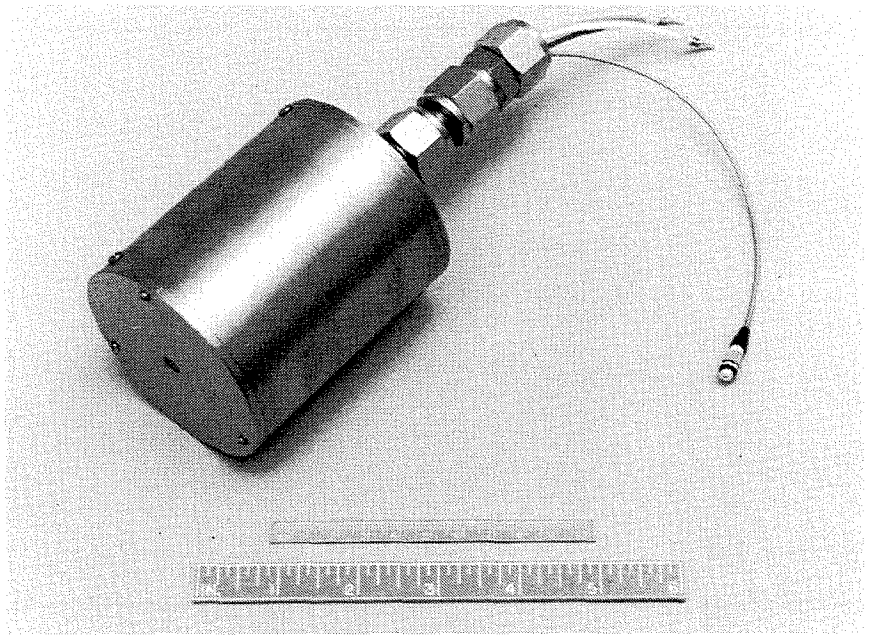

Fig. 3.5a Photograph of Assembled
Electrostatic Energy Analyzer Probe

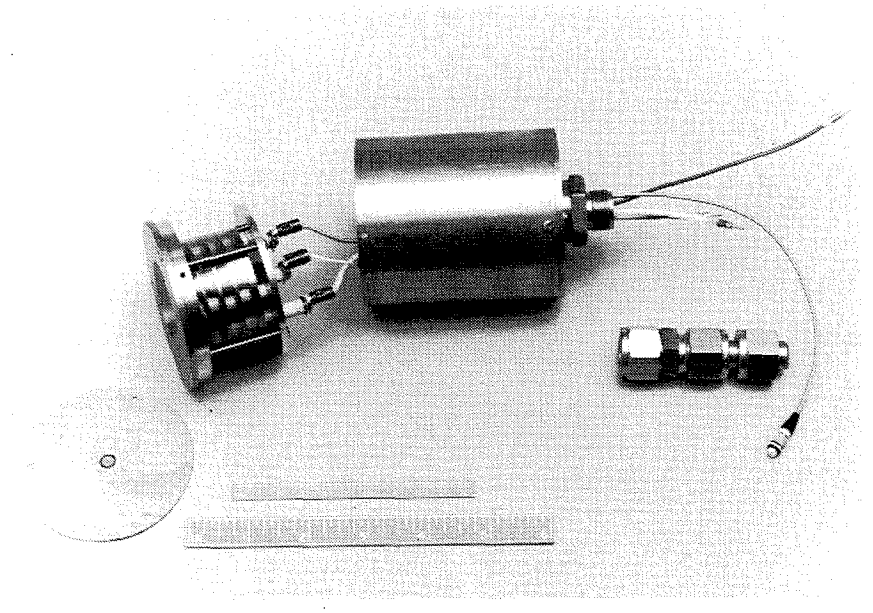

Fig. 3.5b Photograph Partially Dis-Assembled
Electrostatic Energy Analyzer Probe

An important design criterion that we had to consider in developing this probe was the well-known Child-Langmuir law of space-charge-limited current in a planar diode:

$$n_0 = \frac{4}{9u_0}\sqrt{\frac{2}{eM}}\frac{\varepsilon_0|\phi|^{3/2}}{d^2}. \tag{3.1}$$

In Eq. (3.1) n_0 is the plasma density entering the space between the grids, u_0, is the velocity at which the plasma enters this region, d is the distance between grids, and ϕ is the potential drop between the grids. Derivations of Eq. (3.1) can be found in many elementary text books on plasma physics or related subjects (see Chen 1984 or Jahn 1968). For our retarding potential analyzer, the grid spacing was about 0.005 m; the potential drop between, the second and third grid was typically 300 volts; and the velocity of the incoming ions was typically a few thousand meters per second. As such, the space charge limited maximum plasma density that our analyzer could handle in an argon plasma was in the range of 10^{14} to 10^{15} m^{-3}. We think the plasma density in the accelerated beam in the region where the analyzer was located was typically one to two orders of magnitude higher than this Child's law limit. The device functioned properly in spite of the high plasma density because the combined effect of the attenuator and ground screen reduced the plasma density between grids by a factor of about one hundred and because the finite diameter of the hole in the attenuator plate ensured that the behavior of the plasma between grids was not governed exclusively by the purely one-dimensional Childs law analysis. Two-dimensional effects are less restrictive than are suggested by Eq. (3.1).

In the experiments reported here, a digital pico-ammeter detected the ion collector plate current and provided a zero to one volt output to a high impedance x-y pen plotter. We used the pen plotter to display the ion current on the vertical scale and the ion repel grid voltage on the horizontal scale. Current levels detected by the pico-ammeter were usually within one or two orders of the nanoamp range. Figure 3.6a is a photo-reduced copy of a typical probe characteristic for our electrostatic energy analyzer. Notice, in the figure, that the collected current contains considerable noise. This noise was probably caused by turbulence or ion acoustic waves in the plasma and was also apparent in the measurements we made using other probes, as described later in this chapter. Fig. 3.6b shows the ion energy distribution obtained from the probe characteristic of Fig. 3.6a.

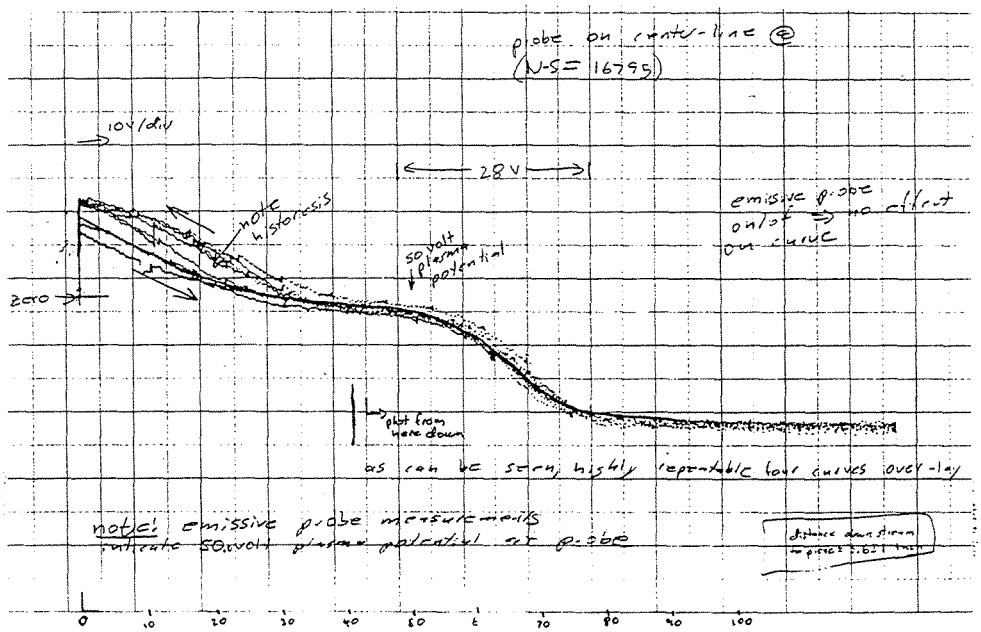

Fig. 3.6a Typical Probe Characteristic for Electrostatic Energy Analyzer

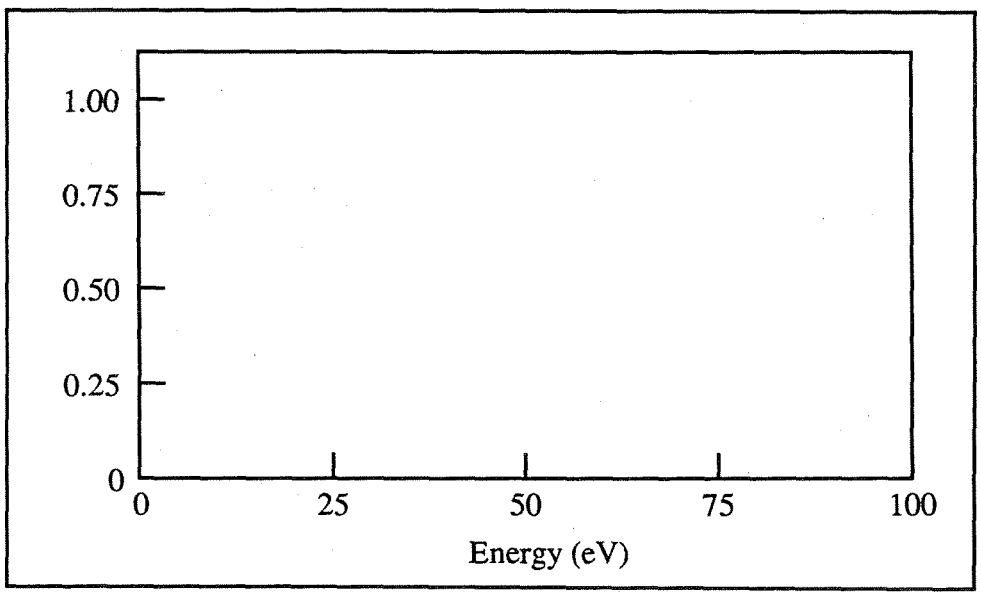

Fig. 3.6b Ion Energy Distribution Obtained From Example

We obtained ion energy distributions from probe characteristics like the one shown in Fig. 3.6a using simple graphical techniques. The first step in the data reduction was to draw a smooth line through the noisy curve. This smooth line represented the probe characteristic that we then differentiated to obtain the ion energy spectra. Likewise, differentiation was accomplished graphically by measuring the slope of the smoothed probe characteristic at several points. By plotting the inverse of the resulting slopes versus the grid potential at which they were measured, we obtained a curve showing the measured ion energy distribution. A presentation and discussion of the results of several measurements made in this fashion is presented in Chapter 5.

3.3.2 Beam-Density Analyzer

The beam-density analyzer consists of a simple hollow metallic ion collecting tube that collects ion current. Figure 3.7a is a simplified drawing of this device. Figure 3.7b is a photograph of the device partially unassembled showing its internal structure. The collecting tube is located inside a grounded Faraday cup with an open aperture of known area (7.85×10^{-5} m^2). This geometry allows the plasma stream to pass through the aperture into the Faraday cup. A power supply applies a negative potential of two-to-three hundred volts to the ion collection tube to remove electrons from the plasma beam and allow a measurement of ion current. The geometry of the ion collection tube ensures the suppression of secondary electrons. We calculate the beam density by knowing the area of the collecting aperture and the magnitude of the ion current.

This device was developed as part of this research effort to provide a direct measurement of the magnitude of the flux of plasma that is accelerated downstream from the ECR region. Such measurements are important because they give an indication of the fractional propellant utilization of the accelerator. Measured centerline beam densities obtained from this device at a location approximately 30 cm downstream of the engine are about 1.0 mA/cm^2 at mass flow rates of 5 to 10 sccm of argon and microwave power levels of up to 3 kW. Chapter 5 includes a description of the results of use of this device under various operating conditions.

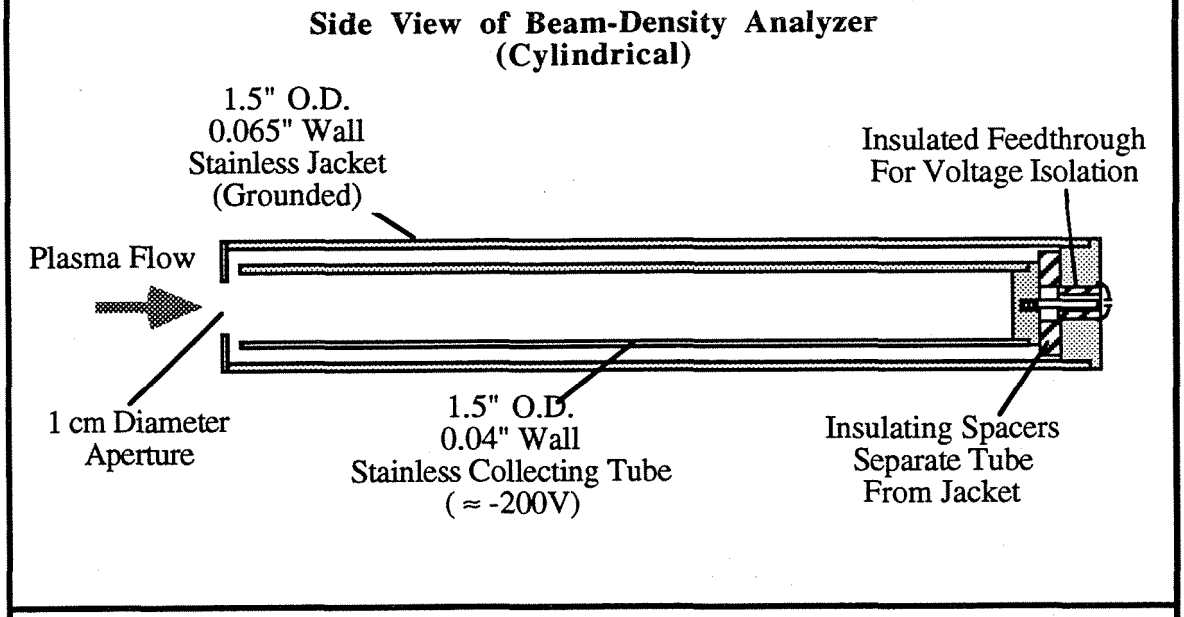

Fig. 3.7a Approximate Half-ScaleSchematic of Beam Density Analyzer

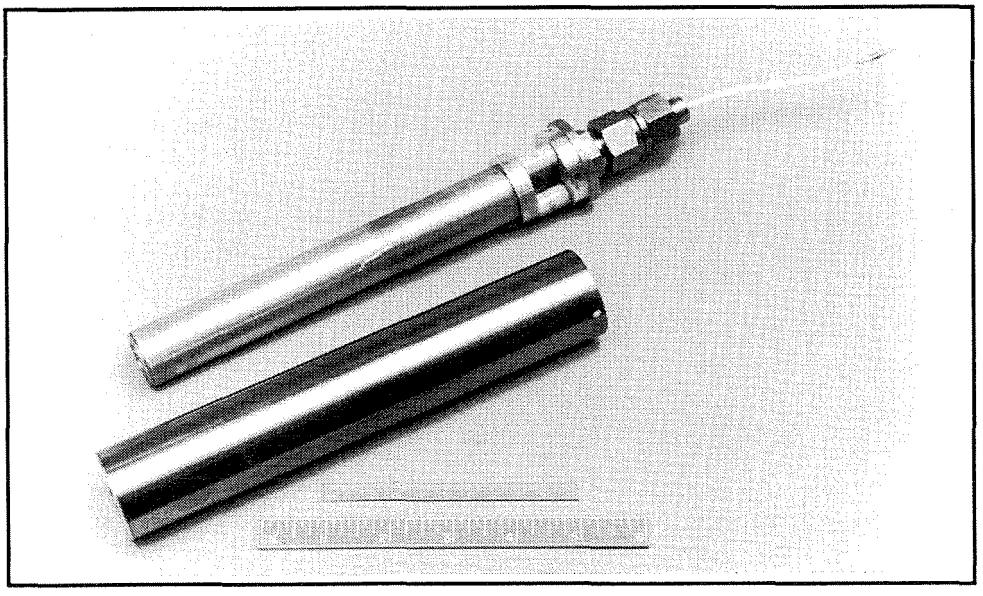

Fig. 3.7b Photograph of Partially Assempled Beam Density Analyzer

3.3.3 Langmuir Probes

We used cylindrical Langmuir probes oriented perpendicular and parallel to the local applied magnetic field to measure the perpendicular and parallel components of the electron temperature in a manner described by Crimi, Eckert, and Miller (1967). These

measurement are important because they shed light on how far the ECR heating effect drives the electron energy distribution out of thermal equilibrium. The theory behind the use of Langmuir probes to measure electron temperature is very well understood and documented and therefore will not be repeated here (see Hutchinson 1987 or Huddelstone and Leonard 1965). Our use of cylindrical probes to resolve the two components of electron temperature is based on Crimi's (Crimi, Eckert, and Miller 1967) work and on the work of Dote and Amemiya (1964). These authors suggest that this approach is useful when: i) the electron gyro-radius is smaller than the probe's dimensions and, ii) the probes are significantly longer than they are wide. In the ECR plasma engine experiments, the electron gyro-radius is typically on the order of 10^{-4} to 10^{-5} m, somewhat smaller than the probe diameter of $5x10^{-4}$ m and much smaller than the probe length of 10^{-2} m.

To understand how cylindrical probes are used to resolve the two components of the electron temperature in a magnetized plasma, recall that an electron in an unmagnetized plasma will be collected by a Langmuir probe only if the electron's kinetic energy is great enough to overcome the potential difference between the probe and the plasma. In a magnetized plasma such as the one under study here, electrons are confined to move primarily along magnetic field lines. As such, a probe oriented perpendicular to the field lines as depicted in Fig. 3.8a can only intercept electrons as a result of their longitudinal motion along the magnetic field. In this case, an electron will strike the probe surface if its *longitudinal* kinetic energy is great enough to overcome the potential difference between the probe and the plasma. Hence, by varying the probe potential, this configuration allows a measurement of the component of electron temperature parallel to the magnetic field lines. In contrast to Fig. 3.8a, Fig. 3.8b shows a configuration in which the probe is oriented parallel to the magnetic field lines. In this case, an electron will strike the probe surface if its *transverse* kinetic energy is great enough to overcome the potential difference between the probe and the plasma. Hence, the configuration of Fig. 3.8b can be used to measure the component of the electron temperature perpendicular to the magnetic field lines. Errors in these measurement will arise because some fraction of the probe's surface area will be oriented in a direction other than that desired and because collisions and drifts allow electrons to move across field lines to some extent.

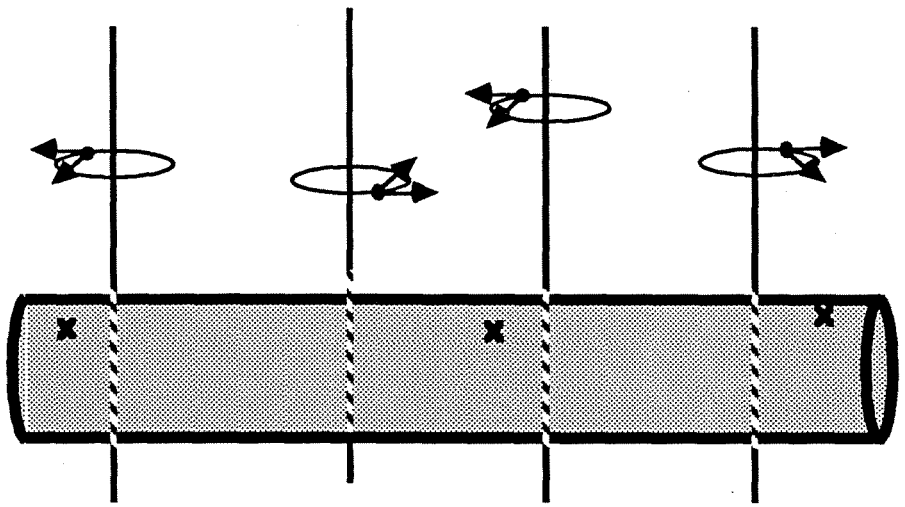

Fig. 3.8a Concept drawing of cylindrical probe perpendicular to field lines. In this case, the flow of electrons to the probe depends more on the parallel component of the electron temperature than on the perpedicular component, so the probe provides an indication of $T_{//}$.

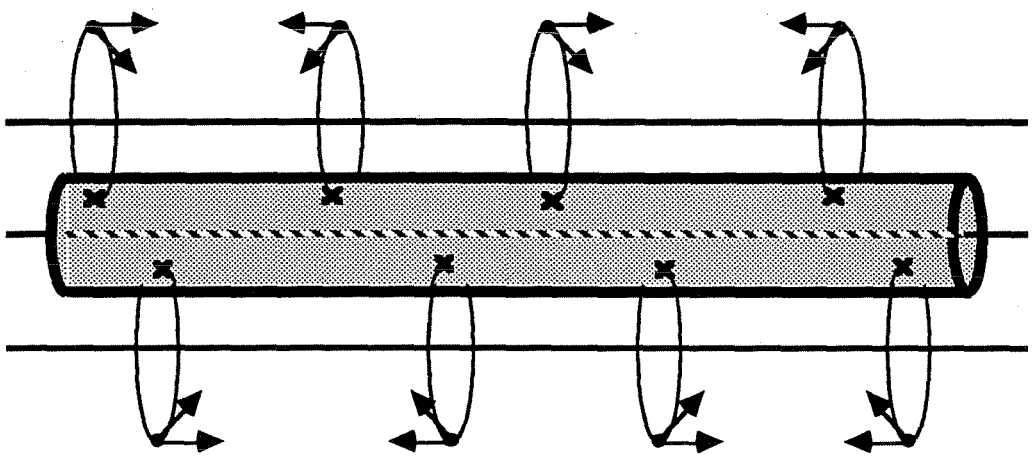

Fig. 3.8b Concept drawing of cylindrical probe parallel to field lines. In this case, the flow of electrons to the probe depends more on the perpedicular component of the electron temperature than on the parallel component, so the probe provides an indication of $T_{\perp}$.

Figure 3.9 shows a diagram of the circuit we used in our Langmuir probe measurements. The procedure for Langmuir probe measurements involved sweeping the probe potential over a range of plus or minus two hundred volts. Using the circuit of Fig. 3.9, the plot of probe current as a function of probe would then yield a probe characteristic in the region of the plasma near the probe tip. To derive the electron temperature from the probe characteristic, we used the standard graphical technique.

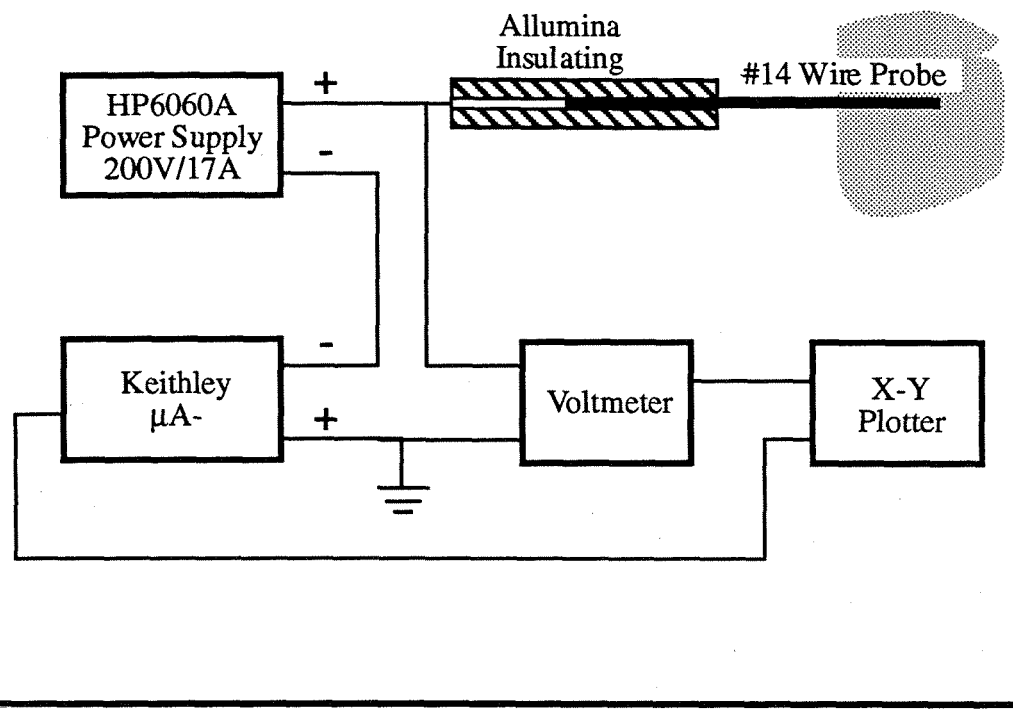

Fig. 3.9 Diagram of circuit for Langmuir probe measurements of electron temperature.

3.3.4 Emissive Probe

We used a floating emissive probe to measure the plasma potential at various locations in the plasma. The plasma potential is an important parameter to measure in this research because is provides a direct experimental comparison with the quasi-one-dimensional theory that gives clear predictions of the trends of how plasma potential should vary with axial position. Also, the basic acceleration mechanism of the ECR plasma engine is the acceleration of ions as they fall through differences in the plasma potential. Therefore, these measurements provide a check for the ion energy measurements conducted using the gridded probe described previously. The theory of the emissive probe for measuring plasma potential is well and broadly understood and will not be repeated here. The uninitiated reader can refer to any one of several standard texts on plasma diagnostics (see Hutchinson 1987 or Huddelstone and Leonard 1965).

In our experiments we used an electrically isolated power supply to heat a tungsten wire to incandescence. Figure 3.10 depicts a diagram of the emissive probe circuit that we used in our measurements. We adjusted the current flow through the emissive element up

to the point at which additional current did not substantial increase the floating potential of the circuit. We surmise that at this current level the electron emission exceeded the electron-saturation current and the circuit was floating at the plasma potential. With the electron temperature typically well over 15 eV in the ECR plasma and with the effective temperature of electrons emitted from a tungsten filament being less than 1 eV, the error introduced by the thermal energy of the emission electrons was deemed sufficiently small. Because Chen (see Huddelstone and Leonard 1965) shows that there exists a potential problem of a double layer forming in this type of diagnostic, we validated the approach in our experiments by providing several comparisons between the floating emissive probe measurement of plasma potential and Langmuir probe measurements of the same. In all cases we found the emissive probe potential to be the same as the voltage at which an extension of the electron saturation region intersected with an extension of the negative potential region of the Langmuir probe characteristics.

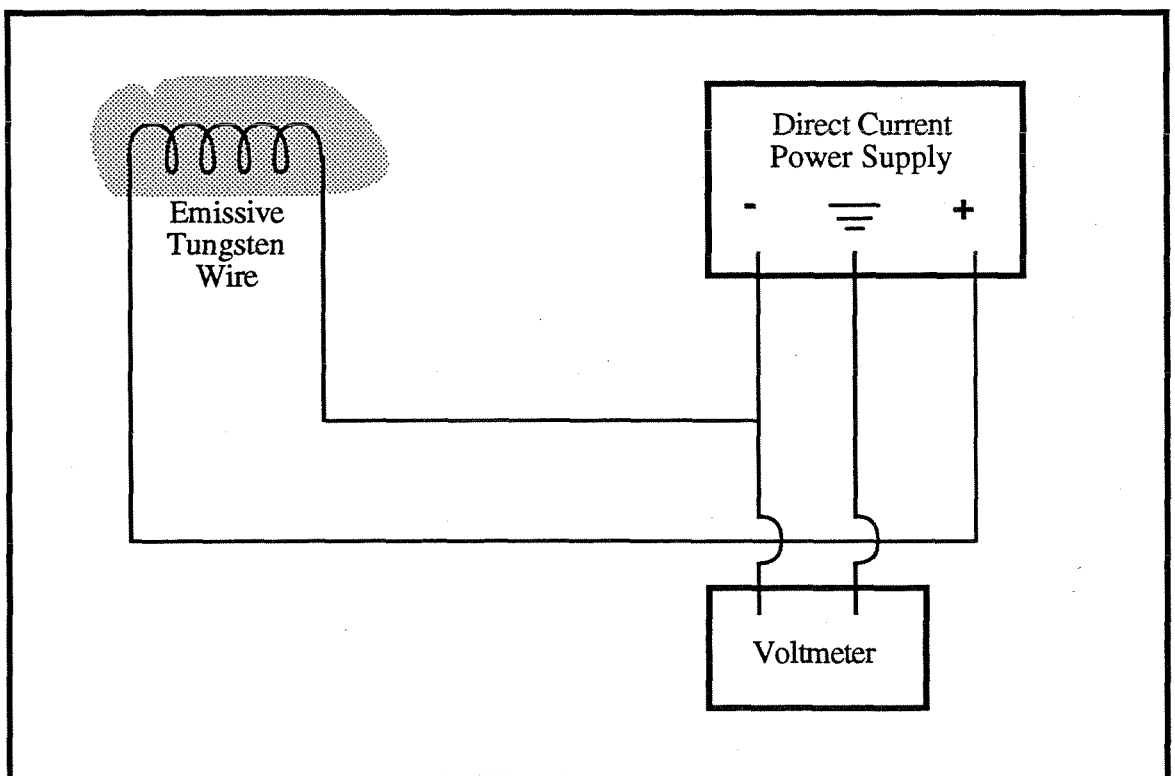

Fig. 3.10 Diagram of circuit used in emissive probe measurements of plasma potential.

3.3.5 Diamagnetic Loop

One might expect the measurement of the diamagnetic effect in the heating region of the ECR plasma accelerator to be important because the diamagnetic effect is usually a measurement of the total thermal energy per unit volume contained in a plasma and is proportional to plasma pressure (Chen 1984). Further, because the plasma pressure is the force (per unit area) that ultimately gives rise to thrust in this device, through Newton's Second Law, a thorough measurement of plasma pressure could in principle give an indication of the magnitude of thrust produced by the plasma acceleration. Actually, because we can expect the electron temperature in our plasma to be anisotropic, the pressure is also anisotropic and the diamagnetism depends only on the perpendicular pressure, which acts in the radial direction. In this particular case then, a measurement of the diamagnetic effect gives an indication of the perpendicular component of the plasma's thermal energy. It is therefore a good measurement of how much energy is coupled by the microwave radiation into the perpendicular component of the electron energy in the ECR heating region.

One can measure the diamagnetic effect of a low beta plasma by measuring how much the magnetic field changes due to the presence of the plasma. An approximate calculation predicts that the field will change by about 0.1 percent when the ECR device starts or stops (based on the assumed conditions of Table 2.1). A diamagnetic loop is a device that can measure this magnitude of change in magnetic field by making use of Faraday's Law of Induction. This apparatus is simply a multi-turn loop of wire wound around the exterior of the plasma tied to an integrating circuit. As the plasma is created or extinguished the magnetic field inside the loop changes due to the diamagnetic effect and the magnetic flux passing trough the interior of the loop therefore changes. According to Faraday's Law the changing flux induces a voltage. The circuit integrates the voltage induced on the current loop to measure the diamagnetic effect.

For these measurements we constructed a diamagnetic loop and located it at the end of the waveguide. The loop contained 100 turns of high temperature AWG #22 transformer wire wound on an aluminum spool. The inner diameter of the spool matched the waveguide diameter at the end adjacent to the waveguide, and diverged at an angle of 30°, to minimize obstruction of the plasma flow. The mean diameter of the coil was about 13.6 cm, providing an open coil area of 145 cm^2 (0.145 m^2). The spool piece was cut radially and a piece of kapton insulation was placed in the gap to prevent currents induced in the

spool piece from interfering with the measurements. An elementary description of the theory of this diagnostic follows, along with a description of the circuitry we developed to support these measurements and the procedure we used.

Changes of the magnetic-flux density inside the coil produce an induced voltage in the coil (Faraday's law)

$$V = NA\frac{dB}{dt} \tag{3.2}$$

where V is the instantaneous voltage induced in the coil, N is the number of turns on the coil, and A is the area enclosed by the coil.

Equation (3.1) can be rearranged to determine the net change in the magnetic-flux density:

$$\Delta B \approx \frac{1}{NA}\int V dt \tag{3.3}$$

where we take the integral over the period of the transition (plasma turn-off or turn-on).

We developed an integrator circuit (Fig. 3.11) to perform the integration using an operational amplifier. The output of the operational amplifier provided a voltage

$$V_O = \frac{1}{RC}\int V dt \tag{3.4}$$

where V is the instantaneous voltage at the input, R is the input resistance, and C is the storage (or integrating) capacitor. We combine the last two equations to give

$$\Delta B \approx \frac{RCV_O}{NA}. \tag{3.5}$$

We chose R and C to be 1000 W and 0.1 μF, respectively to give reasonable values of signal to noise ratio. With these values and the estimated change of 0.1 percent of the 0.075 T magnetic field, we estimated that the output voltage, V_O, of the integrator would be about 1 volt. This is considerably larger than the noise in the output (typically 10 mV peak to peak) but lower than the 15-V saturation value for the operational amplifier.

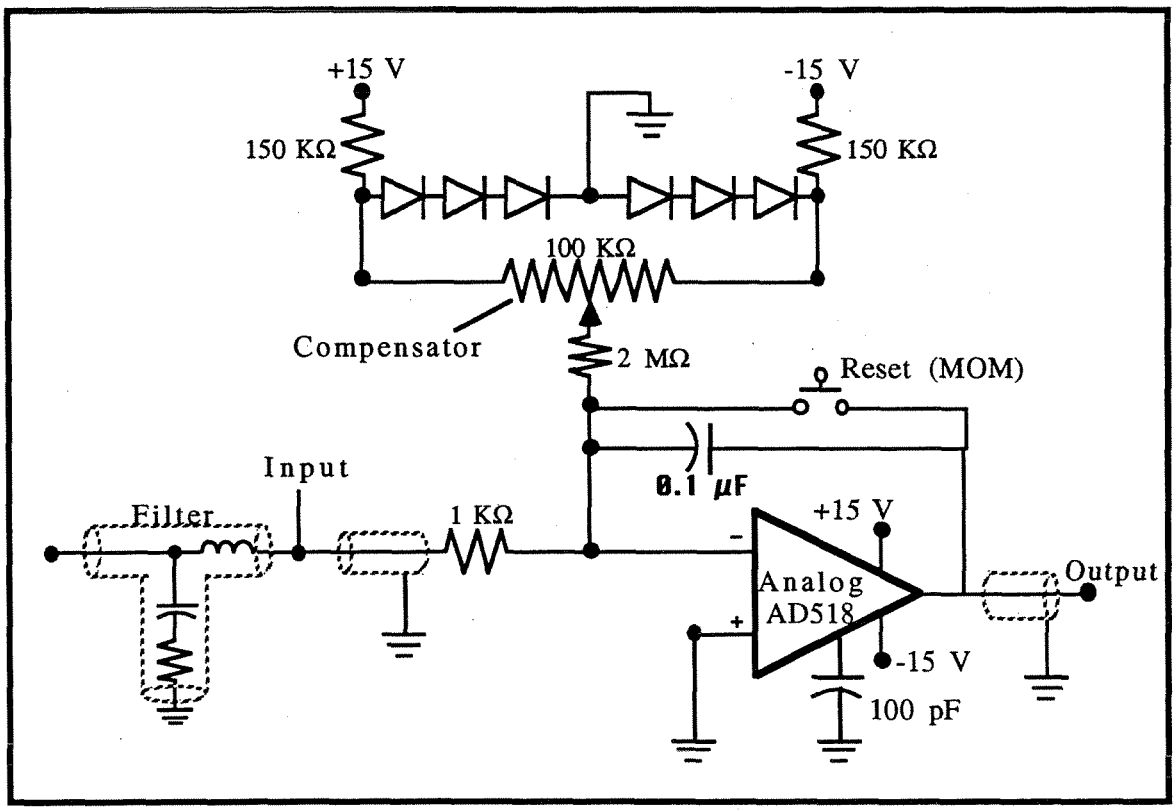

Fig. 3.11 Operational-amplifier integrating circuit used to record diamagnetic loop measurements.

Note that the circuit diagram includes a compensation circuit that provides current for the operational amplifier. This current offsets any inherent imbalance between the inputs and other external voltage sources, such as contact potentials at solder joints and connectors. The compensation current is adjustable over a range of ± 1 mA. We included a momentary shorting switch across the integrating capacitor to provide a reset to zero. The compensation potentiometer was adjusted to minimize drift, but some drift was inevitable. Therefore, we had to use the shorting switch to zero the output immediately before each test sequence (plasma turn-off or turn-on). Noise associated with the microwave power caused the operational amplifier to drift very rapidly into saturation. We therefore found it necessary to install a filter to selectively terminate the high-frequency microwave signal into a 50-Ω matched load (no reflection) and permit the lower frequency signal to pass onto the operational amplifier.

Chapter 4

CALCULATED OPERATING CONDITIONS

Chapter 2 provided a description of a mathematical formulation of a quasi-one-dimensional model of the ECR plasma accelerator. Chapter 4 describes the numerical approach that we used to solve the equations that comprise the model and it outlines the results of our calculations. A listing of the FORTRAN computer program developed for this work is presented in Appendix E. A complete set of the results of our calculations is presented in graphical form in Appendix F.

4.1 Problem Description and Solution Approach

In this computational study we use Eqs. (B.22) or Eqs. (B.23) and Eqs. (C.1) through (C.5) to model the ECR plasma engine that we tested in our experimental program. Figure 4.1 is a schematic that depicts some of the features that must be considered in this problem. The plasma is assumed to flow axially through two regions, a waveguide of constant cross sectional area, and a diverging magnetic nozzle. Neutral gas is introduced into the waveguide under conditions specified in Appendix C near the upstream end of the modeled region coinciding with the location of the microwave window in our experimental apparatus. We assume that ECR plasma heating takes place in a specified region within the waveguide section because in practice the location of the ECR heating region can be controlled by tailoring the magnetic field and microwave frequency.

The boundary conditions derived in Appendix C include relationships between the dependent variables but they do not include an explicit statement of where, in terms of the independent variable z, the boundary conditions are to be applied. The boundary conditions do, however, contain relationships that constrain where they are to be applied in terms of functions of the dependent variables: at the stagnation point and at the point at which the flow transitions from subsonic to supersonic. The location, in terms of the independent variable, of the point of transition to supersonic flow is unknown a-priori.

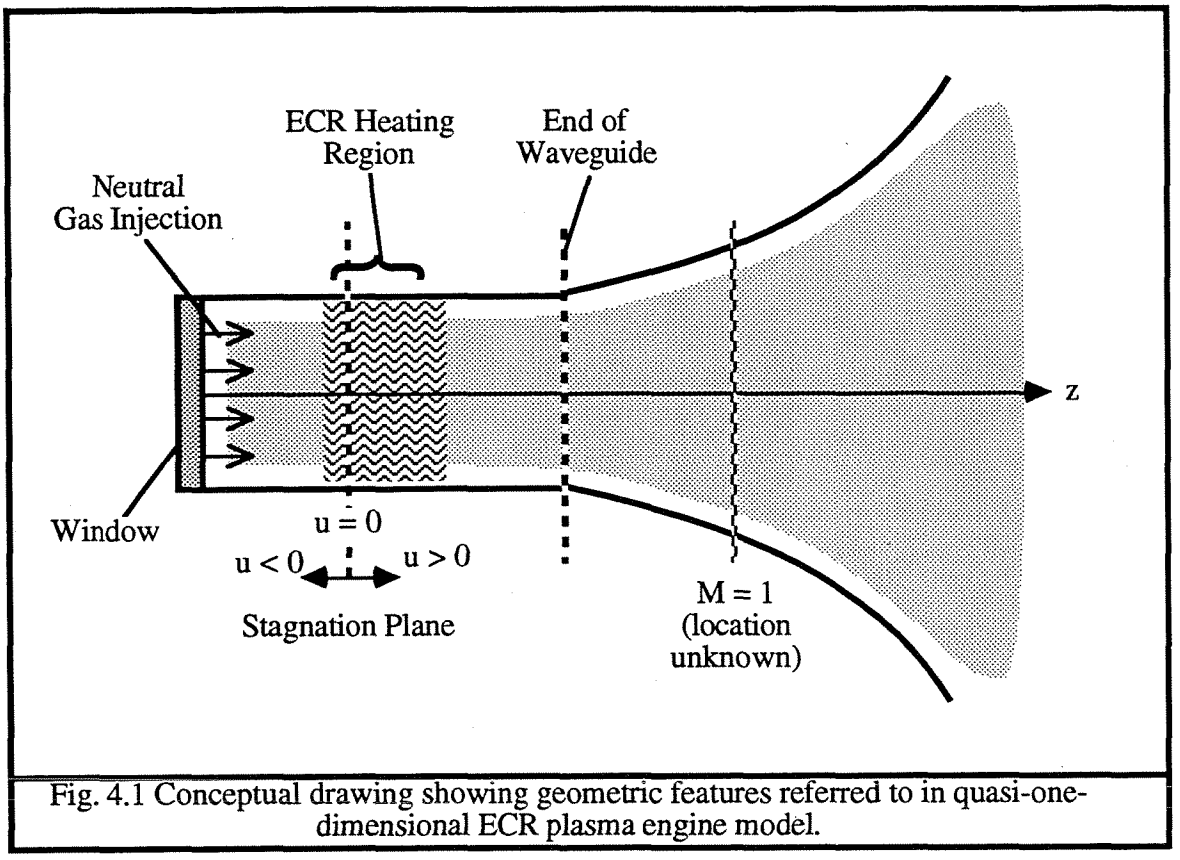

Fig. 4.1 Conceptual drawing showing geometric features referred to in quasi-one-dimensional ECR plasma engine model.

The first boundary condition, Eq. (C.2), describes a requirement that must be met at the axial location where the flow transitions from subsonic to supersonic. In quasi-one-dimensional models developed for conventional gas dynamics this transition can usually be assumed to take place at the location of minimum area, the throat. Unfortunately, in the present problem distributed sources and sinks, non-isotropic effects, body forces, and other effects complicate the situation obviating the assumption of transition to supersonic flow at a throat. In fact, there is no geometric throat in this flow, which starts out at a constant area, as limited by the waveguide walls, and then diverges along the magnetic field lines downstream of the waveguide as suggested in Fig. 4.1.

To solve this problem we have employed a shooting method based on repeated use of the LSODAR (Stepleman 1983 and Hindmarsh 1983) computer subroutine. LSODAR is a powerful tool for solving systems of ordinary differential equations expressed as initial value problems. To use LSODAR for the present boundary value problem we first make a guess at the value of one of the independent variables, n, the plasma density. We then apply the boundary conditions that are applicable at the stagnation point of the plasma, Eqs. (C.3) and (C.4) to obtain guesses for the initial values of $W_\perp$ and $W_{//}$ based on the guess

for n. The continuity equation, Eq. (C.5), gives the value of n_a, the remaining independent variable for which we need an initial value at the stagnation point. These five guesses of the state variables (including the trivial $u=0$) represent a set of initial conditions that are input to LSODAR. LSODAR then accomplishes the integration of the system of differential equations downstream from the assumed location of $u=0$ until the Mach number approaches unity.

If the initial guess for the plasma density were perfect, LSODAR could proceed with the integration right up to the transition from subsonic to supersonic; and the final remaining boundary condition at this point, Eqs. (C.1) and (C.2), would be satisfied. In general, however, the guess will not be perfect and the final boundary condition will not be satisfied. In this case, a small perturbation from the original guess for the plasma density is made and the entire procedure repeated, including the application of the stagnation point boundary conditions, the continuity equation, and the integration of the differential equations by LSODAR. By comparing the error in the boundary condition at transition resulting from the first guess to the error in the boundary condition at transition resulting from the perturbed guess, a Newton-Raphson scheme can be used to refine the guess of the plasma density. The entire procedure is then repeated using the improved value of the plasma density. We have found that after several iterations of this approach in which increasingly improved guesses are generated, the error in the final boundary condition can be decreased by several orders of magnitude, and relative changes in the independent variables from one attempt to the next improved attempt can be less than one part in 10^6. Further, we find that changes in the initial conditions of this magnitude result in small (one part in 10^5) changes in the calculated values of the dependent variables at the transition point. Under these conditions we consider that we have achieved numerical convergence.

In the process of integrating the plasma equations from the stagnation point to the sonic transition point, LSODAR outputs values of all five of the dependent variables that can be used to plot the variation of the dependent variables as a function of axial location. Also, knowing the values of the five dependent variables at the sonic point after a successful convergence of the boundary conditions, we can use LSODAR to integrate the plasma equations down-stream beyond the Mach 1 condition and upstream to the window from the stagnation point. The integration downstream was typically carried out a distance of 0.5m to 1.0m, far enough to capture the important downstream behavior of the plasma.

4.2 Calculated Axial Variation in Plasma Properties

We used the approach described in Section 4.1 to address four different possible conditions regarding the plasma flow process. The first two conditions distinguish between the two extreme possible assumptions of axial heat conduction in the plasma, both the quasi-isothermal case with perfect axial heat conduction (of the parallel component of the electron thermal energy), and the case with negligible axial heat conduction. We also tried to model the middle ground condition of finite axial heat conduction, but we were unsuccessful. However, we have bound the problem with the existing results and our findings shed light on the important question of how significant axial heat conduction is to ECR plasma acceleration.

We addressed the second two conditions, zero back pressure and finite back pressure, to distinguish between an attempt to model the accelerator as it would behave in an ideal vacuum facility (or in outer space) and an attempt to model the experiment as conducted in the existing vacuum facility. These two conditions were important to study because they shed light on how large an effect facility limitations may have had on the results of the experimental effort. The terminology that we have selected, *zero back pressure*, refers to the fact that we do not arbitrarily impose some minimum value on the neutral gas density, but rather allow the neutral gas number density, and hence pressure, to fall to whatever value the model suggests that it should fall to. The condition of finite back pressure implies that we impose a specified minimum gas number density on the calculations to simulate the effect of finite gas pressure in the vacuum system.

4.2.1 Negligible Axial Heat Conduction and Zero Back Pressure

The condition of negligible axial heat conduction and zero back pressure is the simplest case we studied from the perspective that it is closest to the analogous problem of a compressible gas in quasi-one-dimensional flow. Figures 4.2 through 4.5 represent the archetypal result for this condition and are the result of a calculation directed at an operating condition that was typical of the experimental work we conducted. In Figs. 4.2 through 4.5, the 1000 watts of microwave power is assumed to be coupled into the electron cyclotron motion and the assumed argon gas flow rate is 15.0 sccm. This power level and flow rate are also used in the examples of Sections 4.2.2 and 4.2.3. The trends that are discussed for the conditions shown in Section 4.2 are representative of the trends found in

calculations that covered a wide range of operating conditions. Appendix F gives the results of calculations covering the range of conditions addressed in our work.

Figure 4.2 shows the variation of plasma axial velocity and Mach number with axial position. The plasma accelerates very rapidly at first and then the plasma velocity approaches an asymptotic limit of about 3.9×10^4 m/s. The Mach number increases slowly at first and then more precipitously. The Mach number continues to increase rapidly after the plasma velocity has approached its maximum value because the plasma temperature, and hence the ion acoustic velocity, continues to fall even after the flow has expanded considerably.

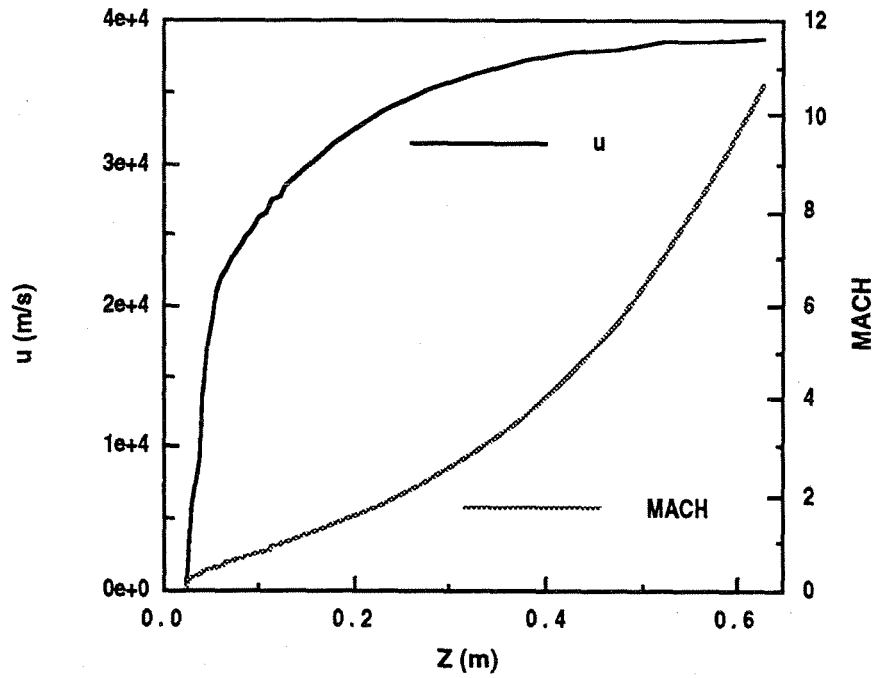

Figure 4.2 Calculated axial variation of plasma velocity and Mach number. Coupled ECR Power = 1000 watts. Argon Flow Rate = 15.0 sccm. No Axial Heat Conduction. No Vacuum Tank Back Pressure.

Figure 4.3 shows that both the perpendicular and the parallel components of the electron thermal energy rise precipitously in the ECR heating region (between z=2.0 cm and z=4.0 cm) and then fall rapidly as the electron thermal energy is converted to directed kinetic energy of the plasma. Notice that in the heating region $W_\perp$ is as much as five times as large as $W_\parallel$, corresponding to a perpendicular electron temperature roughly two and a

half times as large as the parallel electron temperature. This non-equilibrium results from the ECR heating of only the perpendicular electron temperature. Energy is coupled to the parallel component of the electron temperature only indirectly by effects such as scattering collisions. In the region from about 15 cm downstream to about 35 cm downstream of the window $W_{\perp}$ is about twice the value of $W_{||}$, corresponding to thermodynamic equilibrium between the two components of the electron temperature. Further than about 40 cm downstream of the window the calculations show $W_{||}$ dropping off more rapidly than $W_{\perp}$. This effect occurs because the plasma density in this downstream region has dropped to a low enough value that the collision frequencies are not adequate to maintain thermodynamic equilibrium between the two components of electron temperature and because in this region the geometric expansion of the plasma cools the parallel component of the electron temperature more rapidly than the invariance of the dipole moment cools the perpendicular component.

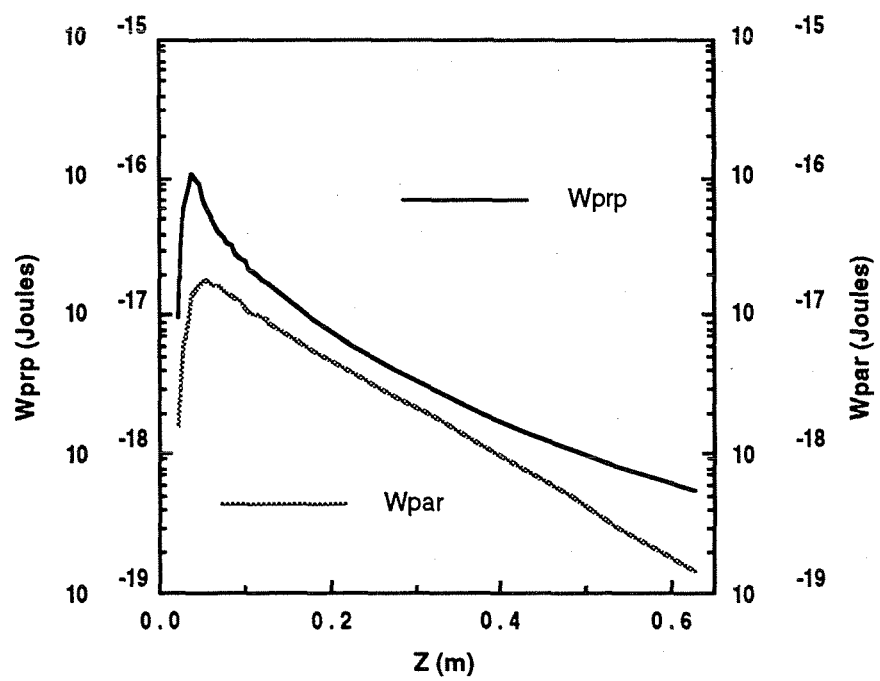

Figure 4.3 Calculated axial variation of perpendicular and parallel components of electron thermal energy. Coupled ECR Power = 1000 watts. Argon Flow Rate = 15.0 sccm. No Axial Heat Conduction. No Vacuum Tank Back Pressure.

Figure 4.4 shows the variation of the number densities of the neutral gas atoms and the ions as a function of distance downstream from the window. As one might expect, the

plasma density drops monotonically throughout the region modeled and most steeply in the region where the plasma is accelerating most rapidly. This is simply an effect of conservation of mass. As the plasma accelerates through a cross section of increasing area, the density must decrease. The behavior of the neutral gas atom number density is somewhat more interesting. The initial steep decline in n_a is the result of copious ionization taking place in the ECR heating region in the local where the plasma density is highest. However, as the plasma density drops, the competition between the neutral gas sink of ionization and the neutral gas source of plasma diffusion and subsequent recombination on the walls of the accelerator shifts, and the diffusion source term begins to dominate. This explains why the neutral gas density actually increases as a function of z over a small region. This increase does not continue, however, downstream of the end of the waveguide for two reasons. First, as the diameter of the flow increases with the diverging magnetic field, the relative importance of cross-field diffusion diminishes, and second, the continuity equation also controls the behavior of the neutral gas in this diverging stream tube.

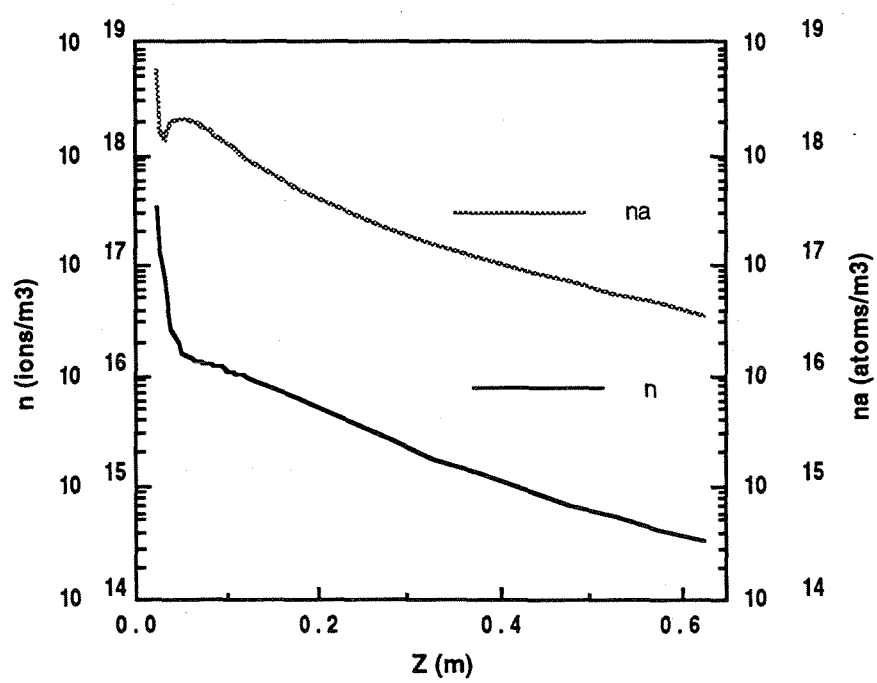

Figure 4.4 Calculated axial variation of plasma density and neutral gas density. Coupled ECR Power = 1000 watts. Argon Flow Rate = 15.0 sccm. No Axial Heat Conduction. No Vacuum Tank Back Pressure.

Figure 4.5 shows the predicted plasma potential and the assumed axial magnetic field as a function of z. The assumed magnetic field is the centerline field of a current loop having a radius the same as the mean radius of the solenoid coil used in our experiments. Downstream of the end of the waveguide, at z = 6 cm, the cross sectional area of the plasma varies inversely with the magnitude of $\boldsymbol{B}$. The relative plasma potential shown in Fig. 4.5 is the electrostatic potential through which the ions must fall to achieve the velocity that our calculations predict that they will achieve. This relative electrostatic potential is maintained in the plasma by the ambipolar electric field that links the mean electron motion to the mean ion motion. It is useful to show the magnitude and spatial variation of the plasma potential here because plasma potential is a quantity that is easy to measure in the laboratory. Notice that for the conditions of Fig. 4.5, the magnitude of the plasma potential tracks the magnitude of the magnetic field fairly closely.

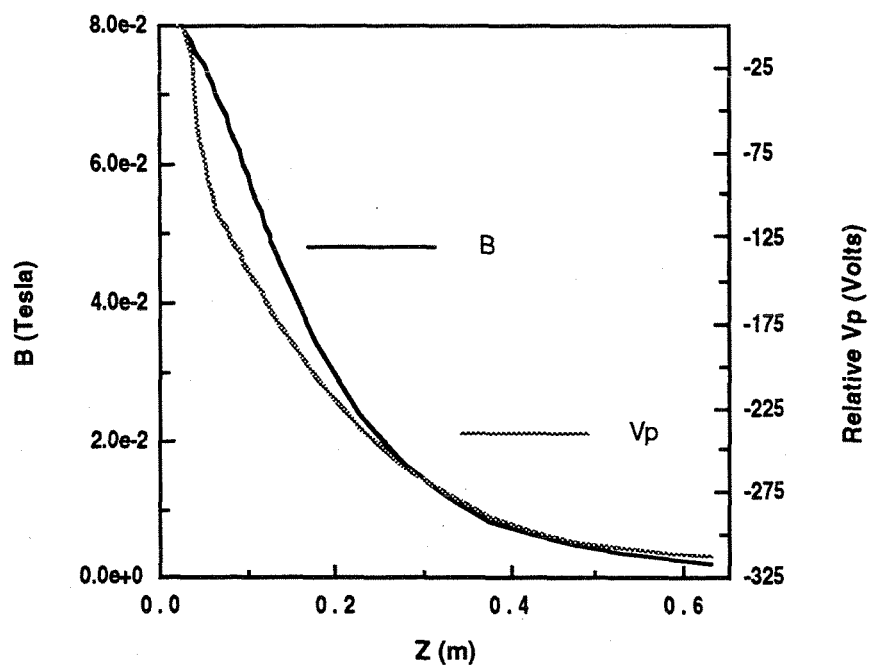

Figure 4.5 Calculated axial variation of plasma potential and magnetic field strength. Coupled ECR Power = 1000 watts. Argon Flow Rate = 15.0 sccm. No Axial Heat Conduction. No Vacuum Tank Back Pressure.

4.2.2 Negligible Axial Heat Conduction and Finite Back Pressure

The case of no axial heat conduction and finite neutral gas pressure in the downstream region is important to study because it gives a direct comparison to the case of zero downstream pressure and therefore provides insight into the effect of limited vacuum facility pumping speeds on the behavior of the plasma accelerator. The example calculation we will show here is identical to that discussed in Section 4.2.1 except for the presence of a finite vacuum-tank back-pressure. In this case we assumed that the number density of neutral gas atoms in the vacuum tank was $5x10^{17}$ atoms/m^3 corresponding to a vacuum pressure in the high 10^{-6} torr range, several times lower than was normally achieved in our experimental work at the argon gas flow rate assumed in our calculations.

Figure 4.6 shows the axial velocity and Mach number as a function of axial position in direct analogy to Fig. 4.1. A cursory comparison of Fig. 4.2 with Fig. 4.6 immediately reveals the first gross effect of finite vacuum tank pressure on the plasma acceleration process. In contrast to Fig. 4.2, the plasma velocity does not increase monotonically in Fig. 4.6, rather, after initially accelerating up to about 80 percent of the maximum velocity achieved in the calculation of Fig. 4.2, the plasma velocity peaks, and the plasma actually decelerates. This deceleration is caused by dynamic friction between the flowing plasma and the (practically) stationary neutral gas of the vacuum chamber.

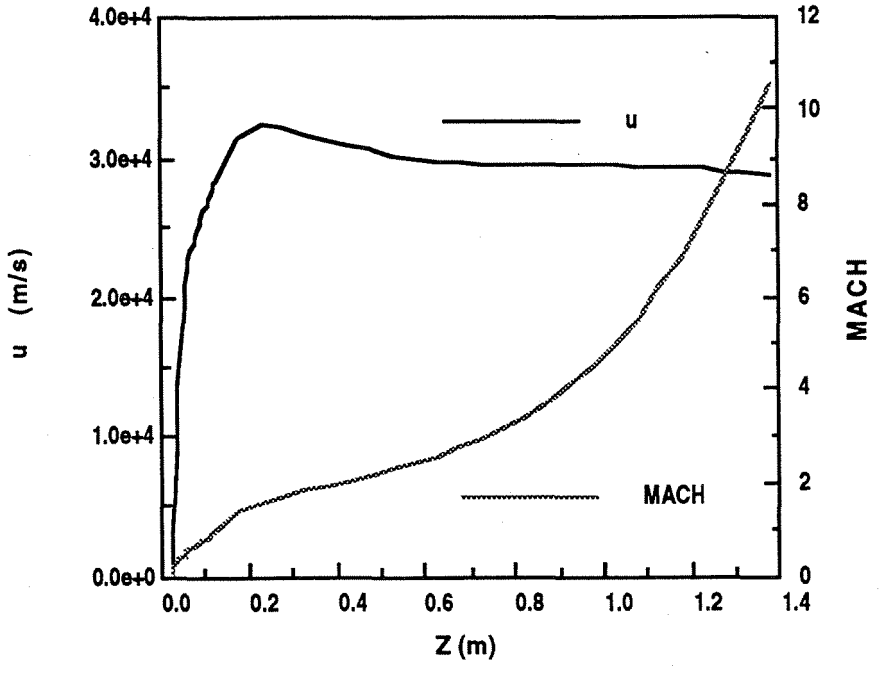

Figure 4.6 Calculated axial variation of plasma velocity and Mach number. Coupled ECR Power = 1000 watts. Argon Flow Rate = 15.0 sccm. No Axial Heat Conduction. Finite Vacuum Tank Back Pressure.

The effect of this dynamic friction is found throughout the results of our calculations. Figure 4.7 shows the perpendicular and parallel components of the electron thermal energy as a function of axial position. Comparison of Fig. 4.7 to Fig. 4.3 shows that $W_{\|}$ is much more strongly effected by the presence of the neutral gas in the vacuum system than is $W_{\perp}$. To understand why, consider the following. First, the quantity of work done by the electrons on the plasma due to the dipole moment force is, to a first approximation, the same with or without the neutral gas in the vacuum system. This work is determined by the approximate invariance of the dipole moment and is therefore a function only of the changing strength of the magnetic field. Therefore, to a first approximation, the cooling effect of falling magnetic field on $W_{\perp}$ is the same in the present calculation as in the former calculation. Second, further than about 35 cm downstream of the window the plasma density is not high enough to allow significant transfer of thermal energy from one component of electron energy to the other by scattering collisions. Hence, as dynamic friction decelerates the plasma and heats the parallel component of the electron thermal motion, it is not transferred to the perpendicular motion of the electrons and the two components move out of equilibrium. Further downstream than about 1m, the expansion

of the plasma is so extreme that the parallel component of the electron temperature does eventually drop below the perpendicular component simply due to expansion effects.

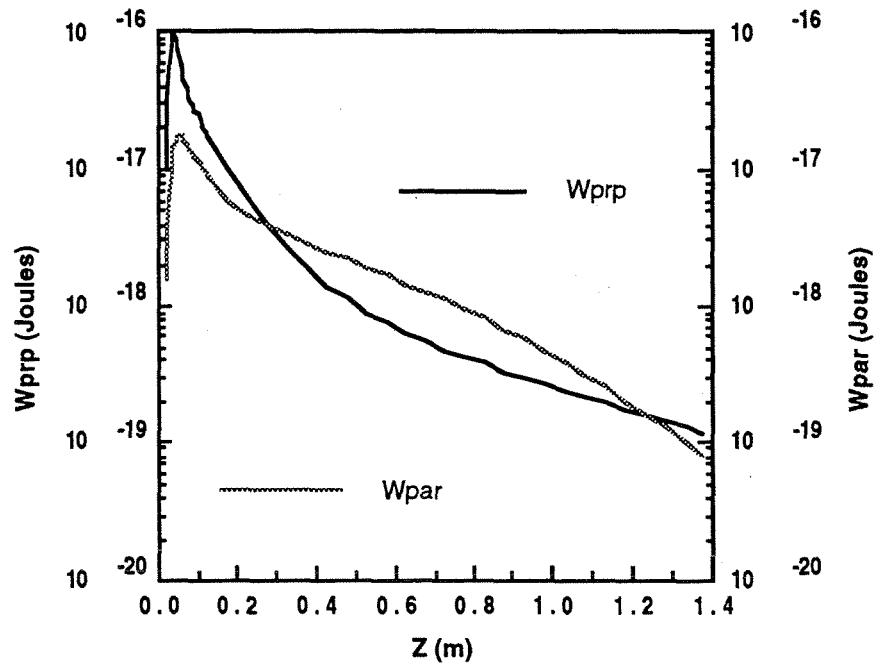

Figure 4.7 Calculated axial variation of perpendicular and parallel components of electron thermal energy. Coupled ECR Power = 1000 watts. Argon Flow Rate = 15.0 sccm. No Axial Heat Conduction. Finite Vacuum Tank Back Pressure.

Figure 4.8 shows the plasma density and the neutral gas density associated with this calculation as a function of distance downstream of the window. The horizontal line shown for the neutral gas density at locations further than about 20 cm downstream of the window is a statement of the assumption we made of constant, finite pressure in the vacuum tank. The location 20 cm downstream of the window where the neutral gas profile becomes constant in this calculation is a product of the way this calculation was performed. This calculation was identical to the calculation of section 4.2.1 as long as the neutral gas density was higher than the value we assumed the vacuum tank would operate at for the specified input conditions. When the neutral gas density fell to the assumed vacuum tank gas density, a fictitious neutral gas source term was added to the neutral gas continuity equation with sufficient value to cause the neutral gas density to remain constant. Values shown for the plasma density downstream of the 20 cm point are somewhat higher than

those shown in Fig. 4.4 because with a higher neutral gas density, the source of plasma due to ionization is larger.

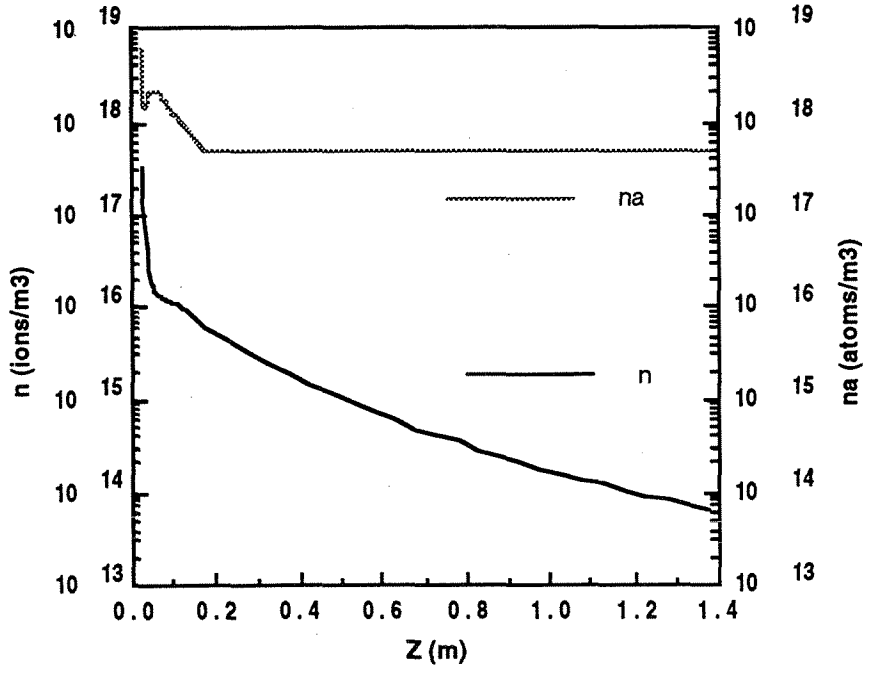

Figure 4.8 Calculated axial variation of plasma density and neutral gas density. Coupled ECR Power = 1000 watts. Argon Flow Rate = 15.0 sccm. No Axial Heat Conduction. Finite Vacuum Tank Back Pressure.

Figure 4.9 shows magnetic field strength and calculated plasma potential as a function of distance from the window for the aforementioned conditions. This figure is especially interesting because the trend of plasma potential verses axial position is clearly different from the trend predicted for plasma potential as shown in Fig. 4.5. It would appear that the presence of a finite vacuum tank back pressure can be expected to cause the plasma potential to flatten out significantly downstream of the accelerator. The plasma potential might be expected to closely track the magnetic field intensity near the accelerator when tank effects are minimal.

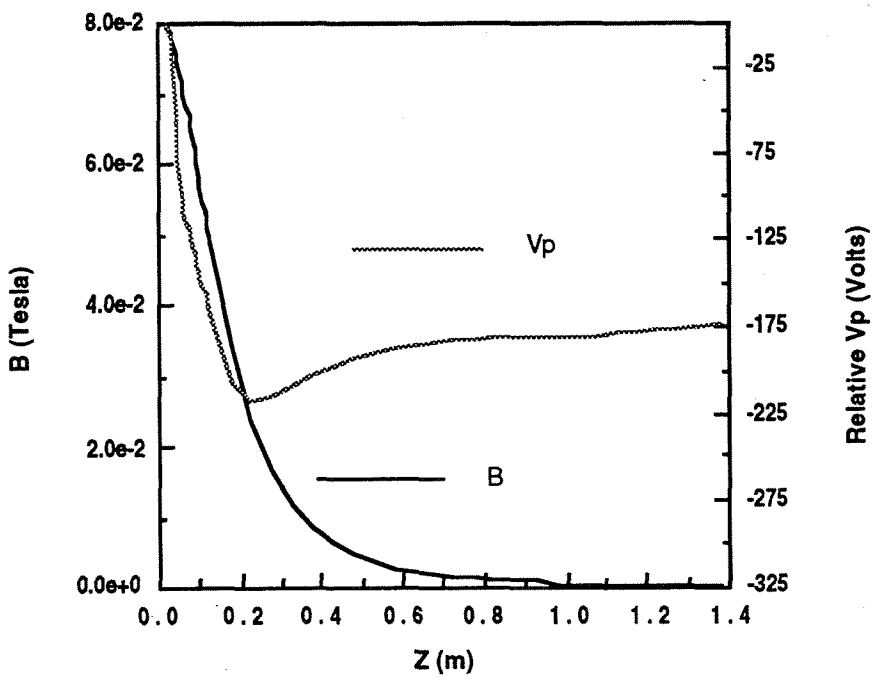

Figure 4.9 Calculated axial variation of plasma potential and magnetic field strength. Coupled ECR Power = 1000 watts. Argon Flow Rate = 15.0 sccm. No Axial Heat Conduction. Finite Vacuum Tank Back Pressure.

4.2.3 Quasi-Isothermal Cases

The quasi-isothermal cases studied here included calculations both with and without vacuum system back pressure. One of the boundary conditions and the method used in these calculations were slightly different than those used in the calculations based on the assumption of negligible axial heat conduction. Differences in the boundary conditions, as described in Appendix C, center around the fact that the ion acoustic velocity is different for the quasi-isothermal plasma than for the plasma with negligible thermal conductivity. This results in a change in the conditions that give rise to the singularity that can occur in modeling the transition from subsonic to supersonic flow. The boundary condition that must be met to prevent the singularity at the transition point is also different in detail for the isothermal case than it is for the case of negligible heat conduction (see Appendix C).

To model isothermal flow in the ECR plasma engine we created a fictitious heat flux term to account for the flow of thermal energy required to maintain the quasi-isothermal

condition. At each step in the integration of the equations of the model we calculated the fictitious heat flux needed to ensure that $dW_{\perp}/dz=0$. In all cases we integrated the fictitious heat flux along with the differential equations upstream from the stagnation point, downstream through the transition to supersonic flow, and out into the expansion region. The upstream integration was continued until the plasma velocity reached the Bohm velocity, at which point we assume that the plasma flows into a sheath that separates the plasma from the upstream window. The downstream integration was continued until the total integral of the fictitious heat flux reached zero. In this way, we could be sure that a power balance was maintained in the plasma and conservation of energy was not violated.

Figures 4.10 and 4.11 show the calculated values of $W_{\perp}$ and $W_{//}$ as a function of distance downstream from the window of the accelerator for the case of zero vacuum tank pressure and finite vacuum tank pressure in analogy to Fig. 4.3 and 4.7. $W_{//}$ is constant in Figs. 4.10 and 4.11, consistent with our assumption of quasi-isothermal flow. The value of $W_{//}$ is determined using the stagnation boundary conditions in the same manner that was used to determine the initial values of $W_{//}$ in Sections 4.2.1 and 4.2.2. Figures 4.12 and 4.13 show the calculated values of plasma velocity and Mach number as a function of distance downstream from the window of the accelerator for the case of zero vacuum tank pressure and finite vacuum tank pressure in analogy to Fig. 4.1 and 4.5. The plasma velocity increases more slowly in the case of quasi-isothermal flow because the contribution of the pressure force (thermodynamic acceleration) to the acceleration process is less with no gradient in $W_{//}$.

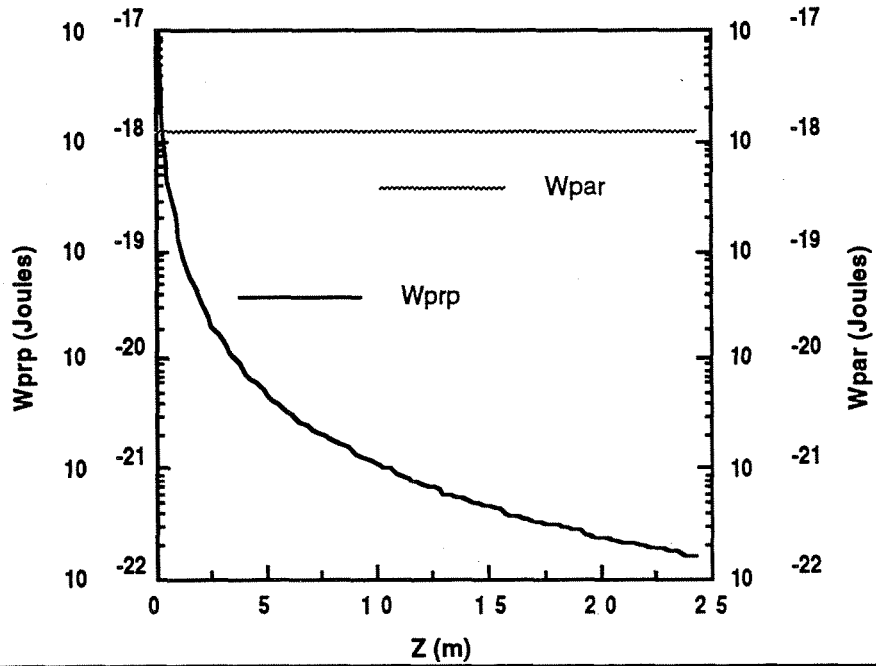

Figure 4.10 Calculated electron thermal energy perpendicular to field lines as a function of axial position. Coupled ECR Power = 1000 watts. Argon Flow Rate = 25.0 sccm. Isothermal Parallel Electron Temperature. Zero Back Pressure.

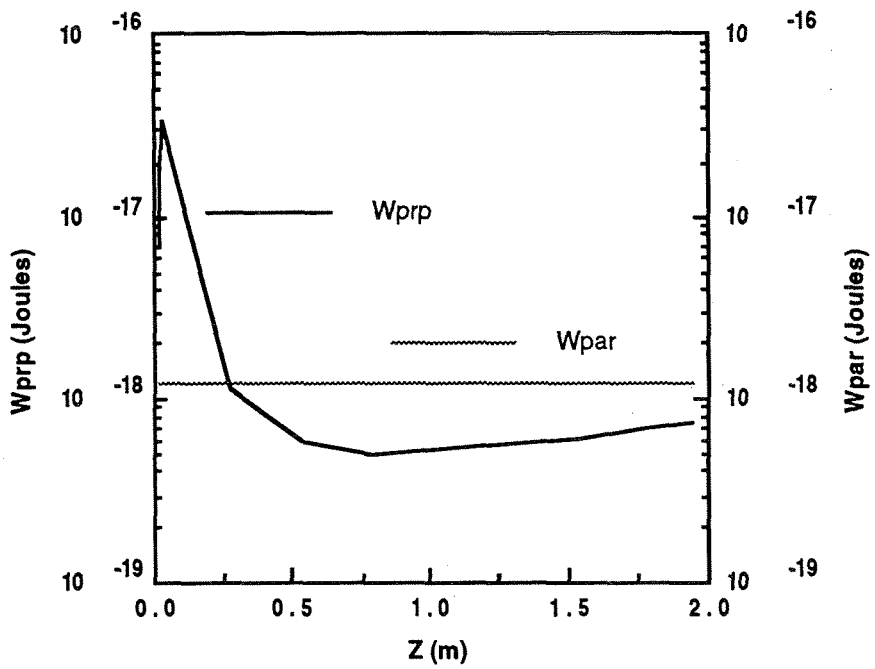

Figure 4.11 Calculated electron thermal energy perpendicular to field lines. Coupled ECR Power = 1000 watts. Argon Flow Rate = 25.0 sccm. Isothermal Parallel Electron Temperature. Finite Vacuum Tank Pressure.

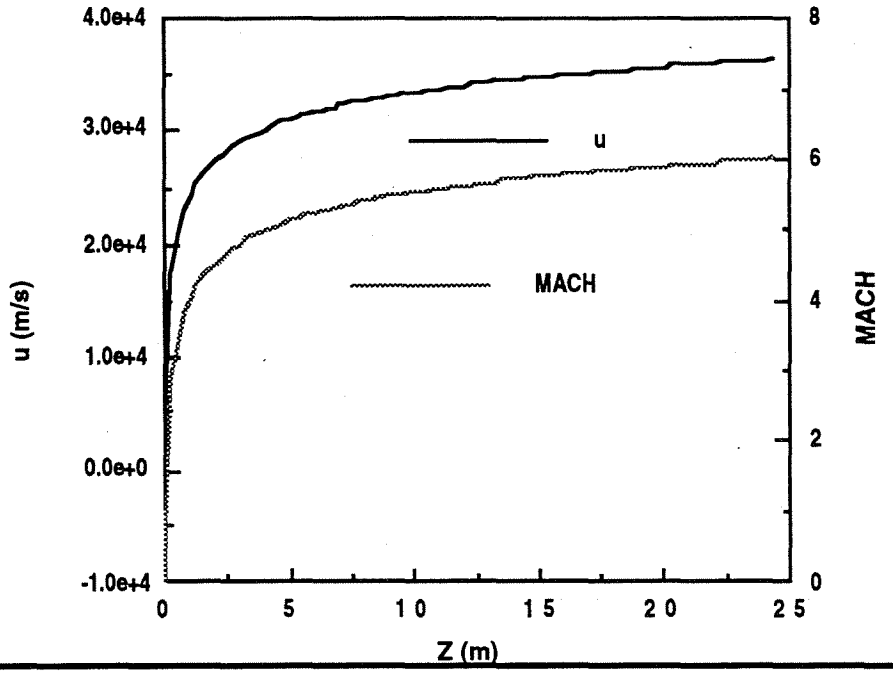

Figure 4.12 Calculated plasma velocity and Mach number as a function of axial position. Coupled ECR Power = 1000 watts. Argon Flow Rate = 25.0 sccm. Isothermal Parallel Electron Temperature. Zero Back Pressure.

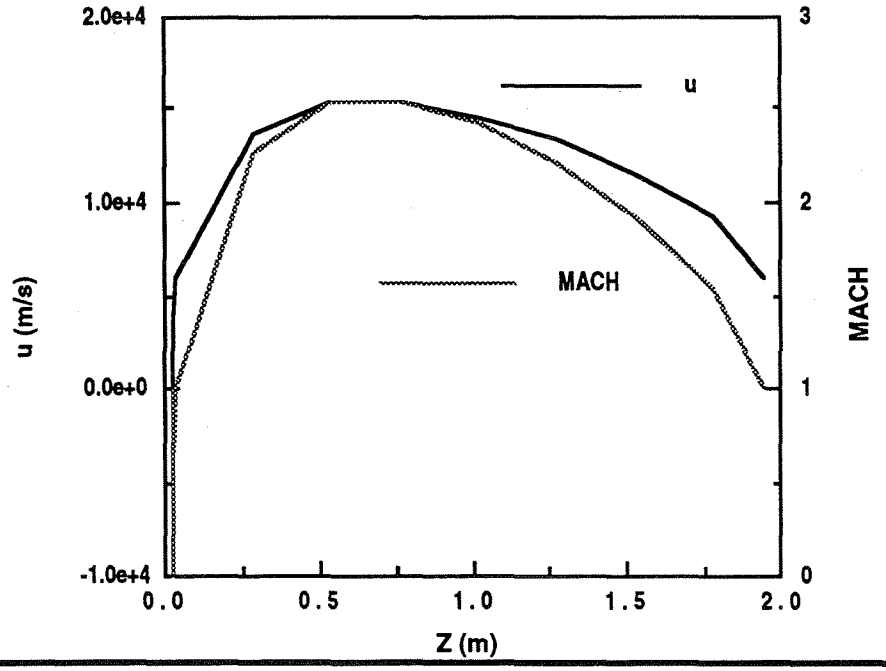

Figure 4.13 Calculated plasma velocity and Mach number as a function of axial position. Coupled ECR Power = 1000 watts. Argon Flow Rate = 25.0 sccm. Isothermal Parallel Electron Temperature. Finite Vacuum Tank Pressure.

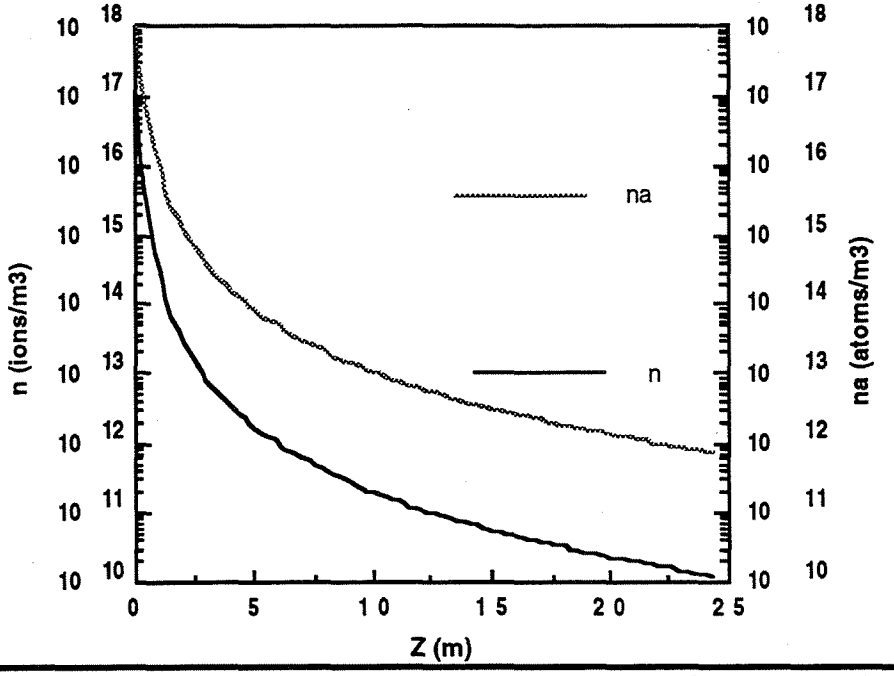

Figure 4.14 Calculated plasma and neutral gas density as a function of axial position. Coupled ECR Power = 1000 watts. Argon Flow Rate = 25.0 sccm. Quasi-isothermal Flow. Zero Back Pressure.

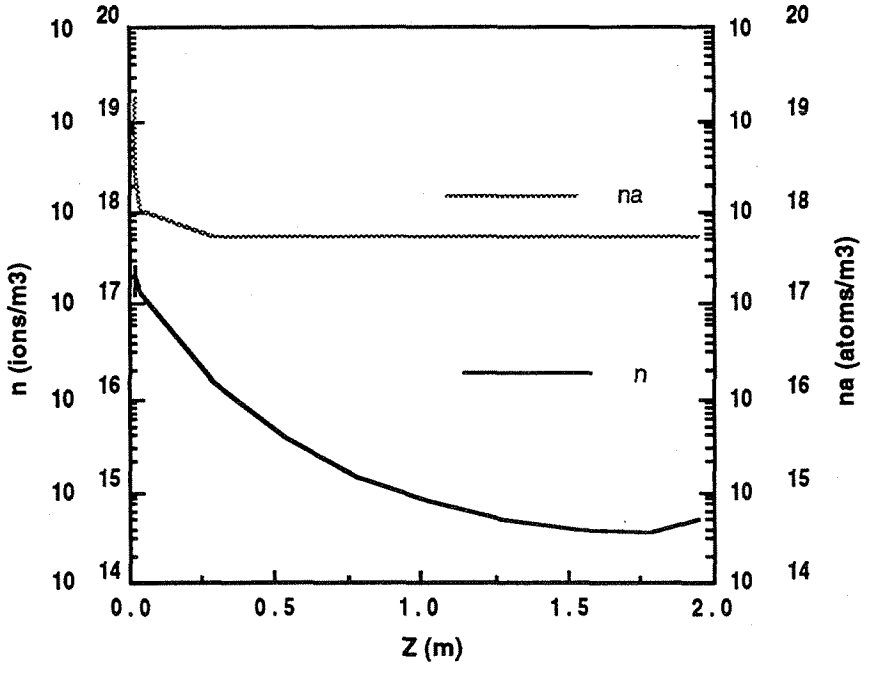

Figure 4.15 Calculated plasma and neutral gas density as a function of axial position. Coupled ECR Power = 1000 watts. Argon Flow Rate = 25.0 sccm. Quasi-isothermal Flow. Finite Vacuum Tank Pressure.

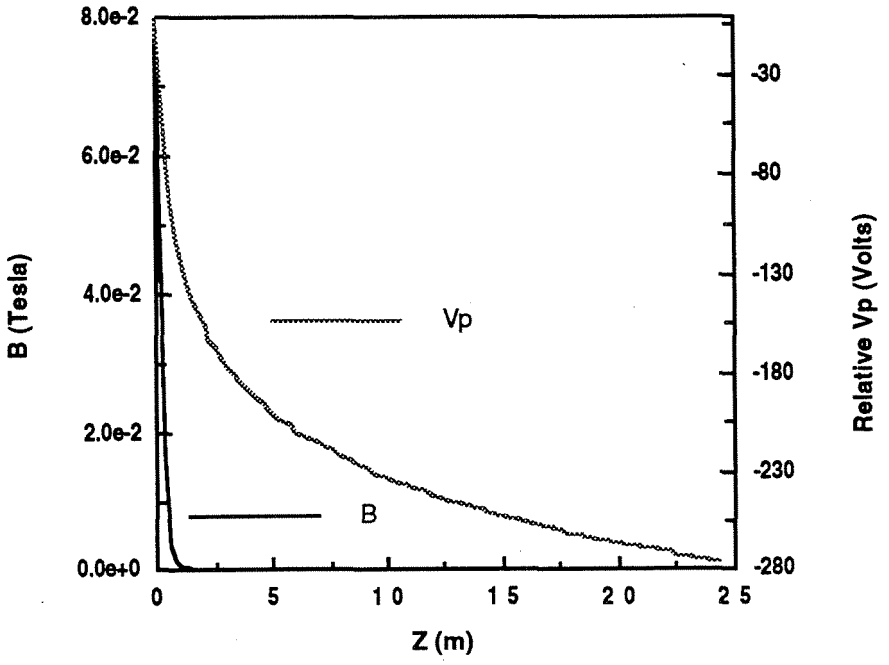

Figure 4.16 Calculated plasma potential and magnetic field strength as a function of axial position. Coupled ECR Power = 1000 watts. Argon Flow Rate = 25.0 sccm. Quasi-isothermal Flow. Zero Back Pressure.

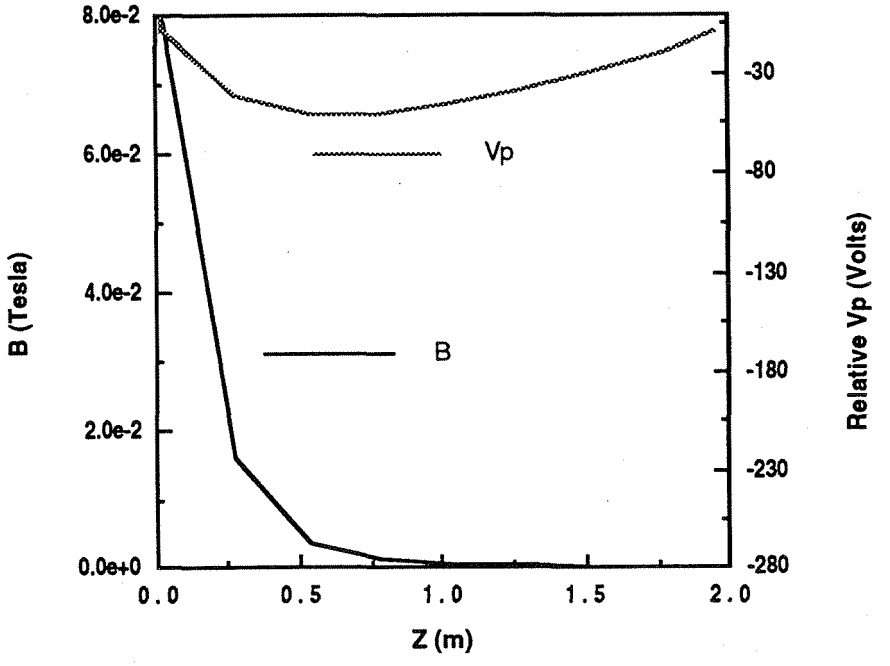

Figure 4.17 Calculated plasma potential and magnetic field strength as a function of axial position. Coupled ECR Power = 1000 watts. Argon Flow Rate = 25.0 sccm. Quasi-isothermal Flow. Finite Vacuum Tank Pressure.

Figures 4.12 and 4.13 show the calculated values of plasma and neutral gas density as a function of distance downstream from the window of the accelerator for the case of zero vacuum tank pressure and finite vacuum tank pressure in analogy to Fig. 4.4 and 4.8. The changes observed in species number densities between the quasi-isothermal cases and the previous cases stem primarily from differences in the rate of cross-field diffusion, a phenomenon that depends strongly on electron temperature. Finally, the chief difference between Figs. 4.16 and 4.17 and their counterparts in the calculation for zero axial heat conduction is that in the quasi-isothermal cases the plasma potential does not track the magnetic field strength as closely.

4.3 Calculated Thruster Performance

Section 4.2 showed calculated predictions of the plasma state variables for an ECR accelerator such as the one we tested in our experimental program based on a few different basic assumptions. In the present section we submit predictions of accelerator efficiency. The two figures of merit we use here to describe the efficiency of the accelerator are the propellant utilization and the power efficiency. The propellant utilization is a parameter familiar to workers in the field of electric propulsion. The propellant utilization is defined as the ratio of the mass flow rate of accelerated plasma to the mass flow rate of input propellant gas. The power efficiency is not familiar to the electric propulsion research community and is defined as the ratio of the kinetic power of the plasma stream to the input power. For these calculations we take the input power to be the microwave power that is coupled to the perpendicular component of the electron motion in the ECR heating region.

Figure 4.18 shows the calculated power efficiency and the propellant utilization of the ECR plasma accelerator that we tested in our experimental effort. Each parameter is plotted against input microwave power for three argon gas mass flow rates: 15 sccm, 17.5 sccm, and 20 sccm. This calculation is based on the assumptions of negligible axial heat conduction and negligible neutral gas pressure in the region downstream of the accelerator. The following trends are made clear by Figure 4.18. First, propellant utilization is predicted to be reasonably good for this device under the assumed conditions and is typically above 80 percent, though never above 90 percent. Power efficiency is not as good, never exceeding 50 percent. We see that in general, reducing the input gas flow rate has the effect of slightly increasing both the propellant utilization and the power efficiency. Both measures of efficiency drop slightly as we go to higher power levels.

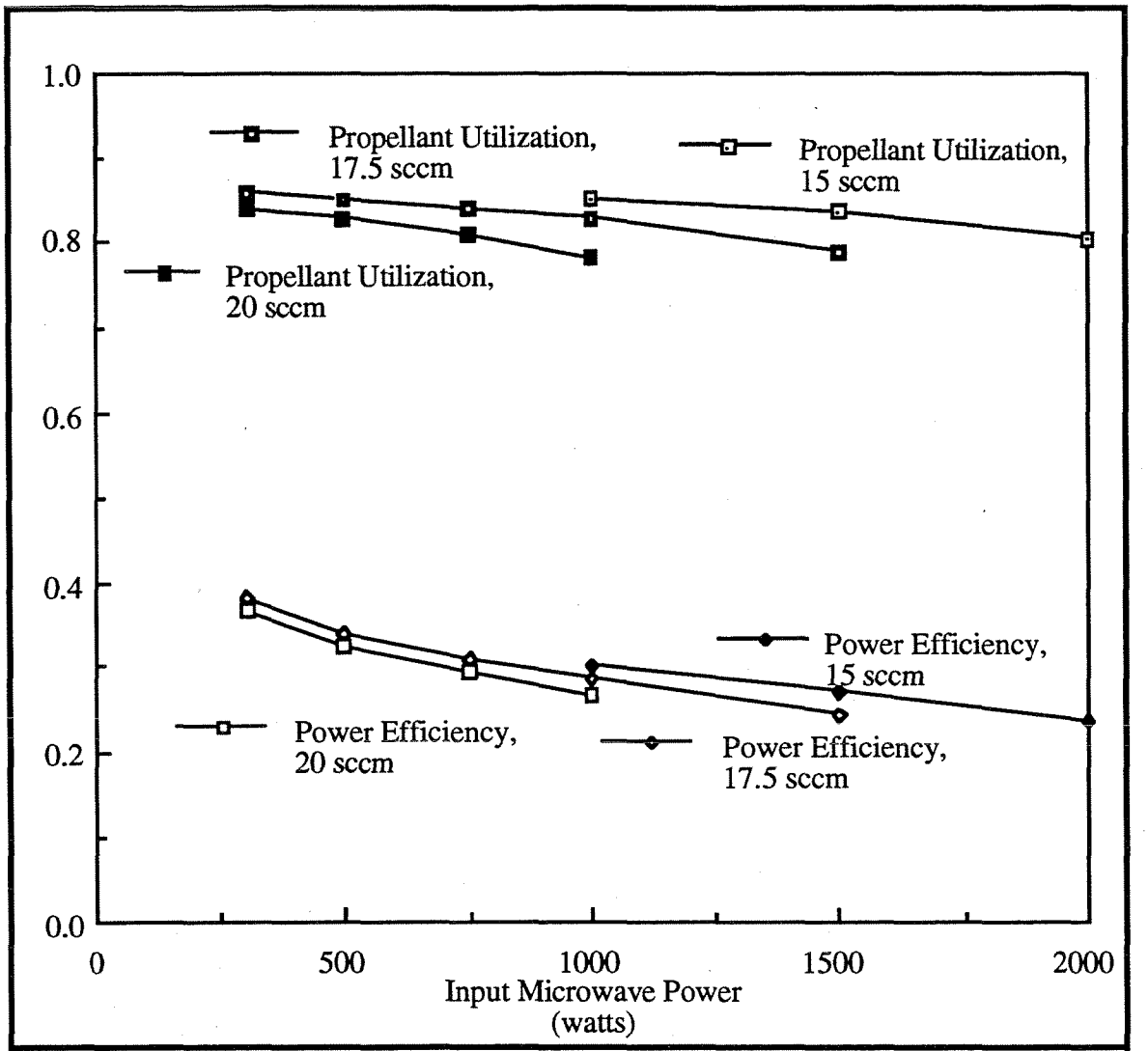

Figure 4.18 Calculated power efficiency and propellant utilization of ECR plasma acclerator tested in experimental effort based on assumptions of zero axial heat conduction and zero vacuum tank back pressure.

Figure 4.19 also shows the calculated power efficiency and the propellant utilization of the ECR plasma accelerator that we tested in our experimental effort. Like Fig. 4.18, these calculations are based on the assumption of negligible axial heat conduction, but unlike Fig. 4.18, in Fig. 4.19 the neutral gas pressure in the region downstream of the accelerator is taken to be similar to that encountered in our experimental work. These calculations suggest that the effect on the efficiencies of the accelerator of the finite downstream gas pressure is dramatic. First, we see that the propellant utilization increases with increasing input power to as high as 2.5 at a power level of 2 kW. In other words, these calculations

suggest that at high power levels as much as one and a half times the input gas mass-flow-rate is ionized and entrained into the plasma flow in the downstream region given the vacuum tank back pressures encountered in our experimental work. Figure 4.19 also predicts power efficiency dropping to very low values at high power levels. This power-efficiency drop is caused by a loss of energy from the electrons as they undergo inelastic collisions with the gas encountered in the vacuum system. These inelastic collisions include the ionizing reactions that are involved in entraining the gas into the plasma flow.

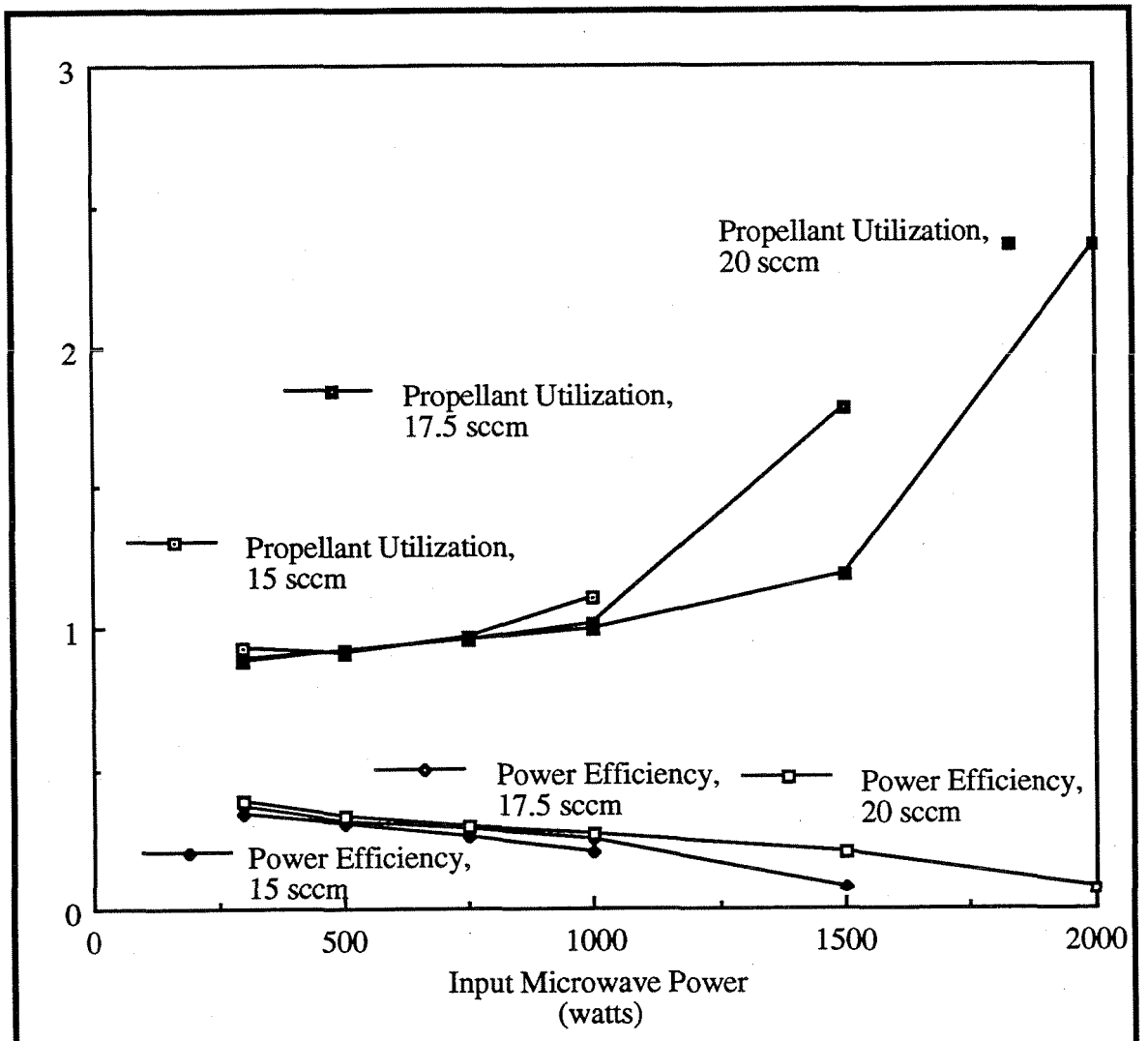

Figure 4.19 Calculated power efficiency and propellant utilization of ECR plasma acclerator tested in experimental effort based on assumptions of zero axial heat conduction and finite vacuum tank back pressure.

Figure 4.20 shows the calculated power efficiency and the propellant utilization of our ECR plasma accelerator plotted against input microwave power for flow rates of 25 sccm and 20 sccm. These predictions are based on the assumptions of quasi-isothermal flow and finite gas pressure in the region downstream of the accelerator. Figure 4.21 also shows the calculated power efficiency and the propellant utilization of the ECR plasma accelerator based on the assumption of quasi-isothermal flow but with the neutral gas pressure in the region downstream of the accelerator taken to be finite. The trends shown in these calculations are similar to those exhibited in the cases of negligible axial heat conduction.

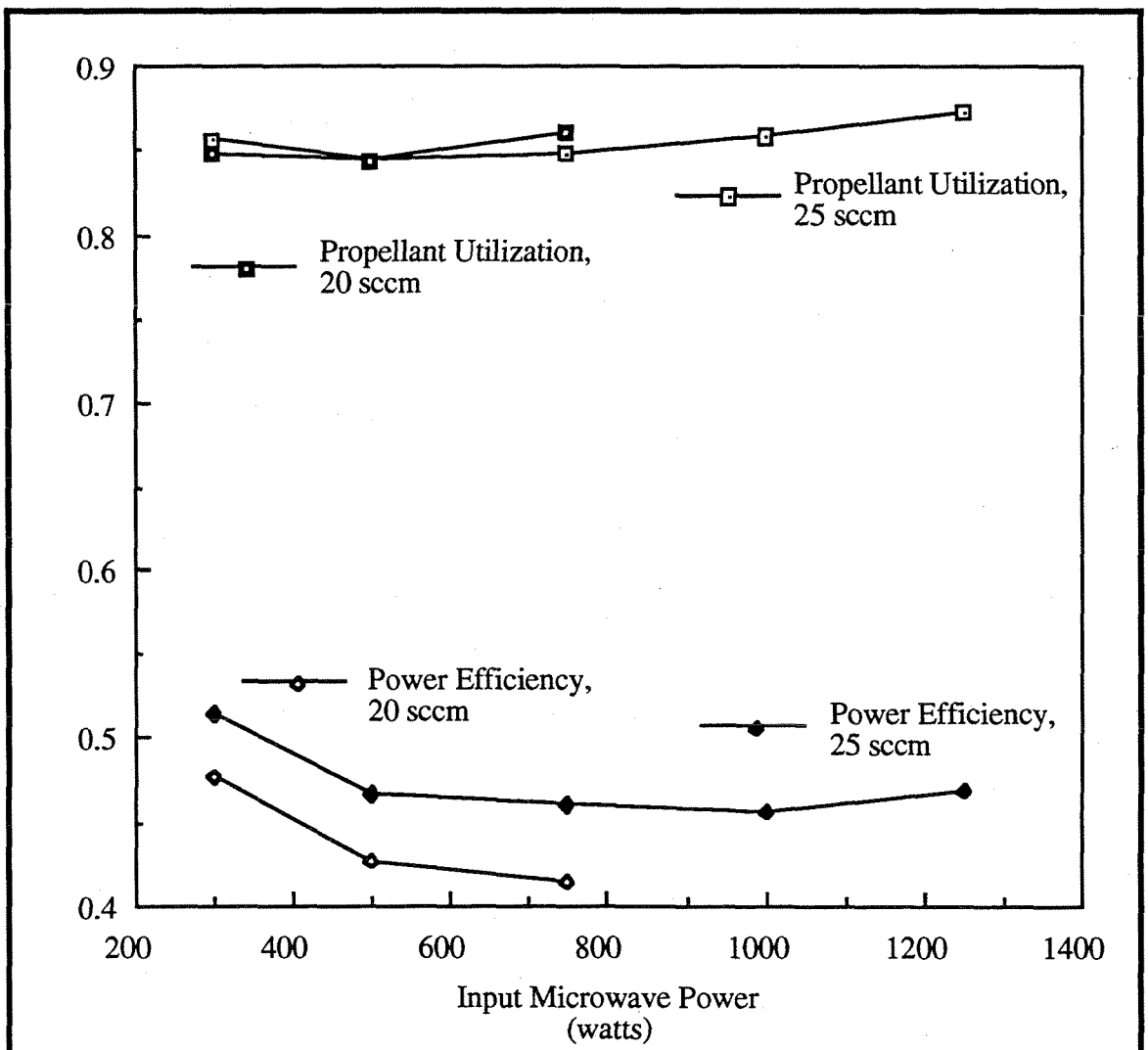

Figure 4.20 Calculated power efficiency and propellant utilization of ECR plasma acclerator tested in experimental effort based on assumptions of quasi-isothermal flow and zero vacuum tank back pressure.

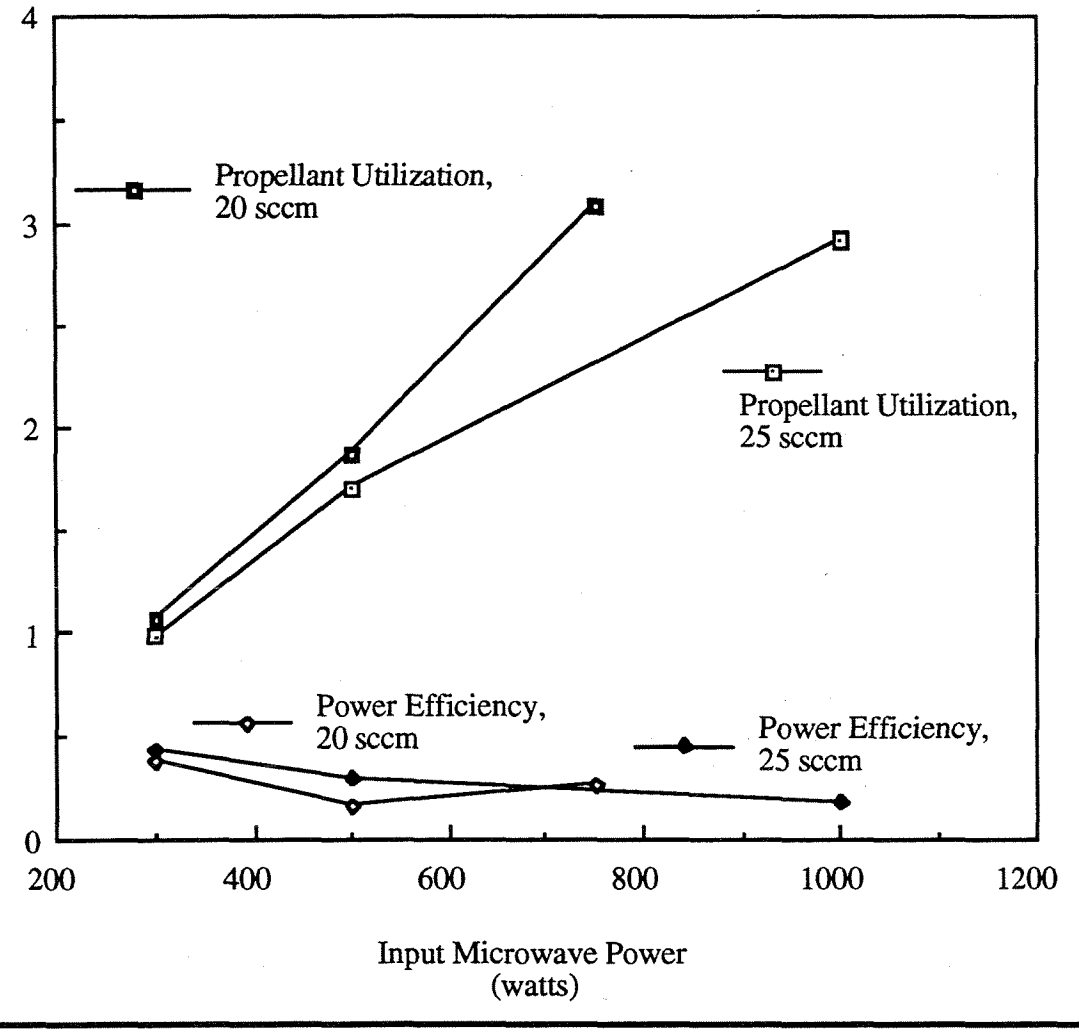

Figure 4.21 Calculated power efficiency and propellant utilization of ECR plasma acclerator tested in experimental effort based on assumptions of quasi-isothermal flow and finite vacuum tank back pressure.

The model suggests in the case of quasi-isothermal flow that once again the effect of neutral gas in the vacuum tank will profoundly alter the propellant utilization of the ECR plasma accelerator by causing considerable entrainment of additional material into the plasma flow. We also continue to observe higher propellant utilization at reduced mass flow rates. The relatively week trend of falling power efficiency at increased power levels is not strictly preserved, but we do see the highest power efficiency at the lowest (300 watt) power level for all the cases studied. It seems remarkable that the differences in efficiency

between the quasi-isothermal cases and the cases of zero axial heat conduction are not larger. Further, the trends in these parameters are so similar for both cases that it would be difficult to discern between them experimentally. However, the dramatic difference in propellant utilization between the cases of negligible and finite vacuum system back pressure is large enough to measure. A discussion of a comparison of these theoretical results against experimental measurements is included in Chapter 5. The implications of these results are discussed in Chapter 6.

Chapter 5

EXPERIMENTAL RESULTS AND COMPARISON WITH THEORY

This chapter gives the results of measurements made using the apparatus described in Chapter 3 and shows how these experimental results compare to the computational results of Chapter 4.

5.1 Ion Energy Distribution

Section 3.3.1 described the electrostatic energy analyzer and the procedure we used to obtain a measurement of the ion energy distribution from the probe characteristic. We utilized this instrument to measure the axial component of the ion energy spectrum for several different laboratory operating conditions.

If the motion of ions in the plasma were predominantly collisionless, each ion would possess a directed kinetic energy equal to the electrostatic potential through which that ion had been accelerated. One would therefore expect that for collisionless ions the distribution of ion energies at a point in space would reflect the distribution in plasma potential over the region where ions are produced. From the theoretical results shown in Chapter 4, we anticipate that most of the ions are formed close to the ECR heating region in a volume over-which the variation in plasma potential is relatively small. Hence, barring scattering collisions and charge exchange collisions, one would expect the ion energy distribution to be sharply peaked in an ECR plasma accelerator.

As the example curve of Fig. 3.6 shows, our measurements indicated that the ion energy distribution was not sharply peaked. A reasonable interpretation of this observation is that a combination of momentum and charge exchange collisions between the moving ions and the neutral gas in the vacuum tank caused the ion energy distribution to broaden upstream of the electrostatic energy analyzer. As we will now show, if these collisional effects are responsible for broadening the ion energy distribution, one would expect the distribution to be wider in measurements taken further downstream and in measurements taken at higher vacuum-tank pressures. The approximate analysis that follows assumes that the ion energy does not vary widely from one run to the next and that the ion-atom collision cross-sections can therefore be treated as constant.

The temperature of the gas in the vacuum tank is determined primarily by the vacuum tank wall temperature (room temperature). As a reasonable approximation we can therefore treat the temperature of the gas in the vacuum tank to be constant. Under this approximation and assuming only ideal gas effects, the number density of gas atoms in the tank is proportional to the tank pressure. Further, the mean-free path between collisions for ions moving through a tenuous neutral gas is inversely proportional to the gas atom number density. As a result, the mean number of collisions that an ion undergoes in traversing the distance from the ECR heating region to the probe is directly proportional to the product of the tank pressure and to the distance between the probe and the accelerator. We define the non-dimensional width of the distribution, W, to be the ratio of the width of the distribution to the maximum energy of ions detected by the probe:

$$W \equiv \frac{E_{MAX} - E_{MIN}}{E_{MAX}}, \tag{5.1}$$

where E_{MAX} is the maximum energy of ions detected by the probe and E_{MIN} is the minimum energy of ions detected. For the example case of Fig. 3.6, E_{MAX} is taken to be 90±5 eV, E_{MIN} is taken to be 45±5 eV, and therefore W = 0.5±0.1 . The tank pressure was measured to be $(3.1\pm 0.2)\text{x}10^{-5}$ torr when the data of Fig. 3.6 was taken and the probe was located 3.6±0.5 inches downstream of the accelerator. The product of pressure and distance, Pz, in this case was $(11.2\pm2)\text{x}10^{-5}$ torr•inches. Table 5.1 presents a summary of the electrostatic probe data obtained in this research. Figure 5.1 is a plot of W versus Pz for the data shown in Table 5-1.

Figure 5.1 shows that the width of the ion energy spectrum as measured by the electrostatic probe is correlated with Pz, in support of the theory that scattering collisions of the ions were important in establishing the ion energy spectrum. If we assume this to be the case, then it is reasonable to suggest that the ion energy distribution would have been more sharply peaked had the experiments taken place in space or in a vacuum system with very high pumping speeds. Further, it is reasonable to suggest that ions in the high energy tail of the measured distributions were those relatively few ions that did not undergo significant energy-reducing collisions while traversing the vacuum tank. In other words, we can interpret the high energy end of the distributions as representing the kinetic energy that the ions would have had, if the experiment been conducted in space or in a much more capable vacuum facility.

Table 5-1 Electrostatic Energy Analyzer Probe Data

RUN #	E_{MAX} (±5ev)	E_{MIN} (±5ev)	10^{-5}•P_{tank} (±0.5torr)	z (±0.5in)	W (#)	Pz (torr•in)	$P_{\mu\lambda}$ (kW)	$\dot{m}$ (sccm)
1A	100	5	7.3	80	.95	584	1.25	6.9
2A	100	5	7.3	80	.95	584	1.25	6.9
3A	100	5	7.3	80	.95	584	1.25	6.9
4A	100	5	7.3	80	.95	584	1.25	6.9
1B	110	75	6.7	N/A	.32	40.2	.75	5.0
2B	110	75	6.7	N/A	.32	40.2	.75	5.0
3B	110	75	6.7	N/A	.32	40.2	.75	5.0
4B	110	75	6.7	N/A	.32	40.2	.75	5.0
C	70	10	8	8	.85	640	.51	6.9
D	80	10	5	80	.88	400	N/A	N/A
E	60	10	5	80	.83	400	N/A	N/A
F	50	5	8	80	.90	640	N/A	N/A
G	85	55	3.3	3.	.35	9.9	1.1	3.0
1H	80	40	5.3	4.2	0.5	22.1	.52	3.2
2H	80	40	5.3	4.2	0.5	22.1	.52	3.2
3H	80	40	5.3	4.2	0.5	22.1	.52	3.2
4H	80	40	5.3	4.2	0.5	22.1	.52	3.2
5H	80	40	5.3	4.2	0.5	22.1	.52	3.2
1I	90	54	3.1	3.6	0.50	11.16	1.09	4.1
2I	40	85	3.2	12.6	0.53	40.3	1.0	4.1
3I	85	45	3.0	12.6	0.47	37.8	1.0	2.8
4I	85	45	3.0	12.6	0.47	37.8	1.35	2.8
5I	85	47	3.0	1.1	.45	3.3	1.03	2.8
J	100	15	9.0	80	.85	720	.75	6.1

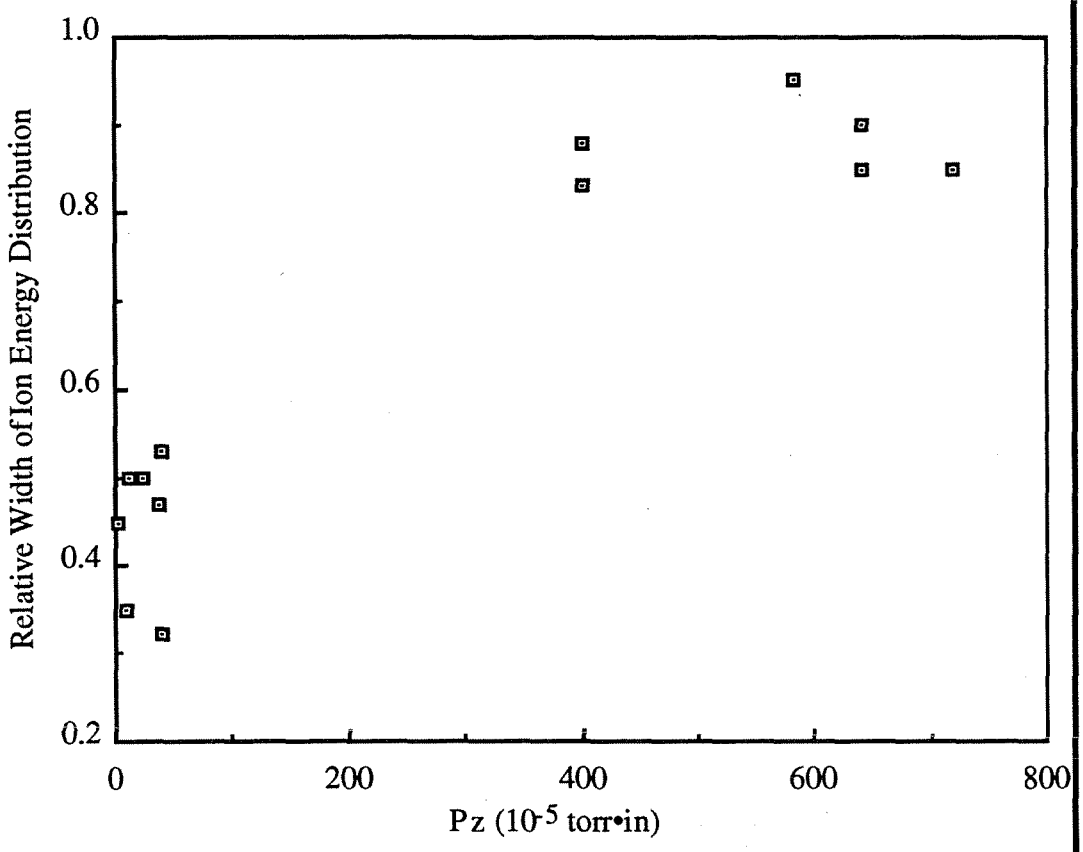

Fig. 5.1 Relative Width of Ion Energy Distribution as a Function of the Product of Tank Pressure and Distance From Probe to Accelerator

If the proposed interpretation of the data is valid, than we would expect that the maximum energy of ions detected by the probe (E_{MAX}) to behave according to the theory presented in Chapter 2 and follow trends like those shown in Chapter 4. To check this hypothesis, we plotted E_{MAX} versus $P_{\mu\lambda}/\dot{m}$, for the useful data of Table 5.1, as shown in Fig. 5.2. We chose $P_{\mu\lambda}/\dot{m}$ as the abscissa in Fig. 5.2 because it represents the microwave energy input per particle and one could reasonably expect E_{MAX} to increase monotonically with $P_{\mu\lambda}/\dot{m}$ based on the expectation that kinetic efficiency does not vary too widely for different cases with the same value of $P_{\mu\lambda}/\dot{m}$.

The data of Fig. 5.2 shows that there is little correlation between the measured kinetic energies and the ratio of input power to mass flow rate. Most of the kinetic energy data is clustered between about 70 eV and 110 eV with one apparently anomalous data point at 40 eV. If we convert the quantity on the ordinate in Fig. 5.2 to electron volts per argon atom,

we find that 0.25 kW/sccm corresponds to about 3500 eV per argon atom. Assuming that the flux of accelerated argon ions is on the same order as the input gas flow rate, a reasonable assumption consistent with the predictions of Chapter 4 and the data presented in the next section, then we can interpret Fig. 5.2 to suggest that the kinetic efficiency of the accelerator tested here varied between about 1 and about 5 percent.

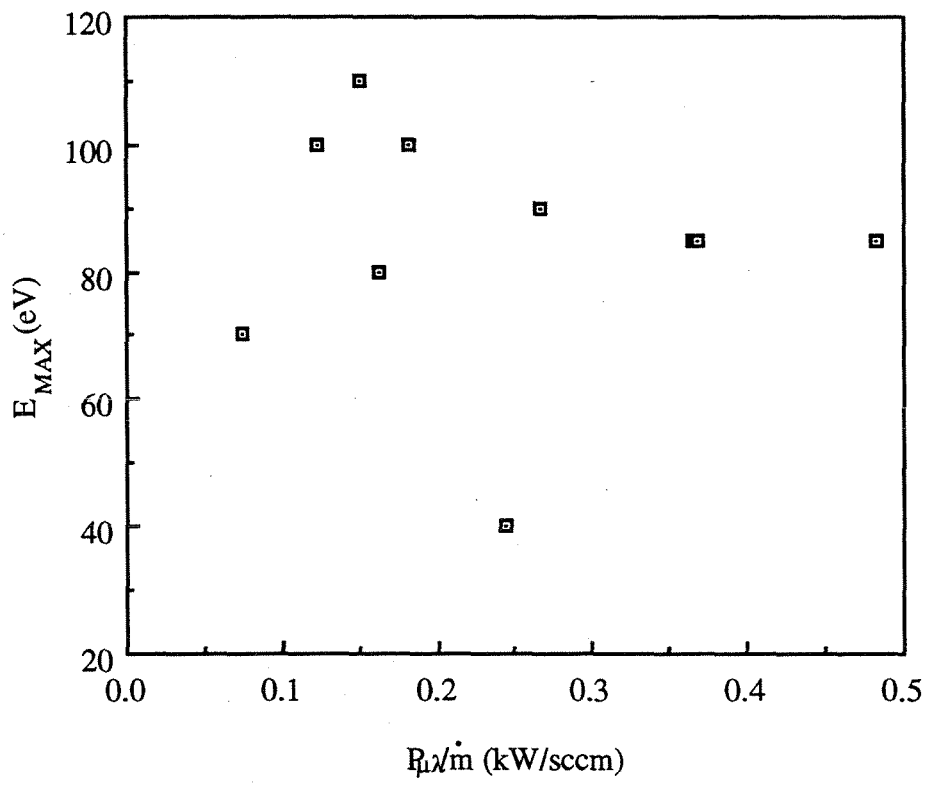

Figure 5.2 Maximum ion energy as measured by electrostatic probe plotted against the ratio of input power to mass flow rate.

The magnitude of the peak ion energy of the data in Fig. 5.2 corresponds to ion velocities of between 1.4×10^4 and 2.3×10^4 m/s. It is interesting to compare the ion energy range of Fig. 5.2 against the predictions of Chapter 4 and Appendix F. To do this we display the calculated predictions for the quasi-isothermal cases in Fig. 5.3 and the calculated predictions for the cases with no axial heat conduction in Fig. 5.4.

We find that the distribution of ion energies for the case of quasi-isothermal electrons and finite vacuum tank effects most closely matches the experimental data of Fig. 5.2. The range of velocities predicted by calculation for this case was 1.0×10^4 to 1.7×10^4 m/s. However, this range of velocities was obtained for values of input microwave energy per input argon atom that were considerably less than those explored in the experimental effort. The reason for this discrepancy is that the experimental facility could not simultaneously duplicate the range of mass flow rates and input power levels that the model could address. Likewise, numerical solutions of the differential equations of the model could not be found for much of the range of operating conditions that the experimental facility could address. To reconcile the abscissa of Fig. 5.2 with the abscissa of Figs. 5.3 and 5.4 we postulate that a loss mechanism not accounted-for in the model is extracting energy from the plasma. Such a loss mechanism would have an effect similar to that of reducing the input microwave power.

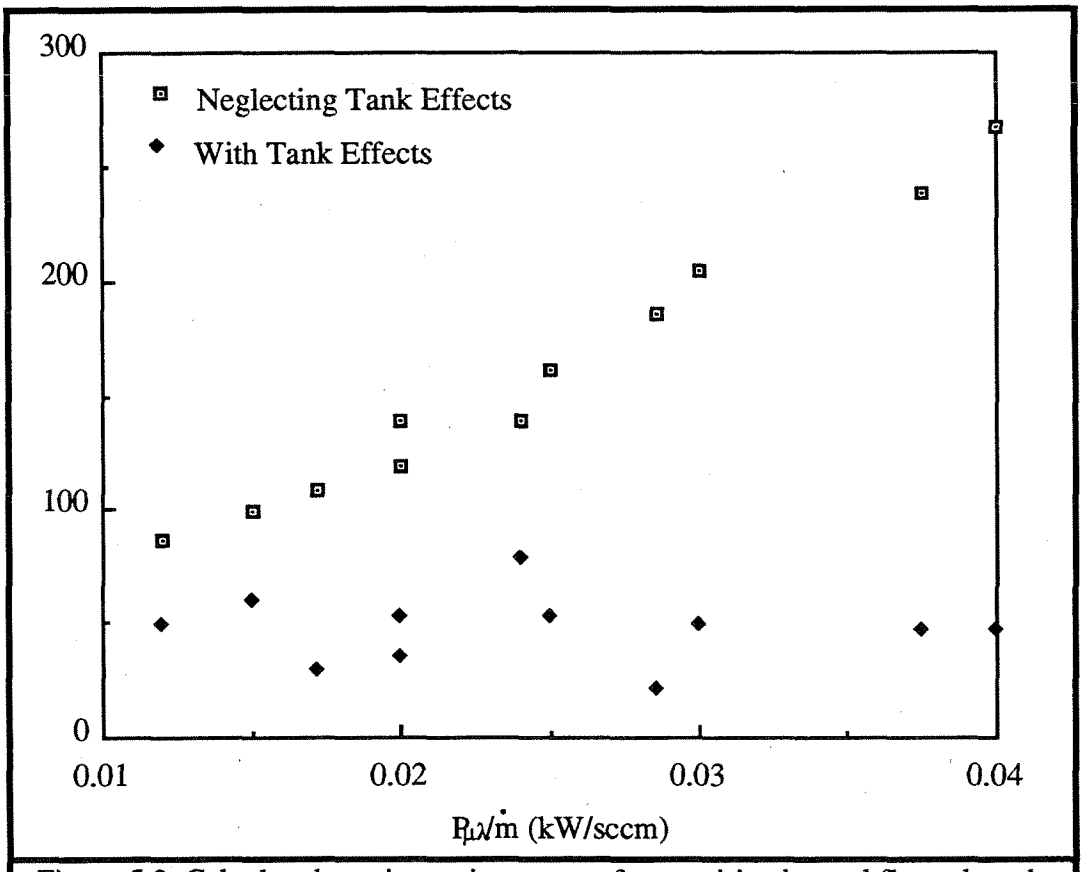

Figure 5.3 Calculated maximum ion energy for quasi-isothermal flow plotted against the ratio of input power to mass flow rate.

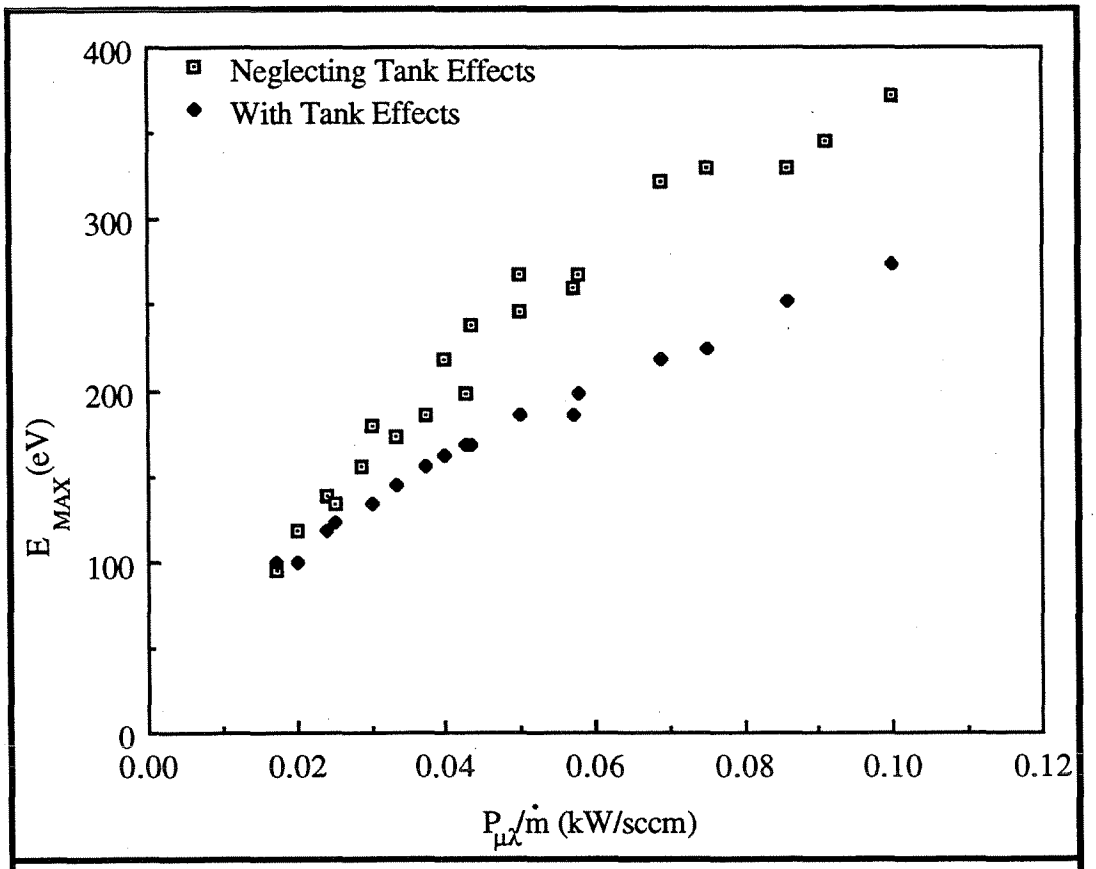

Figure 5.4 Calculated maximum ion energy for flow without axial heat conduction plotted against the ratio of input power to mass flow rate.

It is natural to question why there appears to be scatter in the computational data shown in Figs. 5.3 and 5.4. The apparent scatter stems not from some numerical error or uncertainty in the computation, but rather from our choice of parameters to plot on the ordinate and abscissa of the figures. For example, the two points in Fig. 5.3 that have the same value of 0.02 kW/sccm for $P_{\mu\lambda}/\dot{m}$ correspond to two different operating conditions, one with an input power level of 300 watts at a flow rate of 15 sccm, the other with an input power level of 500 watts and a flow rate of 25 sccm. Because the loss processes in the model are not treated as simple linear functions, these different input conditions yield different kinetic efficiencies and therefore do not produce the same values of E_{MAX}.

5.2 Beam Density

Section 3.3.2 described the beam density analyzer and the procedure we followed using this device. This instrument was useful in measuring beam density for microwave input power levels ranging from about 100 watts up to about 3 kW at different input mass flow rates in the 5 to 15 sccm range. The results of measurements made with the beam density analyzer are shown in Fig. 5.5.

In Fig. 5.5, measured collection cup current is expressed on the abscissa with applied microwave power on the ordinate for three different argon flow rates; 7.2 sccm, 11.6 sccm, and 14.2 sccm. Because the beam density analyzer was fabricated with an open aperture of 1.0 cm^2, the measured collection cup current can also be read as the plasma beam density in amperes per square centimeter.

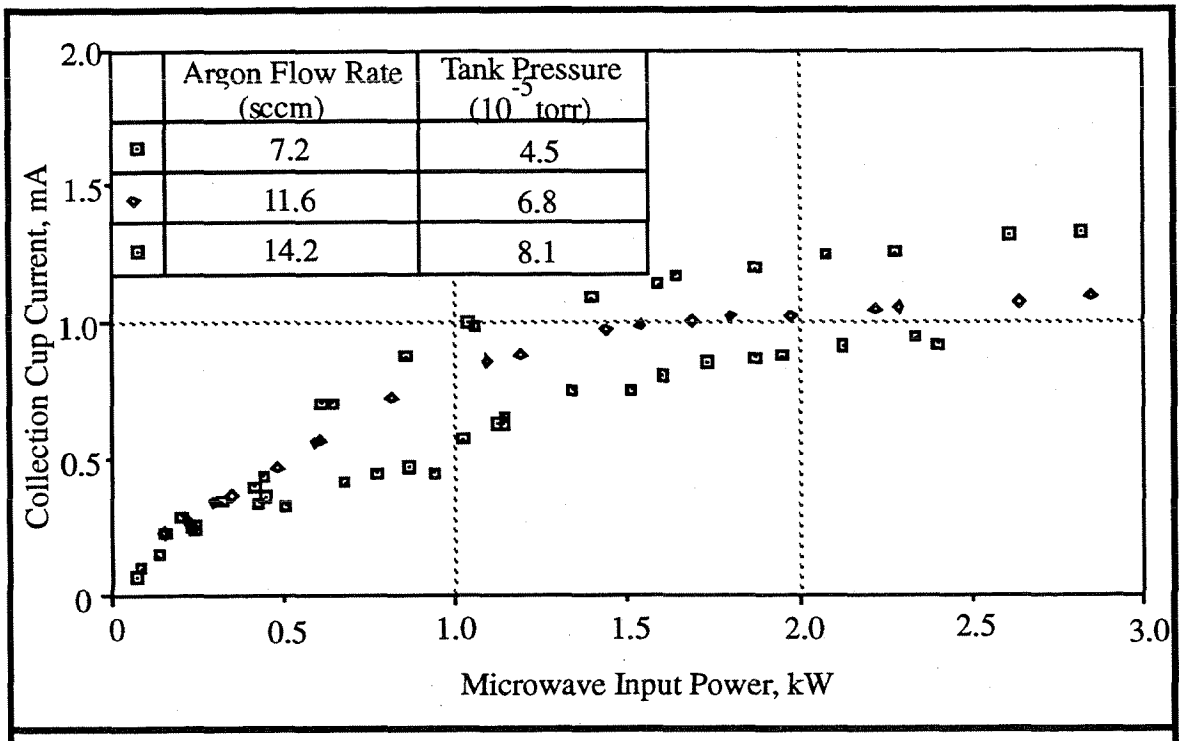

Figure 5.5 Collection cup current as measured by beam density analyzer over a range of input microwave power levels from 0.1 kW to 3.0 kW

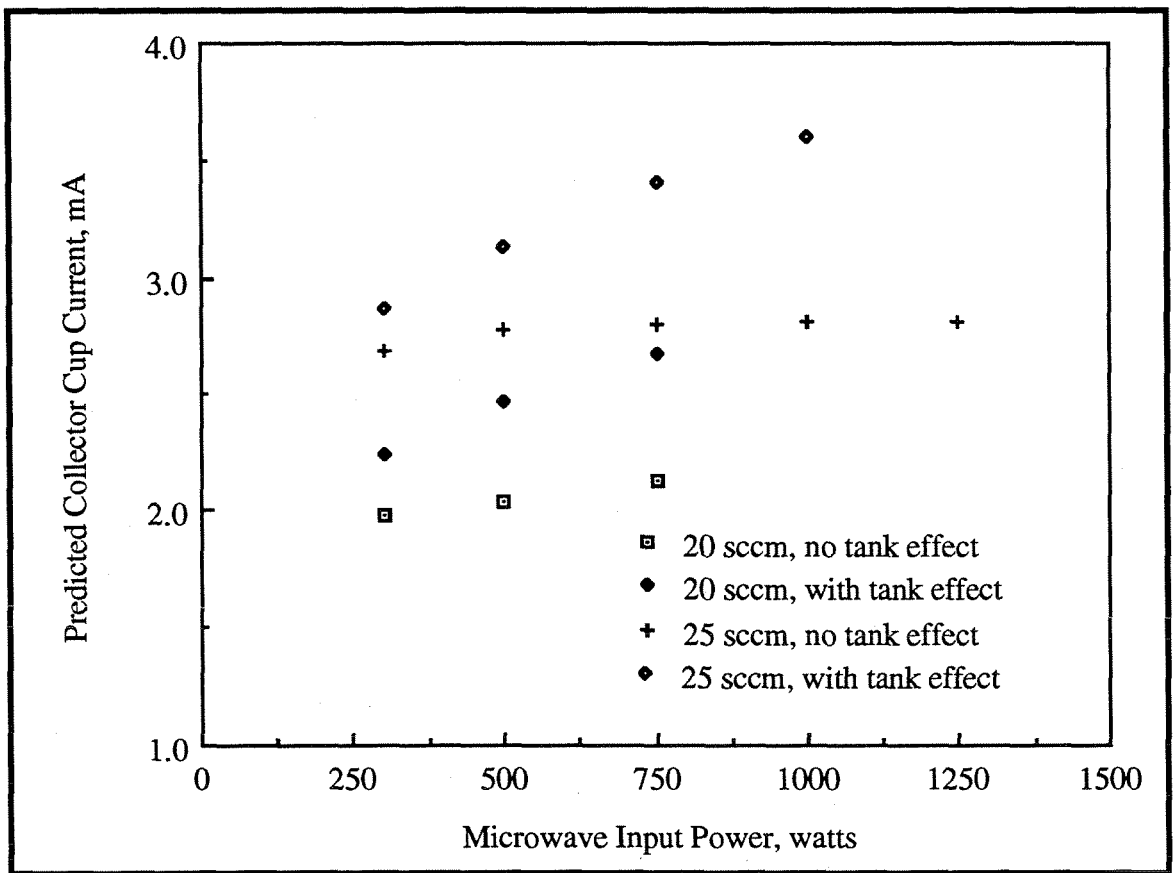

Figure 5.6 Predicted collector cup current as a function of input microwave power level from 0 to 1.5 kW for quasi-isothermal assumption.

For comparison to Fig. 5.5, Figs. 5.6 and 5.7 show the collection cup current as predicted by the quasi-one-dimensional model. Figure 5.6 shows the prediction under the assumption of quasi-isothermal flow and Fig. 5.7 shows the prediction under the assumption of flow without axial heat conduction. As in Section 5.1, and for the same reasons, the values of the parameters used in the calculations are close, but not equal to, the values we were able to use in the experimental measurements. The differences between the parameters of the predictions and those of the measurements in the present case are that the argon flow rate assumed in the predictions is somewhat more than the flow rates used in the experiments and the calculations do not include power levels as high as those in the experiment. However, the parameter space of the calculations and the experiments are close enough to allow reasonable comparisons to be drawn.

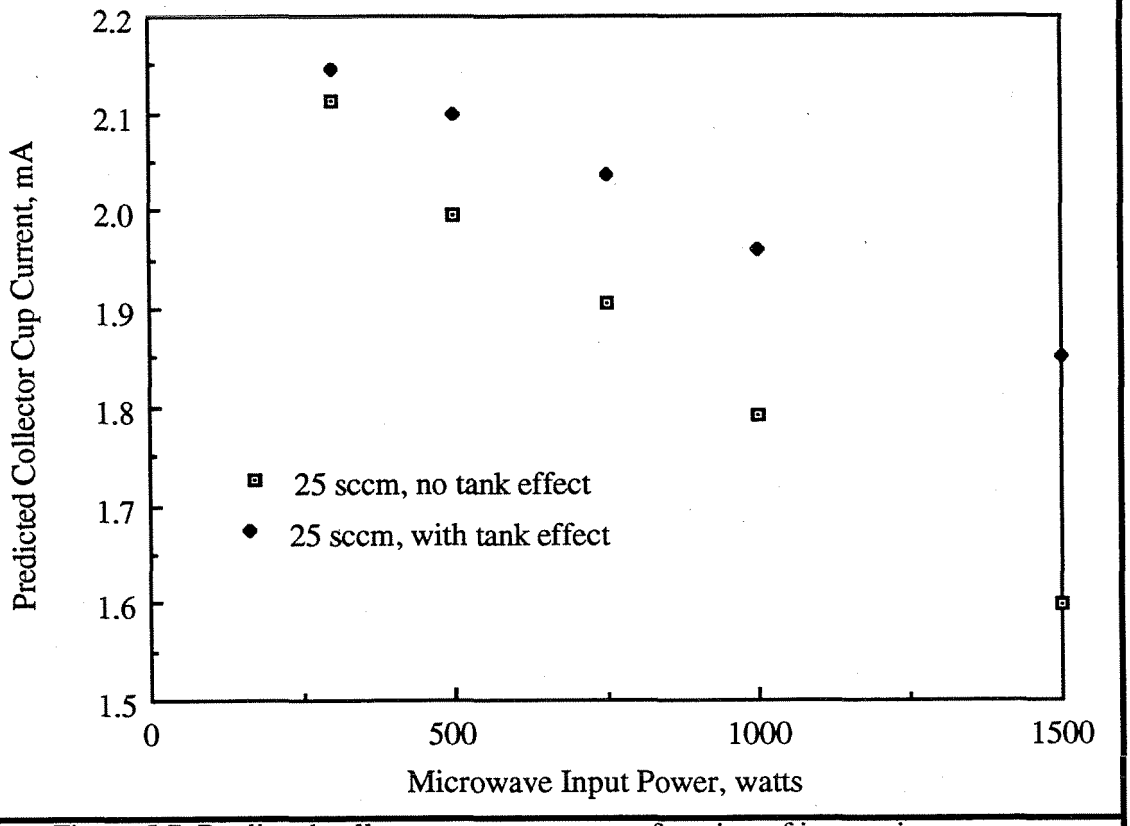

Figure 5.7 Predicted collector cup current as a function of input microwave power level from 0 to 1.5 kW for assumption of zero axial heat conduction.

The predicted trend of rising cup current with rising power levels in Fig. 5.6 is similar to the trend shown in Fig. 5.5, though the measured values of the collector cup current are about a factor of two less than one would expect from the calculation, even accounting for the difference in assumed argon flow rates. The magnitude of the predicted collector cup current in Fig. 5.7 does overlap the measured cup current of Fig. 5.5, but the predicted trend for the case of flow without axial heat conduction is opposite to the measured trend. The difference between the predictions of Fig. 5.6 and the measurements of Fig. 5.5 could be explained by assuming that some fraction of the input microwave power is lost by a mechanism not accounted-for in the model. For example, if the postulated loss mechanism has the same effect as reducing the input power in the measurements of Fig. 5.5 by about a factor of five, than one would expect that the measured collector cup current for the flow rate of 11.6 sccm would be about half that of the prediction of Fig. 5.6 in which the flow rate was assumed to be 20 sccm and tank effects were included. Inspection of Figs. 5.5 and 5.6 reveals that the data is consistent with such an expectation.

5.3 Electron Temperature and Plasma Potential

Sections 3.3.3 and 3.3.4 described the cylindrical Langmuir probes, the emissive probes, and the procedures we followed using them to measure the perpendicular and parallel components of the electron temperature and the plasma potential. The electron temperature and plasma potential data that we obtained using these devices is presented in Table 5-2.* In Table 5-2, V_p is the plasma potential. The titles on the other columns of Table 5-2 have been defined previously.

Table 5-2 Electron Temperature and Plasma Potential

Data Set	$Te_\perp$ (±5eV)	$Te_{//}$ (±5eV)	V_P (±5V)	z (±1cm)	$10^{-5}\cdot P_{tank}$ (±0.5torr)	$P_{\mu\lambda}$ (±5watt)	$\dot{m}$ (±0.5sccm)
1A	26	17	45	5.0	5.0	500	6.0
1B	33	15	55	1.0	8.0	130	5.5
2B	51	32	55	1.0	8.0	500	5.5
1C	27	16	45	5.0	6.4	130	5.5
2C	33	26	40	5.0	6.8	133	6.0
3C	31	32	45	5.0	6.8	500	6.0
1D	35	N/A	68	0.0	8.1	766	5.5
2D	23	N/A	54	5.7	8.1	766	5.5
3D	20	N/A	50	6.1	8.1	766	5.5
4D	24	N/A	59	8.9	8.1	766	5.5
5D	26	N/A	56	12.7	8.1	766	5.5
6D	19	N/A	53	16.1	8.1	766	5.5
7D	17	N/A	58	22.4	8.1	766	5.5
8D	12	N/A	47	27.6	8.1	766	5.5
9D	12	N/A	48	32.5	8.1	766	5.5
1E	N/A	24	64	0.0	9.0	750	5.6
2E	N/A	24	62	2.3	9.0	750	5.6
3E	N/A	20	60	4.1	9.0	750	5.6
4E	N/A	17	60	6.2	9.0	750	5.6
5E	N/A	17	58	8.5	9.0	750	5.6
6E	N/A	17	57	11.7	9.0	750	5.6
7E	N/A	12	59	15.5	9.0	750	5.6
8E	N/A	13	54	18.8	9.0	750	5.6
9E	N/A	13	54	20.8	9.0	750	5.6
10E	N/A	10	45	28.0	9.0	750	5.6
11E	N/A	10	46	33.4	9.0	750	5.6
1F	38	23	71	0.0	9.0	750	5.3
G	N/A	N/A	63	1.5	9.2	760	5.6

* This data was taken in close collaboration with Ms. Stephanie Leifer and Ms. Ann Chopra of the Jet Propulsion Laboratory who are acknowledged for their worthy contribution to this work.

Figure 5.8 is a plot of measured plasma potential versus axial distance downstream from the end of the wave guide into the vacuum tank for data set *E* of Table 5-2. A plot of electron perpendicular temperature versus axial location for data set *D* is presented in Fig. 5.9, while a plot of electron parallel temperature versus axial location from data set *E* is presented in Fig. 5.10. All of the data presented in this section represent measurements taken at locations on the centerline of the plasma plume and downstream of the wave guide.

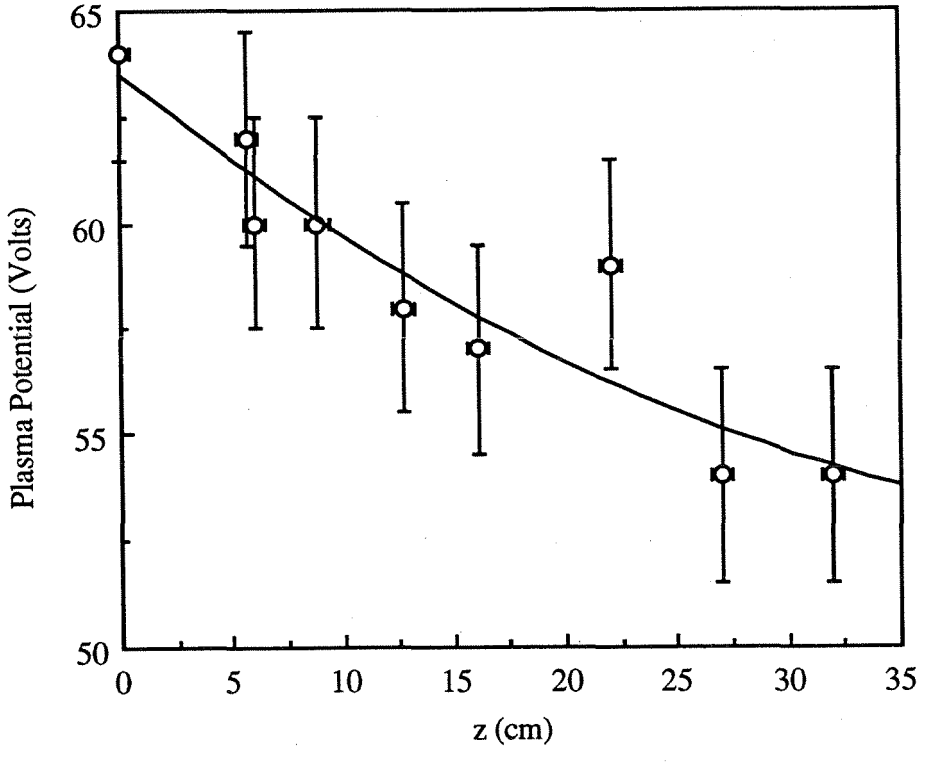

Figure 5.8 Measured plasma potential as a function of distance down stream from end of wave guide on centerline for data set D.

Inspection of Fig. 5.8 shows that the plasma potential decreases as a function of distance downstream of the thruster. This observation is consistent with the predictions made in the calculations of Chapter 4. Unfortunately the uncertainty in the data and the limited distance downstream that the probe was able to reach makes it difficult to distinguish which of the four cases of Chapter 4 follows a trend that is most similar to the trend in the experimental data. We do note, however, that the magnitude of the plasma potential is significantly less than the two to three hundred volt plasma potential predicted

by the model for the case of no back pressure in the vacuum tank and for the case of finite pressure in the vacuum tank in combination with no axial heat conduction. It would seem that for the model to predict plasma potentials within a factor of two or so of the measured values, it must account for both the finite pressure losses and the thermal conduction losses due to electron heat transport.

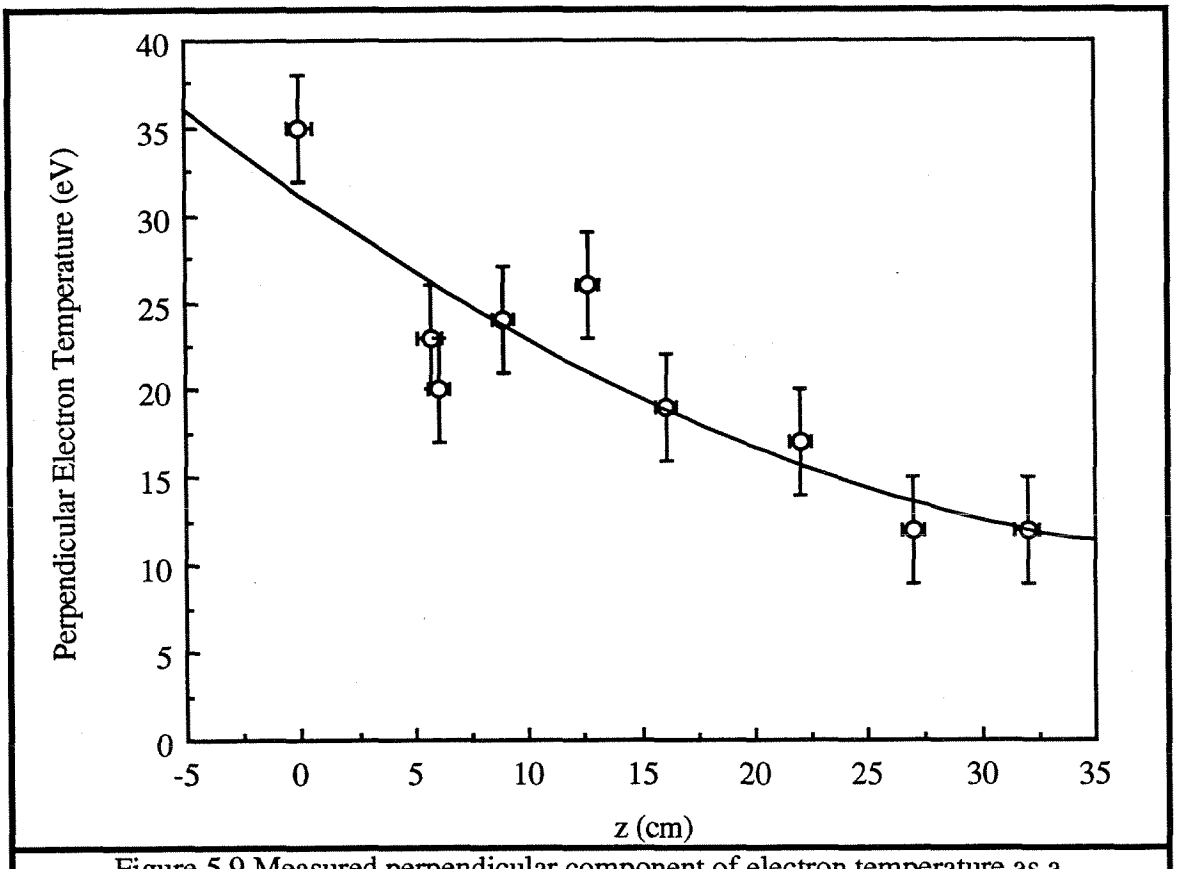

Figure 5.9 Measured perpendicular component of electron temperature as a function of distance down stream from end of wave guide for data set D.

In comparing the temperature measurements of Figs. 5.9 and 5.10 against the predictions of Chapter 4 it is necessary to recall that the Langmuir probe data presented in these figures represents temperature information and that the calculated results of Chapter 4 for $W_{//}$ and $W_{\perp}$ were predictions of average thermal energy per electron. Because the average thermal energy per electron is one half the temperature times the number of degrees of freedom in the motion described by that temperature, the perpendicular electron temperature, with its two degrees of freedom, is equal to the average perpendicular thermal energy per electron. The parallel electron temperature, with its one degree of freedom, is equal to twice the average parallel thermal energy per electron.

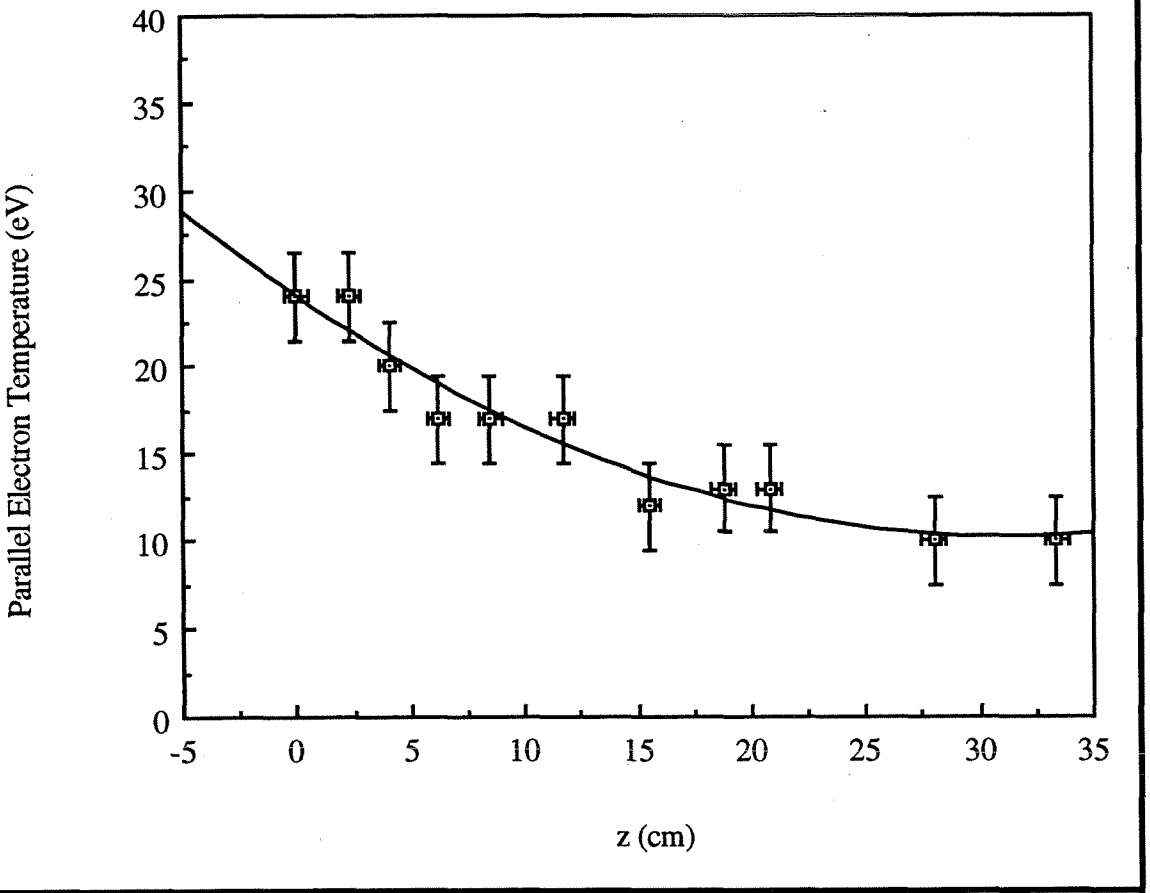

Figure 5.10 Measured parallel component of electron temperature as a function of distance down stream from end of wave guide for data set E.

Figures 5.9 and 5.10 show a remarkable similarity in the magnitude of the electron temperatures as measured perpendicular and parallel to the magnetic field lines for the two cases. The slightly higher temperatures shown in Fig. 5.9 for the perpendicular electron temperature than in Fig. 5.10 for the parallel electron temperature could be explained by the fact that in spite of an attempt to recreate identical conditions in the two runs, the microwave power level was slightly higher in data set *D* than in data set *E*, and the argon flow rate in data set *E* was slightly higher than in data set *D*. Regardless of the explanation for the similarity of the temperature measurements in the two cases, the temperature data of Fig. 5.9 is identical to the temperature data of Fig. 5.10 to within the uncertainty of the data, except in the region close to (within 5 cm) the end of the waveguide, where the perpendicular temperature is significantly (25 to 40 percent) higher than the parallel component of the electron temperature.

This result is consistent with the trends shown in the theoretical predictions of Chapter 4. Notice, (see Figs. 4.3 and 4.7) that in the cases of no axial heat conduction, $W_{\perp}$ is more than twice as high as $W_{//}$ upstream of the end of the waveguide and continues to be more than twice as large for a few centimeters downstream.* We then see that for the first 30 cm or so of flow the magnitude of $W_{\perp}$ is about twice the magnitude of $W_{//}$. The cases of quasi-isothermal flow are difficult to compare with this electron temperature data because $W_{//}$ was assumed to be constant at the calculated value. The value of $W_{//}$ was, however, predicted to be less than one half the value of $W_{\perp}$ upstream of the end of the waveguide in the quasi-isothermal calculations, and $W_{\perp}$ was predicted to fall below the value of $W_{//}$ significantly downstream of the waveguide. The measurements suggest that $W_{\perp}$ and $W_{//}$ become equilibrated significantly downstream of the waveguide and that they become constant at large distances downstream of the waveguide. It appears that experimental results behave more like the case of no axial heat conduction near the waveguide (and the heating region) and more like the case of quasi-isothermal flow far downstream of the waveguide.

For electron temperature, one comparison between experiment and theory is clear. The magnitude of the measured electron temperature is significantly lower than one would expect based on the values of electron thermal energy predicted by the model. The obvious explanation for this effect is the same as the suggested explanation for the discrepancies between the experimental data and the theory in the preceding sections. Some loss mechanism that was not accounted-for in the theory is present and extracting energy from the electron motion in the plasma of our experiments.

---

* In the case of Fig. 4.3, $W_{\perp}$ remains almost exactly twice $W_{//}$ for a considerable distance downstream of the wave guide making the appearance of thermal equilibrium between the two components of the electron temperature. This trend is a coincidence and is not born out by inspection of the other cases of no axial heat conduction and no back pressure in the vacuum tank as presented in Appendix E.

5.4 Plasma Pressure

We made several attempts to measure plasma pressure using the diamagnetic loop described in Section 3.3.5. Although some data was successfully collected, the quantity and quality of the information contained in these measurements was disappointing and of limited utility. We report our diamagnetic loop data here to provide a complete record of our experimental work. Table 5-3 presents a summary of the conditions under which we acquired diamagnetic loop data and the results of our measurements. The column labeled 'Δ B-Field' in Table 5-3 shows the calculated change in magnetic field within the area of the diamagnetic loop as determined by Eq. (3.5). The column labeled $P_{\perp}$ is the plasma pressure as calculated from the measurement of change in magnetic field based on the assumption that the measured change in magnetic field accurately reflects the diamagnetism of the plasma.

Table 5-3 Plasma Pressure Measurements Made Using Diamagnetic Loop

Data Set	$P_{\mu\lambda}$ (±5watt)	10^{-5}•P_{tank} (±0.5torr)	$\dot{m}$ (±0.5sccm)	Δ Voltage (±.1V)	Δ B-Field (±0.1x10^{-4}T)	$P_{\perp}$ (±0.1x10^{-3}Pa)
a	1175	8.9	7.0	.35	.35	.5
b	920	8.6	7.0	.35	.35	.5
c	712	8.4	7.0	.35	.35	.5
d	504	8.3	7.0	.35	.35	.5
e	638	8.3	7.0	.35	.35	.5
f	400	8.1	7.0	.35	.35	.5
g	200	7.7	7.0	.35	.35	.5
h	152	7.7	7.0	.35	.35	.5
i	1320	6.5	5.5	.60	.60	1.4
j	1095	7.2	5.5	.70	.70	1.9
k	820	7.1	5.5	.60	.60	1.4
l	685	9.5	8.6	.35	.35	.5
m	970	9.7	8.6	.35	.35	.5
n	1830	10.0	8.6	.35	.35	.5
o	260	9.4	8.6	.35	.35	.5
p	170	9.4	8.6	.35	.35	.5

Figures 5.11a through 5.11p are photocopies of the screen of a storage oscilloscope that was used to record the output of the operational amplifier circuit of Section 3.3.5. The sensitivity of the oscilloscope was adjusted in such a way that the vertical axis of the images corresponds to 0.4 volts per division. The horizontal axis recorded time data at 0.005 seconds per division. In all of the data presented here the microwave power was initially 'on' and the ECR plasma was ignited at the outset and then the power was turned off, thereby quickly extinguishing the plasma.

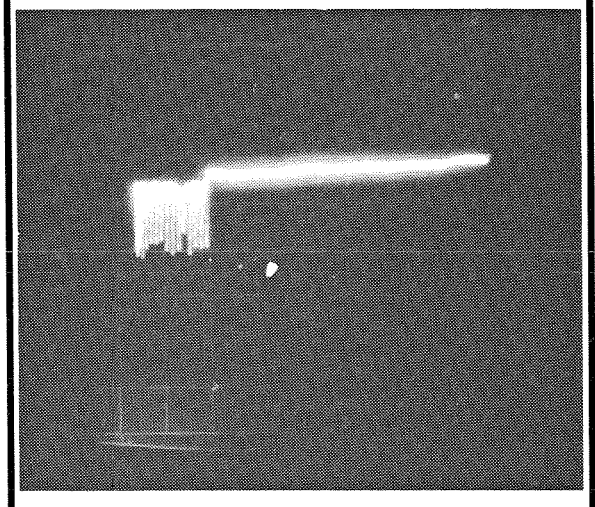

Figure 5.11a

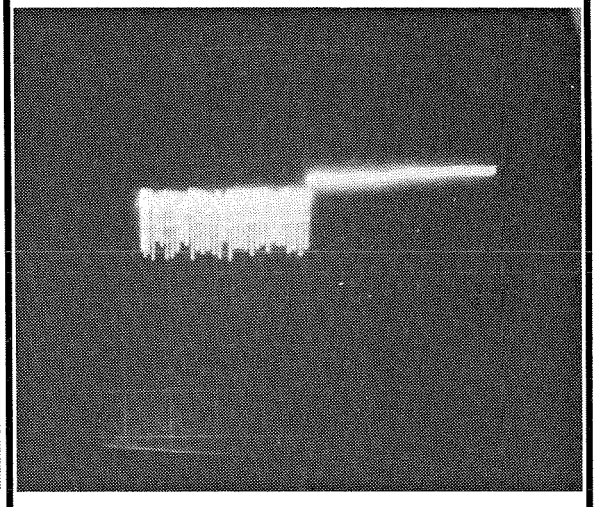

Figure 5.11b

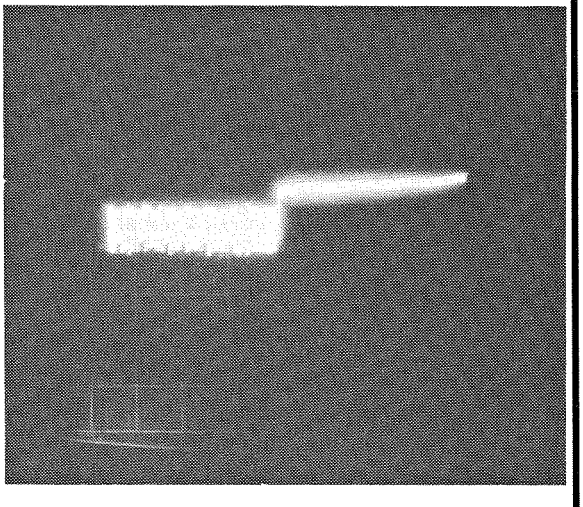

Figure 5.11c

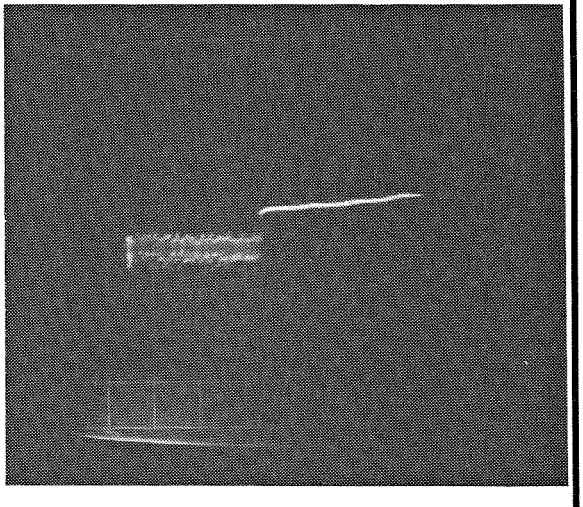

Figure 5.11d

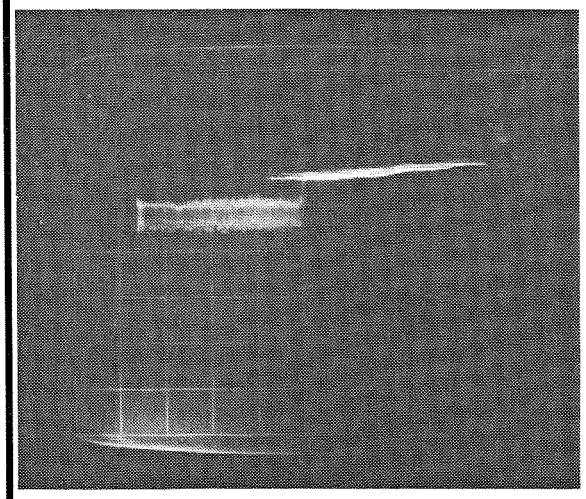

Figure 5.11e

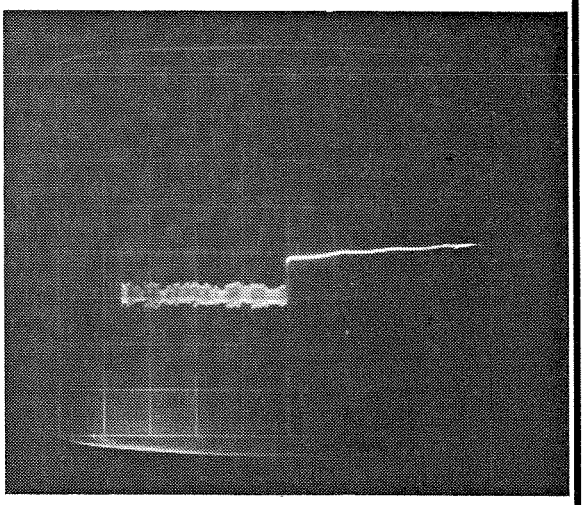

Figure 5.11f

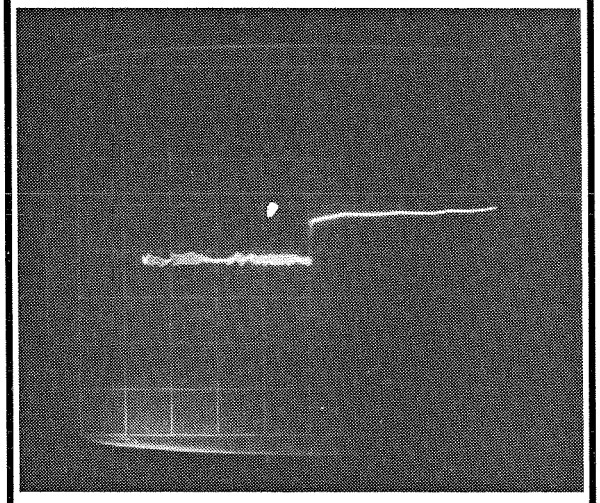

Figure 5.11g

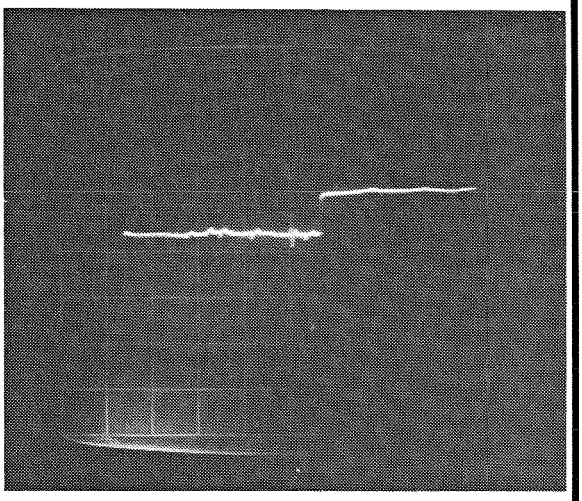

Figure 5.11h

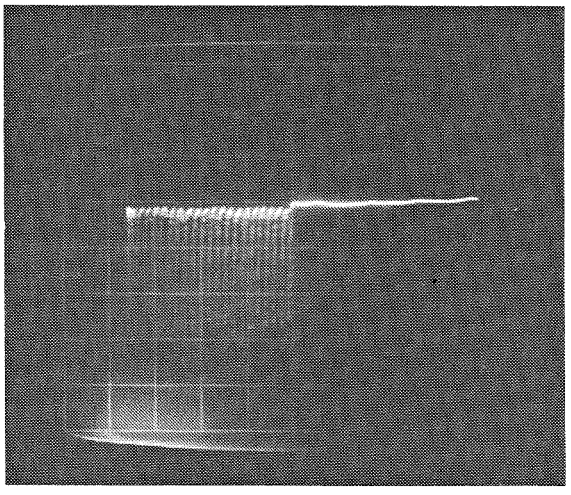

Figure 5.11i

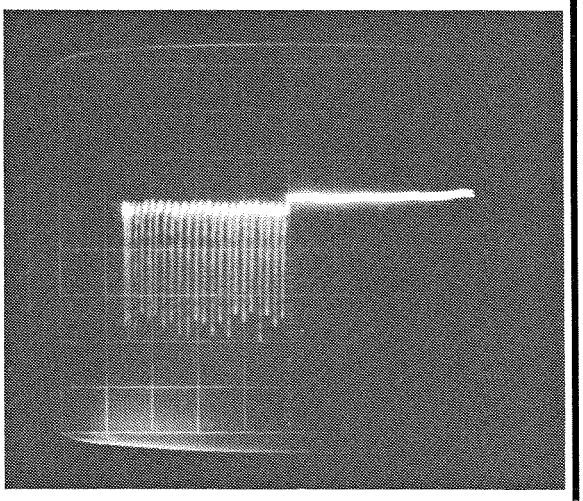

Figure 5.11j

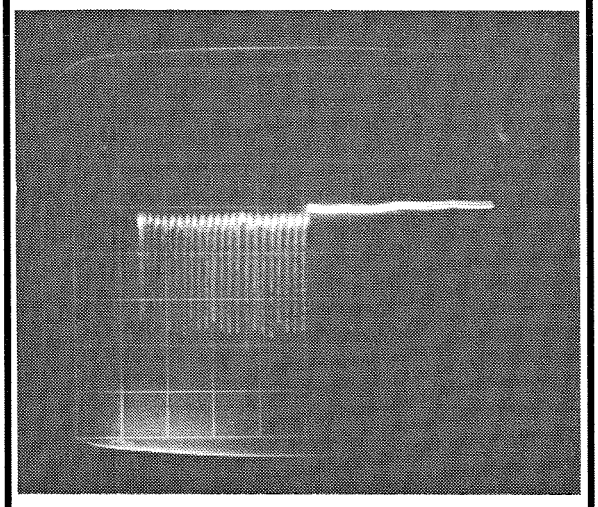

Figure 5.11k

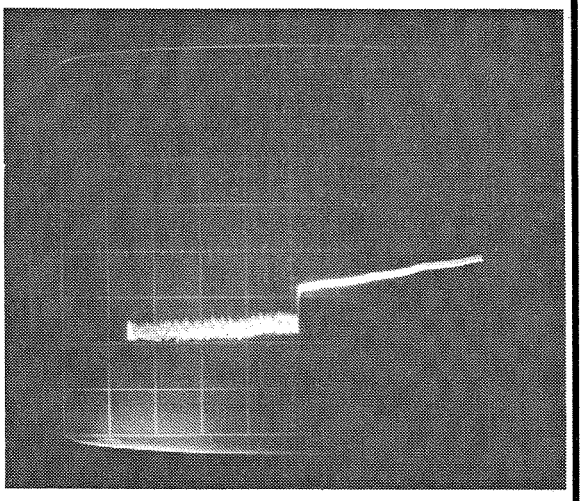

Figure 5.11l

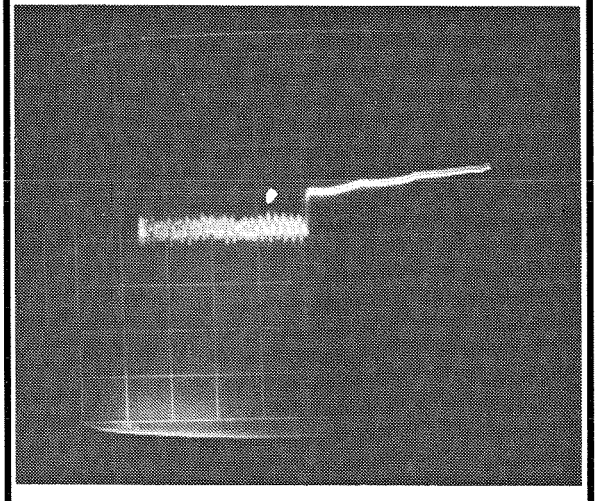

Figure 5.11m

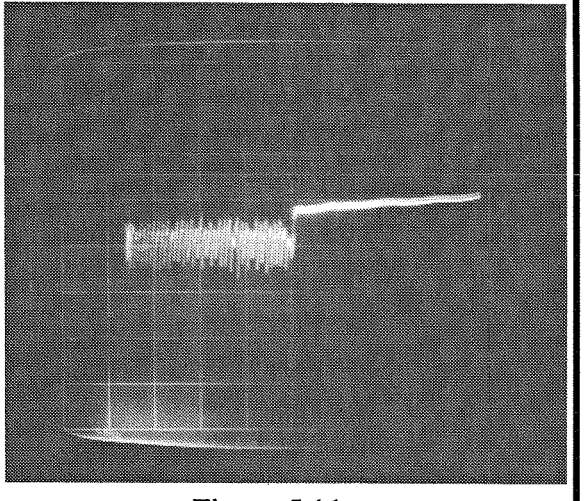

Figure 5.11n

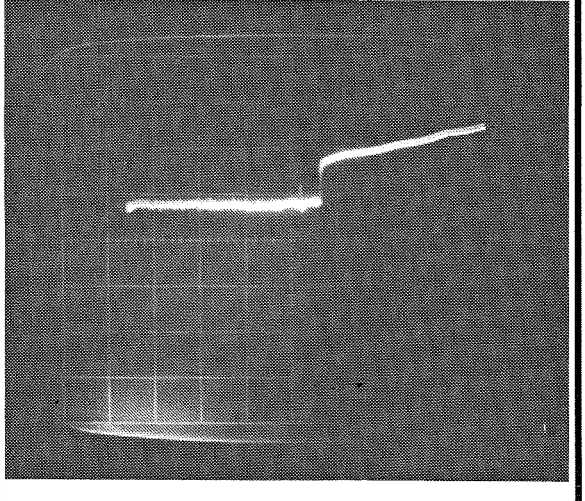

Figure 5.11o

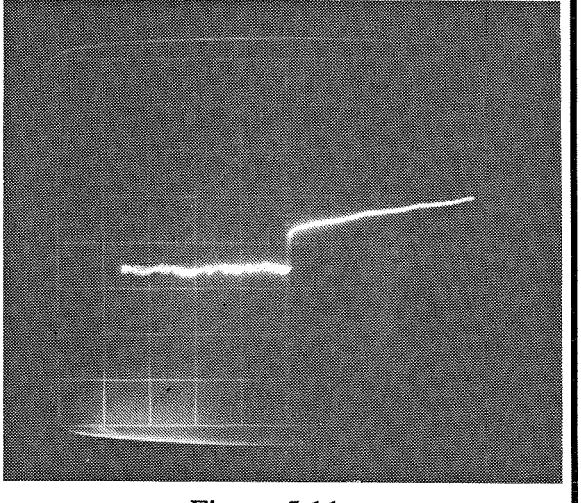

Figure 5.11p

The poorly resolved areas of rapid oscillations in Figs. 5.11 are due to unsteadiness detected by the diamagnetic loop while the plasma was on. The relatively flat line on the right side of the images corresponds to the time after the plasma was extinguished by shutting the microwave power off. The vertical difference between the average voltage value of the hash when the plasma was on and the relatively steady signal recorded after the plasma was tuned-off can be used (via Eq. (3.35)) to calculate the change in magnetic field that this device detected. Notice that the output of the integrator circuit tended to drift, both before and after the on/off event. Because this drift was controlled to relatively small rates compared to the rate of signal change when the plasma was extinguished, the drift did not introduce a significant error into the results of this measurement.

We can summarize the diamagnetic loop measurements data as follows: i) the plasma pressure is on the close order of 10^{-3} Pa, ii) the plasma pressure appears to be independent of the microwave power level, and iii) there is some indication that the plasma pressure varies inversely with mass flow rate. Let us now compare this summary of the diamagnetic loop measurements against the theory and the results of the other measurements. The theory suggests electron temperatures of a few hundred eV and plasma densities of a few times 10^{16} m^{-3}, corresponding to plasma pressures in the range of .1 to 1 Pa, a few orders higher than this measurement. The Faraday cup probe (beam density analyzer) data confirms the theoretical prediction of beam density, and therefore plasma density, to a close order-of-magnitude. The electron temperature data collected with the Langmuir probes indicate electron temperatures of about 30 eV a few centimeters downstream of the diamagnetic loop, suggesting that the electron temperature at the end of the waveguide, where the loop is located, might be about 50 eV. Hence data from other experiments suggests that the plasma pressure is in the range of about .02 to .2 Pa, at least an order of magnitude higher than indicated by the diamagnetic loop measurements.

It seems likely that a significant systematic error was present in the diamagnetic loop measurements. A likely source of this error could be the production of eddy currents in the waveguide caused by the rapidly changing magnetic field we were attempting to measure. Such eddy currents would have the effect of reducing the EMF measured by the diamagnetic loop and would therefore reduce the measured value of plasma pressure. For this reason we do not have high confidence in the magnitude of the plasma pressure as measured by the diamagnetic loop. However, one potentially significant observation we made using the diamagnetic loop has to do with likely unsteady behavior of the plasma.

We do not know the source of the unsteadiness that caused the hash that appears in Figs. 5.11, but one possible explanation is that it represents plasma oscillations. If so, the apparent frequency (a few kilohertz) of the noise suggests that the plasma oscillations could be due to ion acoustic instabilities or turbulence in the plasma flow. Because the apparent magnitude of the pressure oscillations is comparable to the magnitude of the steady-state plasma pressure, it is possible that this unsteady behavior is related to the loss mechanism that we have postulated. Such an unsteady effect would not be captured by the steady-state model of Chapter 3.

Chapter 6

INTERPRETATION OF RESULTS, CONCLUSIONS, AND SUGGESTED FUTURE WORK

6.1 Speculation On Discrepancies Between Theory and Experiment

The presentation of the experimental and theoretical results in this dissertation has pointed out discrepancies between the theoretical and experimental results as cited several times in Chapter 5. We suggested that these inconsistencies might be explained by an unknown loss mechanism not properly explicated by the theory because in each case the discrepancy between experiment and theory suggested that the measured energy content of the plasma, either kinetic or thermal energy, was less than the energy content predicted by theory. Loss mechanisms associated with wall effects, diffusion, radiation, ionization, and various collision phenomena are adequately addressed by the theory and we therefore suggest that none of these are responsible for the inconsistencies between theory and experiment. Rather, it is most likely that the effect responsible for the deficiency of the theory is a phenomena that was not addressed by our modeling effort.

Because this was the first to attempt to provide a quantitative model of the ECR plasma accelerator that takes several major effects into account, we chose to use only steady-state mechanics as a simplifying assumption. Unfortunately, the data collected in the diamagnetic loop experiments indicates that some unsteady behavior of the plasma does occur. The history of applied plasma physics contains numerous examples in which unsteady effects such as plasma turbulence or plasma instabilities cause energy to be lost from flows thereby reducing the effective efficiency of devices under development. It would appear that we have encountered another example of this phenomenon. It is possible that some combination of plasma turbulence and plasma instabilities is responsible for the unaccounted power loss in our experiments.

Another likely source of the discrepancy between the theory and experiment is in the coupling of microwave power to the plasma. Based on the experimental reports of the work conducted on ECR plasma accelerators in the 1960s and on our own preliminary measurements of coupling efficiency conducted at relatively high power levels (1 to 3 kilowatts) we assumed that good coupling of microwave power to the electrons was taking place in our experiments. It now seems however, that the coupling efficiency we assumed

in this work was too high, possibly by more than a factor of two. If so, coupling losses would explain the discrepancies between theory and experiment.

6.2 Research Conclusions and ECR-Thruster Performance Potential

To a space systems engineer, the most important performance parameters that determine the usefulness of an electric thruster for space propulsion are the jet efficiency and the specific impulse. The jet efficiency is defined as the ratio of the jet power to the input power. Jet power is defined as:

$$P_j \equiv \frac{F^2}{2\dot{m}} \tag{6.1}$$

where F is the magnitude of the thrust and $\dot{m}$ is the input mass flow rate. The jet efficiency is normally written:

$$\eta_j \equiv \frac{P_j}{P_i} \tag{6.2}$$

where P_i is the magnitude of input power. Specific impulse is defined as the thrust per unit mass flow rate:

$$I_{sp} \equiv \frac{F}{\dot{m}}. \tag{6.3}$$

Notice that based on this definition, the correct dimensions for specific impulse are impulse (momentum) per unit mass, which is equivalent to distance per unit time or velocity.

In this dissertation we have used four different types of efficiencies to describe the ECR plasma acceleration process: coupling efficiency, power efficiency, propellant utilization efficiency, and nozzle efficiency. The jet efficiency is the product of these four efficiencies. If the jet efficiency is high (typically must be well over 50 percent) and the specific impulse is well suited to a mission of interest, then the device may be of interest to the propulsion community. It is therefore important to ask how high we can realistically expect the jet efficiency of a practical ECR plasma thruster to be. We addressed the first part of this question in our review of the literature, which suggested (Chapter 2) that coupling efficiency can be expected to be very high (>0.95) for ECR plasma propulsion devices. Unfortunately, our microwave diagnostics were not adequate to confidently

confirm this assumption and the coupling losses may be much larger than we assumed. There is, however, a large body of literature on the subject of ECR coupling that suggests that coupling efficiency can be improved for this device if future work determines that coupling efficiency in our research apparatus was indeed low.

The theoretical predictions presented in Chapter 4 give a range of values for power efficiency depending on operating conditions and the choice of assumption regarding axial heat conduction. However, for those conditions in which we attempted to simulate the vacuum of space (i.e., the zero vacuum tank back pressure cases) power efficiency was always less than about 55 percent. This power efficiency was limited primarily by the effects of electron-heavy collisions (ionization and radiation) and wall losses. Based on arguments presented in Chapter 2, these losses could both be made much lower in future designs that utilize deuterium propellant and higher magnetic fields or larger beam diameters, but verification of the advantages of deuterium propellant will require additional computational study, at least. In any case, the experimental measurements did not verify the theoretical predictions due to the effect of some loss mechanism that is still not understood. If this loss mechanism is the result of plasma turbulence or plasma instabilities as we suggest, it is possible that continued research could identify the problem and develop ways to minimize its effects, but unless this is accomplished, power efficiencies for argon-based ECR engines will not likely be higher than about 10 percent. We could speculate based on analogy that even for deuterium-based ECR engines, unless the unknown loss mechanism is identified and controlled, power efficiencies will not be higher than about 25 percent.

For propellant utilization, we found reasonably good agreement between theory and experiment. The results of this research effort suggest that propellant utilization efficiency for ECR thrusters could be in the range of 80 to 90 percent. Although we did not attempt to obtain direct experimental verification of our theory of plasma separation from a magnetic field, the axi-symmetric, collisionless model described in Chapter 2 includes significant conservative assumptions and suggests that nozzle efficiencies could be as high as about 90 percent for magnetic nozzles configured to work on ECR-type plasma engines. However, for the simple solenoid coil configuration generally used in experimental research on magnetic nozzles for space propulsion, significantly lower efficiencies can be expected. For the configuration of our research device the nozzle efficiency was estimated to be 24 percent.

To summarize the conclusions of this research effort concerning the performance potential of the ECR plasma engine, Table 6-1 presents the range of estimated values for each aspect of jet efficiency based on our theoretical and experimental results for argon propellant and our speculations regarding what might be possible after considerable future research and the use of deuterium propellant.

Table 6-1 does not represent raw data, but rather judgments based on the data. For example, there have been no experiments that we are aware-of using deuterium propellant. Based on the results of our experimental effort we would speculate that the efficiency of such a device would be about 3 percent, if it were founded on the design of the devices that have been tested to date. If, on the other hand, the performance level suggested by our theoretical results can be achieved, efficiencies in the 60 percent range for high specific impulse deuterium systems may be possible. However, it does not seem likely that argon-based ECR engines will ever exceed efficiencies higher that about 40 percent, and indeed, the device we have thus-far tested in probably no more than about 2 percent efficient.

Table 6-1 Summary of Conclusions And Speculations Regarding Possible Future Developments

	Existing ECR Test Device		Speculative Deuterium Device	
	Theory	Experiment	Optimistic	Extrapolated
Coupling Efficiency	.98	.30	.98	.95
Power Efficiency	.52	.30	.80	.45
Propellant Use	.90	.85	.90	.85
Nozzle Efficiency	.90	.24	.90	.24
Net Jet Efficiency	.41	.02	.64	.09

This summary of loss mechanisms is expressed in a multiplicative format and is consistent with the table in Chapter 1 (Table 1-1) that expresses similar information in an additive format. The two tables are consistent but show different information and should be interpreted differently. For example, in Table 1-1 the loss estimate for plume divergence in the present research device is 7 percent. This estimate is consistent with the nozzle efficiency shown in Table 6-1 because the nozzle efficiency of 24 percent is applied to a flow with kinetic power that has already been reduced by the other listed effects to just 9 percent of input power.

6.3 Suggested Future Work

These conclusions suggest that justification for future work on the ECR plasma engines should be based on its long range potential to provide reasonably high efficiencies at very high specific impulse. The missions for which such high specific impulse systems are best suited are very high energy missions of space exploration in which short flight time and hence large spacecraft delta-V is desirable. Examples of such missions include piloted exploration of the solar system, robotics orbiters of the outer planets, and robotic probes that go beyond the solar system to such destinations as the Ort Cloud.

Given that our society is unlikely to initiate any such missions within the next few decades, it does not make sense now to embark on an ambitious program of engineering development of the ECR plasma accelerator. It does, however, make sense that a small program be continued in this area in a university environment to further probe the fundamentals of the physics of this device. Such research has the additional benefit of providing basic research results that are applicable to other problems of applied plasma physics. The ECR plasma accelerator provides an ideal platform from which to conduct studies of basic plasma physics because the plasma environment it embodies is rich in scientific unknowns but benign enough that meaningful research can be conducted on the device within a modest experimental budget.

Future theoretical studies of this device should proceed in three areas: i) understanding the effects of changing propellant fluids of the performance of the device, ii) understanding time dependent phenomena, and iii) extending the modeling of this device beyond MHD or continuum models to include a fuller understanding of non-equilibrium effects. The first suggested area of endeavor, understanding the effects of alternative propellant fluids, could be accomplished with no change to the existing theory and only minor changes to the existing computer program. These changes would involve substituting the atomic and molecular physics of deuterium for the atomic physics models of argon presently used in the computer program.

Understanding time dependent phenomena could proceed in one of two ways. The first option would be to rewrite the existing theory in time dependent form and then use one of several existing numerical packages to attempt to find time dependent solutions to the resulting equations. The other possibility would be to obtain a copy of one of the standard MHD computer models that have been developed by the department of energy for fusion

and other exotic physics research and apply or modify the program to address the problem of the ECR plasma accelerator. The former option would likely be more desirable for research in an educational setting, the latter would probably be a more direct, cost effective approach.

A key conceptual problem with the existing model is its use of continuum mechanics to represent a plasma for which continuum mechanics are not strictly justified. The mean-free-path for electron scattering collisions in this plasma is many times larger than the characteristic length scales of the device. We used the continuum model because it is relatively simple, provides results that are amenable to intuitive understanding, and most importantly because there exists a large body of empirical results that suggest the continuum model gives good results even when it is not strictly justified. Given the projected power of the next generation of super-computers, it is quite likely that by the time a complete particle-in-cell model of the ECR plasma engine can be formulated, a computer will be available to simulate the device in at least two dimensions without the usual limiting approximations now made in the field of particle in cell modeling.

On the experimental side, significant effort has recently been put into automating the data collection capability of the existing ECR research apparatus. This automated data collection should be used to fully explore the parameter space of the argon ECR plasma engine to provide a more complete and reliable experimental backdrop against which the theory can be improved. A the same time it is vital that diagnostics be constructed to measure microwave-to-plasma coupling efficiency over the range of conditions treated in the theoretical calculations of this report. Such measurements should be the top priority of any continuing research effort on this device because they could confirm or invalidate the theoretical work reported here. If coupling efficiency was in fact low, the promise of this device is greater because a large part of the problem of building an efficient ECR plasma accelerator would be reduced to finding a more efficiency approach to coupling microwave power into the plasma. Following that, an experimental effort should be initiated to verify the model of plasma separation from a magnetic field that was developed for this dissertation. In the long run a more capable vacuum facility must be found to continue meaningful experimental research on this device, or methods of interpreting pulsed and sub-scale experimental results should be developed.

In closing, the author would like to remark that learning this little bit of the physics of the ECR plasma accelerator has been a fun, rewarding, and frequently frustrating process. To those who continue down this path I wish the best of luck. The last Ph.D. dissertation published on this subject was 26 years ago (Crimi 1967). One year after Crimi published the first human left his footprint on the Moon. I sincerely hope that twenty six years from now, a half century after the Moon landings, the state of aerospace propulsion technology will have advanced to include the use of a technology at least equivalent to the projections of Table 6-1 and that people will be exploring and settling the solar system beyond cis-lunar space. If I have contributed even in a small way to such an end, this effort will have been worthwhile.

BIBLIOGRAPHY

Asmussen, J., Nakanishi, S. and Whitehair, S., "Demonstration of a New Electrothermal Thruster Concept," Applied Physics Letters, Vol. 44, No. 10, May 15, 1984.

Bardet, R., Consoli, T., and Geller, R., "Acceleration continue de plasma a Gradients de Champs Electromagnetique et Magnetique Statique. Resultats Experimentant," Physics Letters, Vol. 10, No. 1, May 15, 1964.

Ben Daniel, B. J. et al., "Electron Conductivity at Cyclotron Resonance," Physics of Fluids, Vol. 6, No. 884, 1963.

Bohm, D., "The Use of Probes for Plasma Exploration in Strong Magnetic Fields," The Characteristics of Electrical Discharges in Magnetic Fields, Eds. Guthrie, A. and Wakereling, R. K., p. 65, McGraw-Hill, New York, New York, 1949.

Bornatici, M. et al., "Electron-Cyclotron Emission and Absorption in Fusion Plasmas," Nuclear Fusion, Vol. 23, p. 1153, 1983.

Brophy, J. R., "Ion Thruster Performance Model," NASA CR-174810, December 1984.

Brown, W. C., "The SPS Transmitter Designed Around the Magnetron Directional Amplifier," Paper C1, presented at the Conference on Solar Power Satellites, State of the Art, June 5 - 6, Paris, France, June 1987.

Brown, W. C., "New Findings With Respect to the Interactive Behavior Between a Carburized Thoriated Tungsten Cathode and a Crossed Field Device," presented at the Tri-Service Cathode Workshop, Naval Research Laboratory, Anacostia, Washington, D.C., March 1984.

Brown, W. C., "Satellite Power System (SPS) Magnetron Tube Assessment Study," NASA CR 3383, Raytheon Company, Waltham Massachusettts, 1981.

Brown, W. C., "Earth to Space DC to DC Power Transmission System Utilizing a Microwave Beam as the Source of Energy for Electric Propelled Interorbital Vehicles," AIAA IEPC, Alexandria , Virginia, October 1985.

Chen, F. F., Introduction to Plasma Physics and Controlled Fusion, Second Edition, Plenum Press, New York, New York, 1984.

Chew, G. F., Goldberger, M. L., and Low, F. E., "The Boltzmann Equation and the One-Fluid Hydromagnetic Equations in the Absence Of Particle Collisions," Proc. Roy. Soc., (London), 236A, 112, (1956).

Crimi, G. F., "Investigation of Microwave Generated Plasma in a Non-Uniform Magnetic Field," A Dissertation in Electrical Engineering, University of Pennsylvania, Philadelphia, 1967.

Crimi, G. F., Eckert, A. C., and Miller, D. B., "Microwave Driven Magnetic Plasma Accelerator Studies (Cyclops)," prepared for NASA Lewis Research Center by General Electric Company, NASA CR-72227, Philadelphia, Pennsylvania, March 24, 1967.

Dahimene, M. and Asmussen, J., "The Performance of a Microwave Ion Source Immersed in a Multicusp Static Magnetic Field," Journal of Vacuum Science Technology, Vol. 4, No. 1, January-February 1986.

Dote, T., and Amemiya, H., "Negative Characteristic of a Cylindrical Probe," Journal of the Physical Society of Japan, Oct. 1964, Vol. 19, No. 10, pp. 1915-25.

Dugan, J. V. and Sovie, R. J., "Volume Ion Production Costs in Tenuous Plasmas: A General Atom Theory and Detailed Results for Helium, Argon, and Cesium," NASA TN D-4150, NASA Lewis Research Center, Cleveland, Ohio, 1967.

Dugan, J. V. and Sovie, R. J., "Energy Required for Ion Production by Electron Bombardment in Helium, Argon, and Cesium," NASA Technical Memorandum, NASA TM X-52064, NASA Lewis Research Center, Cleveland, Ohio, 1964.

Freeman, R. L. and Jones, E. M., "Atomic Collision Processes in Plasma Physics Experiments: Analytic expressions for sellected cross sections and Maxwellian rate coefficients," UKAEA research group, Culham Laboratory, Abingdon, Berkshire (Great Britan, no date on document).

Gerwin, R. A., "Characterization of Plasma Flow Through Magnetic Nozzles," Astronautics Laboratory (AFSC) Report AL-TR-092, February 1990.

Gryzinski, M., "Classical Theory of Atomic Collisions, I. Theory of Inelastic Collisions," Physical Review, Vol. 138, p. A341, April 19, 1965.

Haug, R., Felden, M., and Schirmann, D., "The Grid Prob as an Ionic Diagnostic Tool in Cesium Plasma," Journal of Applied Physics, Vol. 39, No. 10, September 1968.

Hendel, H., Faith, T., and Hutter, E., "Plasma Acceleration by Electron Cyclotron Resonance," RCA Review, Vol. 26, No. 2, June 1965.

Hindmarsh, A. C.,"ODEPACK, A Systematized Collection of ODE Solvers," Scientific Computing, R. S. Stepleman et al. (eds.), North-Holland, Amsterdam, 1983 (Vol. 1 of IMACS Transaction on Scientific Computation), pp. 55-64.

Hooper, E. B., "Plasma Detachment From a Magnetic Nozzle," AIAA-91-2590, June 1991.

Huddlestone, R. H., and Leonard, S. L.,"Plasma Diagnostics Techniques," Academic Press, New York, 1965.

Hutchinson, I. H.,"Principles of Dlasma Diagnostics," Cambridge University Press, Cambridge, Massachusetts, 1987.

IInoya, F., "Pulsed Expansion of Plasma in a Magnetic Thruster," Thesis in Partial Fulfillment of the Requirements for the Degree of Doctor of Philosophy, California Institute of Technology, Pasadena, California, 1993.

Jahn, R. G., Physics of Electric Propulsion, McGraw-Hill, New York, New York, 1968.

Kaufman, H. R., "Electron Diffusion in a Turbulent Plasma," NASA TN D-1324, June 1962.

Kieffer, L. J. and Dunn, G. H., "Electron Impact Ionization Cross-Section Data for Atoms, Atomic Ions, and Diatomic Molecules: I. Experimental Data," Reviews of Modern Physics, Vol. 38, No. 1, January 1966.

Kilpatrick, W. D., "Propulsion Application of the Modified Penning Arc Plasma Ejector," AIAA Journal, Vol. 1, No. 4, pp. 806-813, April 1963.

Knecht, J. P. and Micci, M. M., "Analysis of a Microwave-Heated Planer Propagating Hydrogen Plasma," AIAA preprint from the Pennsylvania State University, University Park, Pennsylvania, 1986.

Kosmahl, H. G., "Three-Dimensional Plasma Acceleration Through Axisymmetric Diverging Magnetic Fields Based on Dipole Moment Approximation," NASA TN D-3782, NASA Lewis Research Center, Cleveland, Ohio, January 1967.

Logan, G. B., "D-He^3 Fusion Using Direct Conversion of Microwave Synchrotron Radiation," presented at the American Physical Society Division of Plasma Physics, Baltimore, Maryland, November 1986.

Longhurst, G., "Prediction of Plasma Properties in Mercury Ion Thrusters," NASA CR-159448, December 1978.

Manos, D. M.,"Characterization of Laboratory Llasmas with Probes," J. Vac. Sci. Technol. A 3 (3). May/Jun 1985.

Micci, M. M., "Prospects for Microwave Heated Propulsion," AIAA-84-1390, presented at the 20th Joint Propulsion Conference, AIAA/SAE/ASME, June 11-13, Cincinnati, Ohio, June 1984.

Miller, D. B., Bethke, G. W., and Crimi, G. F., "Final Report: Investigation of Plasma Accelerator (Cyclotron Resonance Propulsion System)," NASA CR-54746, prepared for NASA Lewis Research Center by General Electric Company, Philadelphia, Pennsylvania, November 1, 1965.

Minovitch, M. A., "Solar Powered, Self-Refueling, Microwave Propelled Interorbital Transportation System," AIAA-83-1446, presented at the AIAA 18th Thermophysics Conference, June 1-3, Montreal, Canada, June, 1983.

Nagatomo, M., "Plasma Acceleration by High Frequency Electromagnetic Wave in Static Magnetic Field Gradient," Proceedings of the Seventh International Symposium on Space Technology and Science, Tokyo, Japan, 1967.

Post, R. F., "A Theory of Microwave-Produced Potentials in Plasma - Pleiade Revisited," Presented at the 31st Annual Meeting of the Division of Plasma Physics of the Applied Physics Society, November 1989.

Schmidt, G., Physics of High Temperature Plasmas, Second Edition, Academic Press, New York, New York, 1979.

Sercel, J. C., "A Simple Model of Plasma Acceleration in a Magnetic Nozzle," AIAA-90-2597, July 1990.

Sercel, J. C., "Beamed Energy for Spacecraft Propulsion: Conceptual Status and Development Potential," Proceedings of the Eighth Princeton/AIAA/SSI Conference, May 6 -9, 1987.

Sercel, J. C., "Electron-Cyclotron-Resonance (ECR) Plasma Acceleration," AIAA -87-1407, presented at the AIAA 19th Fluid Dynamics, Plasma Dynamics and Lasers Conference, Honolulu, June 8-10, 1987.

Sercel, J. C., "Electron-Cyclotron-Resonance (ECR) Plasma Thruster Research," AIAA-88-2916, presented at the AIAA/ASME/SAE/ASEE 24th Joint Propulsion Conference, Boston, Massachusetts, July 11-13, 1988.

Spitzer, L. and Harm, R., "Transport Phenomena in a Completely Ionized Gas," Phys. Rev. Vol. 89, No. 5, 1 March 1953.

Stepleman, R.S. et al. (eds.),"ODEPACK, A Systematized Collection of ODE Solvers," Scientific Computing, North-Holland, Amsterdam, 1983 (Vol. 1 of IMACS Transactions of Scientific Computation), pp. 56-64, also as a preprint under UCRL-88007.

Thompson, P. A., Compressible-Fluid Dynamics, Department of Mechanical Engineering, Rensselaer Polytechnic Institute, Troy, New York, 1984.

Thompson, W. B., An Introduction to Plasma Physics, Pergamon Press, Great Britain, 1962.

Tobinaga, T., Hayashi, N., Araki, H., and Nakayama, S., "Anisotropy of Low-Energy Ion Etching via Electron Cyclotron Resonance Plasma," J. Vac. Sci. Technol. B.6 (1) Jan/Feb 1988.

Informational Notes:

Conference Papers from the American Institute of Aeronautics and Astronautics (AIAA) can be obtained from the AIAA Technical Information Service, 555 West 57th Street, New York NY 10019. Phone Number (212) 247-6500.

NASA Contractor Reports can be obtained from the National Technical Information Service (NTIS) 5285 Port Royal Road, Springfield VA 22161. Phone Number (703) 487-4600.

APPENDIX A - Collision Cross Sections and Rate Coefficients for Argon

The quasi-one-dimensional model of the ECR plasma accelerator that Section 2.3 describes requires rate coefficients and cross sections for several different collision effects. The collision phenomena addressed here include i) both elastic and inelastic electron-atom collisions, including ionization and excitation; ii) both elastic and inelastic electron-ion collisions; and iii) ion-atom charge exchange and scattering collisions. In this appendix we derive these rate coefficients and we present curves of rate coefficient as a function of temperature over the electron-energy range of interest for the ECR plasma. In some cases we based cross-section data on published experimental measurements, in other cases, we based cross-section data on the Gryzinski model, which past workers have found to provide projections that agree closely with experimental results.

A simplifying feature of the quasi-one-dimensional model used in our theoretical studies is the use of a single, equivalent, lumped excited state characterized by a total-excitation cross section and lumped excitation energy. We use this lumped approximation as developed by Dugan and Sovie (1964), in place of the usual collisional-radiative model that considers cross sections and energy levels for numerous individual excited states. Past workers have shown the lumped model to be very accurate and it significantly simplifies the details of the analysis.

The Gryzinski theory is an atomic-collision cross-section model that provides estimates of the inelastic-electron-atom collision-cross sections by simple calculation. Although Gryzinski derived his model using classical physics under the assumption that the inelastic electron-atom collision can be treated as a purely two-body encounter between the incident and bound electrons, past researchers have found that cross sections calculated by this technique have generally agreed well with experimental data. This agreement between the Gryzinski theory and experimental data justifies its use here in cases where we could not find experimental data.

The Gryzinski theory yields a convenient equation that provides the cross section for an inelastic electron-atom collision:

$$Q = \frac{I \sigma_o g}{U^2} \tag{A.1}$$

where I denotes the integer number of electrons in the outer shell of the target atom, σ_o is a numerical constant with a value of 6.51×10^{-18} (eV•m)^2, U is the minimum energy lost by the incident electron to accomplish the specified transition, and g is a function which can be written

$$g = \frac{E_1}{E_2}\left(\frac{E_2}{E_1+E_2}\right)^{3/2} \cdot \left[\frac{U}{E_1} + \frac{2}{3}\left(1-\frac{U}{2E_2}\right) ln\left(2.7 + \left(\frac{E_2-U}{E_1}\right)^{1/2}\right)\right]\left(1-\frac{U}{E_2}\right)^{(2E_1+U)/(E_1+U)}. \quad \text{(A.2)}$$

In Eq. (A.2), E_1 is the energy level of the bound electrons, and E_2 is the kinetic energy of the incident (plasma) electron.

Electron-Atom and Electron-Ion Inelastic Collisions

We used Eqs. (A.1) and (A.2) to calculate the collision cross section for the lumped excitation of the argon atom and the argon ion as a function of the kinetic energy of the incident electron. For atomic argon, I is 6. In the case of singly charged argon ions, we took I to be 5. When using the lumped approximation developed by Dugan and Sovie, the energy lost by the incident electron is equal to the lumped excitation energy ($U=U_{ex}$) as given by Eq. (2.2). Also, within the context of the lumped approximation, the energy level of bound electrons is the energy level of the lowest excited state, U_1. Table A.1 gives the values of the various energy levels of bound electrons of the argon atom and the argon ion as assumed in this study.

Table A.1 Values of Various Energy Levels of Bound Electrons of the Argon Atom and the Argon Ion as Assumed in This Study

Energy Level or Transition	Assumption for Argon Atom (eV)	Assumption for Argon Ion (eV)
Lowest Excited State	11.55	8.88
Ionization Energy	15.76	27.62
Lumped Excitation Energy	13.65	18.25

After determining the functional relationship between the incident electron impact energy and the cross section for a given atomic transition, we calculated rate coefficients by integrating over the entire electron-speed distribution function. For example, in the case of the rate coefficient for ionization of argon atoms by electron impact, the appropriate equation is

$$< \sigma_i v_r >= \frac{\int_0^\infty \sigma_i(v_r) v_r F(v_r) dv_r}{\int_0^\infty F(v_r) dv_r} \tag{A.3}$$

where $F(v_r)$ represents the electron distribution function. In the case of a Maxwellian electron distribution, as assumed in this research, the form of the electron distribution function used in Eq. (A.3) is the well-known one:

$$F(v) = 4\pi(\frac{m}{2\pi kT})^{3/2} v^3 \exp(\frac{-mv^2}{2kT}). \tag{A.4}$$

We numerically integrated Eq. (A.3) and curve-fit the results to the fourth-order polynomial:

$$y = a + bx + cx^2 + dx^3 + ex^4 \tag{A.5}$$

where y is the base-ten logarithm of the rate coefficient and x is the base-ten logarithm of the electron temperature in electron volts. Table A.2 presents the values of the coefficients for Eq. (A.5) for three types of electron-heavy impacts.

Table A.2 Values of Coefficients in Eq. (A.5)

Reaction	a	b	c	d	e
Atom Ionization	-16.198	4.0383	-1.6296	0.26371	-1.5707
Atom Excitation	-16.716	3.9633	-1.6743	0.29668	-2.0062
Ion Excitation	-17.946	6.6480	-3.2462	0.68128	-5.3788

We produced Fig. A-1 using Eq. (A.5) and the data presented in Table A.2. Figure A-1 shows the base-ten logarithm of the rate coefficients determined for this research as a

function of the base-ten logarithm of the temperature of the plasma electrons. In Fig. A.1, rate coefficients for atom ionization, atom excitation, and ion excitation all peak at electron temperatures between 100 and 300 eV. The rate coefficient for atom ionization is the largest of the reactions plotted, and the rate coefficient of atom excitation is the smallest; yet all three rate coefficients are similar in magnitude over the entire range plotted. This suggests that each of these reactions can have an important impact on the operation of an argon-based ECR system.

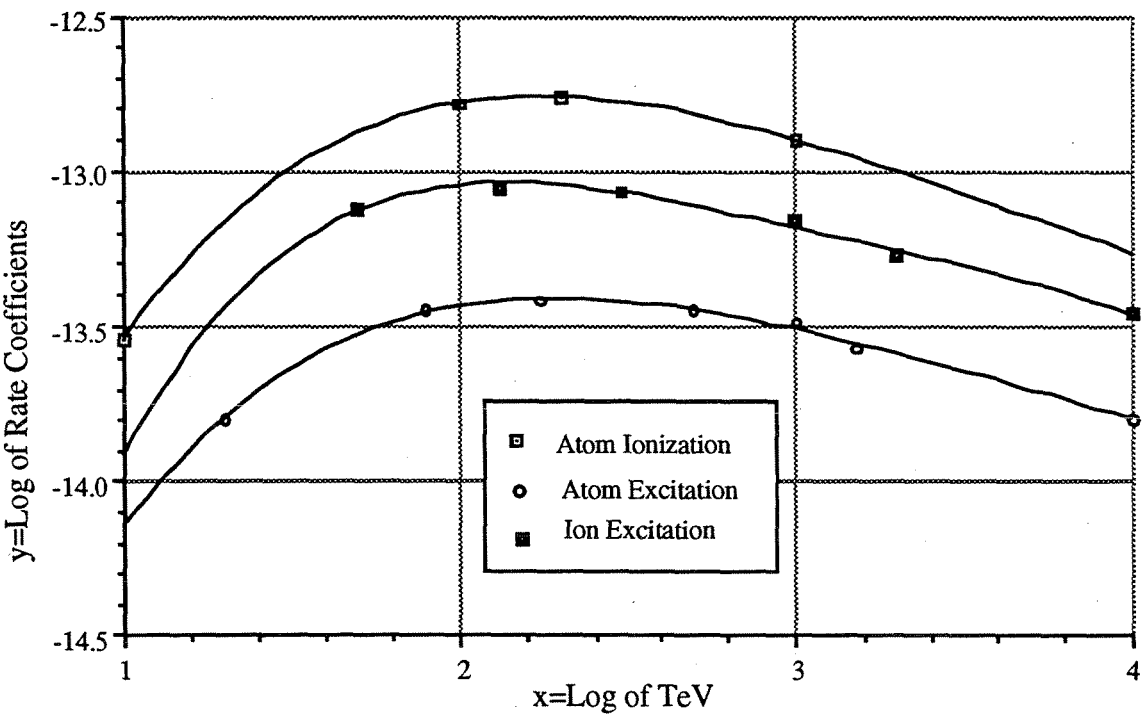

Fig. A.1 Rate coefficients for
electron inelastic collisions with argon

APPENDIX B - Derivation and Explicit Formulation of Conservation Equations

The following derivations produce the conservation equations used in the theory of ECR plasma acceleration, as presented in Chapter 2. The *explicit* formulation of the conservation equations is a restatement of the relevant differential equations with one equation for each derivative term (i.e., $\dot{y} = f(t,y)$). We chose to present the equations in explicit form because this form is convenient for use in computer programs that require the differential term to be on the left side of the equations and the somewhat complicated expressions, including other variables and in some cases, other differential terms, on the right side.

Assumptions

We develop these equations under the assumptions of steady, quasi-one-dimensional flow of a plasma consisting of singly charged ions and electrons interacting with a neutral gas. We use the term *quasi-one-dimensional* in the same way Thompson (1984) uses it: at any given cross section, all flow variables are represented by average values, and all properties vary only along the axis of the flow, which we take to be the z-direction. In the present case of a quasi-one-dimensional plasma flow along magnetic field lines, we make the additional assumption that the plasma streamlines coincide with the magnetic field lines. Although this supposition is not strictly true, as shown in Section 2.2, in this model we seek to explore the flow conditions near the ECR heating region where the streamlines do not significantly cross field lines.

In the plasma we seek to model, peak neutral densities are in the range of 10^{17} to 10^{19} m^{-3}. Peak plasma densities* are generally equal to or less than peak neutral densities. Fractional ionization varies from a few percent to over 90 percent as a function of flow boundary conditions and axial position in the flow. This range of densities allows us to treat the plasma as optically thin. In other words, we assume that the plasma is so tenuous that it can not recapture any line radiation produced by electronic de-excitation. The conservation equations include the effects of inelastic collisions of electrons with ions, electrons, and atoms. This model neglects the effect of electron energy lost due to elastic collisions with ions or neutral atoms because the average energy loss per encounter is

---

* In this quasineutral plasma, electron and ion number densities are approximately equal, allowing us to use the term *plasma density* to refer to the common number density.

proportional to the ratio of masses, and this ratio is small ($\approx 10^{-5}$ for argon). Accordingly, we neglect ion thermal energy in this analysis and the ion temperature is therefore treated as zero.

Following Chew and Goldberger (1956), we approximate the electron-energy as a special type of Maxwellian distribution with two temperatures, one characterizing motion perpendicular to magnetic field lines and one characterizing motion parallel to magnetic field lines. Elastic collisions between electrons and heavy species significantly affect the exchange of electron thermal energy between the components of thermal motion perpendicular and parallel to magnetic field lines. We assume that the exchange of thermal energy between the perpendicular and parallel motion of the electrons occurs with a rate constant given by the electron elastic collision period. The presence of microwave radiation near the electron-cyclotron frequency couples energy into the perpendicular motion of the electrons, establishing non-equilibrium between the perpendicular and parallel motion.

We assume that the electrons absorb microwave power into their motion only in a region near the surface that meets the electron-cyclotron-resonance condition. To account for the effects of the well-known Doppler broadening of this ECR heating region, we assume that the microwave power couples to the plasma in a region 2 cm upstream and downstream of the resonance plane as described in Section 2.1. We apply this simplification because the actual physical processes responsible for coupling the microwave power to the electron gas go far beyond simple Doppler-broadened ECR heating to include various unstable coupling modes and Landau damping. A detailed treatment of all the relevant coupling phenomena is somewhat beyond the scope of the present study, and would not contribute substantially to determining the engineering feasibility of the ECR plasma engine.

This analysis explicitly treats the production of singly charged ions by electron-atom collisions but does not address double ionization. An approximate calculation of the effects of double ionization based on the plasma conditions calculated from this model suggests that the effects of double ionization are not central to the feasibility and performance of the ECR plasma engine. Ionization of metastable electronic states in atoms is treated under the lumped approximation of Dugan and Sovie (1964, 1967). We ignore volumetric ion recombination because it is negligible at the relatively low density and low pressure associated with this system. The flux of plasma reaching the upstream window and side walls of the accelerator is assumed to undergo heterogeneous ion recombination. Gas

atoms produced by the recombination of ions with electrons are added to the neutral gas flow at the axial position where the recombination takes place. We model the net gas flow by assuming the gas atoms are injected into the accelerator near the window in thermal equilibrium with the wall.

Thrust is determined by calculating the momentum flux flowing across the exit plane of the accelerator. The rule used to determine the location of the exit plane depends on which of the two cases of axial heat conduction is being studied. For the case of negligible axial heat conduction the location of the exit plane of the accelerator is determined to be at the plane where the ion acoustic Mach number reaches ten. Under this criterion the exit plane is typically found to be more than one-half meter downstream of the ECR region and in a location where the magnetic field has fallen to less than a few percent of the peak magnetic field*. This position of the exit plane is far enough down-stream to fully include the important plasma dynamic acceleration and particle collision effects and observation of calculated results shows that the plasma velocity appears to reach an asymptotic limit in this region..

The rule used to determine the location of the exit plane in the case of quasi-isothermal flow involves the calculation of a global energy balance for the plasma. This global energy balance is needed because we utilize a fictitious heat flux term to simulate the effect of an axial flow of thermal energy that would maintain the quasi-isothermal condition. We calculate the fictitious heat flux needed to ensure that $dW_{\perp}/dz=0$ and we integrate the fictitious heat flux along upstream from the stagnation point, downstream through the transition to supersonic flow, and out into the expansion region. The upstream integration is continued until the plasma velocity reached the Bohm velocity, at which point we assume that the plasma flows into a sheath that separates the plasma from the upstream window. The downstream integration is continued until the total integral of the fictitious heat flux reaches zero. In this way, we can verify that a power balance was maintained in the plasma and that conservation of energy is not violated.

---

* We assume that the magnetic field is equivalent to the field produced by an ideal current loop on axis.

Plasma Continuity Equation

The condition of quasi-neutrality is valid throughout. Further, no net flow of charge can be supported because the accelerator is electrically isolated from ground. The mean stream-wise velocity of electrons in this analysis is therefore equal to the mean stream-wise velocity of ions. On this basis, the density and mean velocity of the ions are equal to the density and mean velocity of the electrons. Therefore, we need only one plasma continuity equation to describe both species. For convenience and clarity, the subscripts i and e (for electron and ion respectively) are omitted where they are redundant. The steady-state continuity equation is usually expressed as

$$\nabla \bullet (n\mathbf{u}) = S_p \quad . \tag{B.1a}$$

Equation (B.1a) can be written in quasi-one-dimensional terms as:

$$\frac{d(nuA)}{dz} = AS_p \quad . \tag{B.1b}$$

The source term, S_p, must include source terms for the production of plasma species by electron-atom impact ionization and for the loss of plasma due to diffusion across magnetic field lines. The ionization source term is well known and can be expressed

$$S_i = n_a n < \sigma_i v_e > \tag{B.2}$$

where $< \sigma_i v_e >$ represents the product of the ionization cross section for electron-atom collisions taken with the electron speed averaged over the entire electron speed distribution. Equation (B.2) does not account for the production of electrons by electron-ion collisions, since only singly charged ions are treated in detail here.

The diffusion source term is based on Bohm diffusion. In Bohm diffusion one approximates the flux of plasma across magnetic field lines by the expression (Chen 1984)

$$\Gamma_B = -D_B \nabla n \approx -\frac{kTen}{16eBr} \tag{B.3}$$

where Γ_B is the flux of plasma, D_B is the Bohm diffusion coefficient, and the radius of the plasma is r. If this diffusion occurs in a control volume constituting a section of the

accelerator of length Δz, then the total loss of plasma from the control volume due to Bohm diffusion will be given by

$$\dot{N}_B = 2\pi r \Delta z \Gamma_B. \tag{B.4}$$

To obtain a source term of the appropriate form to be used in Eq. (B.6), the right side of Eq. (B.4) must be divided by the volume of the control element, $\pi r^2 \Delta z$. The resulting source term for the loss of plasma due to cross-field diffusion is

$$S_d = -\frac{kT_e n}{8eBr^2}. \tag{B.5}$$

If we express the effective electron temperature in electron volts as a function of $W_{//}$ and $W_{\perp}$, the components of the electron thermal energy perpendicular and parallel to the magnetic field, Eq. (B.5) can be approximated by:

$$S_d \approx -\frac{(W_{\perp} + W_{//})n}{12eBr^2} \approx -\frac{\pi(W_{\perp} + W_{//})n}{12eBA}. \tag{B.6}$$

We now combine Eq. (B.6) with Eqs. (B.2) and (B.1) to obtain the plasma continuity equation in final form

$$\frac{1}{A}\frac{d(nuA)}{dz} = n_a n < \sigma_i v_e > -\frac{\pi(W_{\perp} + W_{//})n}{12eBA}. \tag{B.7}$$

Atom Continuity Equation

We require an equation to account for conservation of neutral atoms because the neutral atoms are relevant to the ionization source term that is needed in the model. Because the neutral atoms are in free molecular flow we can not use a continuum fluid model to treat their behavior. In cases such as this other researchers in electric propulsion (see Longhurst 1978, or Brophy 1984) have found it useful to treat the neutral gas as perfect and monatomic and calculate the mean atom drift velocity by assuming that the gas is in thermal equilibrium with the accelerator walls, which are assumed to be at room temperature. In this treatment u_a, depends only on the accelerator wall temperature and on the atomic mass of the gas and u_a, is taken to be independent of axial position. Because atoms making contact with the side walls or upstream walls (the window) are re-introduced

to the accelerator in thermal equilibrium and because the gas density in the vacuum tank is much lower than the gas density in the region where most of the ionization takes place, the net atom flux crossing a given plane can reasonably be approximated by the well-known expression obtained from elementary kinetic theory (see Chen 1984).

$$\Gamma_{random} = n_a u_a = \frac{1}{2}\, n_a \overline{|v_z|} \,. \tag{B.8}$$

In Eq. (B.8), n_a is the density of atoms, u_a is the mean velocity, and $\overline{|v_z|}$ is the mean value of the absolute magnitude of the atom thermal velocity averaged over the atom velocity distribution. For the case of a Maxwellian distribution, $\overline{|v_z|}$ is given by

$$\overline{|v_z|} = \sqrt{\frac{2kT}{\pi M}} \,. \tag{B.9}$$

Applying Eq. (B.9) to Eq. (B.8) we obtain an expression that can be used to approximate the average axial velocity of gas atoms:

$$u_a = \sqrt{\frac{kT}{2\pi M}} \,. \tag{B.10}$$

Justification for the use of Eq. (B.9) comes from the theoretical arguments sketched here and from the fact that this approach has been used in models that provide predictions of ionization source rates within a few percent of measured values for devices with geometry and plasma conditions similar to the ECR accelerator. If the neutral gas is argon at a temperature of 300 K, Eq. (B.10) yields a gas velocity of approximately 100 m/s. This value of gas velocity is used throughout this study for all cases in which argon is the propellant gas.

The rate at which the gas feed system injects argon atoms into the accelerator determines the total flux of heavy species through the device. Because these neutral gas atoms are injected near the window, we treat them as though they emanate from the window at the upstream end of the accelerator. We need a continuity equation for the neutral gas in order to use the conservation of heavy species (ions plus atoms) to calculate the number density of gas atoms at any point in the accelerator. We can obtain such a

quasi-one-dimensional, steady-state continuity equation for gas atoms in the same manner as we obtained Eqs. (B.1),

$$\frac{1}{A}\frac{d(n_a u_a A)}{dz} = -S_p \,. \tag{B.11}$$

Combining Eqs. (B.2), (B.10), and (B.11) gives

$$\frac{1}{A}\frac{d(n_a A)}{dz} = \frac{-\frac{\pi(W_\perp + W_{//})n}{12eBA} - n_a n < \sigma_i v_r >}{\sqrt{\frac{KT}{2\pi M}}} \,. \tag{B.12}$$

Plasma Momentum Equation

The plasma momentum equation must account for effects on the axial component of momentum for both electrons and ions. We use control volume analysis to derive the momentum equation and the energy equations that are needed for the quasi-one-dimensional model. Figure B.1 depicts the control volume associated with the model and shows the nomenclature used in these derivations. The plasma enters the control volume through surface A_1, on the upstream side, with ion number density, mass-averaged velocity, perpendicular and parallel thermal energy, and neutral gas number density as depicted with subscript '1'. We assign the average values of these quantities within the control volume the symbols shown without numerical subscripts. Likewise, the control-volume-averaged values of the source and sink terms that were presented in Sections 2.1 and 2.3 are not given numerical subscripts here. We assign the subscript '2' to the exist conditions. Surfaces A_1 and A_2 in Fig. B.1 are defined as normal to the flow while the surface of revolution that encloses the control volume defines the radial extent of the stream tube and is coincident with a surface of constant enclosed magnetic flux.

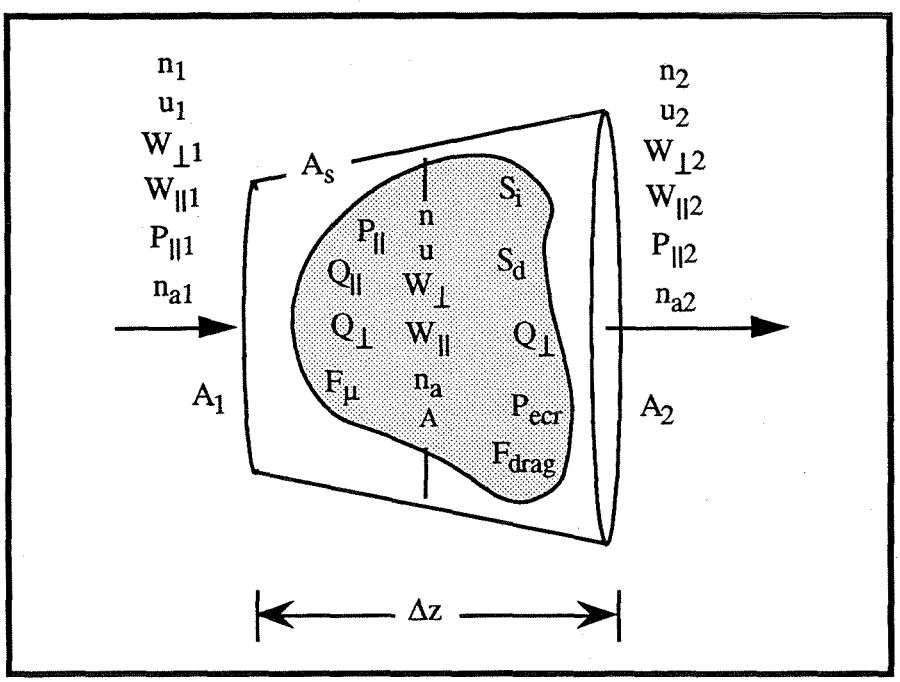

Fig. B.1 Diagram showing nomenclature for control volume used in derivation of conservation equations.

For momentum to be conserved the flux of momentum carried out of the control volume through surface A_2 by the plasma is the sum of the momentum convected into the

control volume through surface A_1 plus the net change in momentum within the volume due to the effects of pressure; sources and sinks; and body forces. Neglecting the contribution of the electron mass to the flux of momentum, this statement of the conservation of momentum can be written mathematically as:

$$MA_2 n_2 u_2^2 = MA_1 n_1 u_1^2 + A_1 P_{//1} + (A_2 - A_1)P_{//} - A_2 P_{//2} + A_{av}\Delta z(\sum_s m_s S_s u_s + F_{body}), \quad \text{(B.13)}$$

where A_{av} is the average cross sectional area of the stream tube. The terms in Eq. (B.13) containing the plasma pressure can be obtained from the equation of state for a plasma with an anisotropic temperature (see Chen 1984), which is:

$$P_{//} = 2nW_{//} \; . \quad \text{(B.14)}$$

The plasma source and sink terms in this problem are those due to ionization and diffusion as described by Eqs. (2.21) or Eqs. (B.2) and (B.5). There are two body forces present in this problem; the dipole-moment force, F_μ, described by Eq. (2.23) and the plasma-slip drag force, F_{drag}, described by Eq. (2.24). Specifying these three quantities in Eq. (B.13), rearranging some terms, and dividing by $A\Delta z$ we obtain:

$$\frac{M}{A}\frac{\Delta(Anu^2)}{\Delta z} = -\frac{2\Delta(AnW_{//})}{A\Delta z} + \frac{2nW_{//}}{A}\frac{\Delta A}{\Delta z} + M(S_i u_a + S_d u) + F_\mu + F_{drag} \; . \quad \text{(B.15)}$$

The next steps are to take the limit as Δz goes to zero, expand the expression containing $AnW_{//}$, and cancel out the two equal and opposite terms involving derivatives of A. This procedure gives:

$$\frac{M}{A}\left(\frac{d(nu^2 A)}{dz}\right) = F_\mu + F_{drag} - 2\frac{d(nW_{//})}{dz} + M(uS_d + u_a S_i), \quad \text{(B.16)}$$

which is equivalent to Eq. (2.22), the quasi-one-dimensional momentum equation for the ECR plasma accelerator. The derivation of the quasi-isothermal version of this equation (Eq. (2.30)) proceeds in exactly the same manner except that in the last step we assume that $dW_{//}/dz=0$. An alternative way to derive the plasma momentum equations for the ECR accelerator would have been to start with the general momentum equation for a plasma species and use it to specify the species momentum equations for electrons and ions separately. The two species momentum equations could then be combined by equating the

electric field terms in the two equations using the assumptions of zero axial electric current, quasi-neutrality, and neglecting ion thermal motion. Such an approach is similar to the treatment of ambipolar diffusion commonly found in the literature (see Chen 1984).

Energy Conservation Equations

As stated previously, the electron energy distribution in the ECR plasma accelerator is not necessarily an equilibrated, Maxwellian. For example, near the microwave heating region one would generally expect to find that the electron temperature perpendicular to magnetic field lines is higher than the parallel component of the electron temperature because the transverse-electric mode microwave power preferentially heats the perpendicular component of the electrons. This preferential heating is most pronounced near electron-cyclotron-resonance, especially with right-circularly polarized waves such as those applied to an ECR plasma engine. The energy balance analysis in this model must, therefore, separately account for the electron temperatures perpendicular and parallel to magnetic field lines. To do this we will derive two conservation equations: one for electron energy perpendicular to field lines and one for electron energy parallel to field lines.

We start with the equation for perpendicular energy. Because the magnetic dipole moments of the electrons are so closely related to their perpendicular energy, we will alternatively refer to this as the dipole moment energy and describe the governing equation as the dipole moment equation. We begin by once again referring to Fig. A.1. The flux of dipole-moment energy carried out of the control volume through surface A_2 by the plasma is the sum of the dipole-moment energy convected into the control volume through surface A_1 plus the net change in dipole-moment energy within the volume. Sources and sinks of dipole-moment energy within the control volume include: i) the loss of plasma and associated dipole-moment energy due to radial diffusion, ii) work done by the dipole moment force that results in acceleration of the plasma in the diverging magnetic field, and iii) flux of thermal energy into the perpendicular component of the electron thermal motion due to ECR heating, inelastic collisions with heavy species, and elastic scattering effects. In mathematical terms this statement is expressed:

$$A_2 n_2 u_2 W_{\perp 2} = A_1 n_1 u_1 W_{\perp 1} + A_{av} \Delta z (-u F_\mu + S_d W_\perp + Q_\perp), \qquad \text{(B.17)}$$

where $W_\perp$ is defined in Eqs. (2.27) and (2.28). Dividing Eq. (B.17) by $A\Delta z$ and taking the limit as Δz goes to zero we obtain the dipole moment energy equation:

$$\frac{1}{A}\frac{d(nuAW_\perp)}{dz} = Q_\perp - uF_\mu + W_\perp S_d. \tag{B.18}$$

We neglect the directed kinetic energy of the electrons because the mass of the electrons is so small compared to the mass of the ions. We neglect the thermal energy of the ions because their temperature is so small compared to the temperature of the electrons. As such, we assume that the total energy of this plasma is the sum of the directed kinetic energy of the ions and the thermal energy of the electrons, including the dipole moment energy. To derive a conservation equation for this quantity we once again refer to the control volume of Fig. A.1. The flux of energy carried out of the control volume through surface A_2 by the plasma is the sum of the energy convected into the control volume through surface A_1 plus the net change in energy within the volume. Sources and sinks of energy within the control volume include: i) the loss of plasma and associated energy due to radial diffusion, ii) work done on the contents of the control volume by external pressure on surfaces A_1 and A_2, iii) the net flow of energy into electron thermal motion due to ECR heating and inelastic collisions with heavy species, and iv) loss of directed kinetic energy of the plasma due to drag force in the interaction with neutral atoms. In mathematical terms this statement is expressed:

$$\begin{aligned} A_2 n_2 u_2 (M\frac{u_2^2}{2} + W_{\perp 2} + W_{//2}) = \\ A_1 n_1 u_1 (M\frac{u_1^2}{2} + W_{\perp 1} + W_{//1}) + A_1 u_1 P_{//1} - A_2 u_1 P_{//2} + \\ A\Delta z\left[Q_\perp + Q_{//} + uF_{drag} + S_d (M\frac{u^2}{2} + W_\perp + W_{//}) \right]. \end{aligned} \tag{B.19}$$

The dipole moment force does not appear in Eq. (B.19) the effect of the dipole moment force is to transform dipole-moment energy into directed kinetic energy of the plasma: it does not change the total specific energy of the plasma. Notice also that the equation does not contain the ionization source term. We assume that new ions formed by

electron-atom impact appear with zero energy.* If we appeal to the definitions of $Q_{\perp}$ and $Q_{//}$ provided in Chapter 2 we can see that the elastic scattering terms cancel out in Eq. (B.19). This is physically correct because the effect of elastic scattering is to transfer energy from one direction to the other and it has no effect on the total specific energy. Dividing Eq. (B.19) by $A\Delta z$, rearranging some terms, and taking the limit as Δz goes to zero we obtain the specific energy equation:

$$\frac{1}{A}\frac{d[nuA(M\frac{u^2}{2}+W_{\perp}+W_{//})]}{dz}=uF_{drag}+S_d(M\frac{u^2}{2}+W_{\perp}+W_{//})+Q_{\mathrm{P}}+Q_{//}-\frac{2}{A}\frac{d(unW_{//})}{dz}. \tag{B.20}$$

Multiplying Eq. (B.16) by u and subtracting the result and Eq. (B.18) from Eq. (B.20) gives the equation for electron thermal energy parallel to magnetic field lines:

$$\frac{1}{A}\frac{d(nuAW_{//})}{dz}=Q_{//}-2nW_{//}(\frac{du}{dz}+\frac{u}{A}\frac{dA}{dz})+MS_i(\frac{u^2}{2}-uu_a)+S_dW_{//}. \tag{B.21}$$

* This assumption is not quite right because at a mean velocity of 100 m/s the newly-created ions each contain about 0.03 eV of energy. We estimate that this simplifying assumption introduces an error of about one part in 10^4.

Explicit Form of Equations of Quasi-One-Dimensional Model

The conservation equations derived in this appendix can be manipulated algebraically to obtain a set of differential equations in the form:

$$\frac{du}{dz}=\frac{-2Q_{//}+u(F_{\mu}+F_{drag})-MS_i(u^2+uu_a)-2S_dW_{//}+\frac{6}{A}\frac{dA}{dz}nuW_{//}}{n(Mu^2-6W_{//})} \tag{B.22a}$$

$$\frac{dn}{dz}=\frac{2Q_{//}-u(F_{\mu}+F_{drag})+MS_du^2+MS_i(2u^2-uu_a)-\frac{1}{A}\frac{dA}{dz}Mnu^3-W_{//}(4S_d+6S_i)}{u(Mu^2-6W_{//})} \tag{B.22b}$$

$$\frac{dW_{//}}{dz}=\frac{Q_{//}(Mu^2-2W_{//})-W_{//}[2u(F_{\mu}+F_{drag})+MS_i(u^2-2uu_a)-\frac{2}{A}\frac{dA}{dz}Mnu^3-W_{//}(4S_d+6S_i)]}{nu(Mu^2-6W_{//})} \tag{B.22c}$$

$$\frac{dW_{\perp}}{dz}=\frac{Q_{\perp}-F_{\mu}u-S_iW_{\perp}}{nu} \tag{B.22d}$$

$$\frac{dn_a}{dz}=\frac{-(S_i+S_d)}{u_a} \tag{B.22e}$$

Under the assumption of quasi-one-dimensional flow as described in Chapters 2 and 4, Eq. (B.22c) is not used because $dW_{//}/dz=0$. Equations (B.22d) and (B.22e) do not change, but (B.22a) and (B.22b) do change. Using the quasi-isothermal forms of the equations of the model we find the expressions for du/dz and dn/dz to be:

$$\frac{du}{dz} = \frac{u(F_\mu + F_{drag}) + uMS_i(u_a - u) - 2W_{//}(S_i + S_d) + \dfrac{2nuW_{//}}{A}\dfrac{dA}{dz}}{n(Mu^2 - 2W_{//})} \tag{B.23a}$$

$$\frac{dn}{dz} = \frac{(F_\mu + F_{drag}) - uM(2S_i + S_d) + u_a MS_i + \dfrac{nu^2 M}{A}\dfrac{dA}{dz}}{(2W_{//} - Mu^2)}. \tag{B.23b}$$

APPENDIX C - Boundary Conditions for Quasi-One-Dimensional Model

Eqs. (B.22) constitute a system of five first-order, ordinary, nonlinear, coupled, differential equations. To be solved numerically, a set of boundary conditions must be applied to this system of equations. For the numerical solution to have physical significance, the boundary conditions must correspond to a physically meaningful situation. In this case, we have chosen to use those boundary conditions that yield smooth and continuous solution to the equations of the model. The set of boundary conditions that yield smooth solutions are those that allow us to avoid singularities in the equations of the model. In physical terms we choose the set of boundary conditions that correspond to steady-state, shock-free conditions. In the discussion that follows it may be useful to refer to Section 4.1 and to Fig. 4.1 in particular.

Except under special circumstances Eqs. (B.22a), (B.22b), and (B.22c) are singular when the condition

$$Mu^2 = 6W_{//}, \tag{C.1}$$

is met. Within the context of our model, information moving through the plasma parallel to the magnetic field propagates at the ion acoustic velocity, which has a value of $u = (6W_{//}/M)^{1/2}$ (corresponding to an ion acoustic Mach number of 1, which we will refer to here as Mach 1). Hence, the singularity that we encounter in Eqs. (B.22a), (B.22b), and (B.22c) is similar to the singularity found in conventional gas dynamics in the transition through Mach number 1. At Mach number 1, Eqs. (B.22a) through (B.22c) are non-singular only when their numerators are all zero. This occurs when

$$Q_{//} = \frac{1}{2}[u(F_{\mu} + F_{drag}) - MS_i(u^2 + uu_a) - 2S_d W_{//} + \frac{6}{A}\frac{dA}{dz} nuW_{//}]. \tag{C.2}$$

Equation (C.2) is a constraint that can be used as a boundary condition at Mach number 1. Unless the condition of Eq. (C.2) is met at Mach 1 the derivatives of the dependent variables in this problem go to infinity corresponding to the formation of a shock. The formation of the shock would then cause the upstream conditions of the flow to re-adjust until Equation (C.2) is satisfied. If there is no upstream condition that meets the constraint of Eq. (C.2) there would be no steady-state, shock-free solution and the plasma would either exhibit time-dependent behavior or the appearance of shocks.

Likewise, Eqs. (B.22d) and (B.22e) are singular where the plasma is zero, at the so-called *stagnation plane*. In this case, special conditions must be placed on the plasma state variables to prevent the derivative terms in Eqs. (B.22b) through (B.22d) from becoming infinite. We assume that the plasma stagnates within the waveguide of the ECR accelerator. Within the waveguide, the cross-sectional area of the flow is determined by the dimensions of the waveguide and are constant in the z-direction. Under these conditions, Eq. (B.32c) is finite only if the condition required by Eq. (C.3) is met locally.

$$Q_{//} = W_{//}(3S_i + 2S_d) \tag{C.3}$$

Equations (C.1) through (C.3) provide three of the five boundary conditions that must be met to solve the system of Eqs. (B.22). An additional boundary condition is provided by addressing the singularity that can exist in Eq. (B.22d) when u=0. The condition that must be met for Eq. (B.22d) to be nonsingular where the flow velocity is zero is:

$$Q_{\perp} = S_i W_{\perp} \quad . \tag{C.4}$$

The physical significance of Eqs. (C.3) and (C.4) can be understood by inspection of Eqs. (B.18) and (B.21). By assuming that u=0 and substituting in the continuity equation for $d(nuA)/dz$ in Eq. (B.18) and (B.19) we can see that these equations reduce to Eqs. (C.4) and (C.3). The meaning of this observation is that Eqs (C.4) and (C.3) represent local power balance conditions (conservation of energy) at the stagnation plane.

Eq. (B.22e) does not suffer from the singularities that we encounter in the first four equations. Hence, for the last of the five boundary conditions we appeal to the global conservation of mass. The net flux of charged particles across the plasma stagnation plane must be zero because the plasma velocity is zero at this location. Therefore, the net mass flux across the stagnation plane can result only from the flux of neutral atoms. The total flux of particles across any plane normal to the flow must be equal to the total flux input to the accelerator, the provides another boundary condition used in solving Eqs. (B.22):

$$\frac{\dot{m}}{M} = A_w n_a u_a \tag{C.5}$$

where A_W is the cross-sectional area of the accelerator waveguide, and $\dot{m}$ is the mass flow rate of gas introduced to the accelerator.

Eqs. (C.1) through (C.5) constitute a complete set of boundary conditions that must be met if all of the derivative terms in Eqs. (C.22) are to be finite and mass is to be conserved in the flow. If the conditions of Eqs. (C.3) and (C.4) are met, Eqs. (B.22b) through (B.22d) are not strictly singular at $u = 0$. However, using Eqs. (B.32b) through (B.32d) in a computer program in which the equations are evaluated numerically very near $u = 0$ leads to numerical overflows because the denominators get very close to zero. For this reason, it was necessary to evaluate Eqs. (B.22b) through (B.22d) near the limit as u approaches zero. The resulting forms, applicable only close to $u = 0$ and with $A = A_W$, where A_W represents the cross sectional area of the waveguide, are:

$$\frac{dn}{dz} = \frac{F_\mu + F_{drag} + MS_i u_a}{6W_{//}} \tag{C.6}$$

$$\frac{dW_{//}}{dz} = \frac{F_\mu + F_{drag} + MS_i u_a}{3n} \tag{C.7}$$

$$\frac{dW_\perp}{dz} = \frac{-F_\mu}{n} . \tag{C.8}$$

Thus far this discussion of boundary conditions has not considered the quasi-isothermal case. In the quasi-isothermal case the equations that have potential singularities are (B.23a) and (B.23b). In these equations the denominators go to zero when

$$Mu^2 = 2W_{//} . \tag{C.9}$$

This is because the ion acoustic velocity is one third as high in our quasi-isothermal model as in the case when we neglected axial heat conduction. All of the other boundary conditions stay the same under the assumptions of quasi-isothermal flow.

APPENDIX D - Derivation of Guiding Center Equation

The non-relativistic equation of motion for a charged particle exposed to electric and magnetic fields is

$$\ddot{\mathbf{r}} = \frac{q}{m_s}(\dot{\mathbf{r}} \times \mathbf{B}(r,t) + \mathbf{E}(r,t)) \tag{D.1}$$

where **r** is the instantaneous position (vector) of the particle, q is the charge of the particle, **B**(r,t) and **E**(r,t) are the electric and magnetic fields at a point in time t, and m_s is the mass of the particle. To derive the equation of motion of the guiding center of the particle Northrop (1963) lets $\mathbf{r}=\mathbf{R}_{gc}+\rho$ where $\mathbf{R}_{gc}$ is the position of the guiding center and ρ is the vector from the guiding center to the particle. The precise definition of the vector ρ can be shown in a few lines to be described by the equation $\rho = m_s / (qB^2)\mathbf{B} \times (\dot{\mathbf{r}} - \mathbf{E} \times \mathbf{B} / B^2)$, where **E** and **B** are evaluated at **r**. The next step in Northrop's derivation is to substitute $\mathbf{r}=\mathbf{R}_{gc}+\rho$ into Eq. (D.1) and expand the fields in a Taylor series about $\mathbf{R}_{gc}$. The result is:

$$\ddot{\mathbf{R}}_{gc} + \ddot{\rho} = \frac{q}{m_s}\{\mathbf{E}(\mathbf{R}_{gc}) + \rho\nabla\mathbf{E}(\mathbf{R}_{gc}) + (\dot{\mathbf{R}}_{gc} + \dot{\rho}) \times [\mathbf{B}(\mathbf{R}_{gc}) + \rho\nabla\mathbf{B}(\mathbf{R}_{gc})]\} + \vartheta(\varepsilon) \tag{D.2}$$

where $\vartheta(\varepsilon)$ denotes terms of order ε^2. In this case ε is the smallness parameter and is defined as the ratio of the Larmor radius of the particle's orbital motion to the characteristic distance over which fields change. Notice that when the cross product in Eq. (D.2) is expanded, the term $\dot{\rho} \times \rho \cdot \nabla\mathbf{B}(\mathbf{R})$ appears. This term, which is of order ε, must be retained in this analysis and is very important, as will be explained later.

The next step in Northrop's development is to define three mutually orthogonal unit vectors, $\hat{\mathbf{e}}_1, \hat{\mathbf{e}}_2$, and $\hat{\mathbf{e}}_3$ where $\hat{\mathbf{e}}_1$ points in the direction of the magnetic field lines and $\hat{\mathbf{e}}_2$, and $\hat{\mathbf{e}}_3$ are perpendicular to both the field lines and to each other. To represent the guiding center motion of a particle moving about field lines in a circular orbit we let

$$\rho = \rho(\hat{\mathbf{e}}_2 sin\theta + \hat{\mathbf{e}}_3 \cos\theta) \tag{D.3}$$

where

$$\theta = \int \omega dt. \tag{D.4}$$

ω being the cyclotron frequency of the particle's Larmor motion (eB/ms). Differentiating Eq. (D.3) twice we obtain expressions for $\dot{\rho}$ *a*nd $\ddot{\rho}$:

$$\dot{\rho} = \omega\rho(\hat{\mathbf{e}}_2 \cos\theta + \hat{\mathbf{e}}_3 \sin\theta) + \rho\hat{\mathbf{e}}_2 \cdot \sin\theta + \rho\hat{\mathbf{e}}_3 \cdot \cos\theta, \tag{D.5}$$

and

$$\begin{aligned}\ddot{\rho} = &-[\omega^2\rho(\hat{\mathbf{e}}_2 \sin\theta + \hat{\mathbf{e}}_3 \cos\theta)] + \dot{\omega}\rho[\hat{\mathbf{e}}_2 \cdot \cos\theta - \hat{\mathbf{e}}_3 \cdot \sin\theta] \\ &+2\omega[(\rho\hat{\mathbf{e}}_2 \cos\theta - \rho\hat{\mathbf{e}}_3 \sin\theta)] + [(\rho\hat{\mathbf{e}}_2 \sin\theta - \rho\hat{\mathbf{e}}_3 \cos\theta)]\end{aligned} \tag{D.6}$$

These expressions are then substituted back into Eq. (D.2) and the resulting equation time-averaged over a gyration period. This is accomplished by taking

$$\int_0^{2\pi} (...) d\theta \tag{D.7}$$

and considering coefficients such as $\rho\hat{\mathbf{e}}_2$ to be constants. The result of time averaging is:

$$\ddot{\mathbf{R}}_{gc} = \frac{q}{m_s}[\mathbf{E}(\mathbf{R}_{gc}) + \dot{\mathbf{R}}_{gc} \times \mathbf{B}(\mathbf{R}_{gc})] + \frac{q}{m_s}\frac{\rho^2}{2}[\hat{\mathbf{e}}_2 \times (\hat{\mathbf{e}}_3 \cdot \nabla)\mathbf{B} - \hat{\mathbf{e}}_3 \times (\hat{\mathbf{e}}_2 \cdot \nabla)\mathbf{B}] + \vartheta(\varepsilon) \tag{D.8}$$

because

$$\langle \dot{\rho} \times (\rho \cdot \nabla)\mathbf{B} \rangle = \frac{\rho^2\omega}{2}[\hat{\mathbf{e}}_2 \times (\hat{\mathbf{e}}_3 \cdot \nabla)\mathbf{B} - \hat{\mathbf{e}}_3 \times (\hat{\mathbf{e}}_2 \cdot \nabla)\mathbf{B}] \tag{D.9}$$

Notice that the coefficient $\rho^2\omega/2$ is equivalent to μ/q, where μ is the well-known magnetic moment of the spiraling particle. The adiabatic invariance of μ is not assumed in this (Northrop's) derivation of the guiding center equations of motion. Using some straight-forward vector identities and the fact that $\nabla \cdot \mathbf{B} = 0$ Eq. (D.9) can be simplified to obtain:

$$\ddot{\mathbf{R}}_{gc} = \frac{q}{m_s}[\mathbf{E}(\mathbf{R}_{gc}) + \dot{\mathbf{R}} \times \mathbf{B}(\mathbf{R}_{gc})] - \frac{\mu}{m_s}\nabla B(\mathbf{R}_{gc}) + \vartheta(\varepsilon) \tag{D.10}$$

With the substitution $-\mu\nabla B = \mathbf{F}_\mu$ and neglecting the error term we obtain.:

$$\ddot{\mathbf{R}}_{gc} = \frac{\mathbf{F}_\mu}{m_s} + \frac{q}{m_s}(\dot{\mathbf{R}}_{gc} \times \mathbf{B} + \mathbf{E}_{sp}). \tag{D.11}$$

APPENDIX E - Listing of Computer Program

```
      PROGRAM ECRSODAR

      IMPLICIT REAL*8(A-H,O-Z)
      REAL*8 N,NA,ME,MI,MACH,NDOT,MDOT,NG
      EXTERNAL STAG,INGUIDE,NOZZLE,GEX,LSODARPREP,UPSTREAM

      DIMENSION RWORK(500),IWORK(50),ATOL(13)

      COMMON/ECR/UI,UEA,UEI,UA,U,N,WPAR,WPRP,NA,A,AA,
     &DUDZ,DNDZ,DWPARDZ,DWPRPDZ,DNADZ,NNN,DADZ,BB,AWAVE,DN,
     &SI,SD,FD,FEA,FIA,FIN,PECR,FL,MI,MACH,FDRAG,B,DBDZ,
     &PIN,NG,WPRPG,WPARG,MDOT,EMACH,NDOT,ZSTAG,QPAR,QPRP,ISTATE,
     &ZWAVE,ZECR,BWAVE,CRNT,NHEAT,QHEAT,NPRES,PHEAT,TANKN


      COMMON/ODE/NR,JT,NEQ,ITOL,RTOL,ATOL,ITASK,IOPT,LRW,RWORK,
     &IWORK,LIW

      DATA EC,AMU,PI,ME,ZWAVE
     &/1.6021E-19,1.67265E-27,3.1415927,9.1095E-31,0.06/

*************************************************************************
      PURPOSE OF PROGRAM:

      The program 'ECRSODAR' is designed to find numerical solutions to a
      set of nonlinear first order differential equations that have been
      derived to model the process of ECR plasma acceleration to provide
      theoretical predictions of i) plasma parameters, such as electron
      energy and number density, and ii) propulsive performance parameters,
      such as specific impulse and efficiency.

      The input variables in this program are parameters, such as mass flow
      rate, microwave power level, or vacuum system back pressure that can be
      controlled or measured independently of plasma effects in an experimental
      apparatus.  The output variables that this program is designed to
      produce are those that depend on the plasma effects the system of differential
      equations attempts to model.  Plasma effects treated in the model
      include both elastic and inelastic collisions, cross-field diffusion,
      ionization,wall losses, upstream diffusion, acceleration of ions via ambipolar
      interaction with electrons, the diamagnetic interaction between
      electrons and an applied magnetic field, electron thermodynamic acceleration
      effects, possible tank back pressure effects, and microwave coupling to
      the electron thermal motion

      The model is a quasi-one-dimensional, steady-state treatment of the problem
      and includes two electron temperatures, perpendicular and parallel to the
      magnetic fielC.  Ions are treated as having negligible thermal energy, but
      finite directed kinetic energy.  The electrons have finite thermal energy
      but finite directed kinetic energy.  The neutral gas is assumed to be in
      thermal equilibrium with the walls of the vacuum system at room temperature
      and is assumed to move according to free molecular flow.
```

LIMITATIONS OF PROGRAM:

This program was designed and written as a research tool for studying a very specific set of plasma conditions associated with a very specific set of research goals. It is not designed as a general research tool, it is not designed as a user friendly resource, and it is not designed as a robust solver that can handle any other than the limited conditions addressed in the present research activity. Experience with this program suggests that any attempt to extend its application beyond cases addressed in the present research will probably require additions and/or changes to the present code. It is not recommended for use except by researchers who are intimately familiar with the theory of the ECR plasma accelerator that this program has been written to study.

This program is known to run on an Apple Macintosh using MPW FORTRAN and on an HP 9000 risk machine using UNIX based FORTRAN 77.

HIGH LEVEL PROGRAM DESIGN:

This program consists of a main program and seven subroutines and uses the ordinary differential equation solver 'LSODAR' as developed by the Lawrence Livermore National Laboratory. For more information on LSODAR refer to the paper: "ODEPACK, A Systematized Collection of ODE Solvers" which appears in Scientific Computing, R.S. Stepleman et al. (eds.), North-Holland, Amsterdam, 1983 (Vol. 1 of IMACS Transactions of Scientific Computation), pp. 56-64, also as a preprint under UCRL-88007.

LSODAR numerically integrates a set of first order ordinary differential equations and returns the values of those equations to the user at either pre-specified intervals in the independent variable or at values of the independent variable that give roots to pre-specified algebraic equations relating the dependent variables. In the present problem the independent variable is Z, the axial (stream-wise) coordinate. The dependent variables are U, the plasma velocity, N, the ion number density, Wprp, the mean electron thermal energy perpendicular to magnetic field lines, Wpar, the mean electron thermal energy parallel to magnetic field lines, and Na, the atom number density.

Given a set of initial conditions for the five dependent variables, LSODAR is very good at providing an accurate numerical solution of the problem. Unfortunately, in this case the initial conditions can not be specified a-priori and in fact the problem must be solved as a boundary value problem in which four relationships between the dependent variables are know at the location in Z at which U=0 and one relationship between the dependent variables is known at the location where the plasma has achieved an ion acoustic Mach number of one.

To solve this boundary value problem, ECRSODAR uses a shooting method. The subroutine STAG is used to find a numerical solution to satisfy the four boundary conditions at the stagnation (U=0) point. The method of solution used in STAG is a modified Newton-Raphson iteration. Because there are five dependent variables in the problem and only four boundary conditions at the stagnation plane, one of the variables must be indeterminate at U=0. The undetermined variable at U=0 is arbitrarily chosen to be N. An initial guess for N is made (NG) by the user of the program as an input. Then STAG is called to determine the values of the

other four variables, based on NG.

After STAG is called by the main program to determine a set of initial values, the subroutine NOZZLE is used to call LSODAR and integrate the system of ODEs to the point at which the Mach number is unity. LSODAR returns the values of the dependent variables at Mach number one via its aforementioned root finding capability. The error in the fifth boundary condition, which depends on how good the guess for N was, is then calculated numerically and given the variable name EMACH. A modified Newton-Raphson iteration scheme is then used by the main program via multiple calls to STAG and EMACH to systematically improve the accuracy of the guess for N to minimize EMACH.

At small values of EMACH, the Newton-Raphson iteration scheme is discarded and the main program turns to a less efficient but more robust modified bisection approach to refine the guess for N to sufficient accuracy to meet all five boundary conditions. The differential equations in the model are singular at U=0 and Mach one unless the boundary conditions are satisfied. Sufficient accuracy for meeting the boundary conditions in this case is determined by having values of the dependent variables that do not cause numerical overflows in the machine and typically involve errors of one part in ten to the seventh.

After a numerical solution to the boundary conditions has been found as described above, the program then proceeds to calculate the plasma conditions downstream of the transition from subsonic to supersonic and upstream from the stagnation plane. The subroutines used to do these two calculations are NOZZLE and UPSTREAM, respectively.

All of the differential equations solved in this program are contained in the subroutine GRAD. GRAD is called by all three of the subroutines that use LSODAR to integrate the equations as well as by the main program. The subroutine PLASMA contains many of the same equations that GRAD contains that are needed to evaluate the differential equations but PLASMA does not include the actual differential equations. Plasma is repeatedly called by STAG in its Newton-Raphson iteration scheme.

ECRSODAR can be used for four different classes of problems relating to the ECR plasma acceleration process. The first two classes are distinguished as i) isothermal or ii) without axial heat conduction, the two extremes in axial heat conduction. The second two classes are distinguished as having either i) finite or ii) zero vacuum tank back pressure, corresponding to lab or space conditions. NHEAT and TANKN are the user inputs that control which of these four classes of problems is to be solved. (NHEAT. NE. 1) gives the zero heat conduction case, while the zero tank pressure case is given by TANKN=0.0, otherwise TANKN is given the gas number density corresponding to the desired tank back pressure.

The subroutine GEX provides the equations for which LSODAR returns roots. The specific roots it returns are for the conditions of MACH=1 and Pheat=0. The root finder is used to find MACH=1 in all four classes of problems that can be addressed by this code. Pheat=0 is used only for the isothermal (NHEAT=1) case. Pheat stands for the net heat flux to the plasma required to globally balance the conservation of energy in the problem. When Pheat is used, the integration stops where Pheat=0 to ensure balancing the global energy equations.

INPUT VARIABLES:

AWAVE	wave-guide or thrust chamber area (m**2)
CRNT	magnet coil current (Amperes)
MDOT	mass flow rate of propellant (sccm)
NG	initial guess of stagnation ion density (m**-3)
NHEAT	flag for isothermal versus adiabatic flow (1=isothermal)
PIN	total input microwave power, (watts)
TANKN	vacuum tank gas density [related to pressure] (m**-3)
UA	atom drift velocity (m/s)
UI	argon ionization energy (eV)
UEA	effective excitation energy of argon (eV)
UEI	effective excitation energy of argon ion (eV)
WPRPG	initial guess of stagnation perp. e-temp (eV)
WPARG	initial guess of stagnation parallel. e-temp (eV)
ZECR	axial location of end of ecr coupling region (m)
ZSTAG	axial location of stagnation plane (m)
ZWAVE	axial location of end of wave-guide (m)

PARTIAL LIST OF OUTPUTS:

AREA	cross sectional area of modeled flow (m**2)
B	axial magnetic field (Tesla)
ETAU	calculated propellant utilization
FL	power transferred from perpendicular to parallel electron energy via elastic collisions (watts*m**-3)
MACH	ion acoustic mach number
N	number density of ions [equal to electrons] (m**-3)
NA	number density of atoms (m**-3)
PCOLS	integrated losses due to inelastic collisions (watts)
PECR	density of absorbed microwave power (watts*m**-3)
PHEAT	integrated fictitious heat flux for isothermal flow (watts)
PT	total kinetic power in flow at downstream location (watts)
PWALL	integrated wall losses (watts)
QHEAT	fictitious heat flux for isothermal flow (watts*m**-3)
RFNET	error checker for conservation of axial momentum
RMNET	error checker for conservation of mass
PNET	net error in power flux (watts)
RWPARNET	error checker for conservation of Wpar energy
RWPRPNET	error checker for conservation of Wprp energy
SI	plasma source term due to ionization (m**-3/s)
SOURCE	integrated plasma source terms (s**-1)
SD	plasma source term due to diffusion to walls (m**-3/s)
U	plasma velocity (m/s)
WORK	integrated work done on plasma by atom slip (watts)

TYPICAL INPUT FILE (ECRQ.DAT) FOR TEST CASE:

```
100.0,1.0D17,15.755,13.65,18.25,16.0,400.0,1
0.06,0.02,0.04,0.013,3.0D-18,2.0D-18,5172.5,3.0E17
```

RESULTS OF TEST CASE:

This test case takes about thirty iterations to converge to a set of initial values that meet the boundary conditions. The values of the

five dependent variables at U=0 assuming Zo=0.02m are as follows:

```
  U  =  0.0
  N  =  1.461E+17
WPRP =  8.883E-18
WPAR =  1.332E-18
 NA  =  6.134E+18
```

After integrating through Mach 1 out to a large value of Z the program returns the following values for this test case (@PHEAT=0.0):

```
  Z  =  2.297E+00
  U  =  1.723E+04
  N  =  2.999E+13
WPRP =  4.930E-19
WPAR =  1.332E-18
 NA  =  3.000E+17

ETAU = 1.2715963648350
  PT = 106.330087014298
```

****

```
MI=40.0*AMU
This program is based on the use of argon as a propellant gas.

OPEN(UNIT=20,FILE='ECR.OUT',STATUS='UNKNOWN')
ECR.OUT is the output file the results are sent to.

CALL MOVEOUTWINDOW(5,40,640,872)
MOVEOUTWINDOW is useful for sizing the output window on the MacII.


This section of the program inputs quantities which the user might
wish to vary from run to run.  The information must be placed in a
data file called:"ECRIN.DAT".


OPEN(UNIT=50,FILE='ECRQ.DAT',STATUS='OLD')
READ(50,*)UA,NG,UI,UEA,UEI,MDOT,PIN,NHEAT
READ(50,*)ZWAVE,ZSTAG,ZECR,AWAVE,WPRPG,WPARG,CRNT,TANKN


BWAVE=1.2567E-7*CRNT/(0.04+ZWAVE**2)**1.5
This is the magnitude of the magnetic field at the end of the waveguide.

MDOT=MDOT*2.9743D-8
This converts the mass flow rate from sccm to kg/s for argon.
  CALL STAG
  CALL INGUIDE
  READ(6,*)
EMACH=9.0E6
R2=1.0E18
These are arbitrary numbers to use for these variables to initialize them
to something that doesn't cause trouble.
```

```
The following loop uses a Newton-Raphson iteration scheme to get improved
values of EMACH until EMACH is less than 5000.  Note!  This program will not
work unless your initial guess for N is pretty good (Emach<=1.oe8) and your
initial guess must return a positive value for EMACH.
Do While (ABS(EMACH). GT. 5.0E3)

  WRITE(6,*)"NG=",NG


  CALL STAG
  CALL INGUIDE

  IF(ISTATE. EQ. 2) THEN
    This happens in case of an overshoot.
    R2=NG
    NG = NG-DNG/2.0
    DNG= DNG*0.5
    WRITE(6,*)'PROGRAM IN ISTATE CONDITIONAL'
    GO TO 20
  ENDIF

  IF(ISTATE. EQ. 3) THEN
    This is a valid guess.
    R1=NG
  ENDIF


  IF( ABS(EMACH). LT. 5.0E3) GOTO30

  EMACHOLD=EMACH

  ONG=NG

  IF(NHEAT. EQ. 1)THEN
    DELTANG is the differential step in the independent variable needed
    to calculate the derivative of EMACH w.r.t. NG.
    DELTANG=NG/1.0E6
  ELSE
    DELTANG=NG/1.0E8
  ENDIF

  NG=ONG+DELTANG

  WRITE(6,*)" NG=",NG
  WRITE(6,*)"ONG=",ONG

  CALL STAG
  CALL INGUIDE

  DNG = -(DELTANG/(EMACH-EMACHOLD))*EMACH/2.0
  The factor of two above makes for conservative steps.

  WRITE(6,*)"DNG=",DNG
  WRITE(6,*)"EMACH=",EMACH
  WRITE(6,*)"EMACHOLD=",EMACHOLD
  NG = NG - DELTANG + DNG
```

```
      End Do

      The Newton-Raphson iteration scheme is not very good for small EMACH
      so here the program swtiches to a slower bisection scheme.

        IF(NHEAT .EQ. 1)THEN
           EMIN=50
        ELSE
           EMIN=100
        ENDIF

)     Do While (EMACH. GT. EMIN)

        CALL STAG
        CALL INGUIDE

          IF(EMACH. LE. EMIN)GOTO99

        IF(ISTATE. EQ. 3) THEN
          IF( ABS(EMACHOLD) . LT. ABS(EMACH) )GOTO99
        ENDIF

        IF(ISTATE. EQ. 2) THEN
          R2=NG
        ELSE
          R1=NG
        ENDIF

        NG=(R2+2.0*R1)/3.0
        Practical use of this program suggests that R1 should be more heavily
        weighted than R2

        WRITE(6,*)"NG=",NG

        IF(ISTATE. EQ. 3) THEN
          EMACHOLD=EMACH
        ENDIF

      END DO

9     WRITE(20,100)
00    FORMAT('      Z           U           N          WPRP          WPAR'
     & ,'         NA         MACH          B          PECR         VOLTS')

      IF(NHEAT. EQ. 1)THEN
        The upstream problem is only important for the isothermal problem.
        CALL STAG
        CALL UPSTREAM
      ENDIF

      CALL STAG
      CALL NOZZLE
      NOZZLE integrates through Mach number one and out to high mach number

      WRITE(6,*)''
      WRITE(6,*)"End of program reached."

01    STOP
```

END

```
      SUBROUTINE STAG

      The subroutine STAG calculates a set of stagnation conditions for
      the plasma based on a guess for the stagnation ion density.  The
      values of the state variables which come out of STAG allow a form
      of the equations of motion of the plasma to be non-singular.These
      specific versions of the equations of motion are only valid while
      U, the plasma velocity, is near zero.

      IMPLICIT REAL*8(A-H,O-Z)
      REAL*8 N,NA,ME,MI,MACH,NDOT,MDOT,NG

      COMMON/ECR/UI,UEA,UEI,UA,U,N,WPAR,WPRP,NA,A,AA,
     &DUDZ,DNDZ,DWPARDZ,DWPRPDZ,DNADZ,NNN,DADZ,BB,AWAVE,DN,
     &SI,SD,FD,FEA,FIA,FIN,PECR,FL,MI,MACH,FDRAG,B,DBDZ,
     &PIN,NG,WPRPG,WPARG,MDOT,EMACH,NDOT,ZSTAG,QPAR,QPRP,ISTATE,
     &ZWAVE,ZECR,BWAVE,CRNT,NHEAT,QHEAT,NPRES,PHEAT,TANKN

      DATA EC,AMU,PI,ME,ZWAVE
     &/1.6021E-19,1.67265E-27,3.1415927,9.1095E-31,0.06/

      WRITE(6,*)'STAGNATION INPUT STATE VARIABLES:'

      BWAVE=1.2567E-7*CRNT/(0.04+ZWAVE**2)**1.5

      U=0.0
      Z=ZSTAG
      B=1.2567E-7*CRNT/(0.04+Z**2)**1.5
      DBDZ=-3.77D-7*CRNT*Z/(0.04+Z**2)**2.5
      A=AWAVE*BWAVE/B
      NDOT=MDOT/MI
      NA=NDOT/UA/A

      E1=100.0
      E2=100.0

      N=NG
      WPRP=WPRPG
      WPAR=WPARG

01    WRITE(6,1000)
000   FORMAT('           U              N              WPRP           '
     &               'WPAR             NA')
      WRITE(6,102)U,N,WPRP,WPAR,NA

02    FORMAT(5(1P,E12.5,3X))


05    E1=E1
      E2=E2
```

```
      IF(WPRP.LT.0)THEN
       WRITE(6, *)'WPRP LESS THAN ZERO'
       WPRP=1.6E-19
       WPAR=8.0E-20
       NG=NG*1.01
       N=NG
       GOTO101
      ENDIF

      IF(WPAR.LT.0)THEN
       WRITE(6, *)'WPAR LESS THAN ZERO'
       WPRP=1.6E-19
       WPAR=8.0E-20
       NG=NG*1.01
       N=NG
       GOTO101
      ENDIF

   THE SECTION CALCULATES THE ERROR TERMS AND CHECKS FOR CONVERGENCE
*************************************************************************
                                                                       *
      CALL PLASMA

      E1=QPRP-SI*WPRP
      E2=QPAR-WPAR*(3*SI+2*SD)

      IF(ABS(E1).GE.1.0E-7)GOTO110
      IF(ABS(E2).GE.1.0E-7)GOTO110
      GOTO199

      END OF SECTION
                                                                       *
*************************************************************************




      THIS SECTION CALCULATES THE PARTIALS W.R.T.: WPAR
*************************************************************************
                                                                       *

10    DELTAWPAR=WPAR*1.0E-5
      WPAR=WPAR+DELTAWPAR

      CALL PLASMA

      PE1RWPAR=(QPRP-SI*WPRP - E1)/DELTAWPAR
      PE2RWPAR=(QPAR-WPAR*(3*SI+2*SD) - E2)/DELTAWPAR
      END OF SECTION
                                                                       *
*************************************************************************
```

```
      THIS SECTION CALCULATES THE PARTIALS W.R.T.: WPRP
*************************************************************************
                                                                       *
      WPAR=WPAR-DELTAWPAR
      DELTAWPRP=1.0E-5*WPRP
      WPRP=WPRP+DELTAWPRP

      CALL PLASMA

      PE1RWPRP=(QPRP-SI*WPRP - E1)/DELTAWPRP
      PE2RWPRP=(QPAR-WPAR*(3*SI+2*SD) - E2)/DELTAWPRP

      END OF SECTION
                                                                       *
*************************************************************************




      THIS SECTION CALCULATES THE NEW GUESSES FOR WPRP & WPAR
*************************************************************************
                                                                       *

      DE1=-.5*E1
      DE2=-.5*E2
      The factor of 0.5 makes for sonservative steps


      DWPAR = (-(DE2*PE1RWPRP) + DE1*PE2RWPRP)
     &/(-(PE1RWPRP*PE2RWPAR) + PE1RWPAR*PE2RWPRP)

      DWPRP = (DE2*PE1RWPAR - DE1*PE2RWPAR)
     &/(-(PE1RWPRP*PE2RWPAR) + PE1RWPAR*PE2RWPRP)


      WPAR = WPAR + DWPAR
      WPRP = WPRP + DWPRP - DELTAWPRP

      END OF SECTION
                                                                       *
*************************************************************************


      GOTO105

99    WPARG=WPAR
      WPRPG=WPRP

      WRITE(6,*)'OUTPUTS FOLLOW:'
      WRITE(6, 1100)
100   FORMAT('          U             N             WPRP          '
     &      'WPAR            NA')
      WRITE(6,200)U,N,WPRP,WPAR,NA

00    FORMAT(5(1P,E12.5,3X))

      RETURN
      END
```

```
      SUBROUTINE INGUIDE

      IMPLICIT REAL*8(A-H,O-Z)
      REAL*8 N,NA,ME,MI,MACH,NDOT,MDOT,NG,JROOT
      EXTERNAL GRAD,GEX,LSODARPREP

      DIMENSION F(13),DF(13),RWORK(500),IWORK(50),ATOL(13)

      COMMON/ECR/UI,UEA,UEI,UA,U,N,WPAR,WPRP,NA,A,AA,
     &DUDZ,DNDZ,DWPARDZ,DWPRPDZ,DNADZ,NNN,DADZ,BB,AWAVE,DN,
     &SI,SD,FD,FEA,FIA,FIN,PECR,FL,MI,MACH,FDRAG,B,DBDZ,
     &PIN,NG,WPRPG,WPARG,MDOT,EMACH,NDOT,ZSTAG,QPAR,QPRP,ISTATE,
     &ZWAVE,ZECR,BWAVE,CRNT,NHEAT,QHEAT,NPRES,PHEAT,TANKN

      COMMON/ODE/NR,JT,NEQ,ITOL,RTOL,ATOL,ITASK,IOPT,LRW,RWORK,
     &IWORK,LIW

      DATA EC,AMU,PI,ME,ZWAVE
     &/1.6021E-19,1.67265E-27,3.1415927,9.1095E-31,0.06/

      WRITE(6, *) 'INGUIDE:'

      CALL LSODARPREP

      This subroutine uses LSODAR to integrate from U=0 to MACH=1

      First it sets up a few small things and call GRAD once to initialize
      the array DF and ensures that GRAD works OK.  The output is to let
      the user know things went well.

      WRITE(6,*)'Now the results of running LSODAR are displyed:'
      WRITE(6,336)
336   FORMAT('      Z           U           N          WPRP          WPAR',
     &     '         NA        MACH          B          PECR           SI',
     &     '         SD          FD       WORK        QPAR        PHEAT',
     &     '         PCLOS        PWALL     SOURCE      AREA')

      PHEAT=0.0
      PCLOS=0.0
      PWALL=0.0
      SOURCE=0.0
      WORK=0.0
      WPARFLUX=0.0
      WPRPFLUX=0.0
      FFLUX=0.0

      Z=ZSTAG
      DELTAZ=5.0E-3
```

```
      F1 through F5 are the dependent variables to be solved-for.  Pheat
      is a special parameter that is used in the isothermal case.  F6 through
      F13 calculate the values of different source terms and are used to check
      for errors in the outputs... more on that later.

      F(1)=U
      F(2)=N
      F(3)=WPAR
      F(4)=WPRP
      F(5)=NA
      F(6)=PHEAT
      F(7)=PCLOS
      F(8)=PWALL
      F(9)=SOURCE
      F(10)=WORK
      F(11)=WPARFLUX
      F(12)=WPRPFLUX
      F(13)=FFLUX


      CALL GRAD(NEQ,Z,F,DF)

      IF(NHEAT. EQ. 1)THEN
        MACH=((MI*U**2)/(2.0*WPAR))**0.5
      ELSE
        MACH=((MI*U**2)/(6.0*WPAR))**0.5
      ENDIF

      B=1.2567E-7*CRNT/(0.04+Z**2)**1.5

      WRITE(6,344)Z,U,N,WPRP,WPAR,NA,MACH,B,
     &PECR,SI,SD,FD,WORK,QPAR,PHEAT,PCLOS,PWALL,SOURCE,A
344   FORMAT(19(1P,E10.3,2X))

      Calls to LSODAR are done here.

      Z2 = Z + DELTAZ
370   DO 380 IOUT = 1,50

      OLDMACH=MACH
      CALL LSODAR(GRAD,NEQ,F,Z,Z2,ITOL,RTOL,ATOL,ITASK,
     &            ISTATE,IOPT,RWORK,LRW,IWORK,LIW,JAC,JT,
     &            GEX,NR,JROOT)

      U=F(1)
      N=F(2)
      WPAR=F(3)
      WPRP=F(4)
      NA=F(5)
      PHEAT=F(6)
      PCLOS=F(7)
      PWALL=F(8)
      SOURCE=F(9)
      WORK=F(10)
      WPARFLUX=F(11)
      WPRPFLUX=F(12)
      FFLUX=F(13)
```

```
      B=1.2567E-7*CRNT/(0.04+Z**2)**1.5

      IF(NHEAT. EQ. 1)THEN
        MACH=((MI*U**2)/(2.0*WPAR))**0.5
      ELSE
        MACH=((MI*U**2)/(6.0*WPAR))**0.5
      ENDIF

      WRITE(6,375)Z,U,N,WPRP,WPAR,NA,MACH,B,
     &PECR,SI,SD,FD,WORK,QPAR,PHEAT,PCLOS,PWALL,SOURCE,A,FDRAG
5     FORMAT(20(1P,E10.3,2X))

      IF(OLDMACH .GT. MACH) THEN
       ISLOW=-1
       WRITE(6,*)'MACH NUMBER DECREASED'
       GO TO 382
      ELSE
       ISLOW=1
      ENDIF

      IF(ISTATE .EQ. 2) GO TO 380
      IF(ISTATE .EQ. 3) GO TO 382

      IF(ISTATE .LT. 0) GO TO 400
      If LSODAR returns an error then ISTATE is less than zero. The value of
      ISTATE  defines the error.
      See documentation of LSODAR for specific meanings.

30    Z2 = Z + DELTAZ

32    IF(NHEAT. EQ. 1)THEN
        MACH=((MI*U**2)/(2.0*WPAR))**0.5
      ELSE
        MACH=((MI*U**2)/(6.0*WPAR))**0.5
      ENDIF

      WRITE(6,*)'MACH=',MACH

      IF(NHEAT. EQ. 1)THEN
        EMACH=-NDOT*((FD+FDRAG)*U + MI*SI*U*(UA-U)  - 2*WPAR*(SI+SD) +
     &2*DADZ*N*U*WPAR/A)/(A*N*U)
      ELSE
        EMACH = -NDOT*(-2*QPAR + FD*U + FDRAG*U - 2*MI*SI*U**2 +
     &3*MI*SI*U*UA - 2*SD*WPAR + 6*DADZ*N*U*WPAR/A)/(A*N*U)
      ENDIF

      WRITE(6,*)'EMACH=',EMACH

00    WRITE(6,*)'ISTATE =',ISTATE

      RETURN
      END
```

```
 SUBROUTINE GRAD(NEQ,Z,F,DF)

 IMPLICIT REAL*8(A-H,O-Z)
 REAL*8 N,NA,ME,MI,NEU,MACH,NDOT,MDOT,NG

 DIMENSION F(13),DF(13)

 COMMON/ECR/UI,UEA,UEI,UA,U,N,WPAR,WPRP,NA,A,AA,
&DUDZ,DNDZ,DWPARDZ,DWPRPDZ,DNADZ,NNN,DADZ,BB,AWAVE,DN,
&SI,SD,FD,FEA,FIA,FIN,PECR,FL,MI,MACH,FDRAG,B,DBDZ,
&PIN,NG,WPRPG,WPARG,MDOT,EMACH,NDOT,ZSTAG,QPAR,QPRP,ISTATE,
&ZWAVE,ZECR,BWAVE,CRNT,NHEAT,QHEAT,NPRES,PHEAT,TANKN

 DATA EC,AMU,PI,ME,ZWAVE
&/1.6021E-19,1.67265E-27,3.1415927,9.1095E-31,0.06/

 U=F(1)
 N=F(2)
 WPAR=F(3)
 WPRP=F(4)
 NA=F(5)
 PHEAT=F(6)
 PCLOS=F(7)
 PWALL=F(8)
 SOURCE=F(9)
 WORK=F(10)
 WPARFLUX=F(11)
 WPRPFLUX=F(12)
 FFLUX=F(13)

 B=1.2567E-7*CRNT/(0.04+Z**2)**1.5
 DBDZ=-3.77D-7*CRNT*Z/(0.04+Z**2)**2.5

 A=AWAVE*BWAVE/B
 DADZ=-A*DBDZ/B

 IF(NHEAT. EQ. 1)THEN
   MACH=((MI*U**2)/(2.0*WPAR))**0.5
 ELSE
   MACH=((MI*U**2)/(6.0*WPAR))**0.5
 ENDIF

 TEV=0.666667*(WPRP+WPAR)/EC
 IF(TEV.LT.1D-2) THEN
   TEV=1D-2
   WPRP=1.602D-21
   WPAR=8.01D-22
 ENDIF

 X=DLOG10(TEV)

 IF(ABS(UA-U).LE.1.0)THEN
   EEI=2.1E-7
 ELSE
   EEI=MI*(UA-U)**2/(EC*2)
 ENDIF

 REAS=4.69D-14*TEV**0.5
```

```
 REES=(5.48D-12/(TEV**1.5))*DLOG(1.31D13/(N**.2)*TEV**1.5)
 REIS=REAS+REES/2
 RI=10**(-16.197+4.0383*X-1.6296*X**2+0.26371*X**3-0.015707*X**4)
 REA=10**(-16.716+3.9633*X-1.6743*X**2+0.29668*X**3-0.020062*X**4)
 REI=10**(-17.946+6.6480*X-3.2464*X**2+0.68128*X**3-0.053788*X**4)
 RIAS=ABS(UA-U)*1D-20*36.485*EEI**(-0.11848)

 IF(Z.LE.ZWAVE)THEN
   SD=-WPRP*N*PI/(4.0*AWAVE*B*EC)
 ELSE
   SD=-WPRP*N*PI/(4.0*A*B*EC)
 ENDIF

 SI=RI*N*NA
 FD=-WPRP*N*DBDZ/B
 FEA=ME*N*NA*REAS*(UA-U)
 FIA=MI*N*NA*RIAS*(UA-U)
 FIN=N*EC*(NA*(UI*RI+UEA*REA)+N*UEI*REI)

 NEU=N*(REIS+REES)+NA*REAS
 FL=(N/2.0)*(WPAR-WPRP/2.0)*NEU
 W =WPRP+WPAR

 IF(Z.GE.ZECR)THEN
   PECR=0.0
 ELSE
   PECR=PIN/((ZECR-ZSTAG)*A)
 ENDIF

 QPRP  = PECR - FIN*WPRP/W + FL
 QPAR  = (- FIN*WPAR/W - FL)

 IF(NHEAT. EQ. 1)THEN
   QHEAT=( - A*MI**2*SI*U**4 + 2*A*MI**2*SI*U**3*UA +
&4*A*FD*U*WPAR + 4*A*FDRAG*U*WPAR +
&4*DADZ*MI*N*U**3*WPAR - 8*A*SD*WPAR**2 - 12*A*SI*WPAR**2)/
&(2*A*MI*U**2 - 4*A*WPAR) - QPAR
 ENDIF

 QPAR=QHEAT + (- FIN*WPAR/W - FL)

 FDRAG = FIA + FEA

 DUDZ =
&(-2*A*QPAR + A*FD*U + A*FDRAG*U-2*A*MI*SI*U**2+3*A*MI*SI*U*UA-
&2*A*SD*WPAR + 6*DADZ*N*U*WPAR)/(A*MI*N*U**2 - 6*A*N*WPAR)

 IF(NA. GE. TANKN)THEN
   DNADZ = -(SI+SD)/UA - NA/A*DADZ
 ELSE
   DNADZ = 0.0
 ENDIF

 IF(ABS(U).GT.0.0001)THEN

   DNDZ =
&(2*A*QPAR - A*FD*U - A*FDRAG*U + A*MI*SD*U**2 + 3*A*MI*SI*U**2 -
&DADZ*MI*N*U**3 - 3*A*MI*SI*U*UA - 4*A*SD*WPAR - 6*A*SI*WPAR)/
```

```
&(A*MI*U**3 - 6*A*U*WPAR)

   DWPARDZ =
&(-2*A*MI*QPAR*U**2 - A*MI**2*SI*U**4 + 2*A*MI**2*SI*U**3*UA +
&4*A*QPAR*WPAR + 4*A*FD*U*WPAR + 4*A*FDRAG*U*WPAR +
&4*DADZ*MI*N*U**3*WPAR - 8*A*SD*WPAR**2 - 12*A*SI*WPAR**2)/
&(-2*A*MI*N*U**3 + 12*A*N*U*WPAR)

   DWPRPDZ = (QPRP - FD*U - SI*WPRP)/(N*U)

 ELSE
   DNDZ = (FD+FDRAG+3.0*MI*SI*UA)/(6.0*WPAR)
   DWPARDZ = (FD+FDRAG)/(3.0*N)
   DWPRPDZ = -FD/N
 ENDIF


 IF(NHEAT. EQ. 1)THEN
   DWPARDZ = 0.0
 ENDIF

 DF(1)=DUDZ
 DF(2)=DNDZ
 DF(3)=DWPARDZ
 DF(4)=DWPRPDZ
 DF(5)=DNADZ
 DF(6)=QHEAT*A
 DF(7)=-A*FIN
 DF(8)=A*SD*(0.5*MI*U**2+WPAR+WPRP)
 DF(9)=A*(SD+SI)
 DF(10)=A*U*(FDRAG)
 DF(11)=A*(QPAR+SD*WPAR-2*N*WPAR*(DUDZ+U*DADZ/A)+
&            MI*SI*(0.5*U**2-U*UA))
 DF(12)=A*(QPRP-FD*U+SD*WPRP)
 DF(13)=A*(FD+FDRAG-2*(N*DWPARDZ+WPAR*DNDZ)+MI*(SD*U+SI*UA))

99  RETURN
    END
```

```
 SUBROUTINE PLASMA

 IMPLICIT REAL*8(A-H,O-Z)
 REAL*8 N,NA,ME,MI,NEU,MACH,NDOT,MDOT,NG

 COMMON/ECR/UI,UEA,UEI,UA,U,N,WPAR,WPRP,NA,A,AA,
&DUDZ,DNDZ,DWPARDZ,DWPRPDZ,DNADZ,NNN,DADZ,BB,AWAVE,DN,
&SI,SD,FD,FEA,FIA,FIN,PECR,FL,MI,MACH,FDRAG,B,DBDZ,
&PIN,NG,WPRPG,WPARG,MDOT,EMACH,NDOT,ZSTAG,QPAR,QPRP,ISTATE,
&ZWAVE,ZECR,BWAVE,CRNT,NHEAT,QHEAT,NPRES,PHEAT,TANKN

 DATA EC,AMU,PI,ME,ZWAVE
&/1.6021E-19,1.67265E-27,3.1415927,9.1095E-31,0.06/

 Z=ZSTAG

 B=1.2567E-7*CRNT/(0.04+Z**2)**1.5
 DBDZ=-3.77D-7*CRNT*Z/(0.04+Z**2)**2.5

 A=AWAVE*BWAVE/B
 DADZ=-A*DBDZ/B

 TEV=0.666667*(WPRP+WPAR)/EC
 IF(TEV.LT.1D-2) THEN
   TEV=1D-2
   WPRP=1.602D-21
   WPAR=8.01D-22
 ENDIF

 X=DLOG10(TEV)

 IF(ABS(UA-U).LE.1.0)THEN
   EEI=2.1E-7
 ELSE
   EEI=MI*(UA-U)**2/(EC*2)
 ENDIF

 REAS=4.69D-14*TEV**0.5
 REES=(5.48D-12/(TEV**1.5))*DLOG(1.31D13/(N**.2)*TEV**1.5)
 REIS=REAS+REES/2
  RI=10**(-16.197+4.0383*X-1.6296*X**2+0.26371*X**3-0.015707*X**4)
 REA=10**(-16.716+3.9633*X-1.6743*X**2+0.29668*X**3-0.020062*X**4)
 REI=10**(-17.946+6.6480*X-3.2464*X**2+0.68128*X**3-0.053788*X**4)
 RIAS=ABS(UA-U)*1D-20*36.485*EEI**(-0.11848)

 IF(Z.LE.ZWAVE)THEN
   SD=-WPRP*N*PI/(4.0*AWAVE*B*EC)
 ELSE
   SD=-WPRP*N*PI/(4.0*A*B*EC)
 ENDIF

 SD=-WPRP*N*PI/(4.0*AWAVE*B*EC)

 SI=RI*N*NA
 FD=-WPRP*N*DBDZ/B
 FEA=ME*N*NA*REAS*(UA-U)
 FIA=MI*N*NA*RIAS*(UA-U)
```

```
 FIN=N*EC*(NA*(UI*RI+UEA*REA)+N*UEI*REI)

 NEU=N*(REIS+REES)+NA*REAS
 FL=(N/2.0)*(WPAR-WPRP/2.0)*NEU
 W =WPRP+WPAR

 IF(Z.GE.ZECR)THEN
   PECR=0.0
 ELSE
   PECR= PIN/((ZECR-ZSTAG)*A)
 ENDIF

 QPRP  = PECR - FIN*WPRP/W + FL
 QPAR  = (- FIN*WPAR/W - FL)

 FDRAG = FIA + FEA

 IF(NHEAT. EQ. 1)THEN
   QHT=( - A*MI**2*SI*U**4 + 2*A*MI**2*SI*U**3*UA +
&4*A*FD*U*WPAR + 4*A*FDRAG*U*WPAR +
&4*DADZ*MI*N*U**3*WPAR - 8*A*SD*WPAR**2 - 12*A*SI*WPAR**2)/
&(2*A*MI*U**2 - 4*A*WPAR)
 ENDIF

 RETURN
 END
```

```
 SUBROUTINE GEX(NEQ,Z,F,NR,ROUT)

 IMPLICIT REAL*8(A-H,O-Z)
 REAL*8 N,NA,ME,MI,MACH,NDOT,MDOT,NG

 DIMENSION F(13)

 COMMON/ECR/UI,UEA,UEI,UA,U,N,WPAR,WPRP,NA,A,AA,
&DUDZ,DNDZ,DWPARDZ,DWPRPDZ,DNADZ,NNN,DADZ,BB,AWAVE,DN,
&SI,SD,FD,FEA,FIA,FIN,PECR,FL,MI,MACH,FDRAG,B,DBDZ,
&PIN,NG,WPRPG,WPARG,MDOT,EMACH,NDOT,ZSTAG,QPAR,QPRP,ISTATE,
&ZWAVE,ZECR,BWAVE,CRNT,NHEAT,QHEAT,NPRES,PHEAT,TANKN

 DATA EC,AMU,PI,ME,ZWAVE
&/1.6021E-19,1.67265E-27,3.1415927,9.1095E-31,0.06/


 IF(NHEAT. EQ. 1)THEN
   ROUT = 1-((MI*F(1)**2)/(2.0*F(3)))**0.5
     IF(ROUT. LT. -0.001)THEN
        ROUT = PHEAT
     ENDIF
 ELSE
   ROUT = 1-((MI*F(1)**2)/(6.0*F(3)))**0.5
 ENDIF

 RETURN
 END
```

```
      SUBROUTINE LSODARPREP

      IMPLICIT REAL*8(A-H,O-Z)
      REAL*8 N,NA,MI,MACH,NDOT,MDOT,NG
      EXTERNAL GRAD,GEX

      DIMENSION RWORK(500),IWORK(50),ATOL(13)
      COMMON/ODE/NR,JT,NEQ,ITOL,RTOL,ATOL,ITASK,IOPT,LRW,RWORK,
     &IWORK,LIW

      COMMON/ECR/UI,UEA,UEI,UA,U,N,WPAR,WPRP,NA,A,AA,
     &DUDZ,DNDZ,DWPARDZ,DWPRPDZ,DNADZ,NNN,DADZ,BB,AWAVE,DN,
     &SI,SD,FD,FEA,FIA,FIN,PECR,FL,MI,MACH,FDRAG,B,DBDZ,
     &PIN,NG,WPRPG,WPARG,MDOT,EMACH,NDOT,ZSTAG,QPAR,QPRP,ISTATE,
     &ZWAVE,ZECR,BWAVE,CRNT,NHEAT,QHEAT,NPRES,PHEAT,TANKN

      LSODAR control parameters are defined. The meaning are described
      in the LSODAR documentation. Sometimes LSODAR will return an error
      which can be corrected by changing the appropriate control parameter.
      If an error occurs (ISTATE < 0), check the definition of the ISTATE
      value in the documentation and try the reccomended action.

      NR=1
      JT=2
      NEQ=13
      LIW=20+NEQ
      ITOL=2
      ITASK=1
      ISTATE=1
      IOPT=1
      RTOL=1.0D-12
      ATOL(1)=1.0D-9
      ATOL(2)=1.0D+4
      ATOL(3)=1.0D-30
      ATOL(4)=1.0D-30
      ATOL(5)=1.0D+5
      ATOL(6)=1.0D+2
      ATOL(7)=1.0D+2
      ATOL(8)=1.0D+2
      ATOL(9)=1.0D+2
      ATOL(10)=1.0D+2
      ATOL(11)=1.0D+2
      ATOL(12)=1.0D+2
      ATOL(13)=1.0D+2
      LRW = 22 + NEQ*(NEQ+11) + 3*NR

      DO 930 J=1,LRW
        RWORK(J)=0.0
30    CONTINUE

      DO 935 K=1,LIW
        IWORK(K)=0
35    CONTINUE

      IWORK(6)=400000
      IWORK(7)=2
      RETURN
      END
```

```
      SUBROUTINE NOZZLE

      IMPLICIT REAL*8(A-H,O-Z)
      REAL*8 N,NA,ME,MI,MACH,NDOT,MDOT,NG,JROOT
      EXTERNAL GRAD,GEX,LSODARPREP

      DIMENSION F(13),DF(13),RWORK(500),IWORK(50),ATOL(13)

      COMMON/ECR/UI,UEA,UEI,UA,U,N,WPAR,WPRP,NA,A,AA,
     &DUDZ,DNDZ,DWPARDZ,DWPRPDZ,DNADZ,NNN,DADZ,BB,AWAVE,DN,
     &SI,SD,FD,FEA,FIA,FIN,PECR,FL,MI,MACH,FDRAG,B,DBDZ,
     &PIN,NG,WPRPG,WPARG,MDOT,EMACH,NDOT,ZSTAG,QPAR,QPRP,ISTATE,
     &ZWAVE,ZECR,BWAVE,CRNT,NHEAT,QHEAT,NPRES,PHEAT,TANKN

      COMMON/ODE/NR,JT,NEQ,ITOL,RTOL,ATOL,ITASK,IOPT,LRW,RWORK,
     &IWORK,LIW

      DATA EC,AMU,PI,ME,ZWAVE
     &/1.6021E-19,1.67265E-27,3.1415927,9.1095E-31,0.06/

      WRITE(6,*)''
      WRITE(6,*)''
      WRITE(6,*)''
      WRITE(6,*)'NOZZLE:'

      CALL LSODARPREP

      Now we set up a few small things and call GRAD once to initialize
      the array DF and ensures that GRAD works OK.  The output is to let
      the user know things went well.

      WRITE(6,*)'Now the results of running LSODAR are displyed:'
      WRITE(6,836)
836   FORMAT('      Z           U           N          WPRP          WPAR'
     & ,'         NA         MACH           B         PECR           SI',
     & '         SD        QHEAT        WORK           FL       PHEAT',
     & '         PCLOS         PWALL     SOURCE          AREA       RMNET'
     & ,'      RWPARNET    RWPRPNET      RFNET      PNET')

      PHEAT=-PHEAT
      PCLOS=0.0
      PWALL=0.0
      SOURCE=0.0
      WORK=0.0
      WPARFLUX=0.0
      WPRPFLUX=0.0
      FFLUX=0.0

      Z=ZSTAG
      DELTAZ=5.0E-3
      F(1)=U
      F(2)=N
      F(3)=WPAR
      F(4)=WPRP
      F(5)=NA
      F(6)=PHEAT
      F(7)=PCLOS
      F(8)=PWALL
```

```
      F(9)=SOURCE
      F(10)=WORK
      F(11)=WPARFLUX
      F(12)=WPRPFLUX
      F(13)=FFLUX

      CALL GRAD(NEQ,Z,F,DF)

      IF(NHEAT. EQ. 1)THEN
        MACH=((MI*U**2)/(2.0*WPAR))**0.5
      ELSE
        MACH=((MI*U**2)/(6.0*WPAR))**0.5
      ENDIF

      B=1.2567E-7*CRNT/(0.04+Z**2)**1.5
      A=AWAVE*BWAVE/B
      VOLTS = -0.5*MI*U**2/EC

      WRITE(6,844)Z,U,N,WPRP,WPAR,NA,MACH,B,
     &PECR,SI,SD,QHEAT,WORK,FL,PHEAT,PCLOS,PWALL,SOURCE,A

      WRITE(20,845)Z,U,N,WPRP,WPAR,NA,MACH,B,PECR,VOLTS

844   FORMAT(19(1P,E10.3,2X))
845   FORMAT(10(1P,E10.3,2X))

      Z2 = Z + DELTAZ
70    DO 880 IOUT = 1,100

      OLDMACH=MACH
      CALL LSODAR(GRAD,NEQ,F,Z,Z2,ITOL,RTOL,ATOL,ITASK,
     &            ISTATE,IOPT,RWORK,LRW,IWORK,LIW,JAC,JT,
     &            GEX,NR,JROOT)

      U=F(1)
      N=F(2)
      WPAR=F(3)
      WPRP=F(4)
      NA=F(5)
      PHEAT=F(6)
      PCLOS=F(7)
      PWALL=F(8)
      SOURCE=F(9)
      WORK=F(10)
      WPARFLUX=F(11)
      WPRPFLUX=F(12)
      FFLUX=F(13)

      B=1.2567E-7*CRNT/(0.04+Z**2)**1.5

      IF(NHEAT. EQ. 1)THEN
        MACH=((MI*U**2)/(2.0*WPAR))**0.5
      ELSE
        MACH=((MI*U**2)/(6.0*WPAR))**0.5
      ENDIF

      A=AWAVE*BWAVE/B
      FLUX = U*N*A
```

```
      PT = (0.50*MI*U**2 + 3*WPAR + WPRP)*FLUX

      ETAU = FLUX/NDOT
      PNET = PIN - PT + PCLOS + PWALL + WORK
      RMNET = (FLUX+NA*UA*A)/NDOT
      RWPARNET = WPARFLUX/(FLUX*WPAR)
      RWPRPNET = WPRPFLUX/(FLUX*WPRP)
      RFNET = FFLUX/(FLUX*MI*U)
      VOLTS = -0.5*MI*U**2/EC

      WRITE(6,875)Z,U,N,WPRP,WPAR,NA,MACH,B,PECR,SI,SD,QHEAT,WORK,
     &FL,PHEAT,PCLOS,PWALL,SOURCE,A,RMNET,RWPARNET,RWPRPNET,RFNET,PNET

      WRITE(20,876)Z,U,N,WPRP,WPAR,NA,MACH,B,PECR,VOLTS

875   FORMAT(24(1P,E10.3,2X))
876   FORMAT(10(1P,E10.3,2X))

      IF(ISTATE .EQ. 3)THEN
          IF(MACH. GE. 1.1)THEN
          IF(NHEAT. EQ. 1)GOTO 882
        ENDIF
        CALL LSODARPREP
        DELTAZ=10.0*DELTAZ
        U=U*1.01
        WPAR=WPAR
        N=N/1.01
        F(1)=U
        F(2)=N
        F(3)=WPAR
      ENDIF

        IF(MACH. GE. 10.0)GOTO882

80    Z2 = Z + DELTAZ

82    FLUX = U*N*A
      PT = (0.50*MI*U**2 + 3*WPAR + WPRP)*FLUX
      ETAU = FLUX/NDOT
      PNET = PIN - PT + PCLOS + PWALL + WORK

      MDOT=MDOT/2.9743D-8


      WRITE(6,*)'PT',PT
      WRITE(6,*)'ETAU',ETAU
      WRITE(6,*)'FLUX',FLUX
      WRITE(6,*)'PNET',PNET

      WRITE(20,*)'MDOT =',MDOT
      WRITE(20,*)'PIN  =',PIN
      WRITE(20,*)' PT  =',PT
      WRITE(20,*)'ETAU =',ETAU


      RETURN
      END
```

```
      SUBROUTINE UPSTREAM

      IMPLICIT REAL*8(A-H,O-Z)
      REAL*8 N,NA,ME,MI,MACH,NDOT,MDOT,NG,JROOT
      EXTERNAL GRAD,GEX,LSODARPREP

      DIMENSION F(13),DF(13),RWORK(500),IWORK(50),ATOL(13)

      COMMON/ECR/UI,UEA,UEI,UA,U,N,WPAR,WPRP,NA,A,AA,
     &DUDZ,DNDZ,DWPARDZ,DWPRPDZ,DNADZ,NNN,DADZ,BB,AWAVE,DN,
     &SI,SD,FD,FEA,FIA,FIN,PECR,FL,MI,MACH,FDRAG,B,DBDZ,
     &PIN,NG,WPRPG,WPARG,MDOT,EMACH,NDOT,ZSTAG,QPAR,QPRP,ISTATE,
     &ZWAVE,ZECR,BWAVE,CRNT,NHEAT,QHEAT,NPRES,PHEAT,TANKN

      COMMON/ODE/NR,JT,NEQ,ITOL,RTOL,ATOL,ITASK,IOPT,LRW,RWORK,
     &IWORK,LIW

      DATA EC,AMU,PI,ME,ZWAVE
     &/1.6021E-19,1.67265E-27,3.1415927,9.1095E-31,0.06/

      WRITE(6,*)''
      WRITE(6,*)'UPSTREAM FLOW:'

      CALL LSODARPREP

      WRITE(6,*)'Now the results of running LSODAR are displyed:'
      WRITE(6,636)
636   FORMAT('      Z           U           N          WPRP          WPAR'
     & ,'         NA         MACH          B         PECR          SI',
     & '         SD        QHEAT        WORK          FL       PHEAT',
     & '         PCLOS         PWALL     SOURCE         AREA       RMNET'
     & ,'      RWPARNET    RWPRPNET     RFNET      PNET')

      PHEAT=0.0
      PCLOS=0.0
      PWALL=0.0
      SOURCE=0.0
      WORK=0.0
      WPARFLUX=0.0
      WPRPFLUX=0.0
      FFLUX=0.0
      Z=ZSTAG
      DELTAZ=-1.0E-3
      F(1)=U
      F(2)=N
      F(3)=WPAR
      F(4)=WPRP
      F(5)=NA
      F(6)=-PHEAT
      F(7)=PCLOS
      F(8)=PWALL
      F(9)=SOURCE
      F(10)=WORK
      F(11)=WPARFLUX
      F(12)=WPRPFLUX
      F(13)=FFLUX

      CALL GRAD(NEQ,Z,F,DF)
```

```
      MACH=((MI*U**2)/(2.0*WPAR))**0.5
      B=1.2567E-7*CRNT/(0.04+Z**2)**1.5
      A=AWAVE*BWAVE/B

      WRITE(6,644)Z,U,N,WPRP,WPAR,NA,MACH,B,
     &PECR,SI,SD,QHEAT,WORK,FL,PHEAT,PCLOS,PWALL,SOURCE,A
644   FORMAT(19(1P,E10.3,2X))

      Z2 = Z + DELTAZ
680   DO 680 IOUT = 1,50

      OLDMACH=MACH
      CALL LSODAR(GRAD,NEQ,F,Z,Z2,ITOL,RTOL,ATOL,ITASK,
     &            ISTATE,IOPT,RWORK,LRW,IWORK,LIW,JAC,JT,
     &             GEX,NR,JROOT)

      U=F(1)
      N=F(2)
      WPAR=F(3)
      WPRP=F(4)
      NA=F(5)
      PHEAT=-F(6)
      PCLOS=F(7)
      PWALL=F(8)
      SOURCE=F(9)
      WORK=F(10)
      WPARFLUX=F(11)
      WPRPFLUX=F(12)
      FFLUX=F(13)
      B=1.2567E-7*CRNT/(0.04+Z**2)**1.5
      MACH=((MI*U**2)/(2.0*WPAR))**0.5
      A=AWAVE*BWAVE/B
      FLUX = U*N*A
      PT = (0.50*MI*U**2 + WPAR + WPRP)*FLUX
      ETAU = FLUX/NDOT
      PNET = PIN - PT + PCLOS + PWALL + WORK
      RMNET = (FLUX+NA*UA*A)/NDOT
      RWPARNET = WPARFLUX/(FLUX*WPAR)
      RWPRPNET = WPRPFLUX/(FLUX*WPRP)
      RFNET = FFLUX/(FLUX*MI*U)
      VOLTS = -0.5*MI*U**2/EC

      WRITE(6,675)Z,U,N,WPRP,WPAR,NA,MACH,B,PECR,SI,SD,QHEAT,WORK,
     &FL,PHEAT,PCLOS,PWALL,SOURCE,A,RMNET,RWPARNET,RWPRPNET,RFNET,PNET

      WRITE(20,676)Z,U,N,WPRP,WPAR,NA,MACH,B,PECR,VOLTS

675     FORMAT(24(1P,E10.3,2X))
676     FORMAT(10(1P,E10.3,2X))

      IF(ISTATE .EQ. 3) GOTO 682

680   Z2 = Z + DELTAZ
682   FLUX = U*N*A

      RETURN
      END
```

- Coupled ECR Power = 300 watts
- Argon Flow Rate = 12.5 sccm
- Isothermal
- No Vacuum Tank Back Pressure

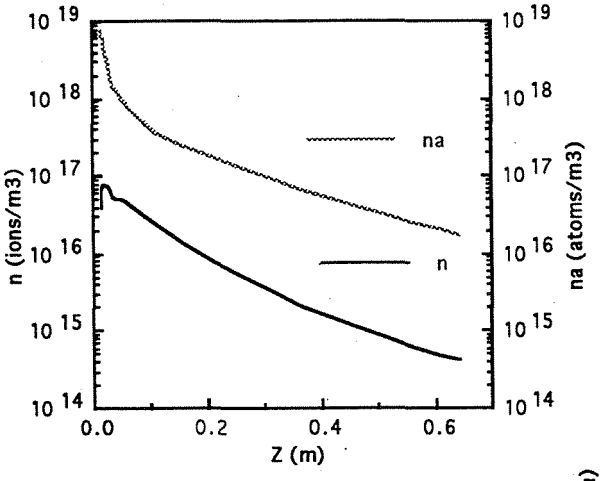

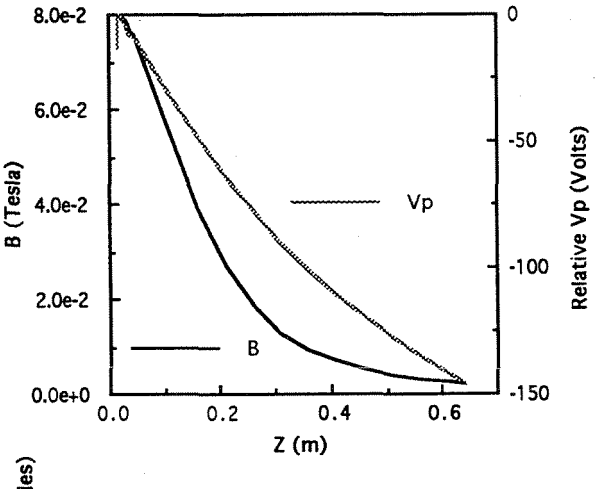

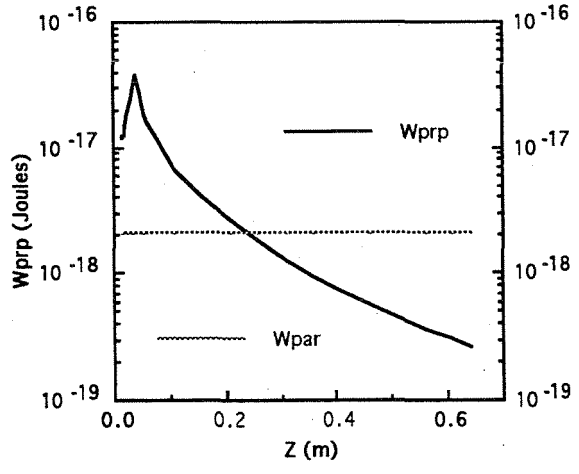

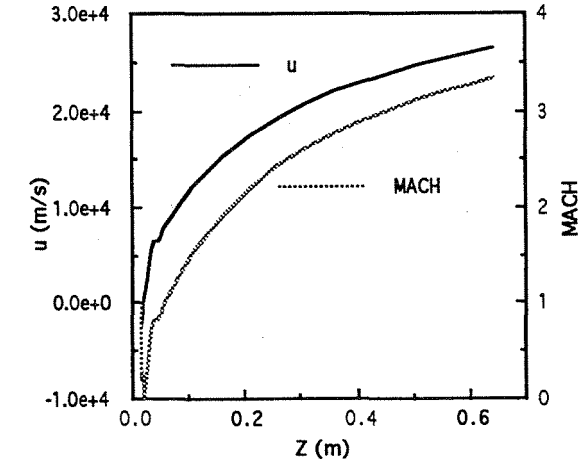

- Coupled ECR Power = 300 watts
- Argon Flow Rate = 12.5 sccm
- Isothermal
- Finite Vacuum Tank Back Pressure

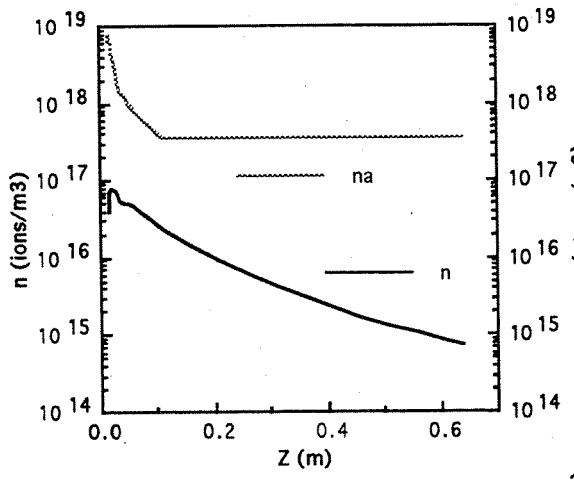

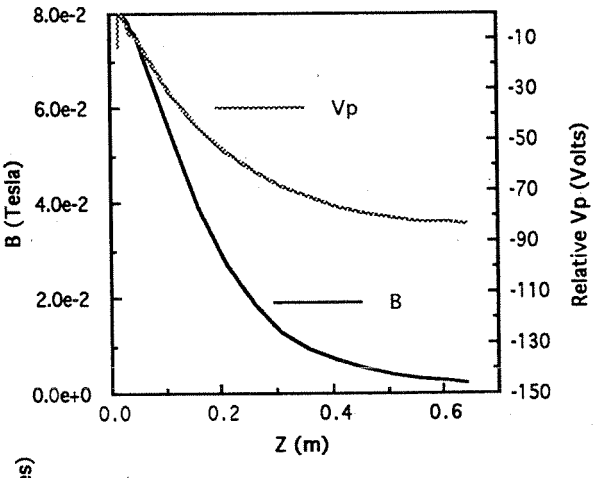

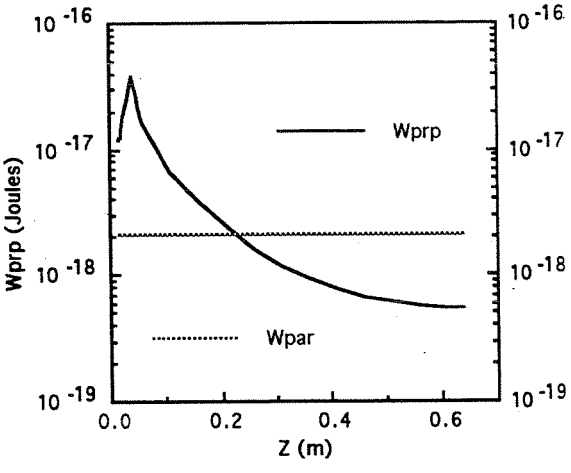

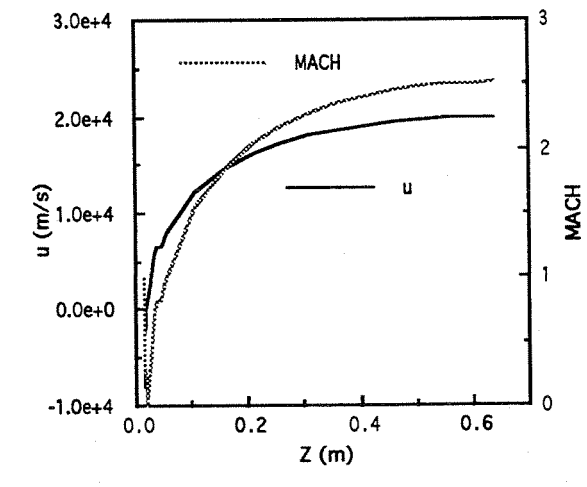

- Coupled ECR Power = 300 watts
- Argon Flow Rate = 15.0 sccm
- Isothermal
- No Vacuum Tank Back Pressure

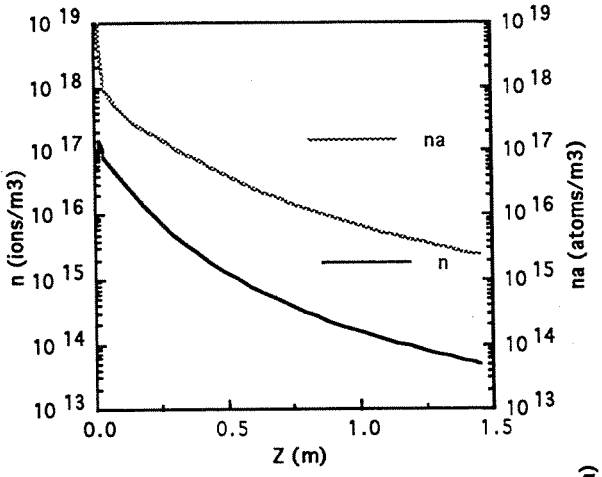

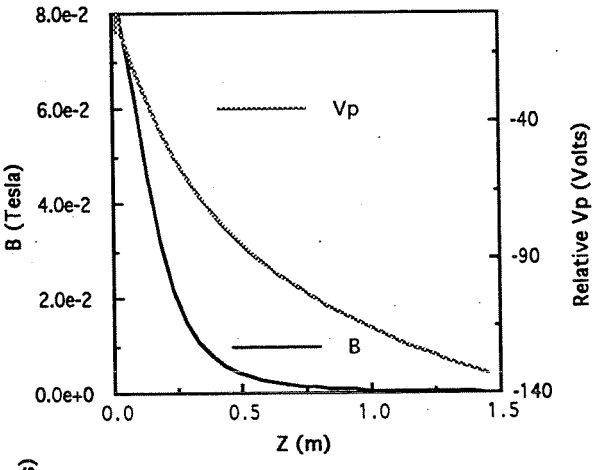

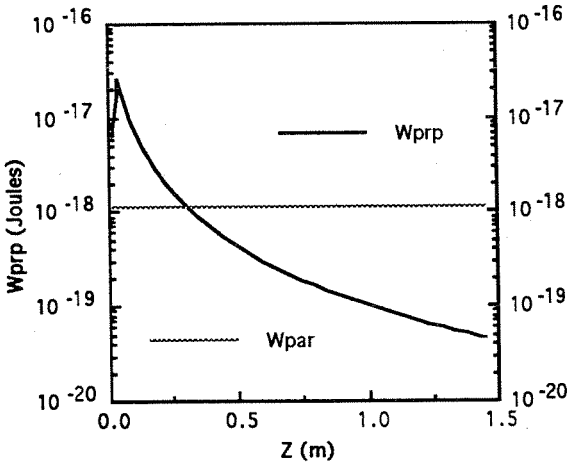

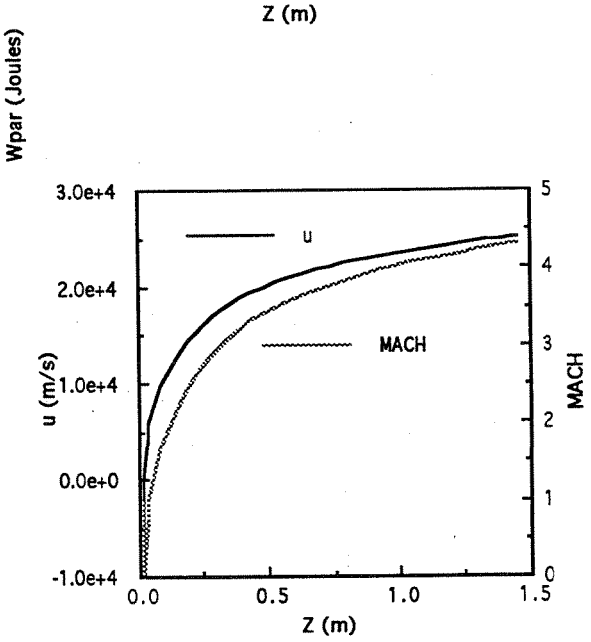

- Coupled ECR Power = 300 watts
- Argon Flow Rate = 15.0 sccm
- Isothermal
- Finite Vacuum Tank Back Pressure

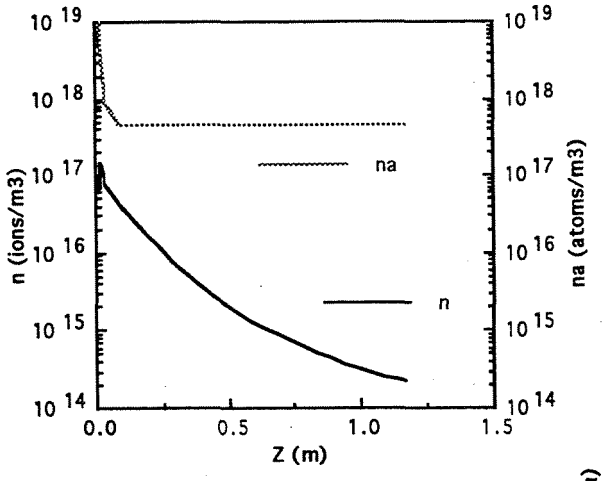

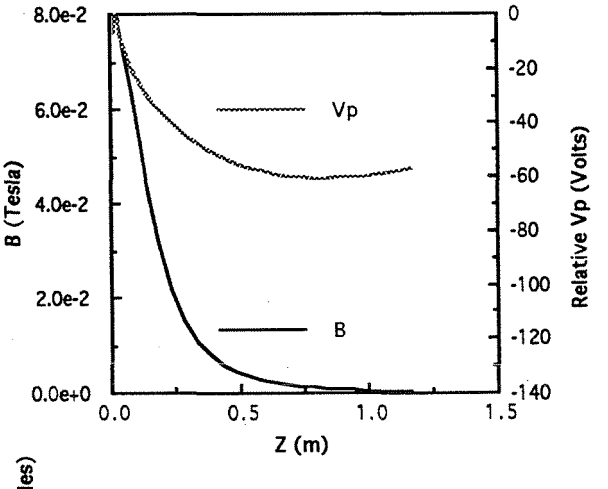

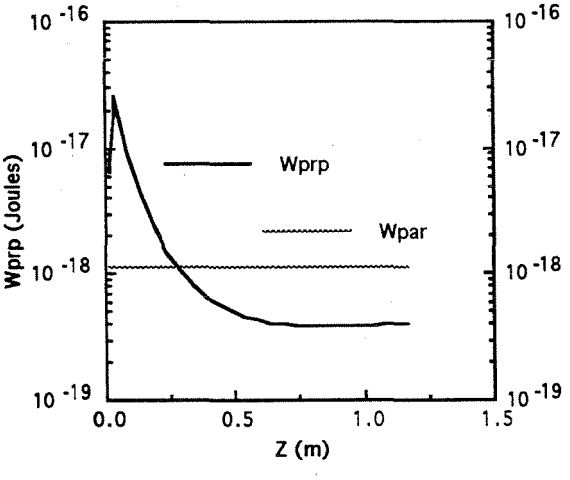

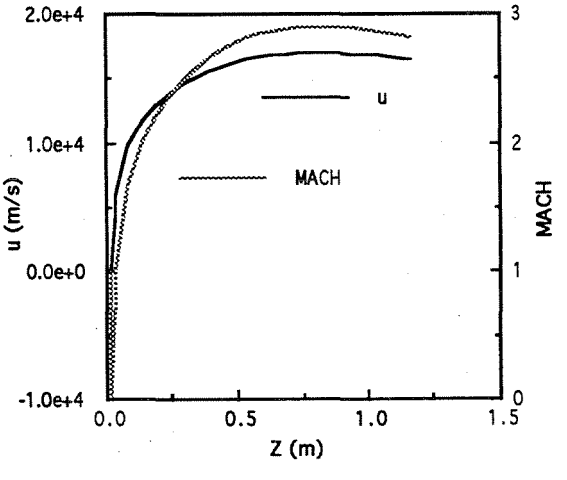

- Coupled ECR Power = 400 watts
- Argon Flow Rate = 16.0 sccm
- Isothermal
- No Vacuum Tank Back Pressure

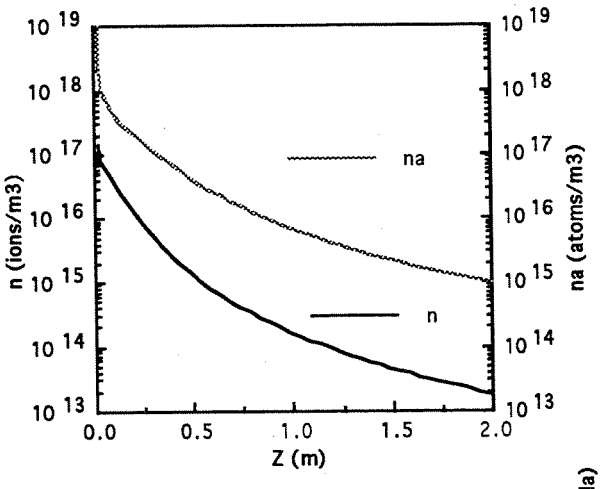

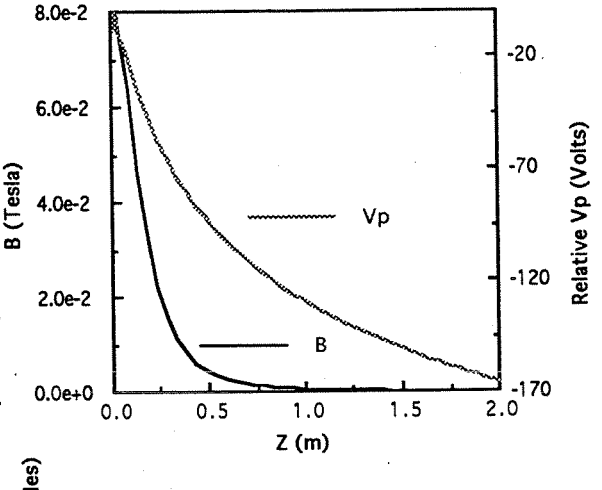

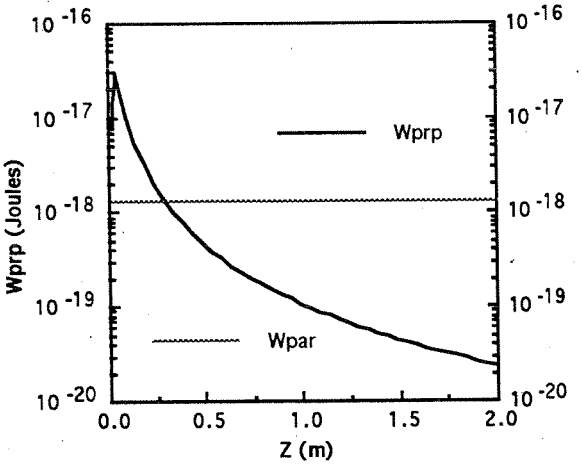

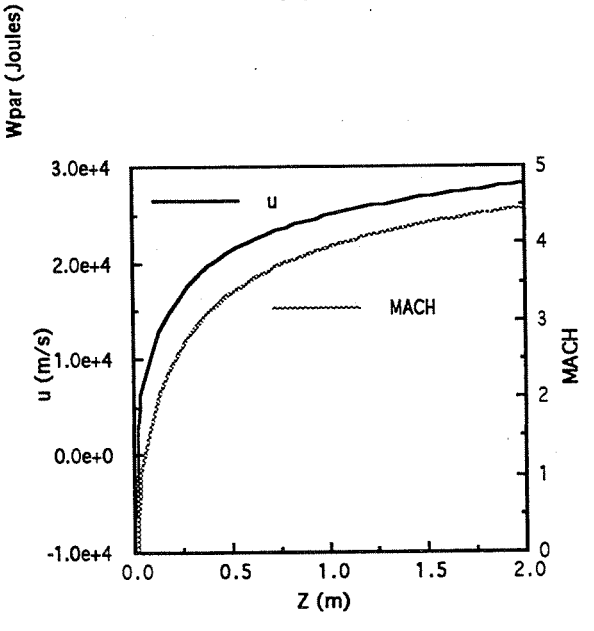

- Coupled ECR Power = 400 watts
- Argon Flow Rate = 16.0 sccm
- Isothermal
- Finite Vacuum Tank Back Pressure

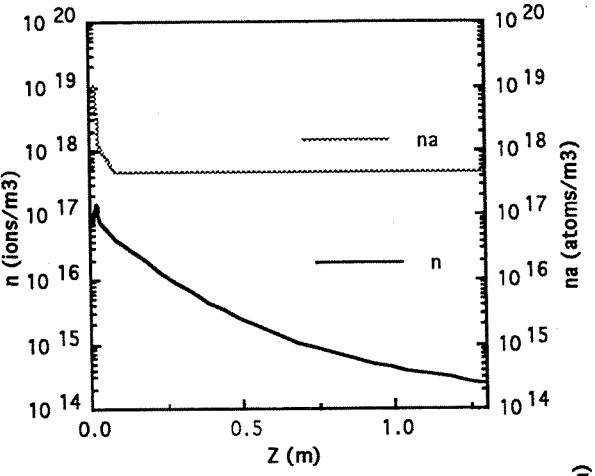

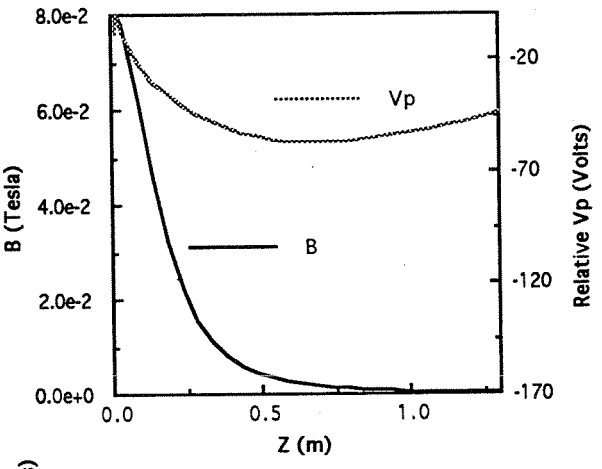

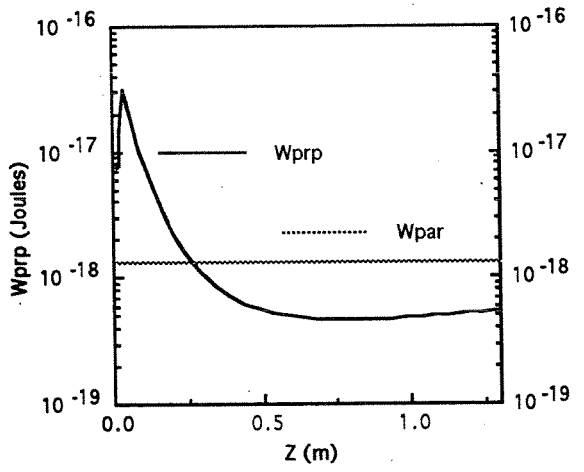

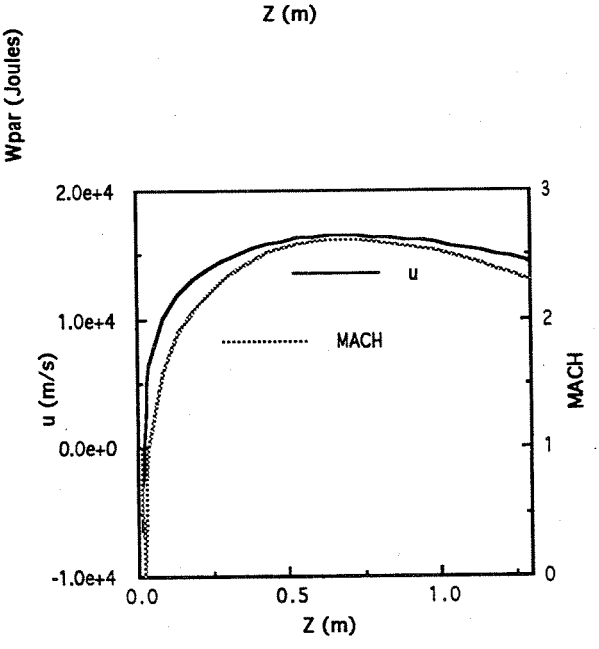

- Coupled ECR Power = 300 watts
- Argon Flow Rate = 17.5 sccm
- Isothermal
- No Vacuum Tank Back Pressure

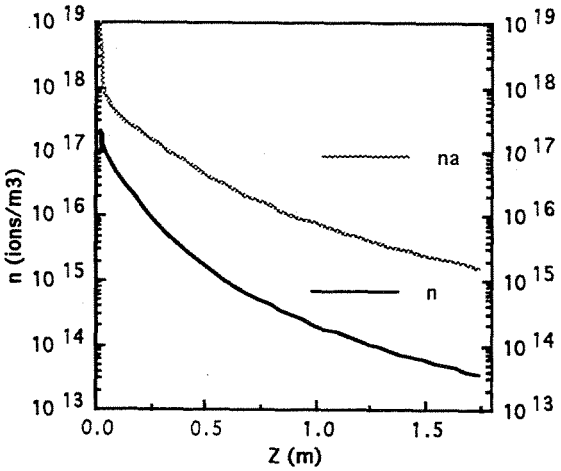

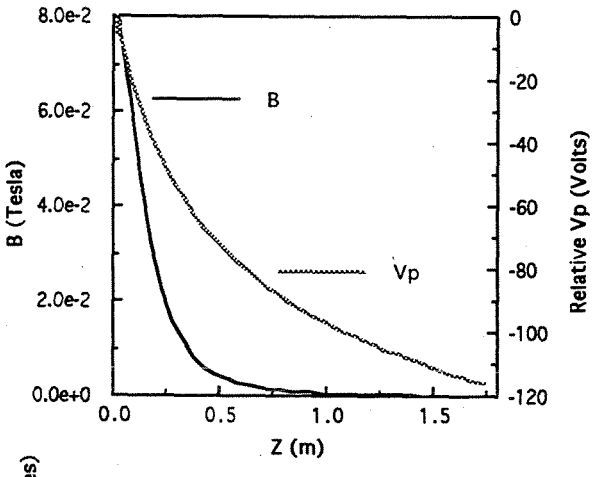

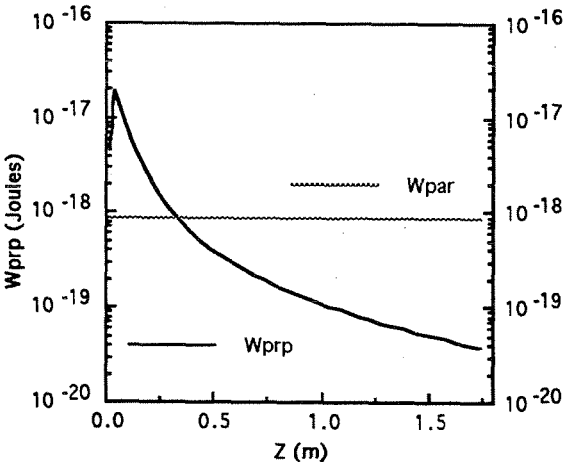

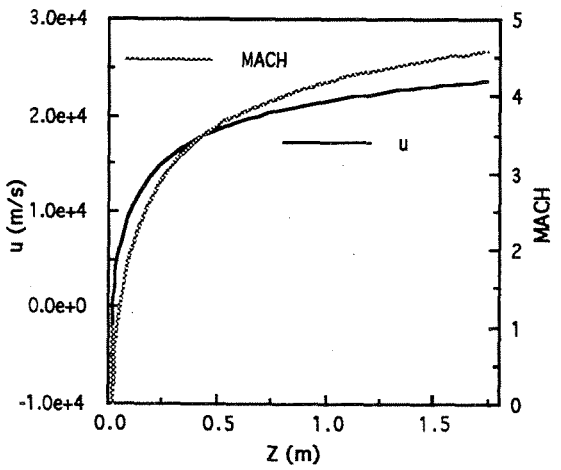

- Coupled ECR Power = 300 watts
- Argon Flow Rate = 17.5 sccm
- Isothermal
- Finite Vacuum Tank Back Pressure

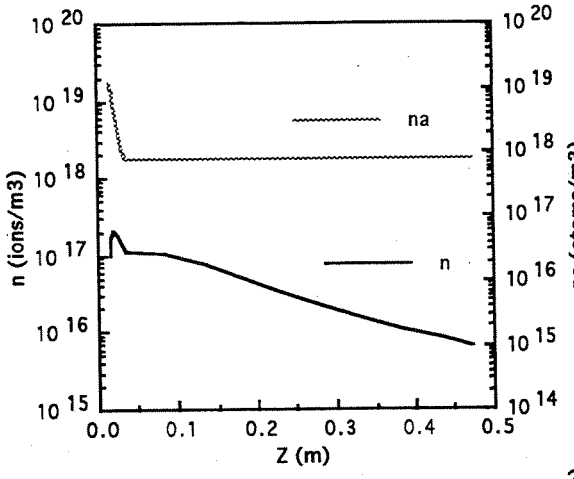

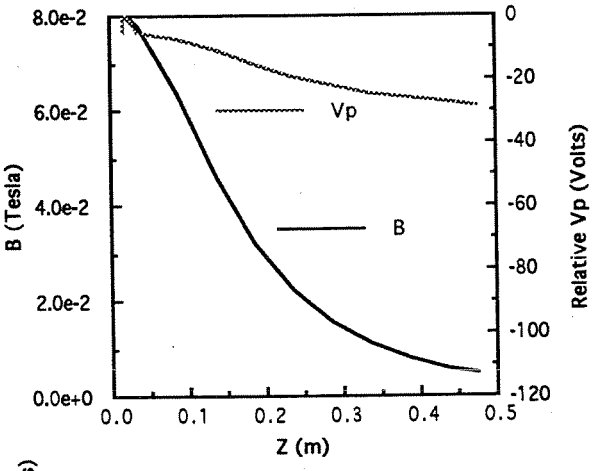

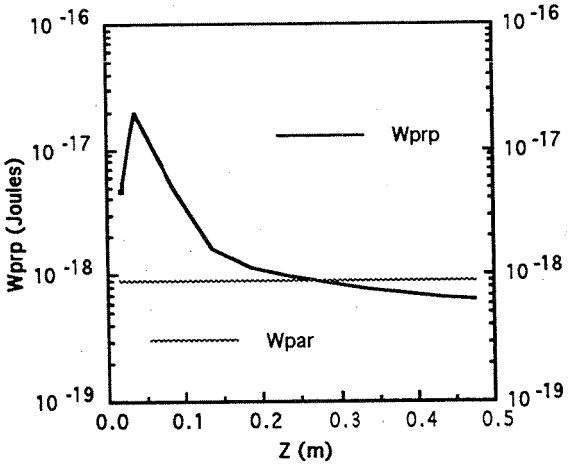

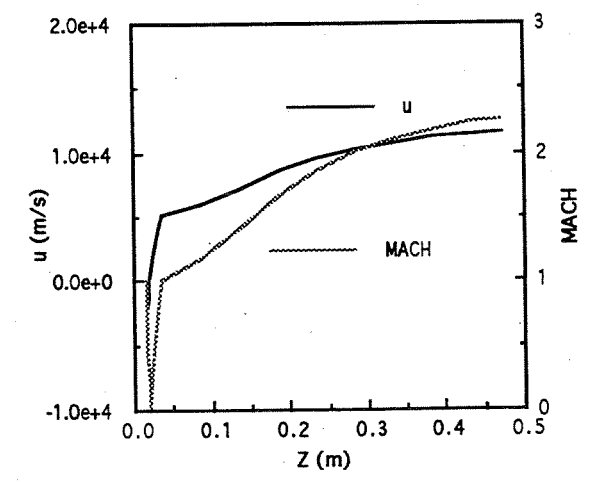

- Coupled ECR Power = 500 watts
- Argon Flow Rate = 17.5 sccm
- Isothermal
- No Vacuum Tank Back Pressure

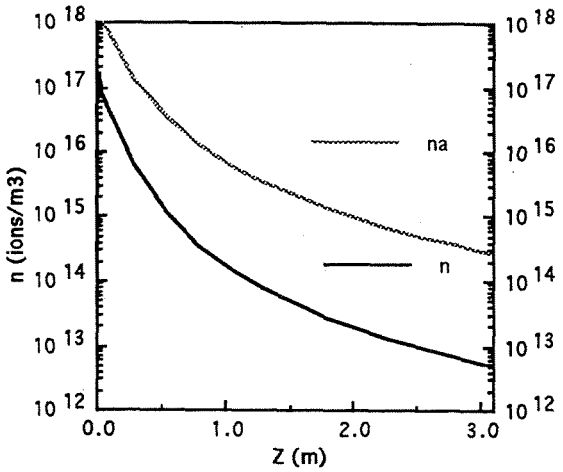

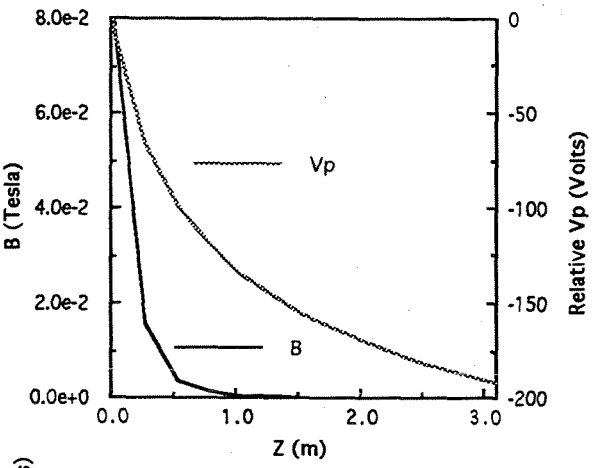

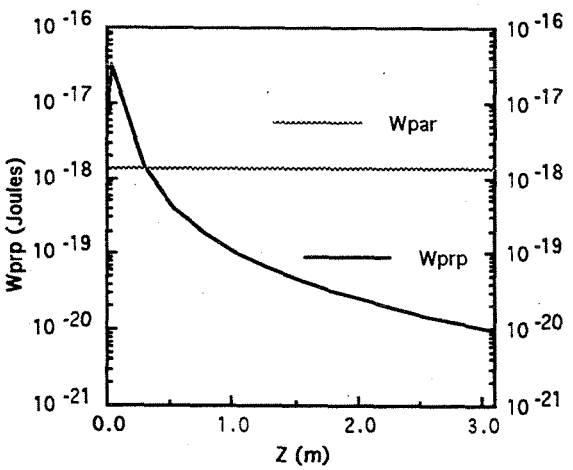

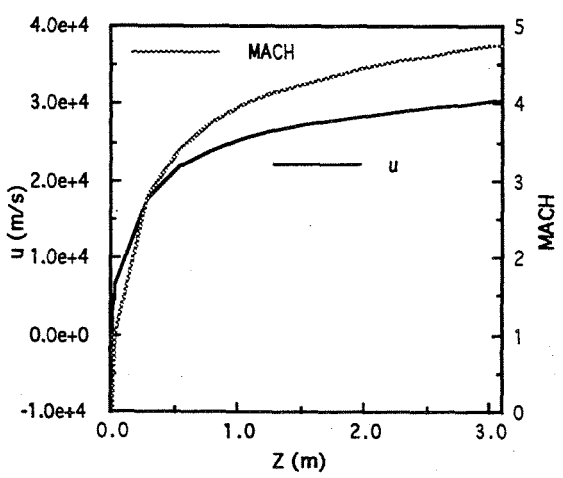

- Coupled ECR Power = 500 watts
- Argon Flow Rate = 17.5 sccm
- Isothermal
- Finite Vacuum Tank Back Pressure

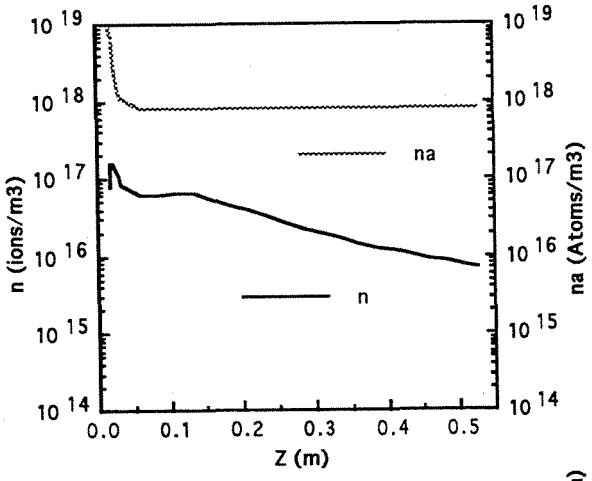

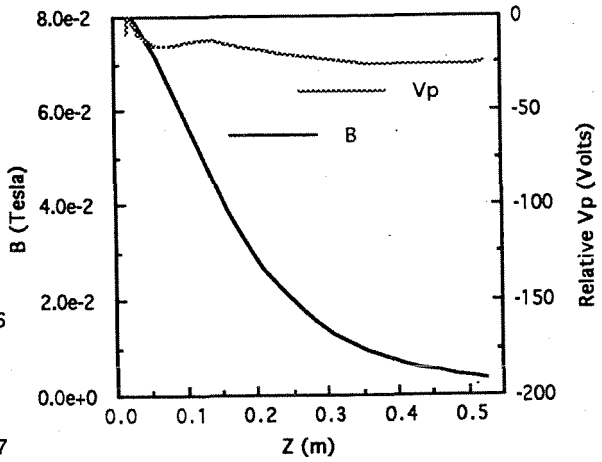

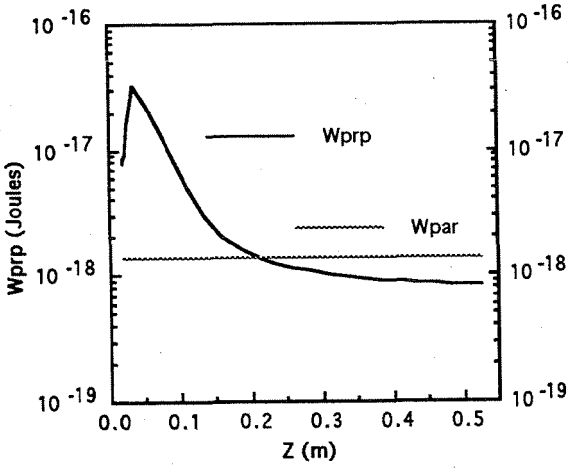

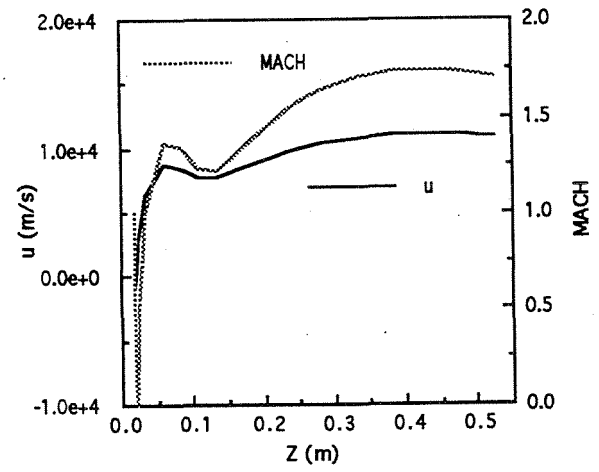

- Coupled ECR Power = 300 watts
- Argon Flow Rate = 20.0 sccm
- Isothermal
- No Vacuum Tank Back Pressure

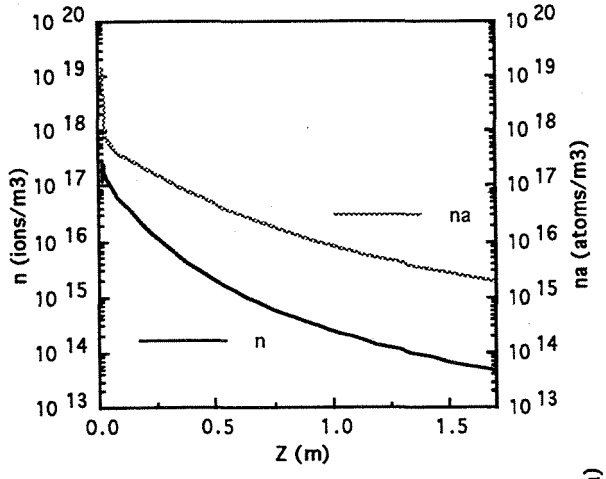

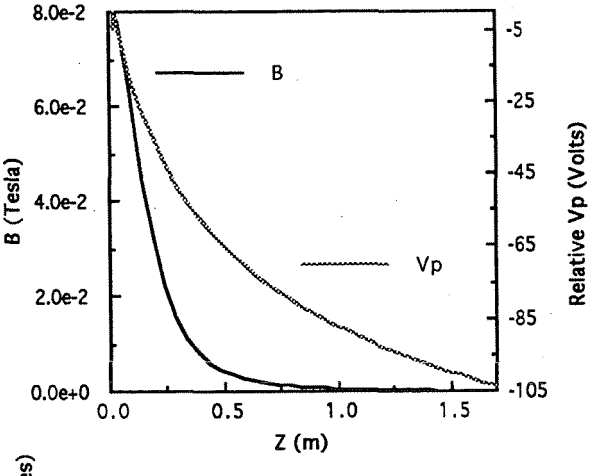

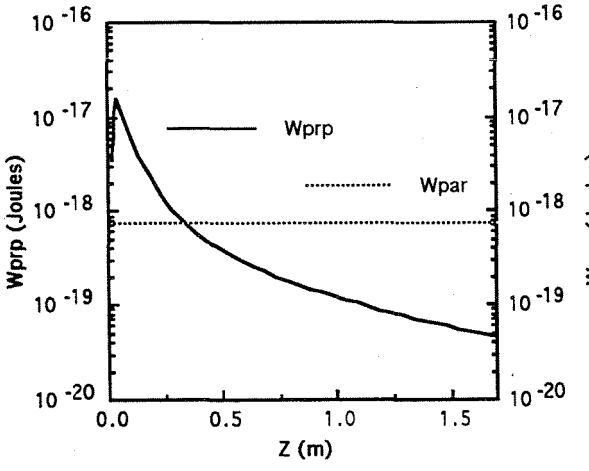

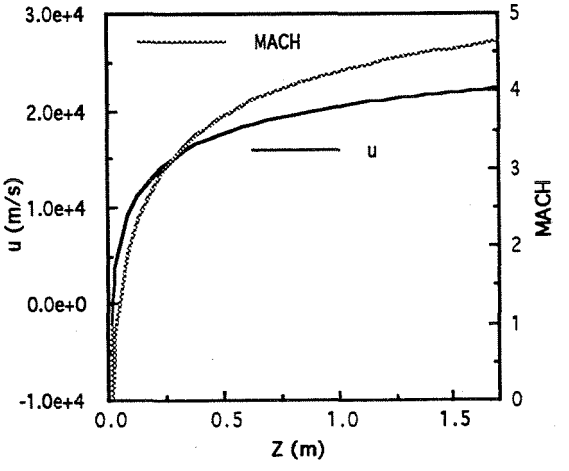

- Coupled ECR Power = 300 watts
- Argon Flow Rate = 20.0 sccm
- Isothermal
- Finite Vacuum Tank Back Pressure

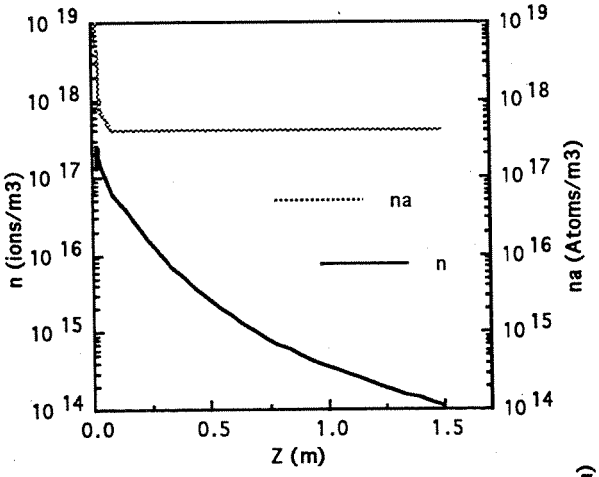

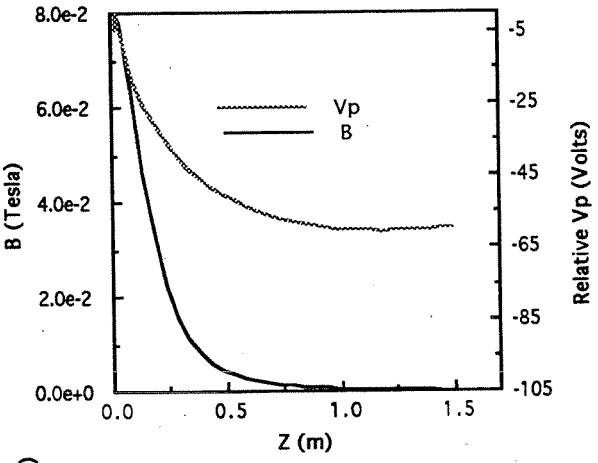

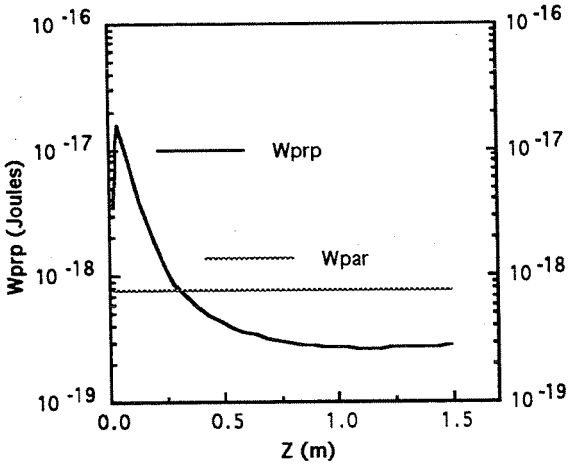

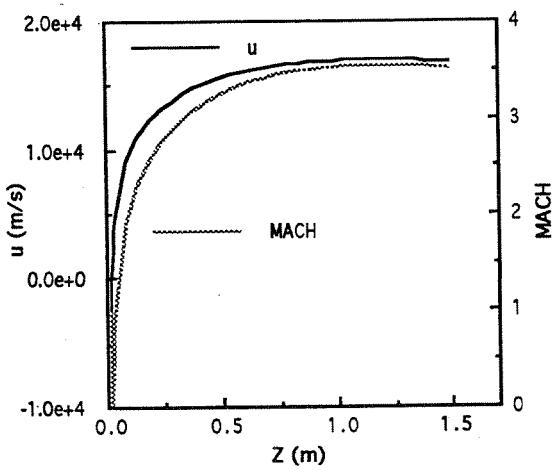

- Coupled ECR Power = 500 watts
- Argon Flow Rate = 20.0 sccm
- Isothermal
- No Vacuum Tank Back Pressure

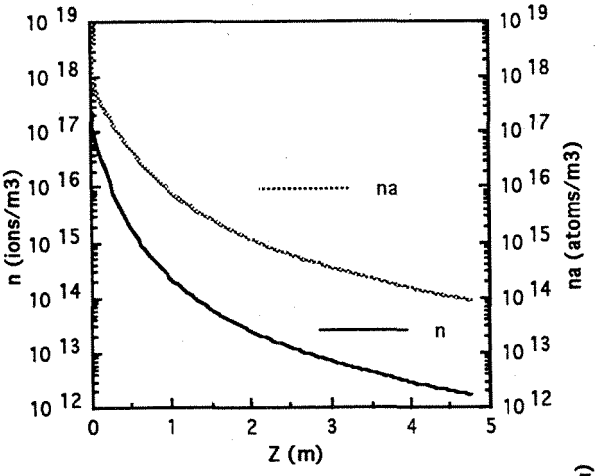

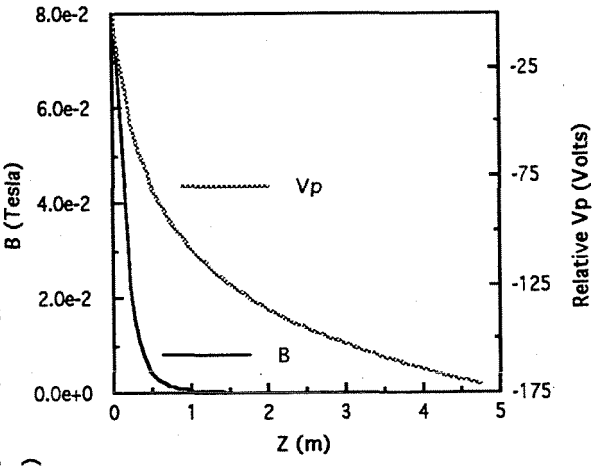

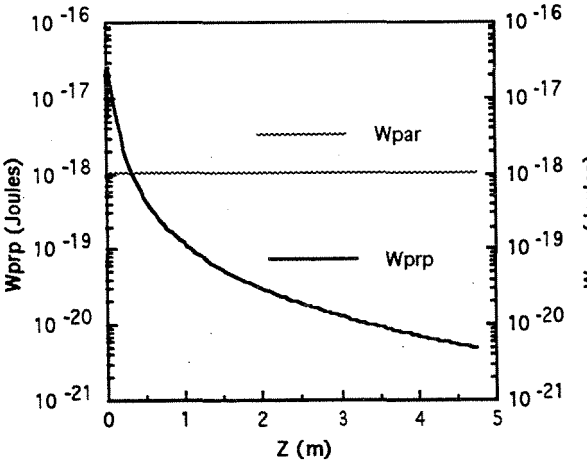

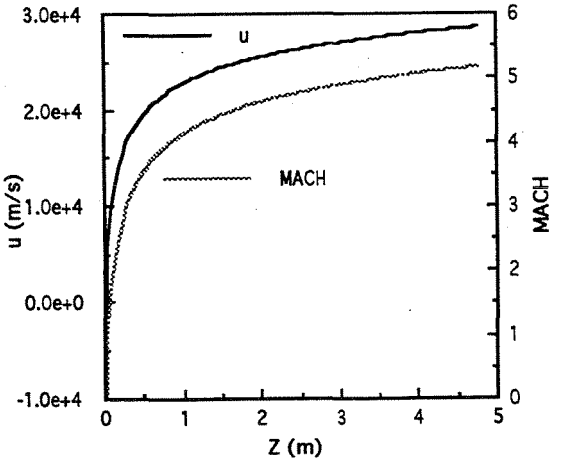

- Coupled ECR Power = 500 watts
- Argon Flow Rate = 20.0 sccm
- Isothermal
- Finite Vacuum Tank Back Pressure

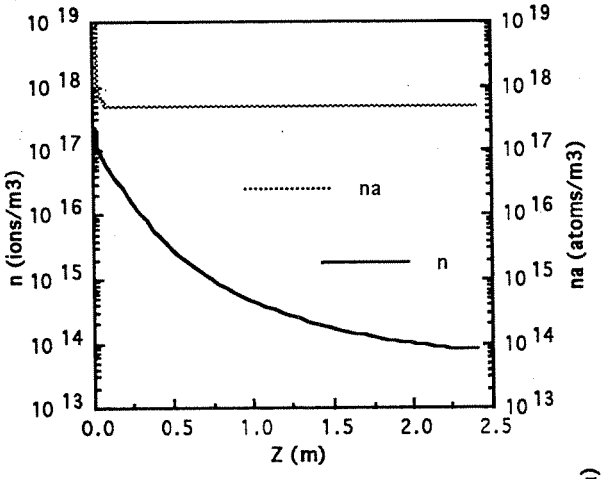

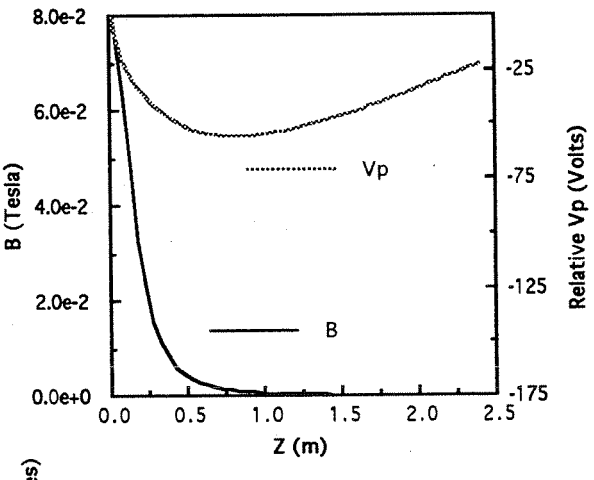

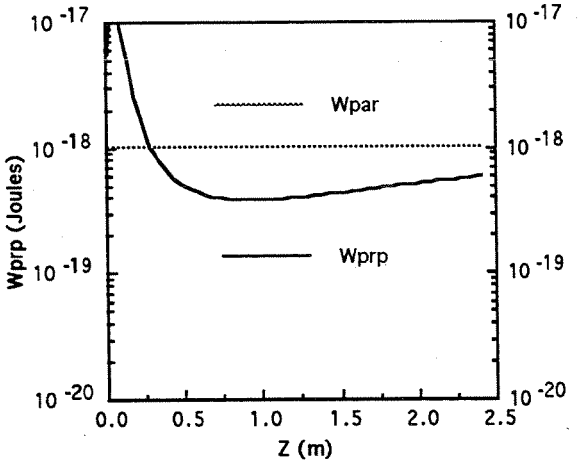

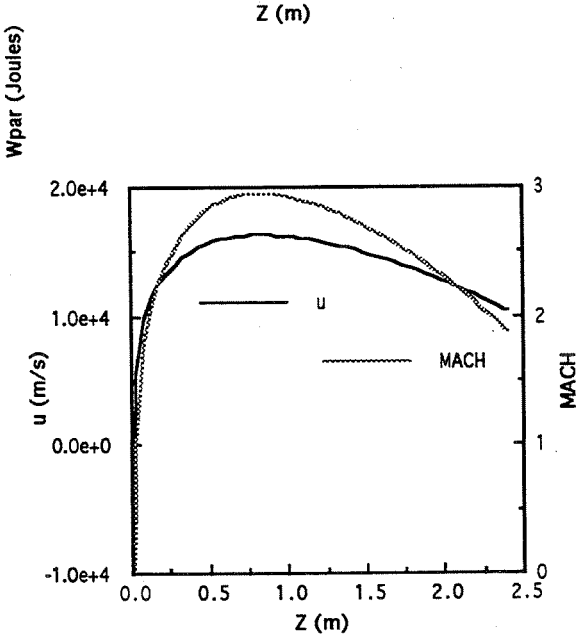

- Coupled ECR Power = 750 watts
- Argon Flow Rate = 20.0 sccm
- Isothermal
- No Vacuum Tank Back Pressure

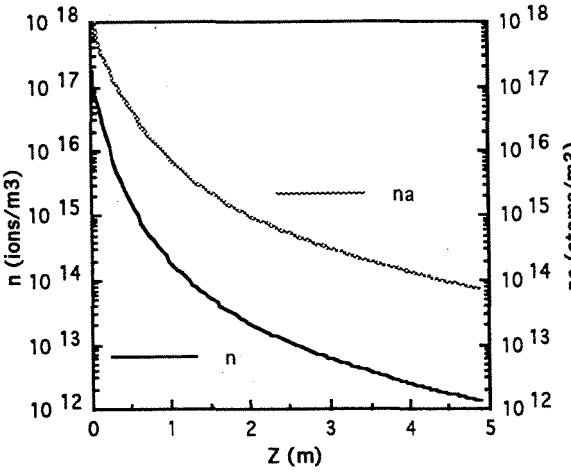

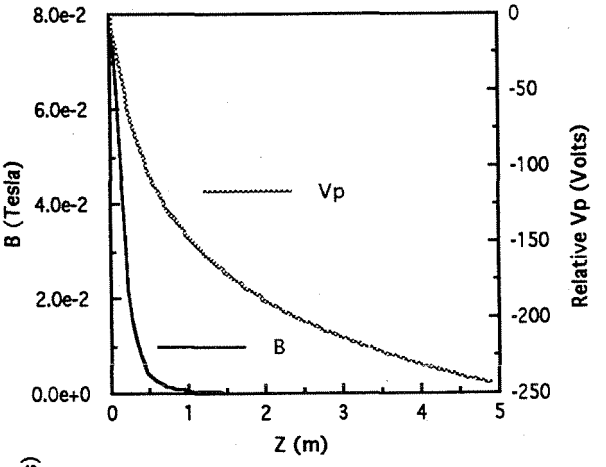

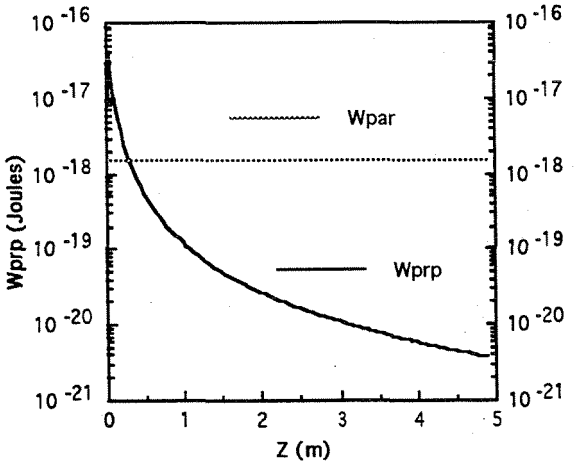

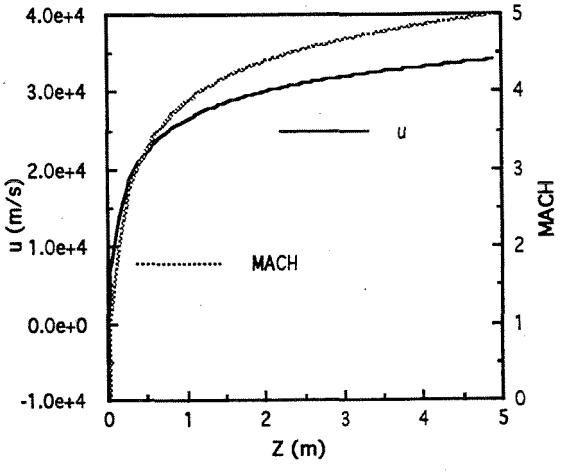

- Coupled ECR Power = 750 watts
- Argon Flow Rate = 20.0 sccm
- Isothermal
- Finite Vacuum Tank Back Pressure

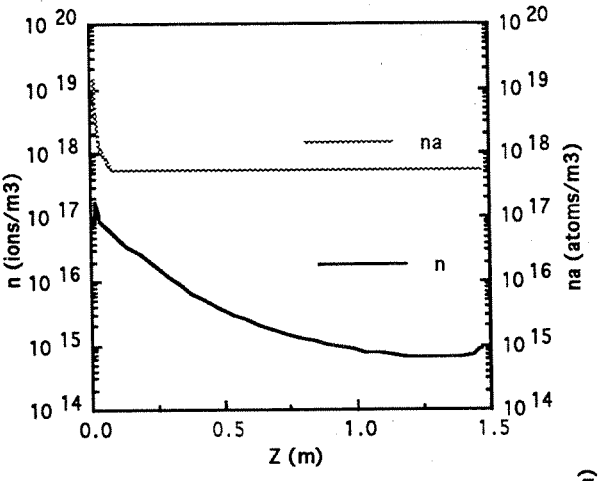

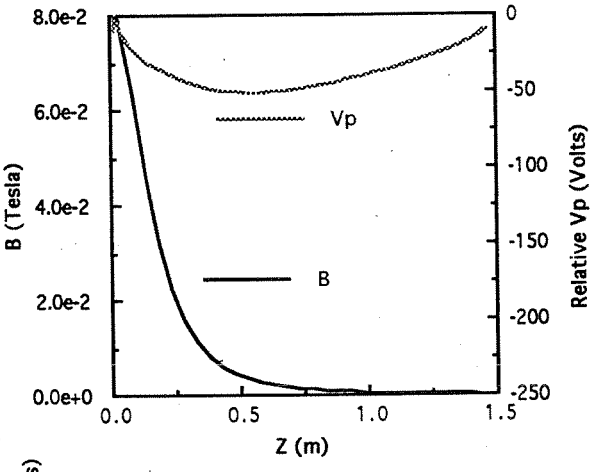

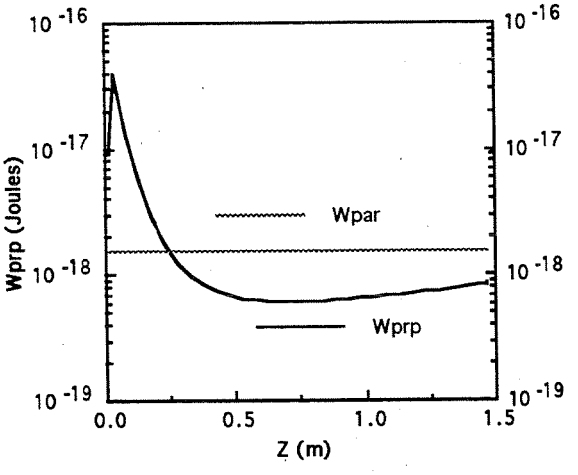

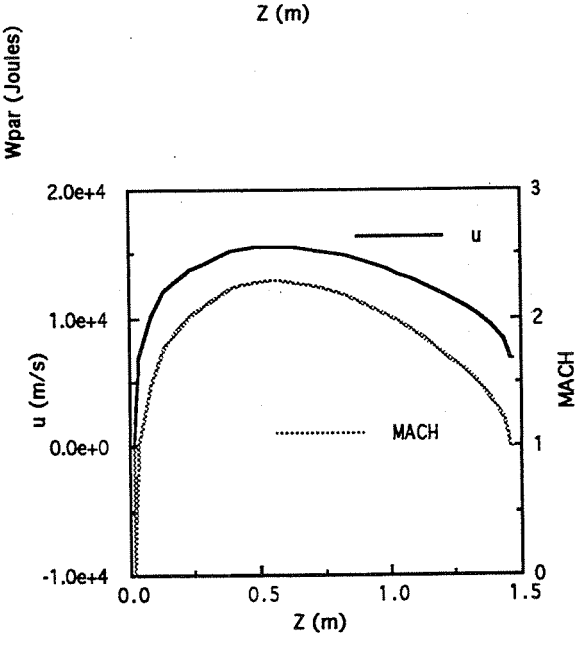

- Coupled ECR Power = 1000 watts
- Argon Flow Rate = 25.0 sccm
- Isothermal
- No Vacuum Tank Back Pressure

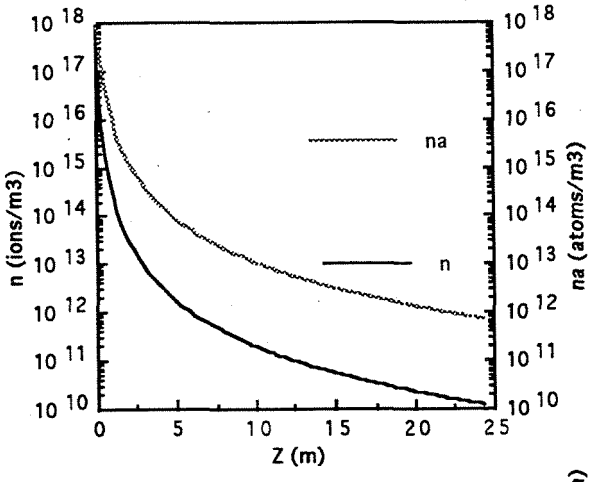

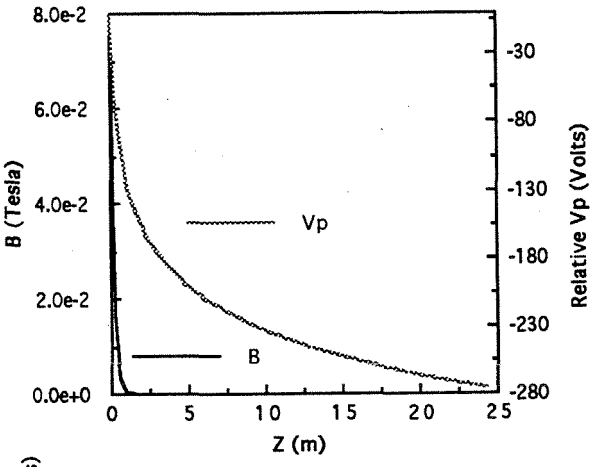

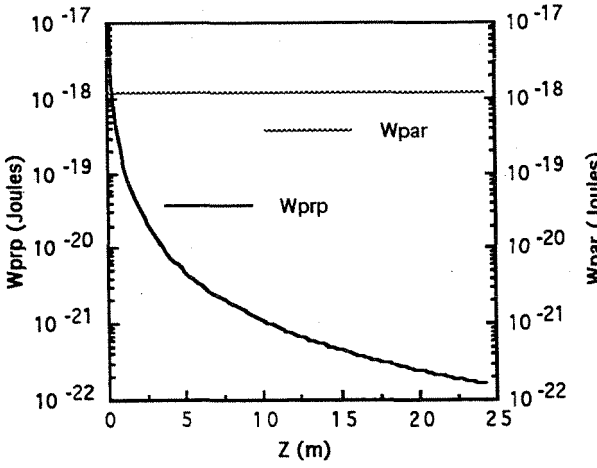

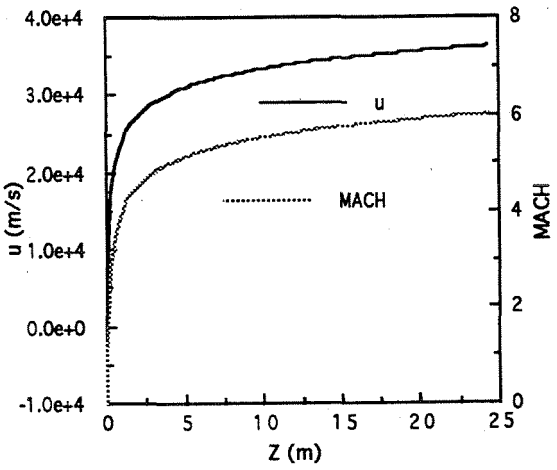

- Coupled ECR Power = 1000 watts
- Argon Flow Rate = 25.0 sccm
- Isothermal
- Finite Vacuum Tank Back Pressure

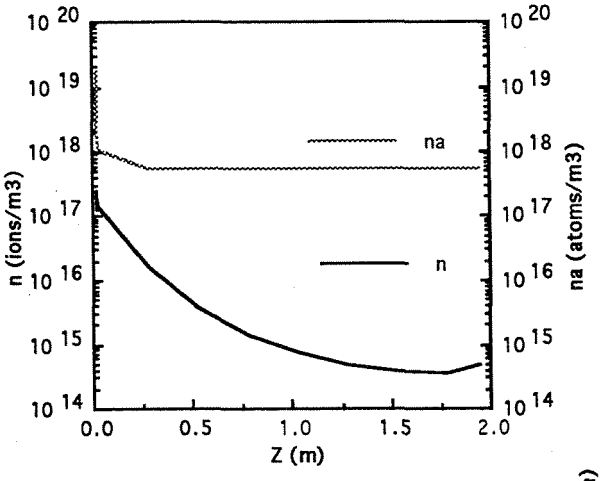

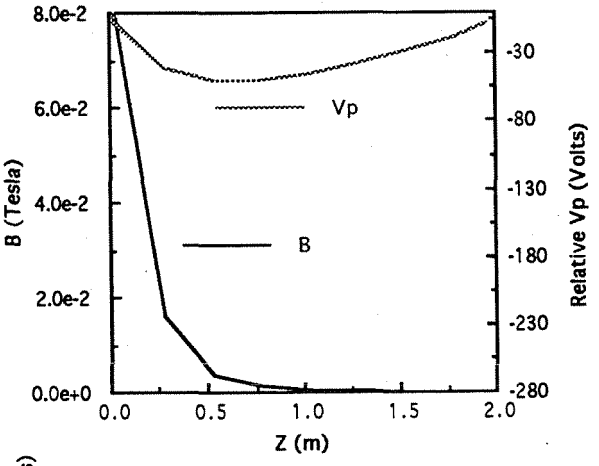

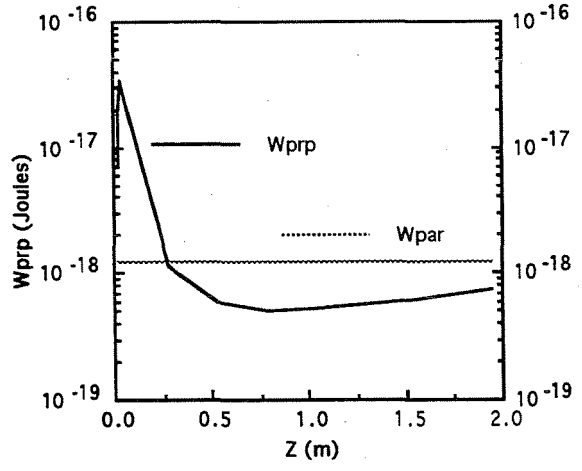

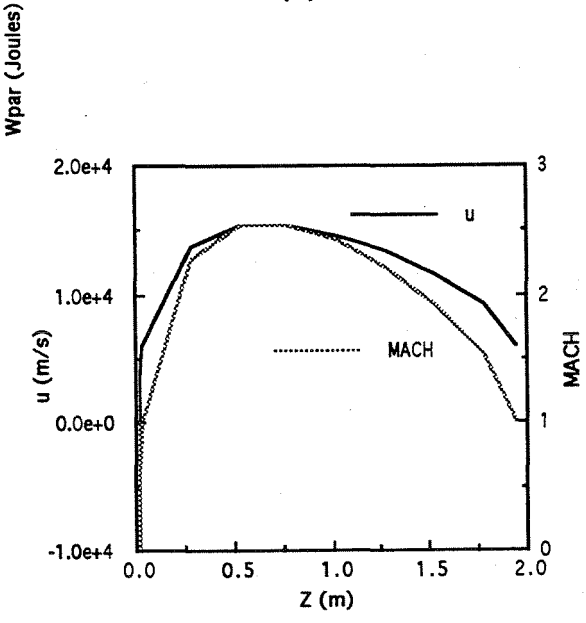

- Coupled ECR Power = 1250 watts
- Argon Flow Rate = 25.0 sccm
- Isothermal
- No Vacuum Tank Back Pressure

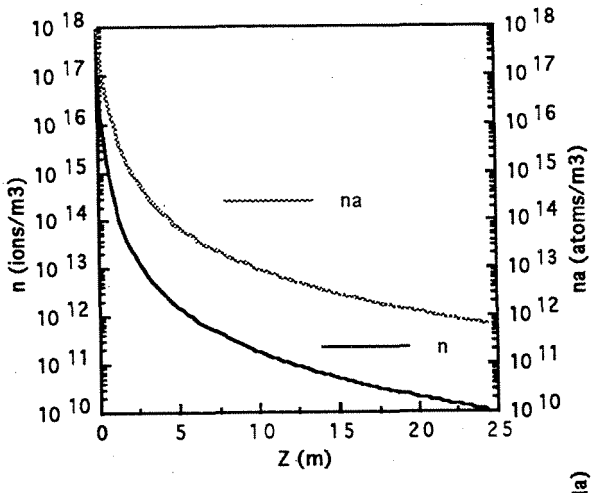

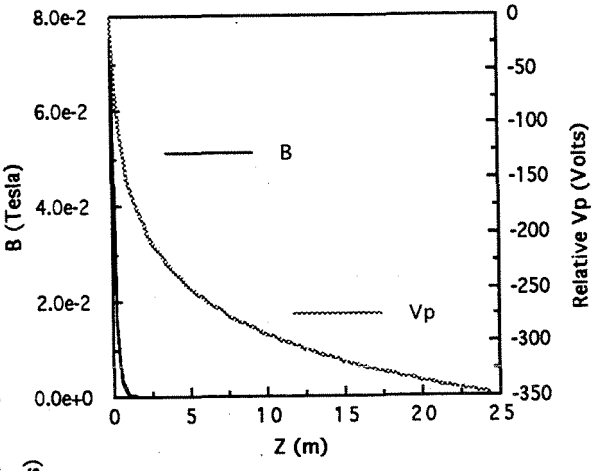

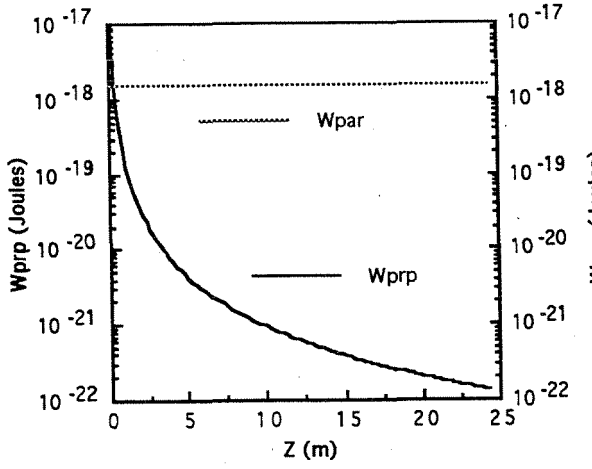

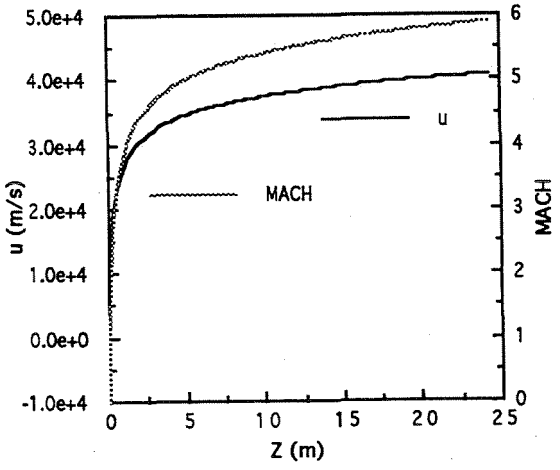

- Coupled ECR Power = 300 watts
- Argon Flow Rate = 25.0 sccm
- Isothermal
- No Vacuum Tank Back Pressure

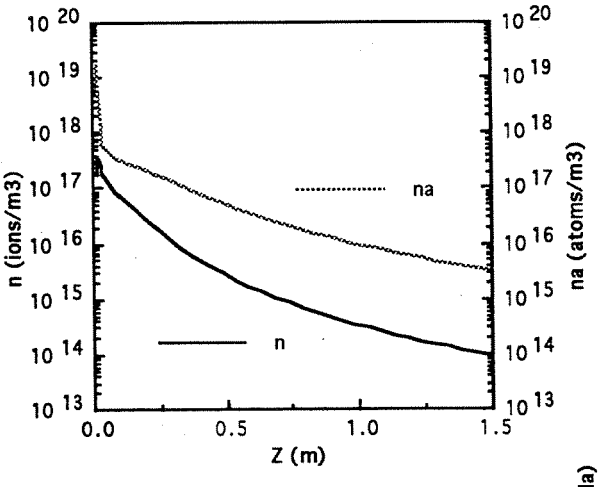

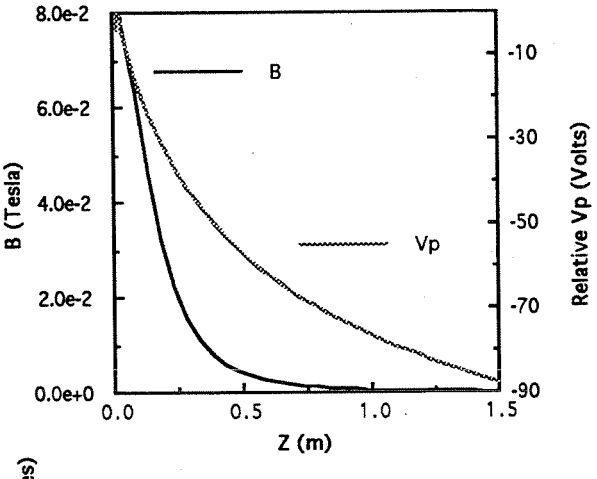

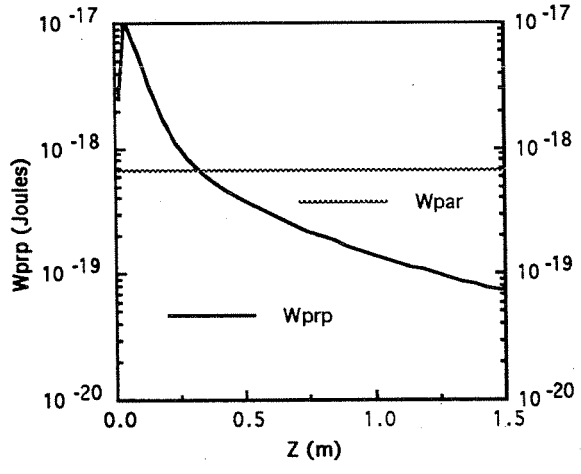

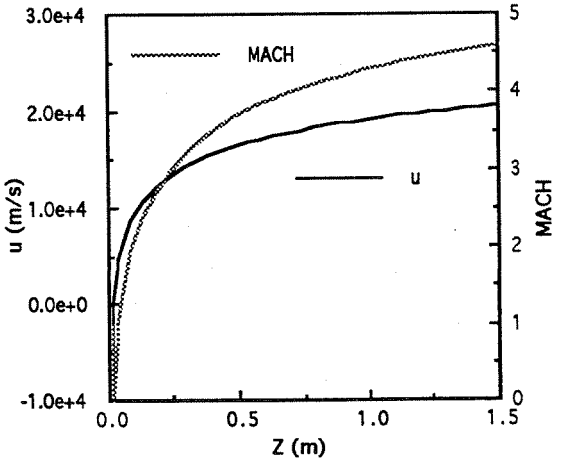

- Coupled ECR Power = 300 watts
- Argon Flow Rate = 25.0 sccm
- Isothermal
- Finite Vacuum Tank Back Pressure

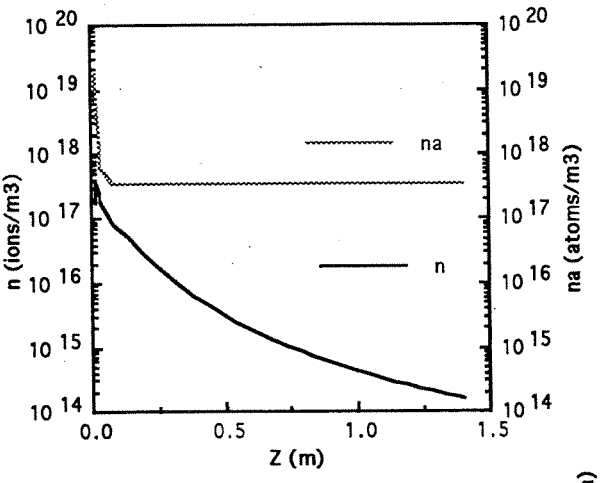

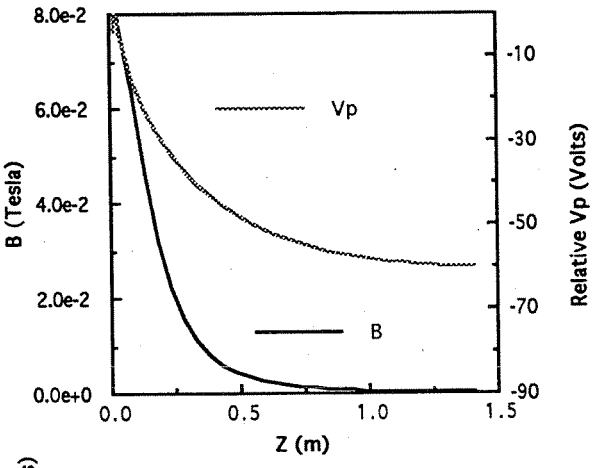

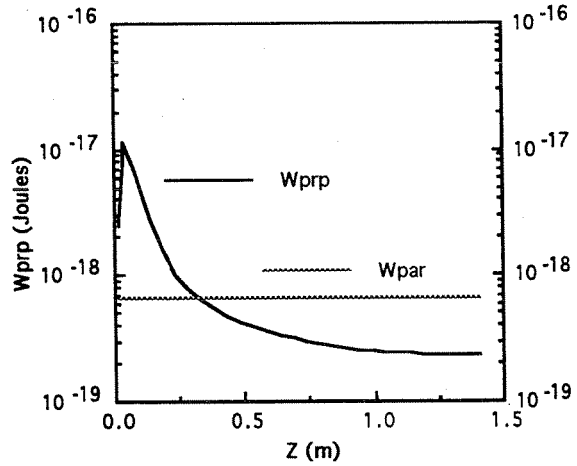

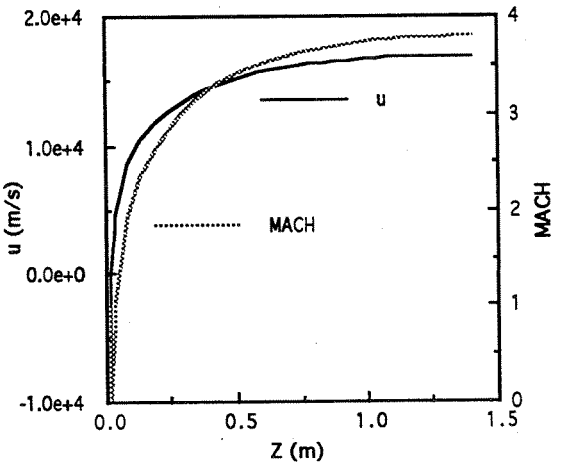

- Coupled ECR Power = 500 watts
- Argon Flow Rate = 25.0 sccm
- Isothermal
- No Vacuum Tank Back Pressure

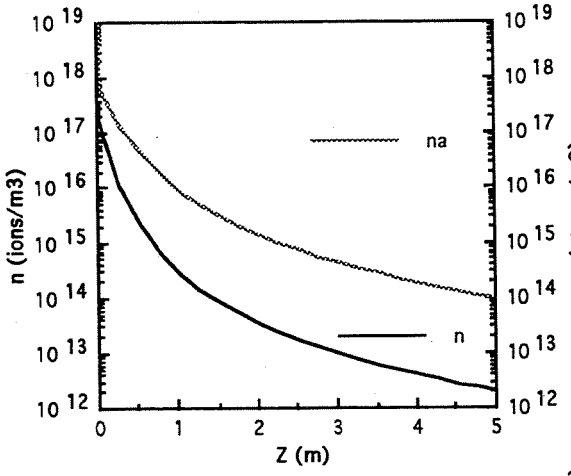

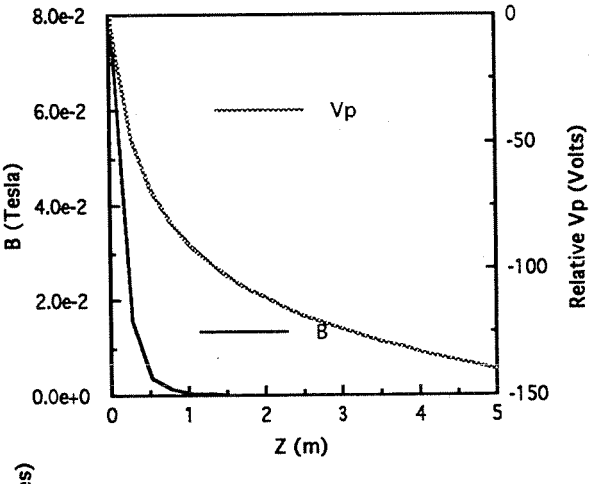

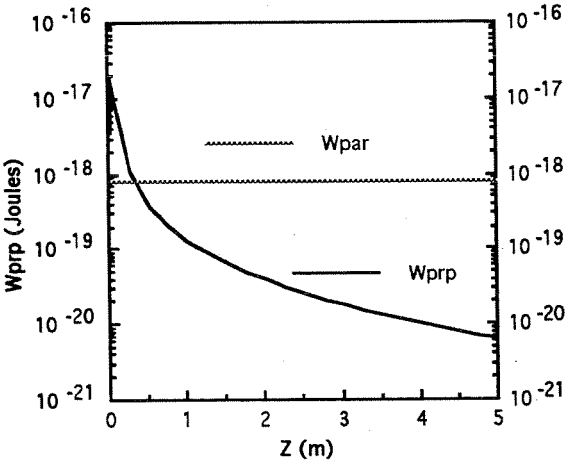

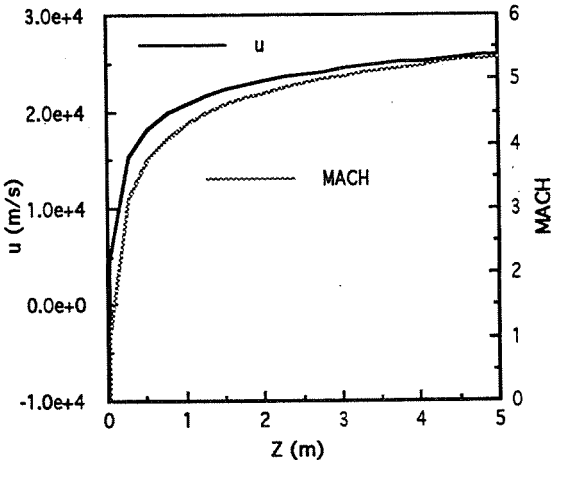

- Coupled ECR Power = 500 watts
- Argon Flow Rate = 25.0 sccm
- Isothermal
- Finite Vacuum Tank Back Pressure

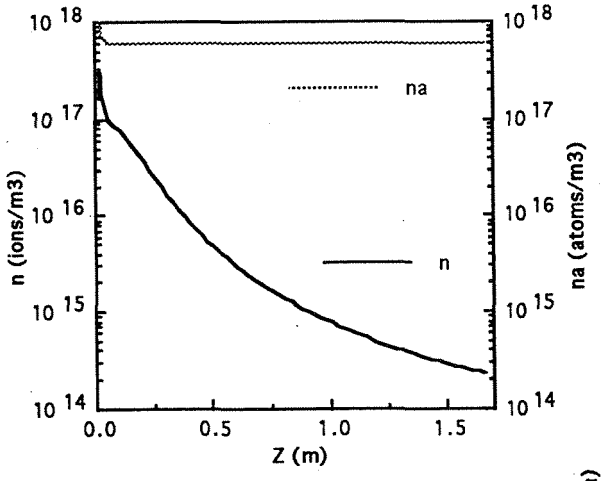

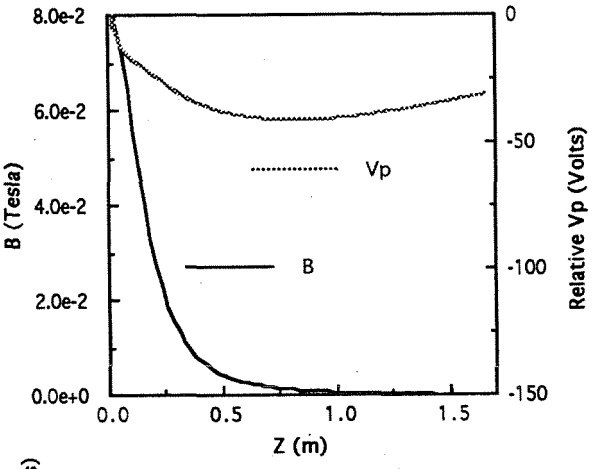

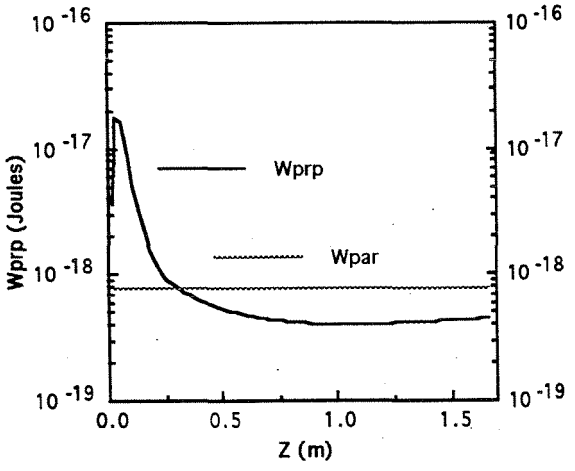

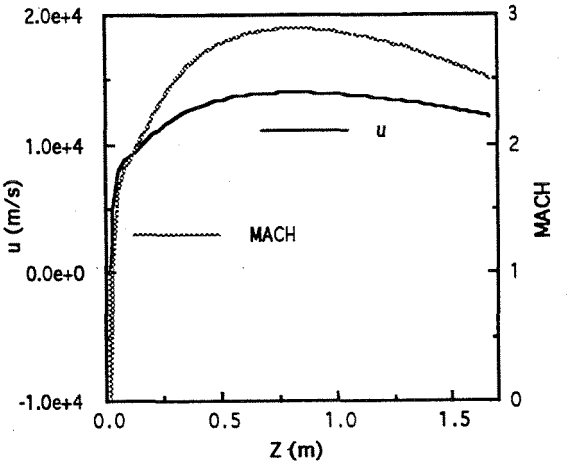

- Coupled ECR Power = 750 watts
- Argon Flow Rate = 25.0 sccm
- Isothermal
- No Vacuum Tank Back Pressure

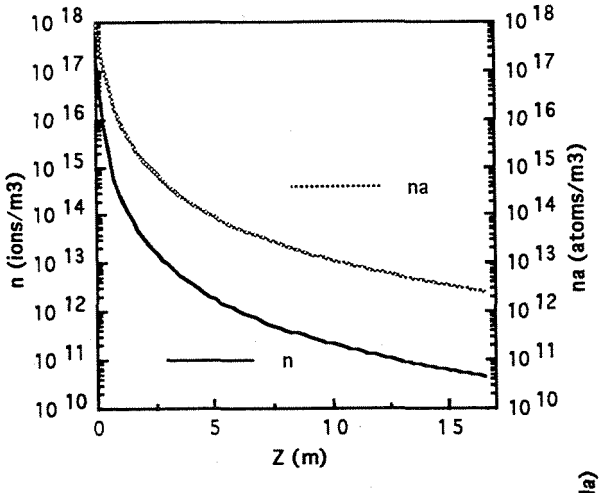

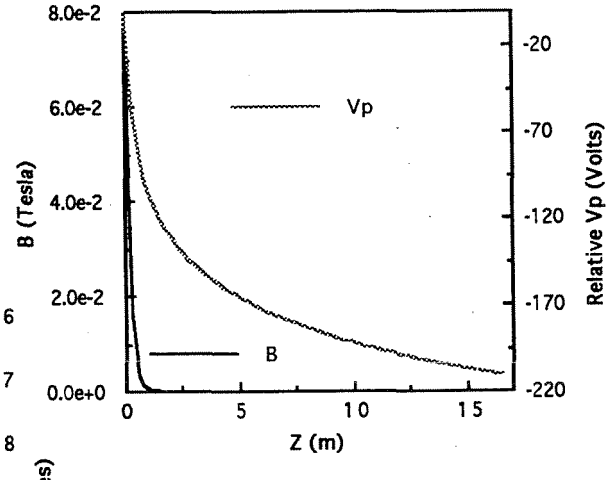

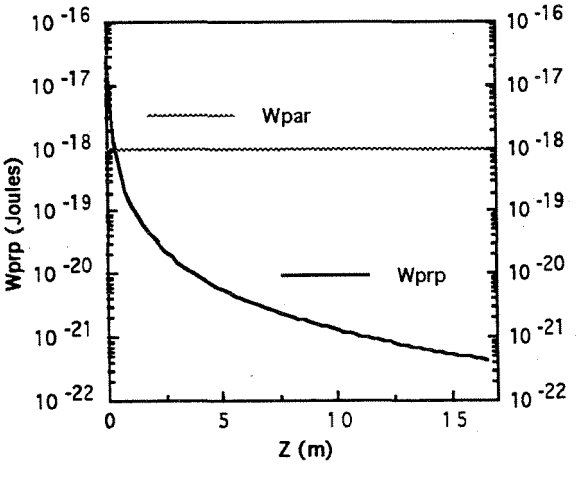

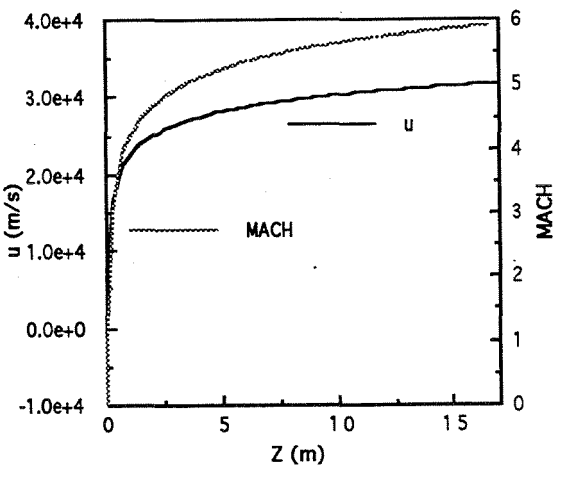

- Coupled ECR Power = 750 watts
- Argon Flow Rate = 25.0 sccm
- Isothermal
- Finite Vacuum Tank Back Pressure

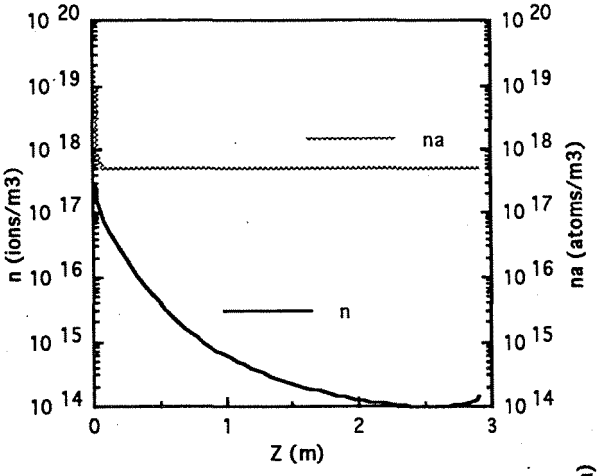

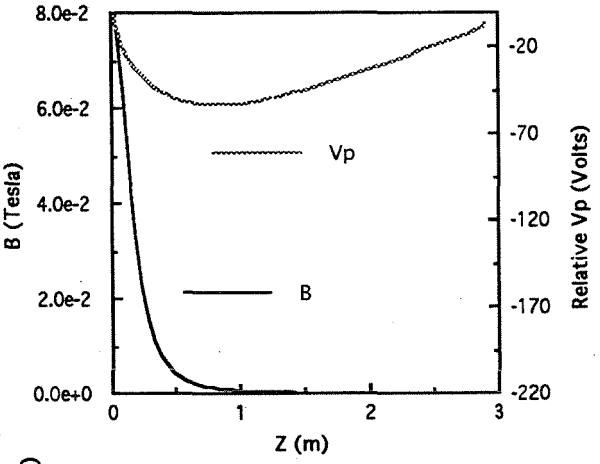

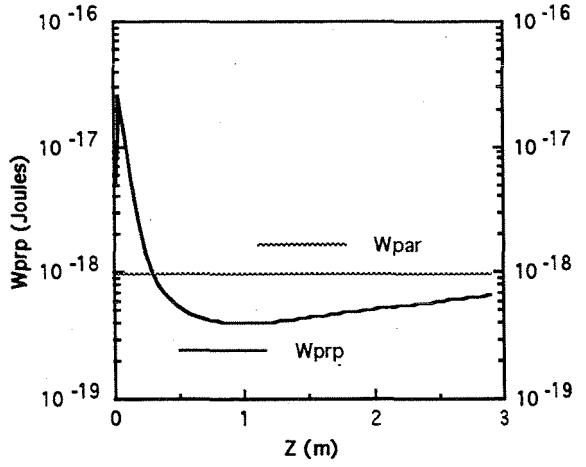

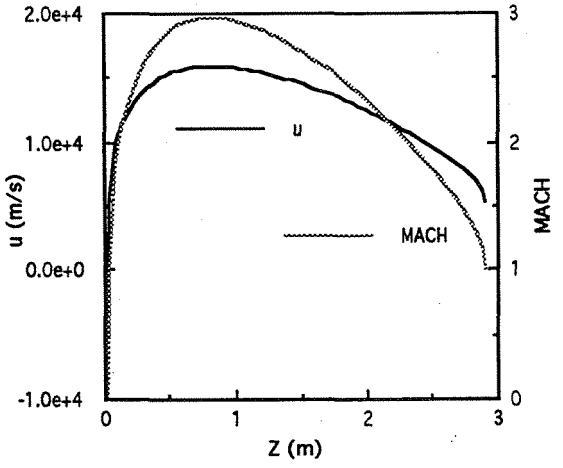

- Coupled ECR Power = 300 watts
- Argon Flow Rate = 10.0 sccm
- No Axial Heat Conduction
- No Vacuum Tank Back Pressure

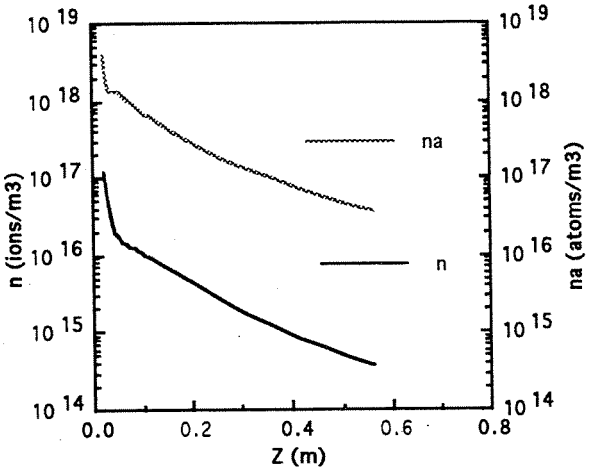

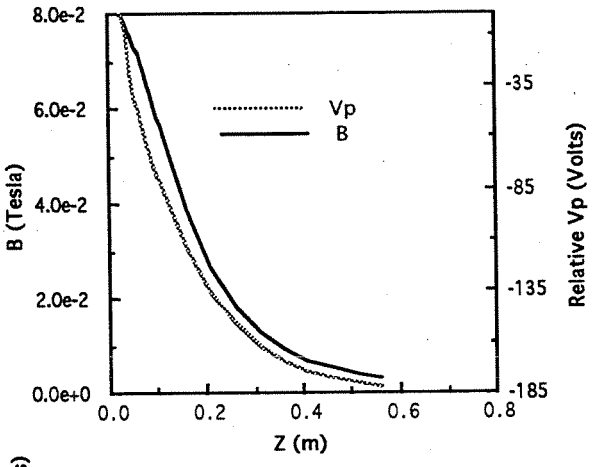

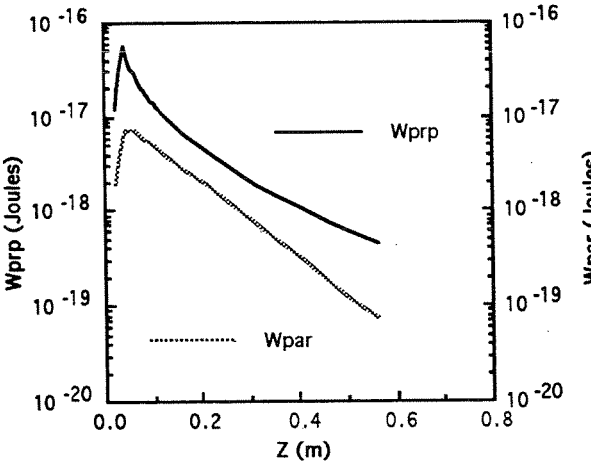

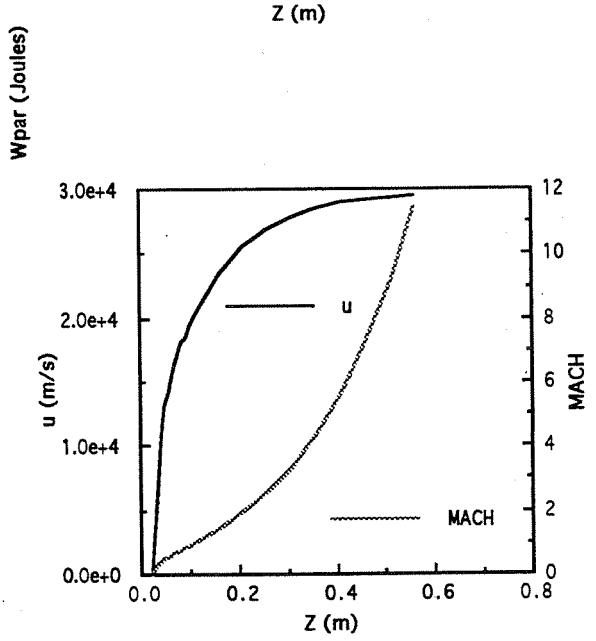

- Coupled ECR Power = 300 watts
- Argon Flow Rate = 10.0 sccm
- No Axial Heat Conduction
- Finite Vacuum Tank Back Pressure

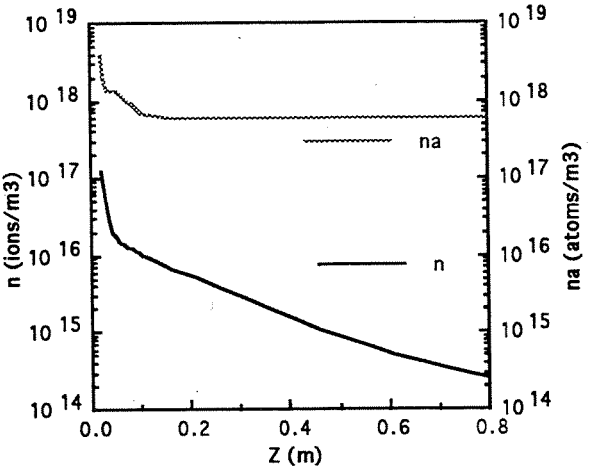

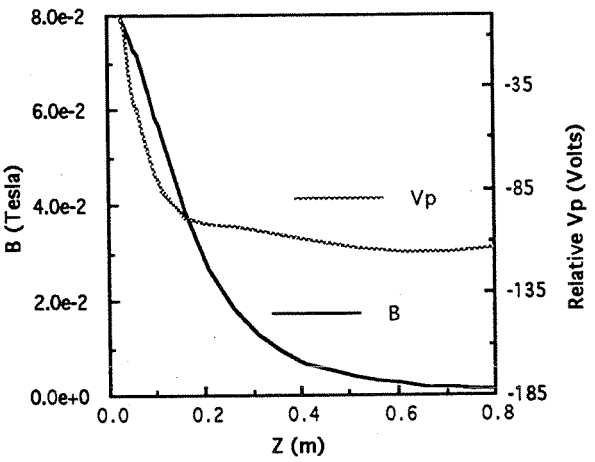

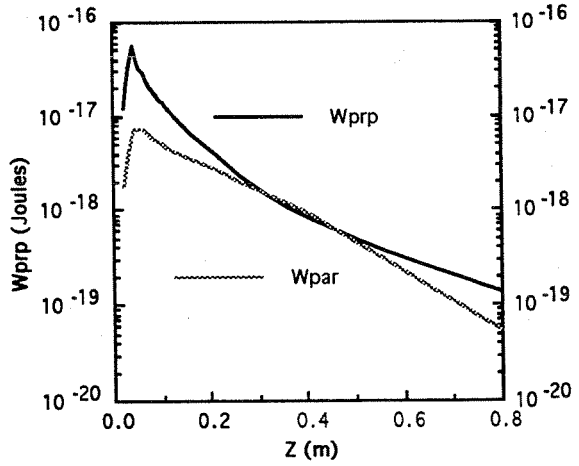

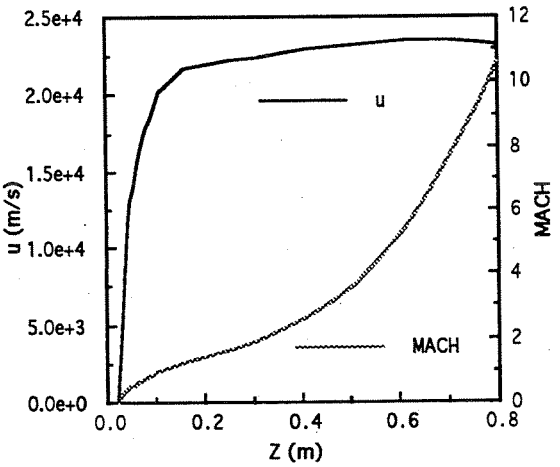

- Coupled ECR Power = 500 watts
- Argon Flow Rate = 11.5 sccm
- No Axial Heat Conduction
- No Vacuum Tank Back Pressure

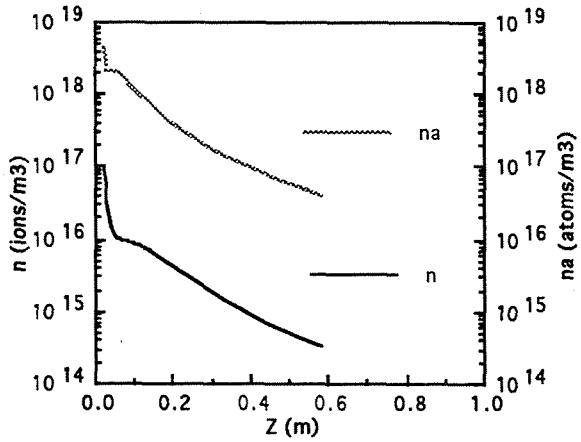

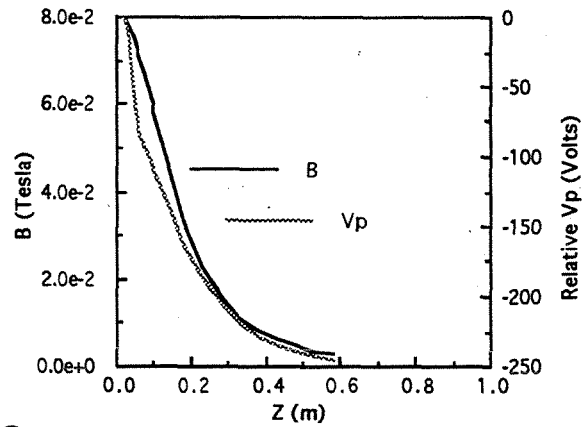

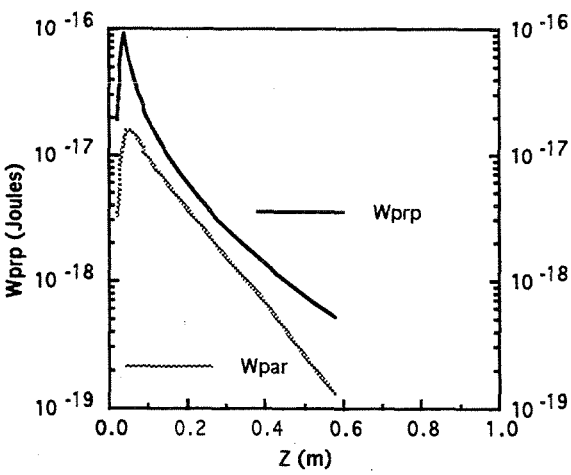

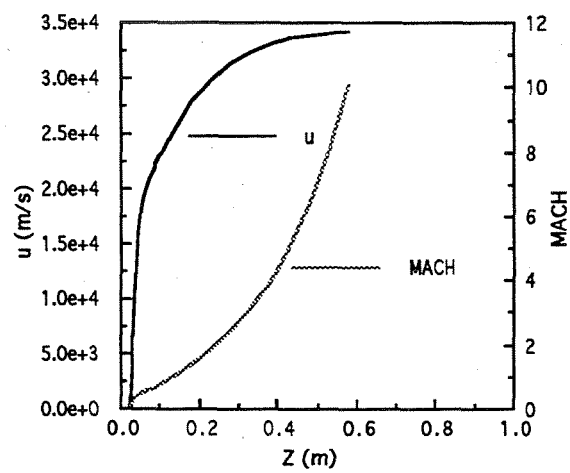

- Coupled ECR Power = 500 watts
- Argon Flow Rate = 11.5 sccm
- No Axial Heat Conduction
- Finite Vacuum Tank Back Pressure

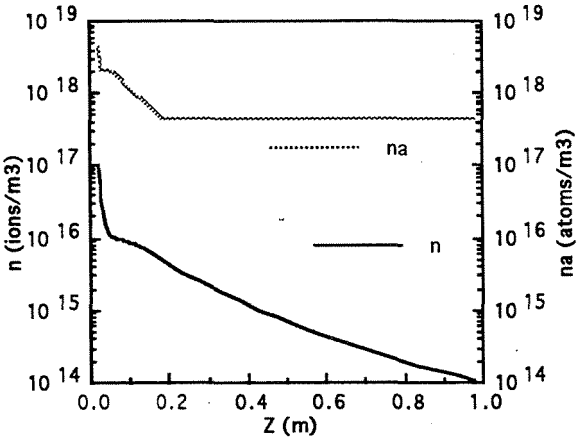

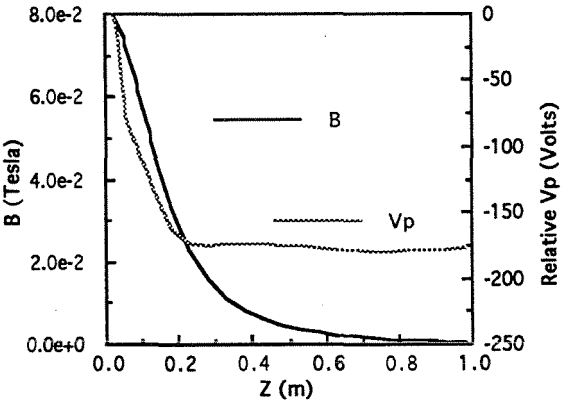

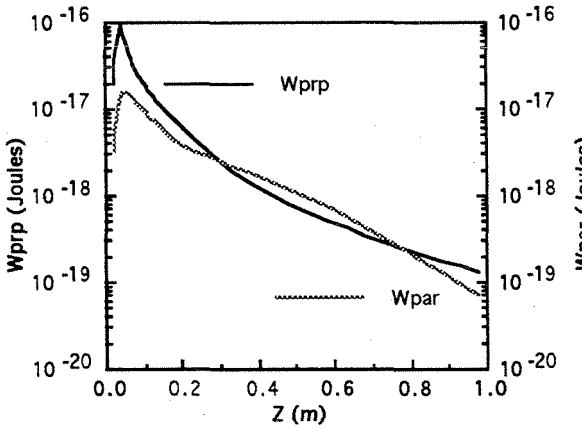

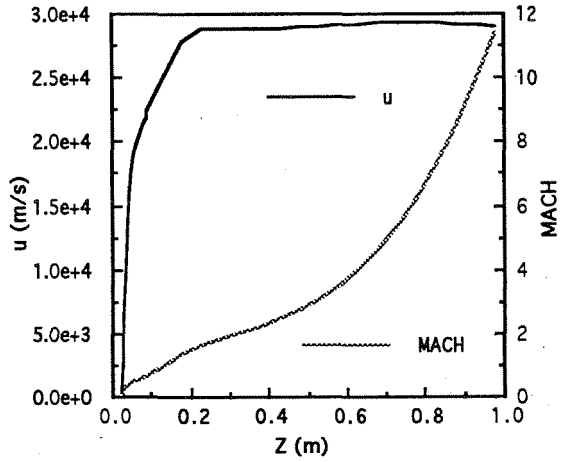

- Coupled ECR Power = 300 watts
- Argon Flow Rate = 12.5 sccm
- No Axial Heat Conduction
- No Vacuum Tank Back Pressure

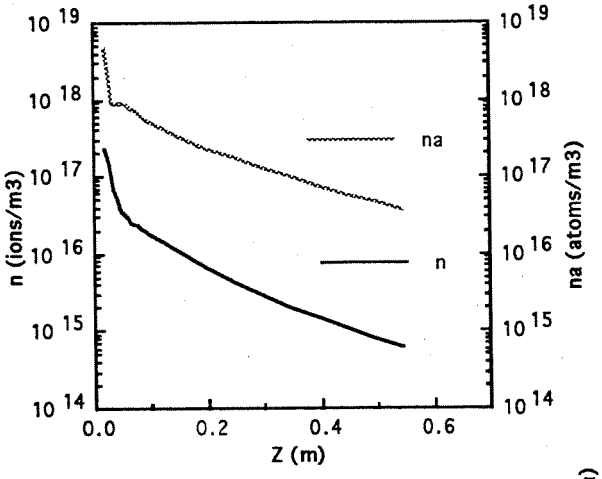

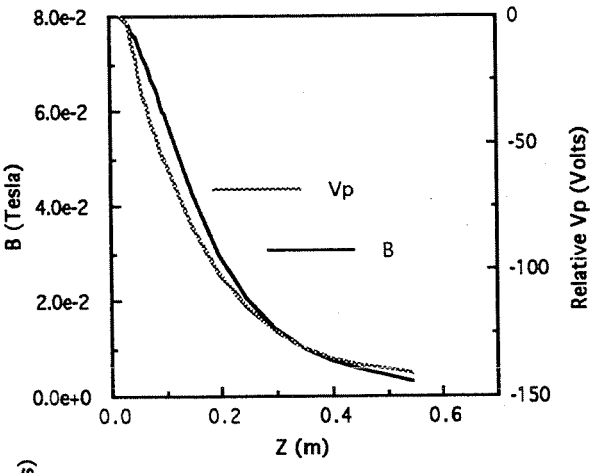

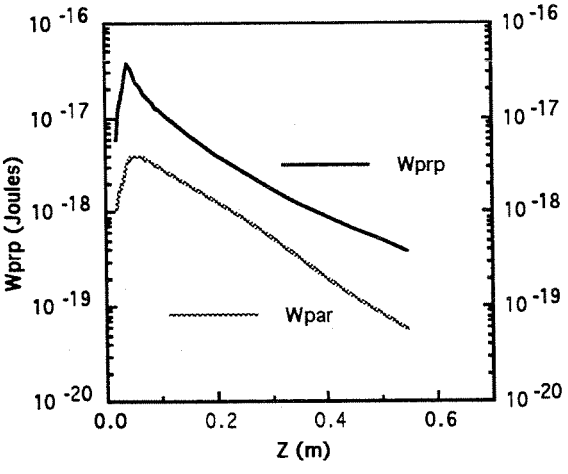

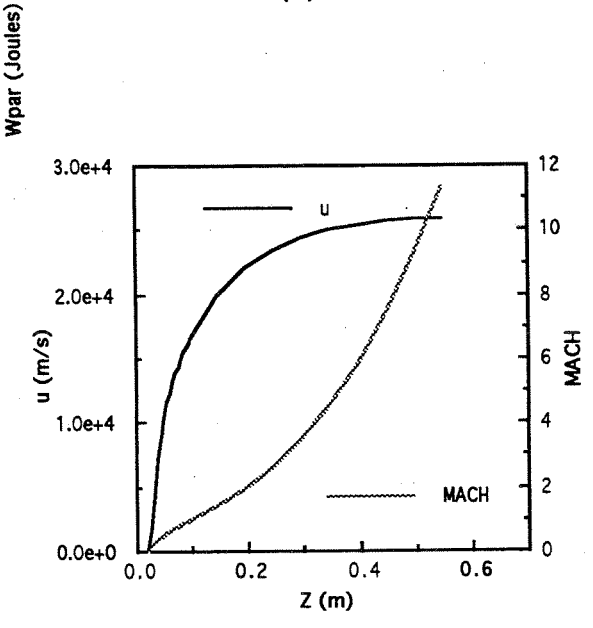

- Coupled ECR Power = 300 watts
- Argon Flow Rate = 12.5 sccm
- No Axial Heat Conduction
- Finite Vacuum Tank Back Pressure

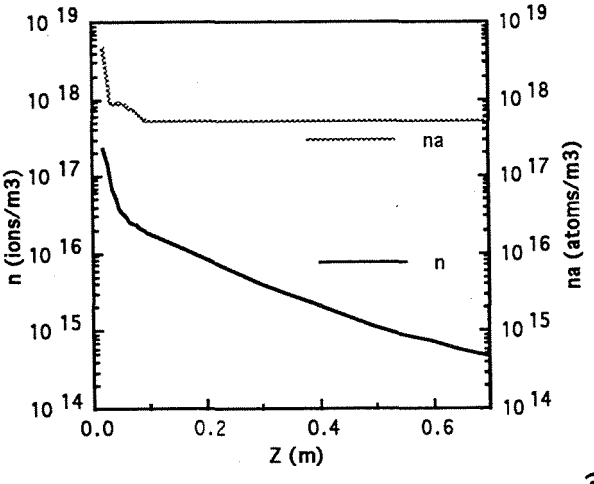

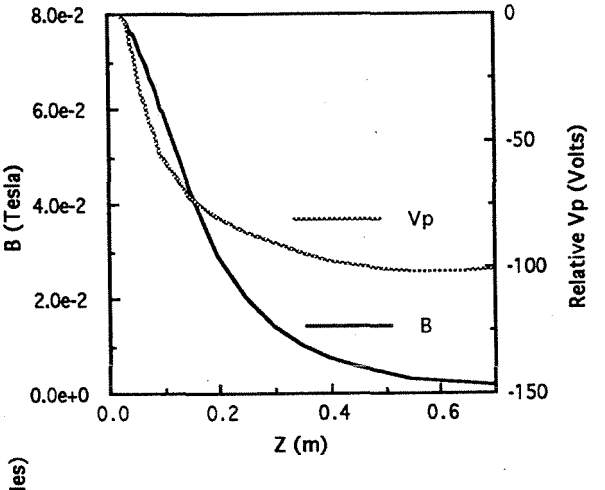

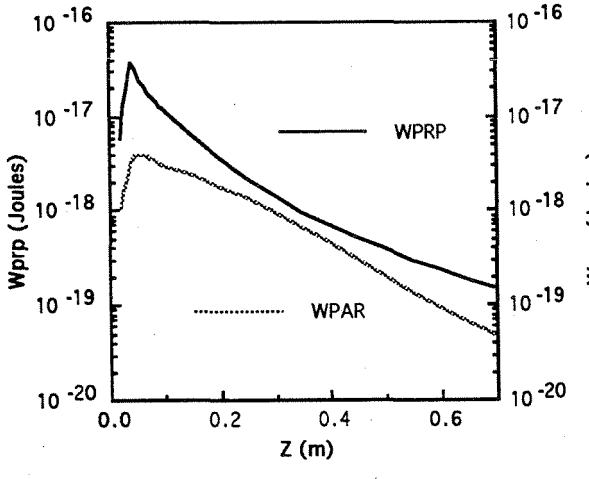

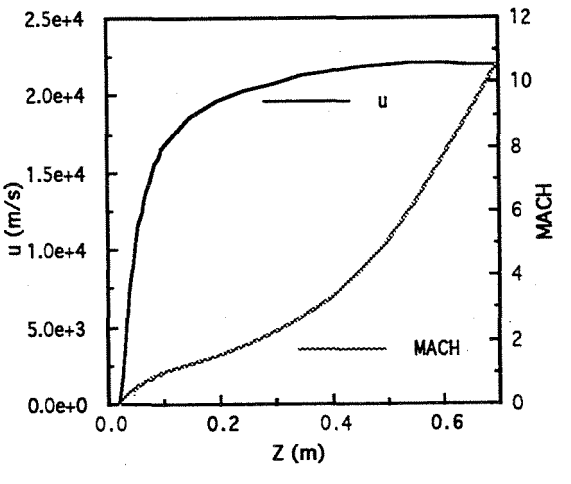

- Coupled ECR Power = 500 watts
- Argon Flow Rate = 12.5 sccm
- No Axial Heat Conduction
- No Vacuum Tank Back Pressure

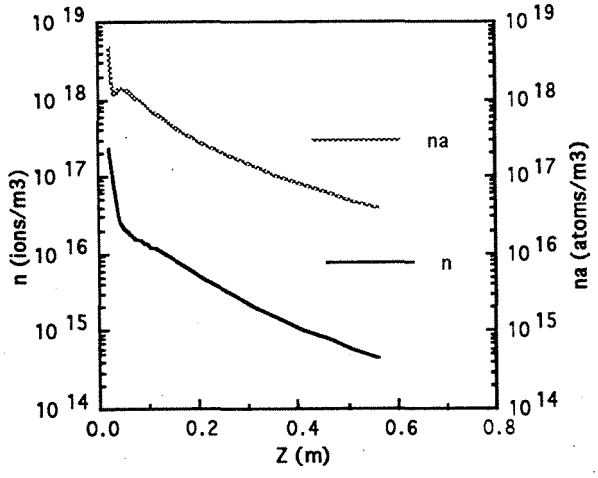

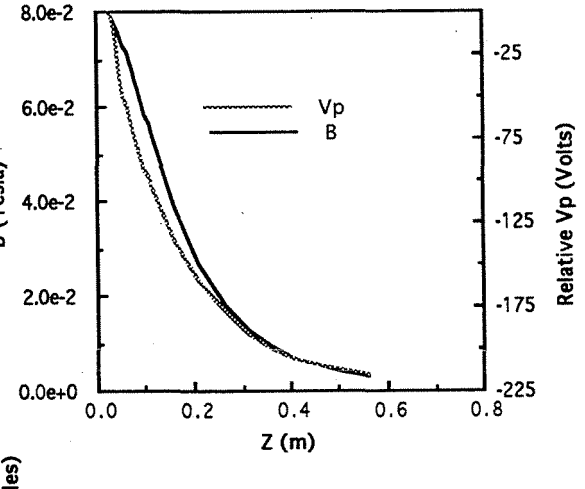

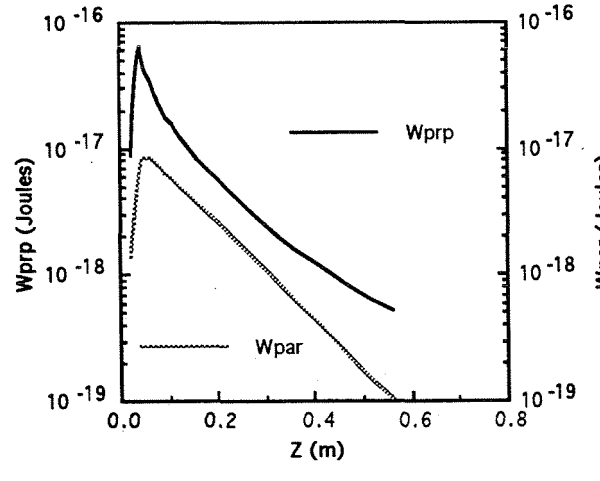

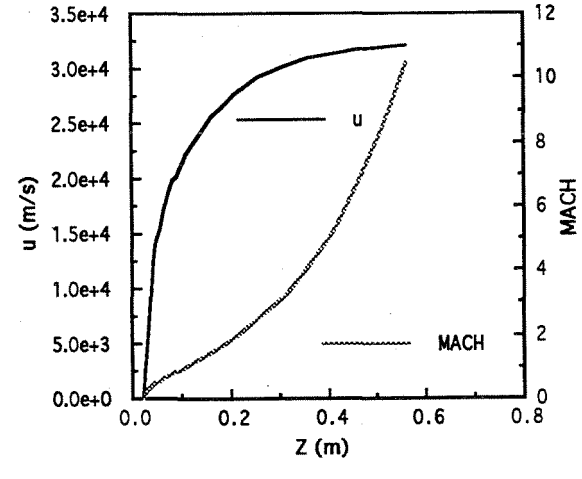

- Coupled ECR Power = 500 watts
- Argon Flow Rate = 12.5 sccm
- No Axial Heat Conduction
- Finite Vacuum Tank Back Pressure

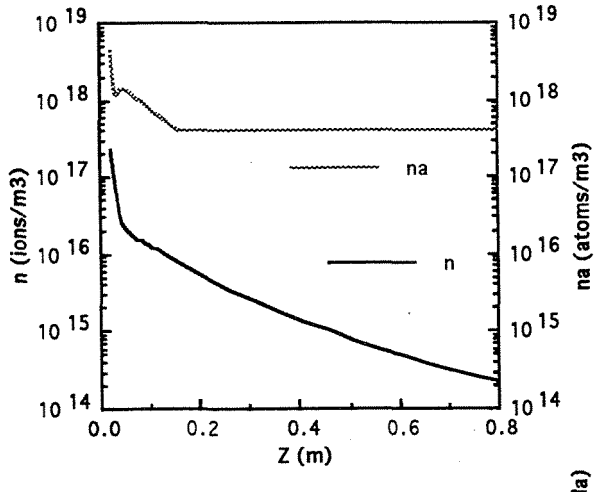

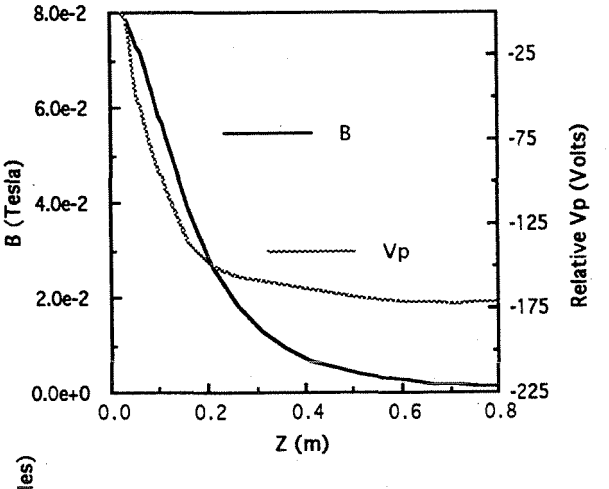

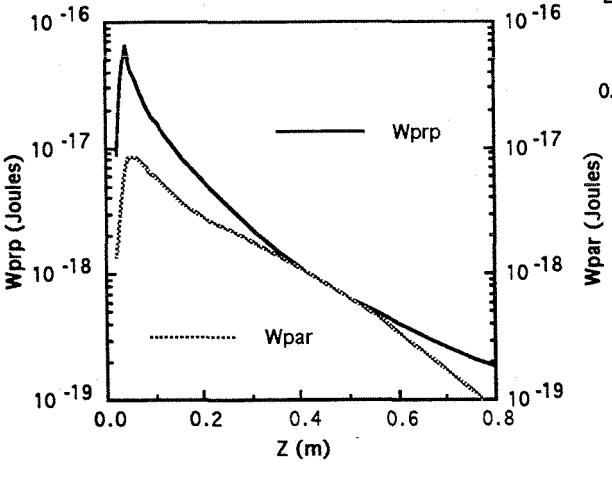

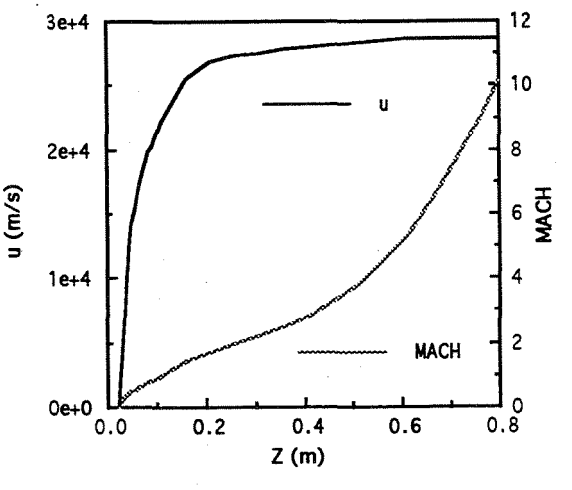

- Coupled ECR Power = 750 watts
- Argon Flow Rate = 13.0 sccm
- No Axial Heat Conduction
- No Vacuum Tank Back Pressure

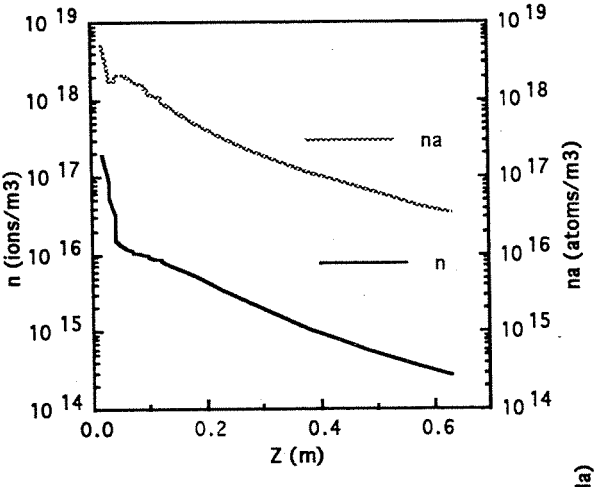

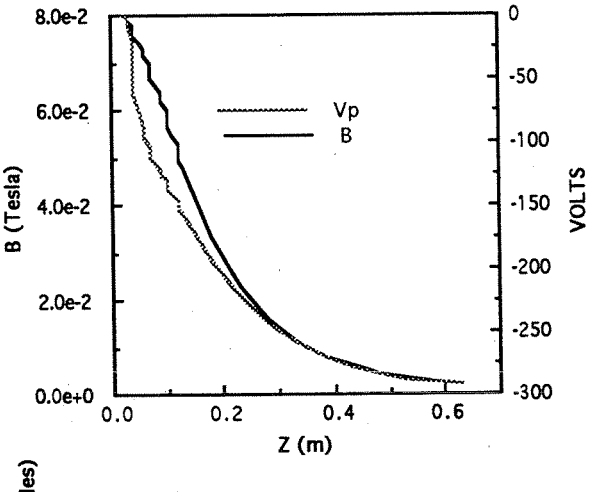

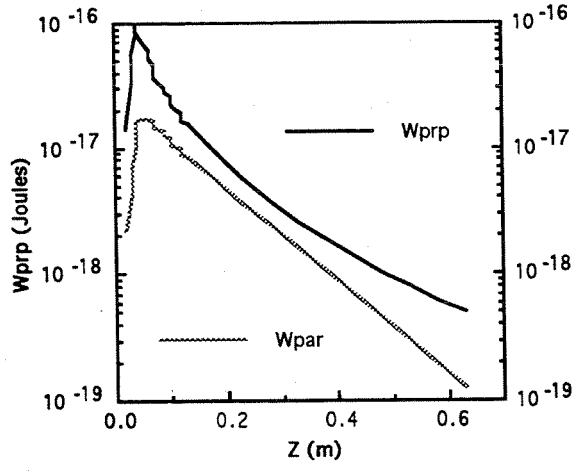

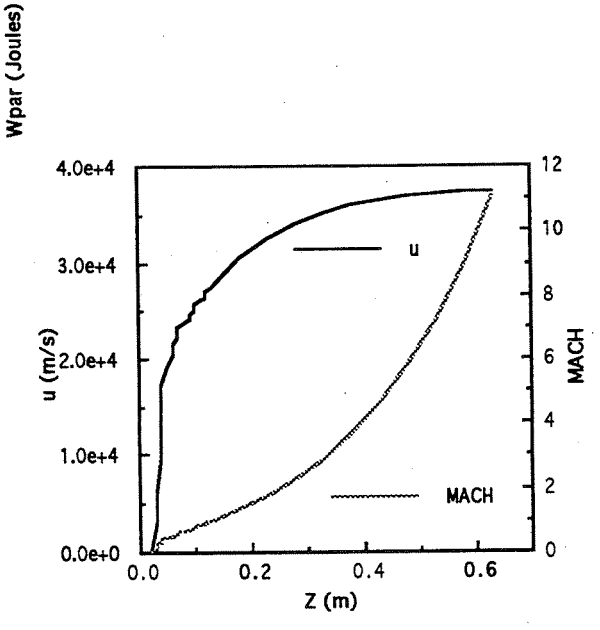

- Coupled ECR Power = 750 watts
- Argon Flow Rate = 13.0 sccm
- No Axial Heat Conduction
- Finite Vacuum Tank Back Pressure

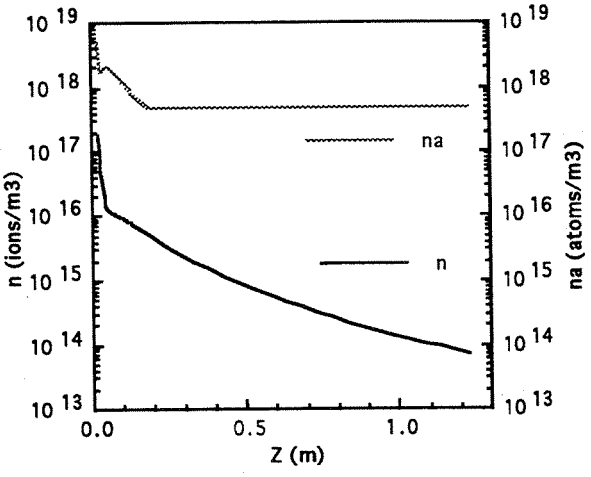

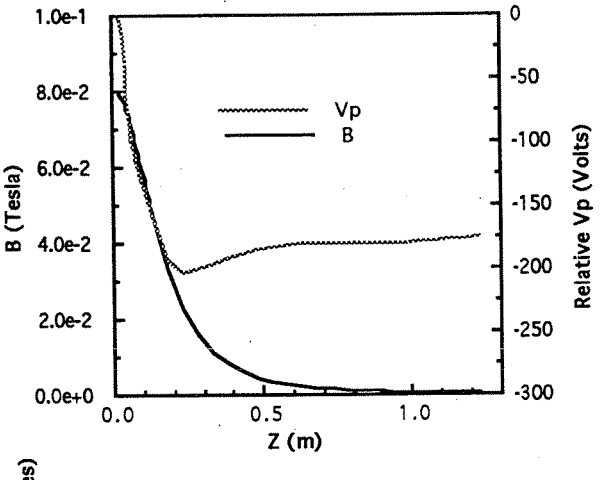

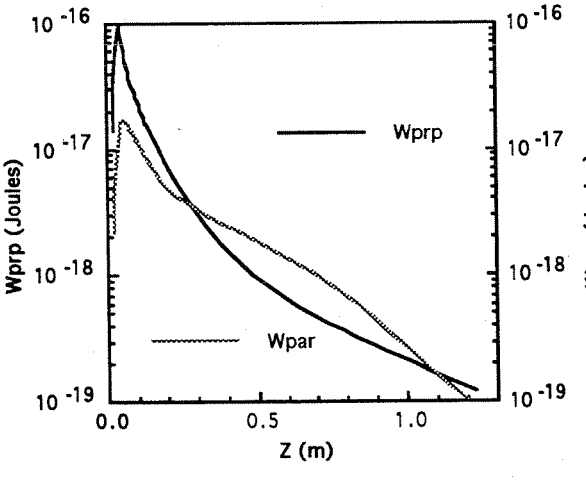

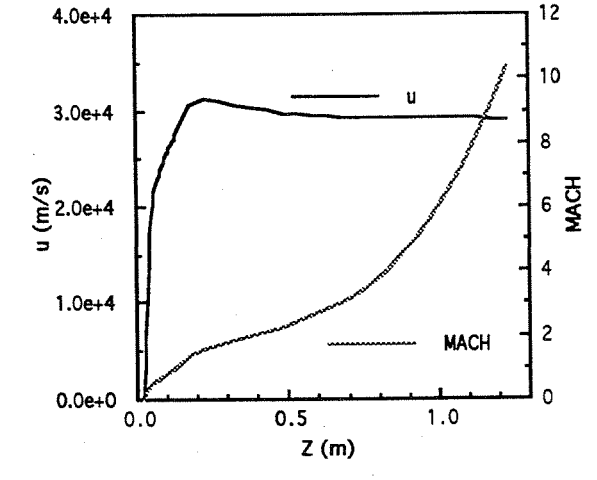

- Coupled ECR Power = 750 watts
- Argon Flow Rate = 13.5 sccm
- No Axial Heat Conduction
- No Vacuum Tank Back Pressure

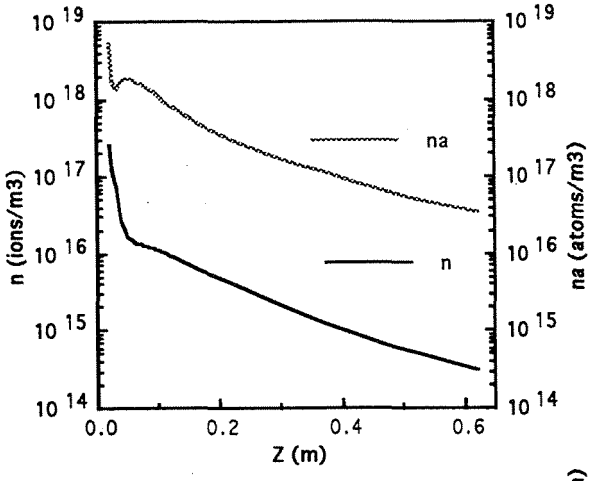

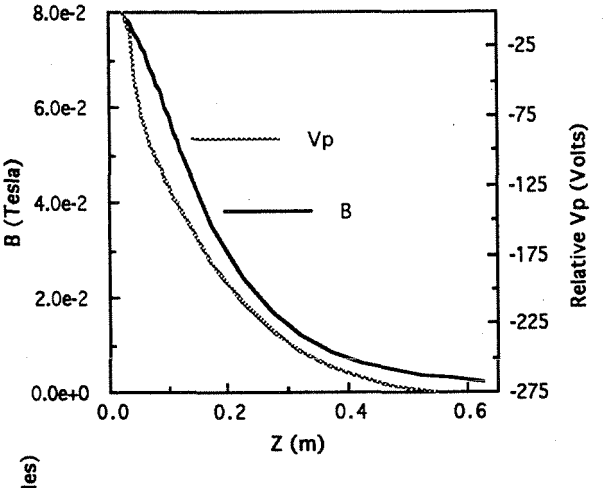

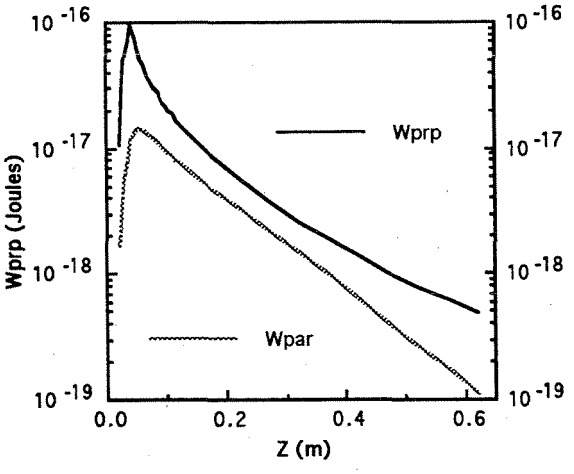

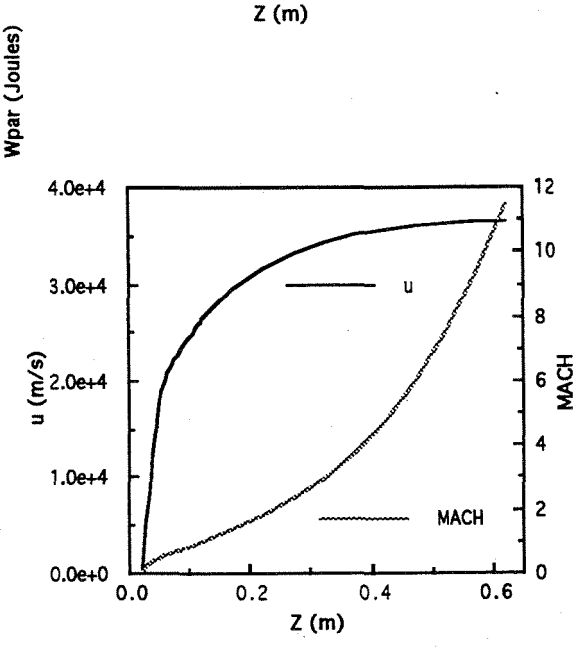

- Coupled ECR Power = 750 watts
- Argon Flow Rate = 13.5 sccm
- No Axial Heat Conduction
- Finite Vacuum Tank Back Pressure

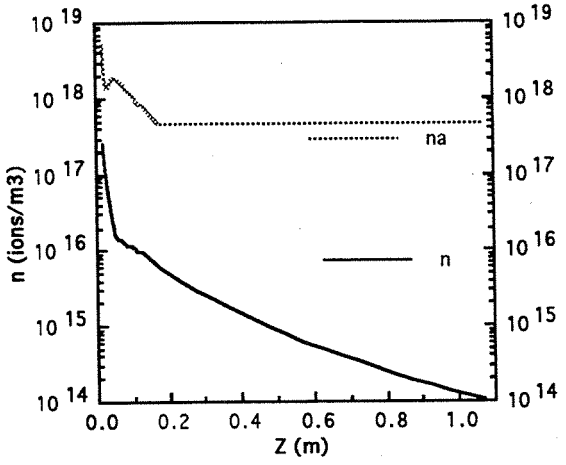

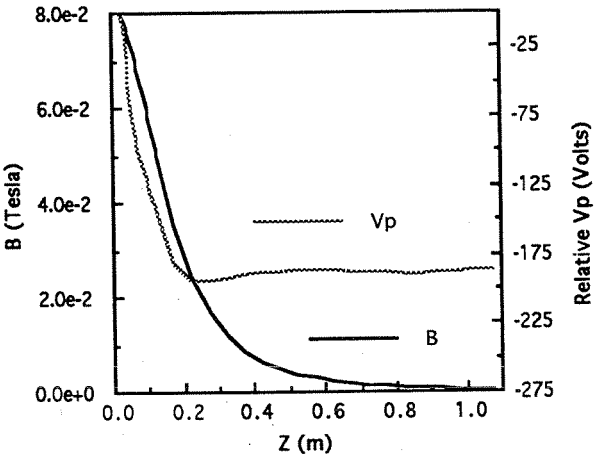

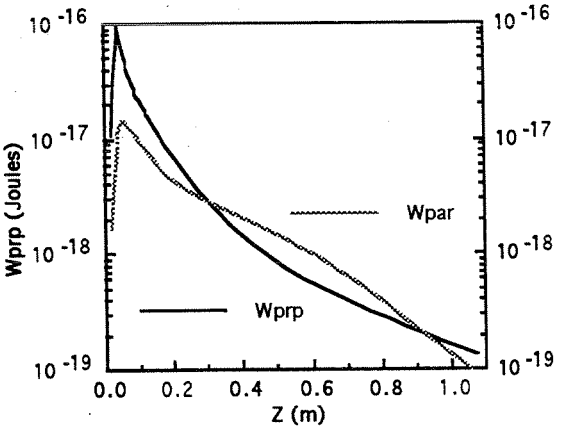

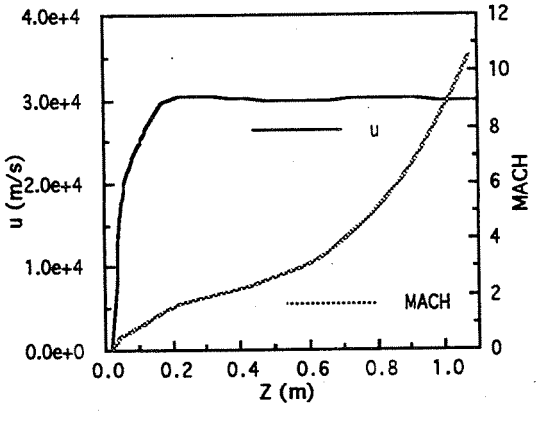

- Coupled ECR Power = 1000 watts
- Argon Flow Rate = 14.5 sccm
- No Axial Heat Conduction
- No Vacuum Tank Back Pressure

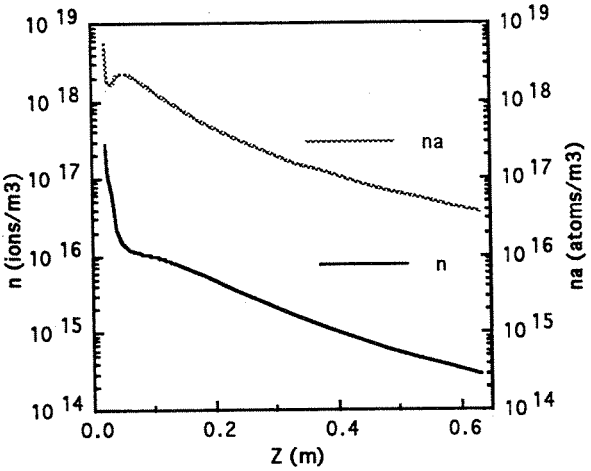

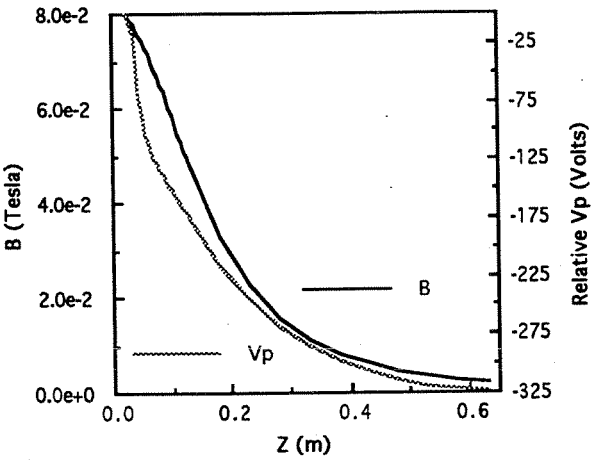

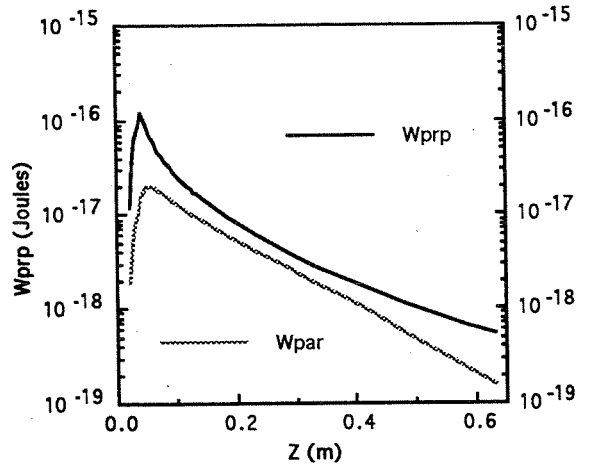

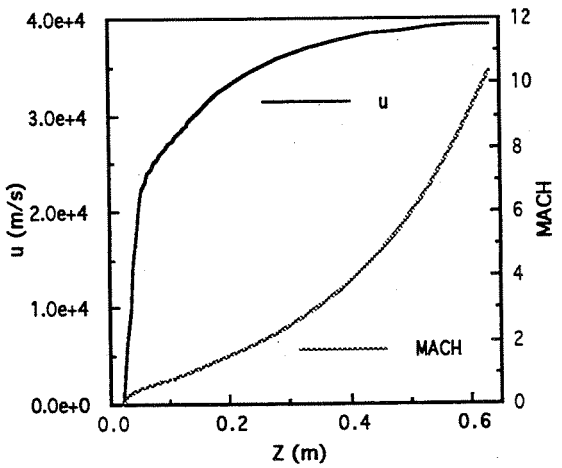

- Coupled ECR Power = 1000 watts
- Argon Flow Rate = 14.5 sccm
- No Axial Heat Conduction
- Finite Vacuum Tank Back Pressure

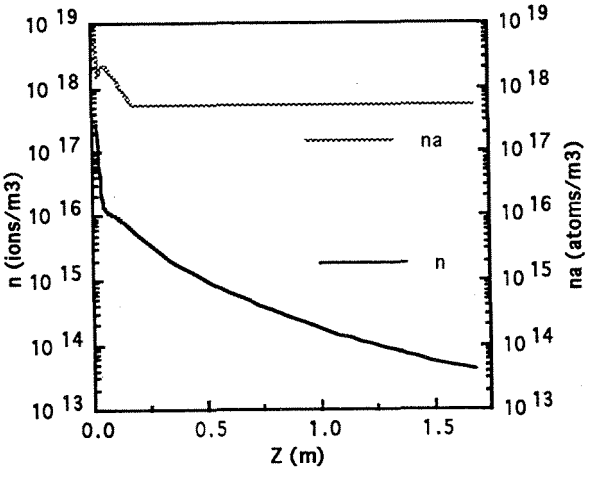

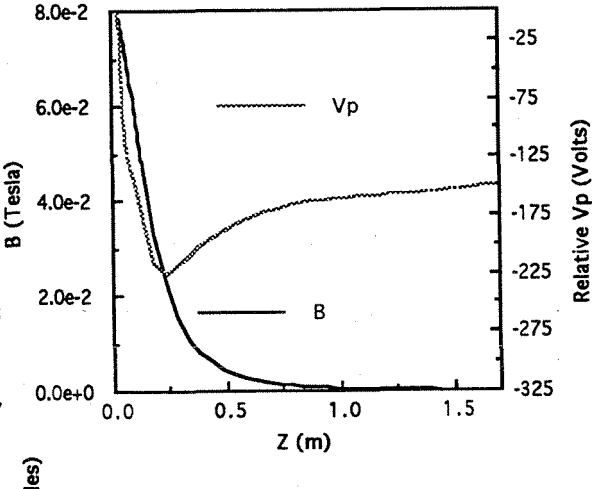

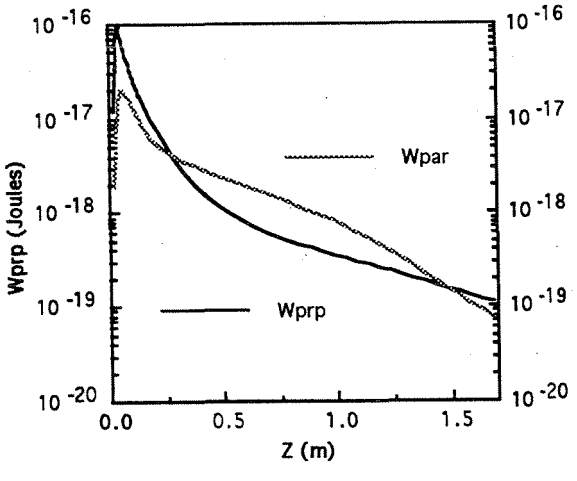

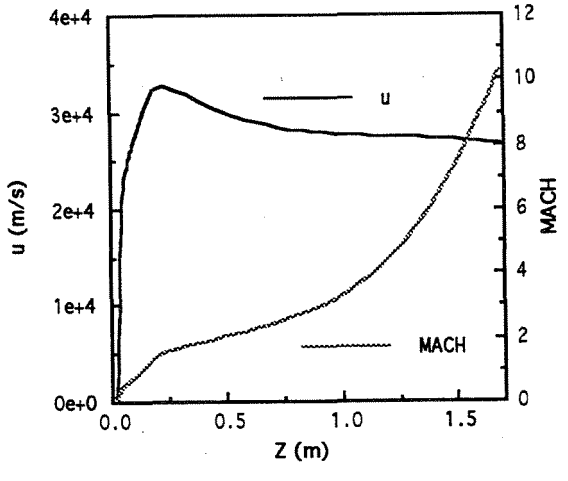

- Coupled ECR Power = 1000 watts
- Argon Flow Rate = 15.0 sccm
- No Axial Heat Conduction
- No Vacuum Tank Back Pressure

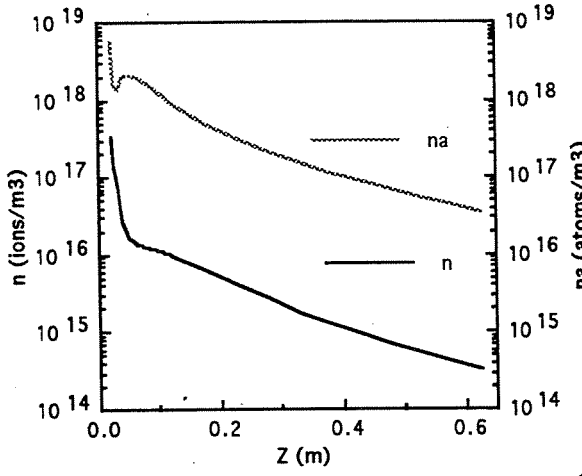

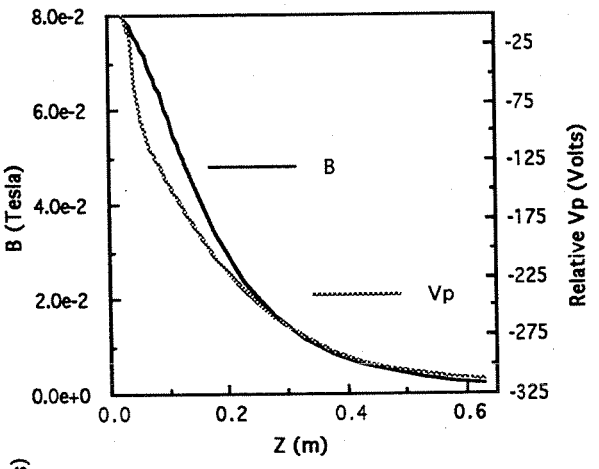

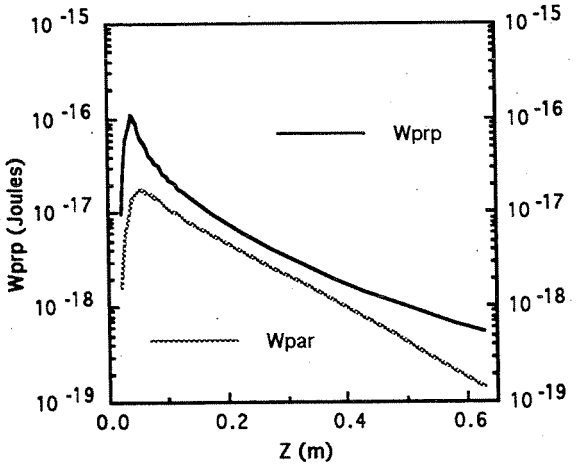

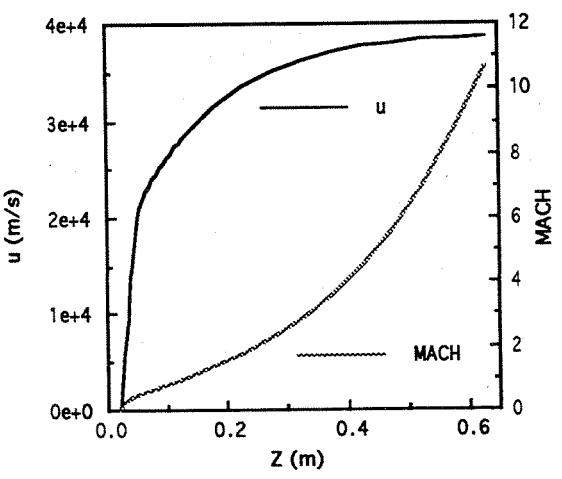

- Coupled ECR Power = 1000 watts
- Argon Flow Rate = 15.0 sccm
- No Axial Heat Conduction
- Finite Vacuum Tank Back Pressure

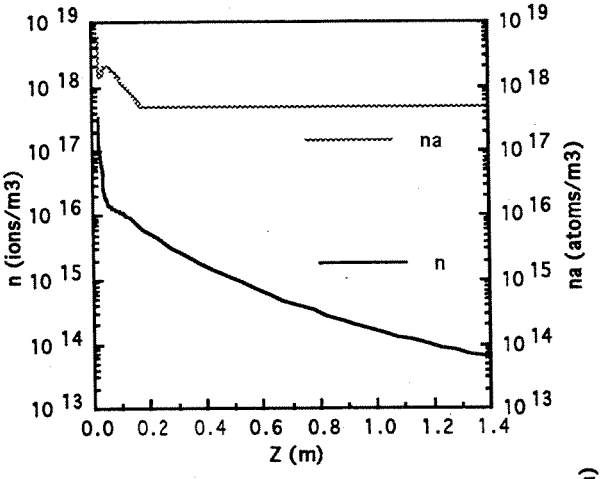

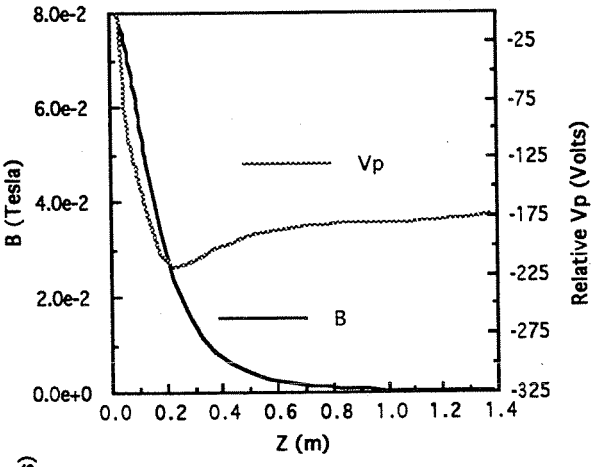

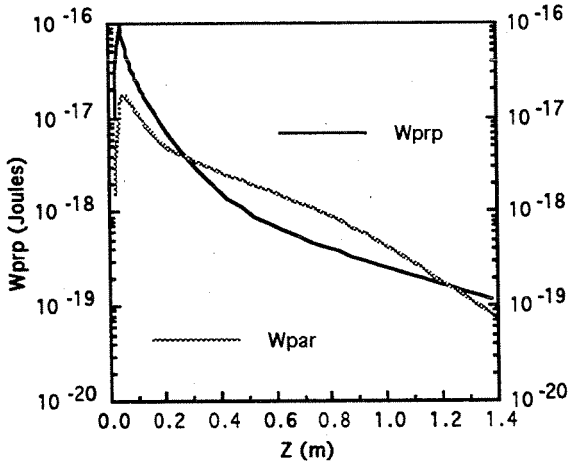

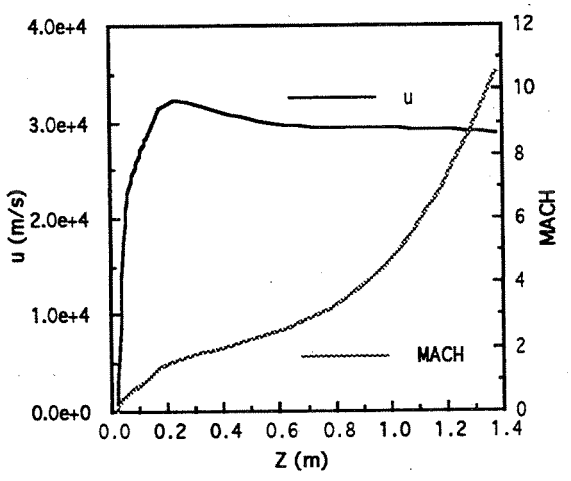

- Coupled ECR Power = 300 watts
- Argon Flow Rate = 15.0 sccm
- No Axial Heat Conduction
- No Vacuum Tank Back Pressure

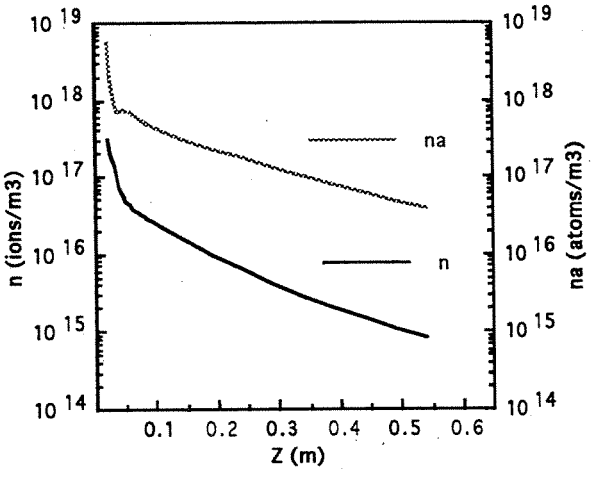

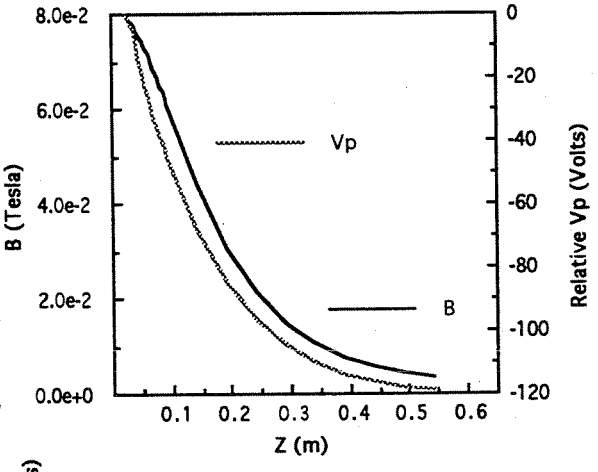

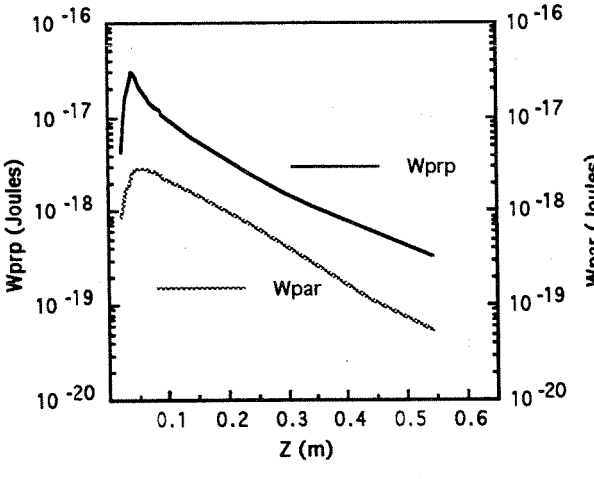

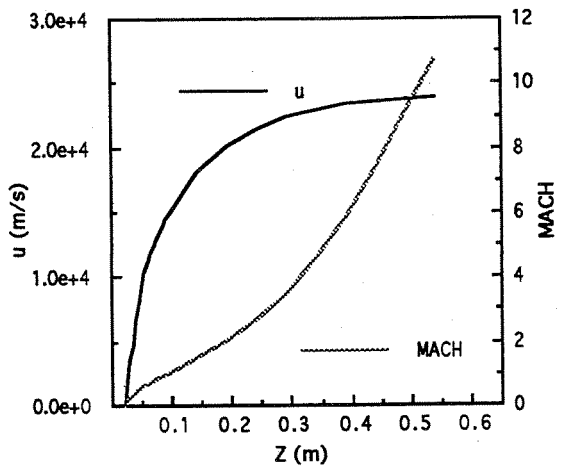

- Coupled ECR Power = 300 watts
- Argon Flow Rate = 15.0 sccm
- No Axial Heat Conduction
- Finite Vacuum Tank Back Pressure

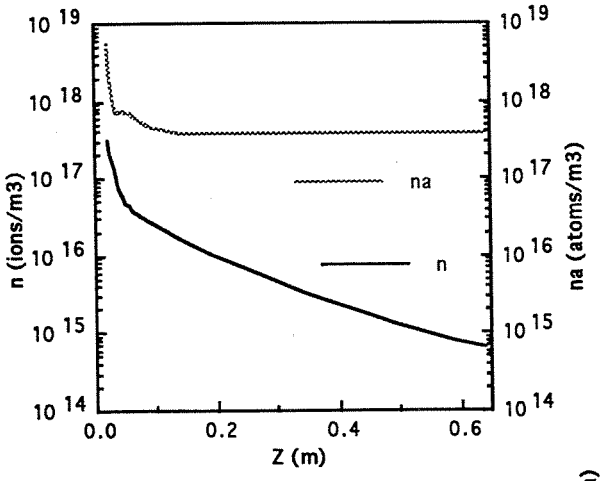

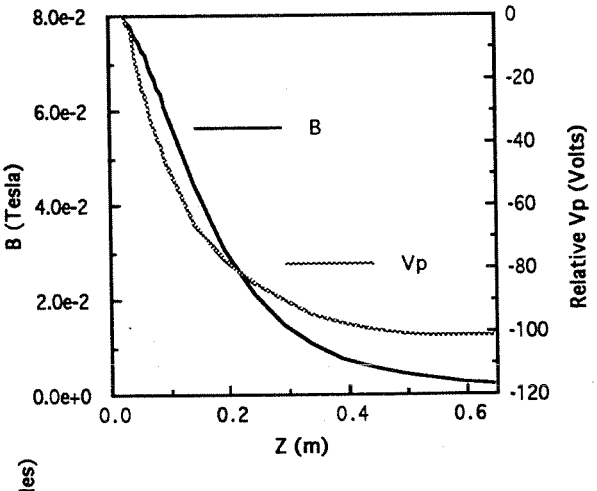

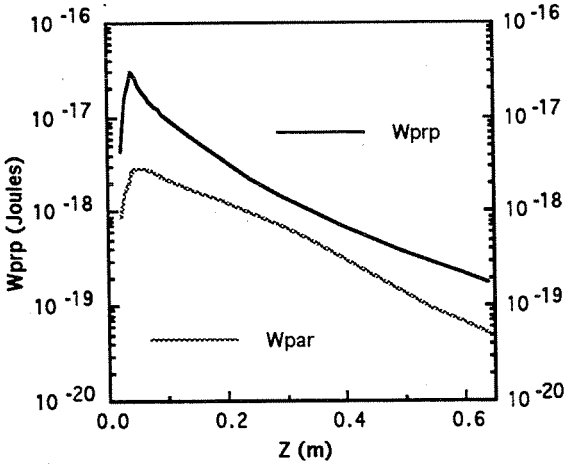

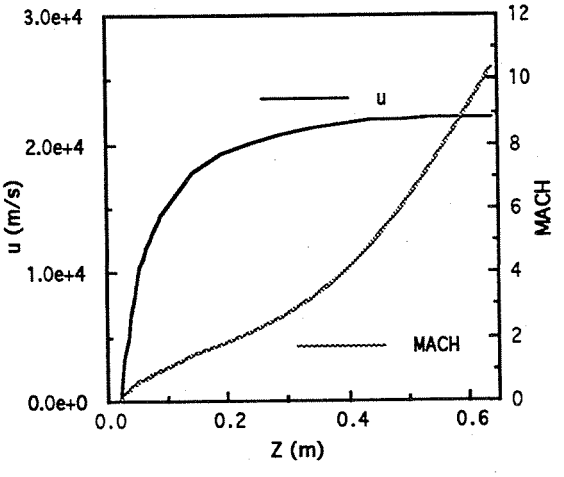

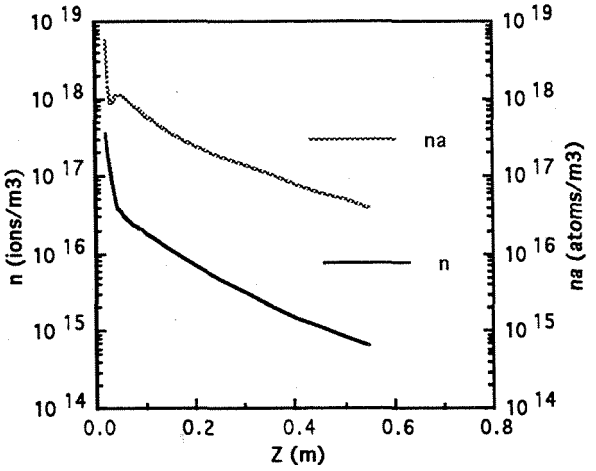

- Coupled ECR Power = 500 watts
- Argon Flow Rate = 15.0 sccm
- No Axial Heat Conduction
- No Vacuum Tank Back Pressure

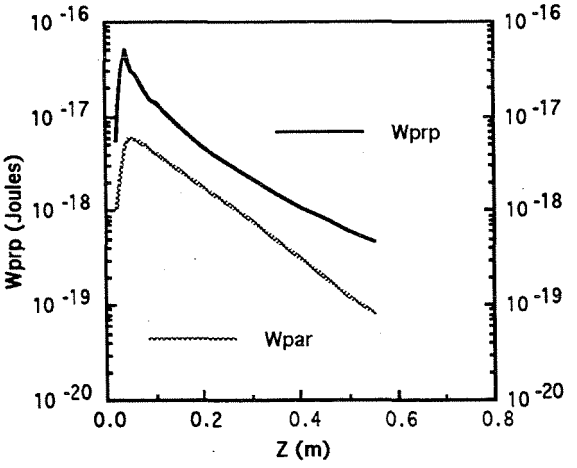

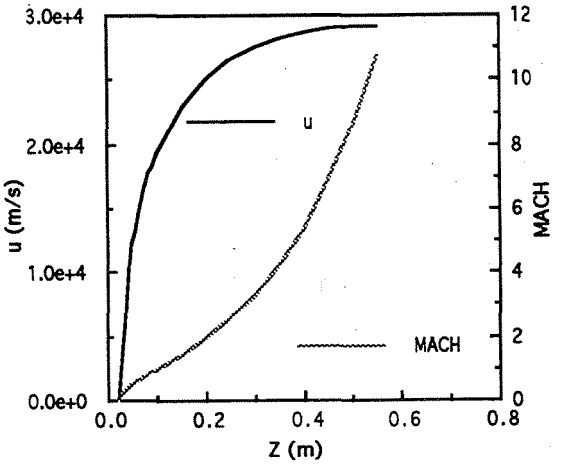

- Coupled ECR Power = 500 watts
- Argon Flow Rate = 15.0 sccm
- No Axial Heat Conduction
- Finite Vacuum Tank Back Pressure

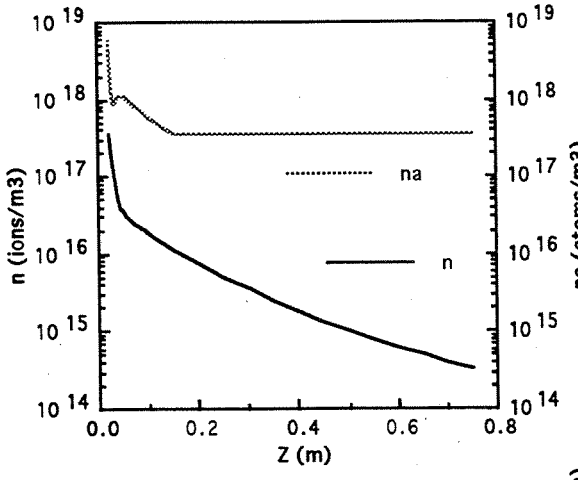

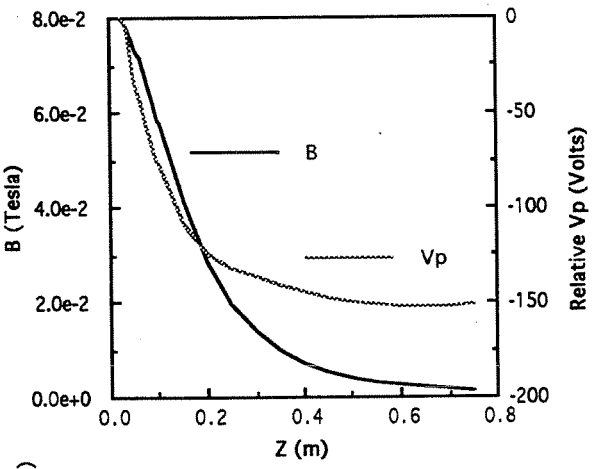

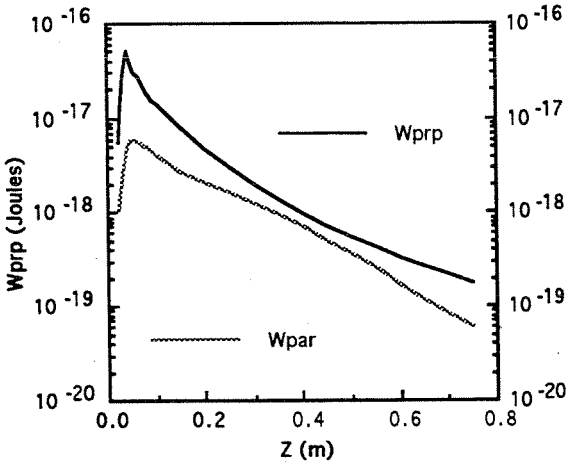

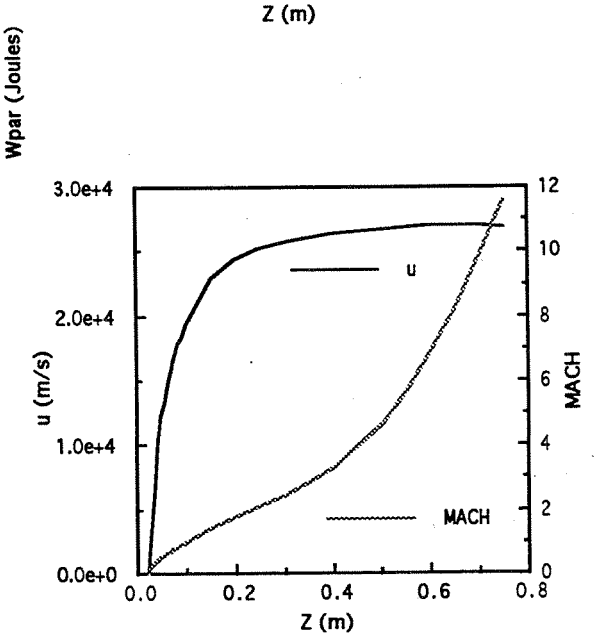

- Coupled ECR Power = 750 watts
- Argon Flow Rate = 15.0 sccm
- No Axial Heat Conduction
- No Vacuum Tank Back Pressure

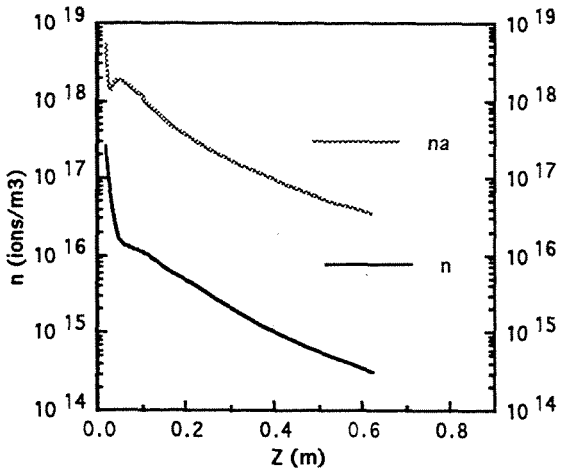

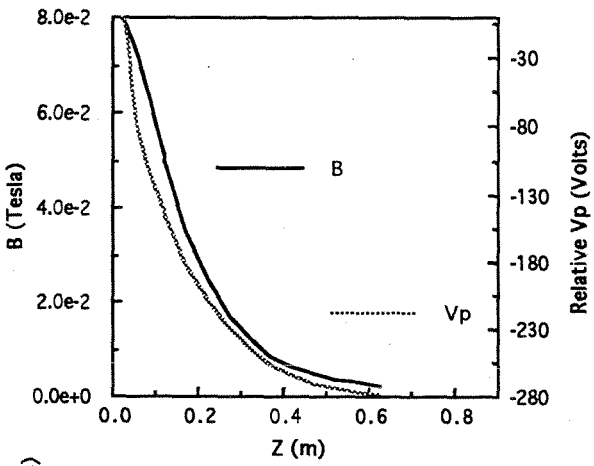

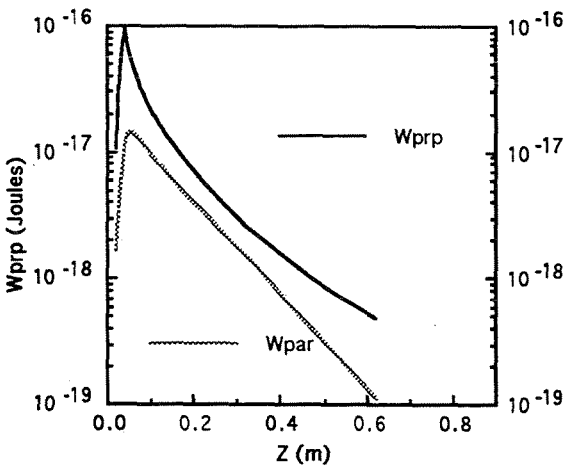

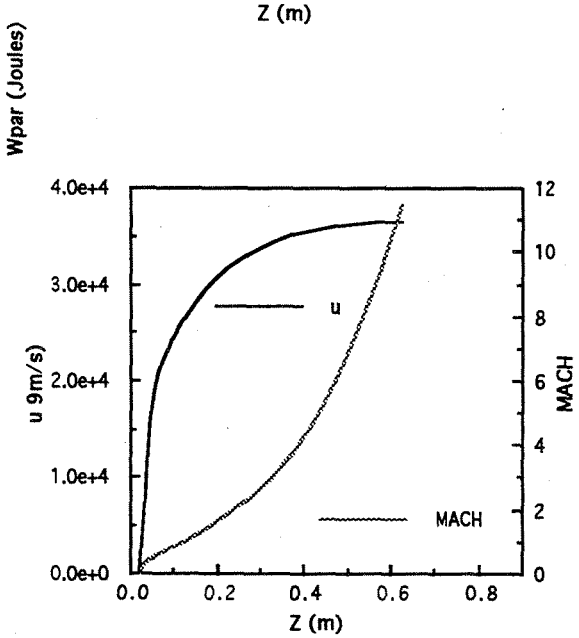

- Coupled ECR Power = 750 watts
- Argon Flow Rate = 15.0 sccm
- No Axial Heat Conduction
- Finite Vacuum Tank Back Pressure

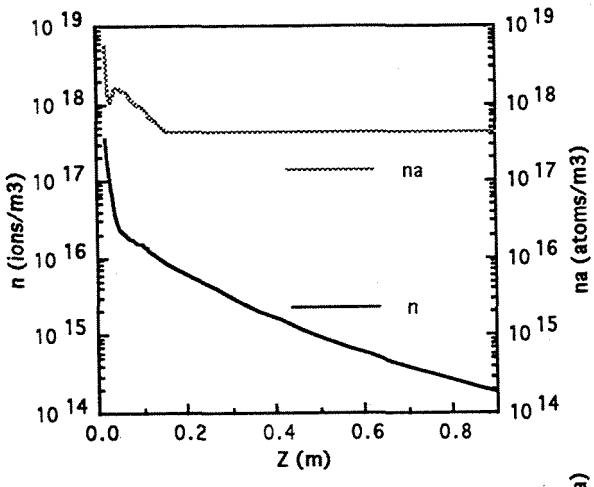

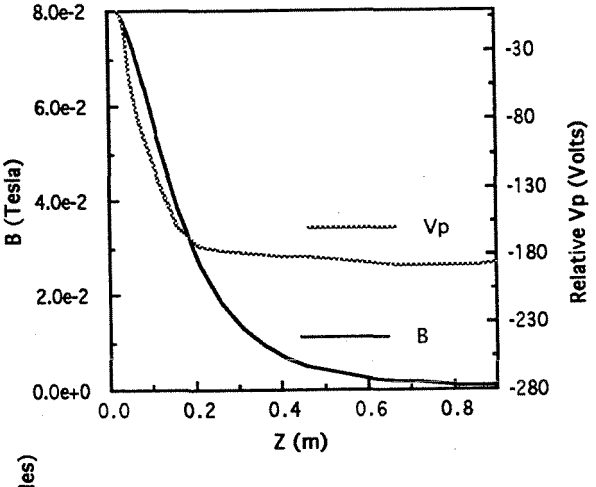

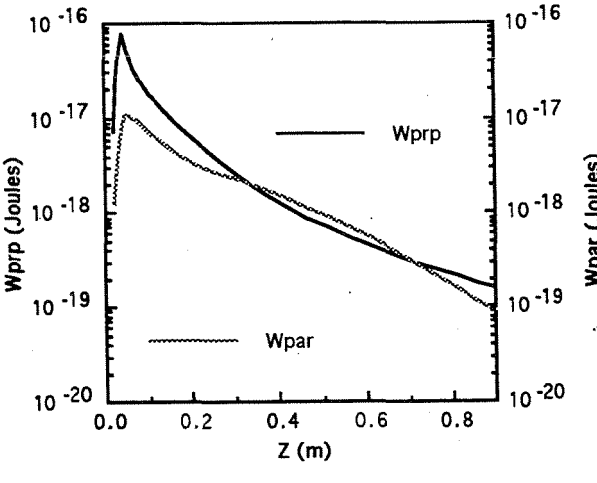

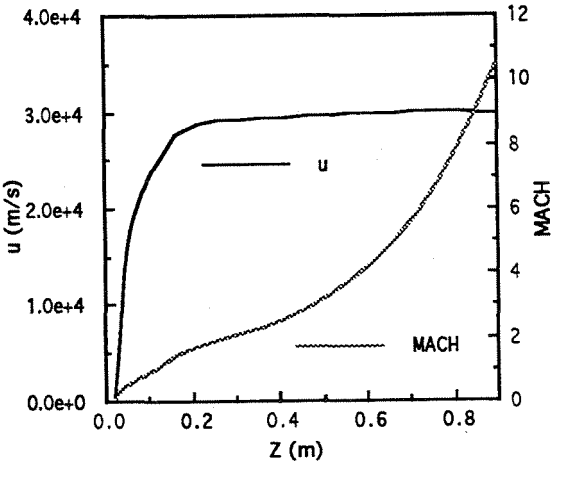

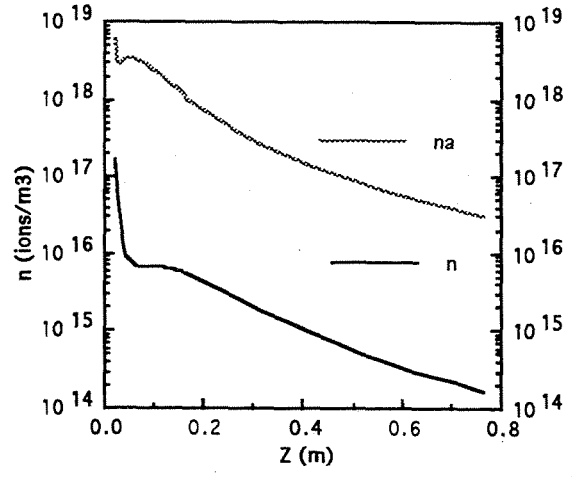

- Coupled ECR Power = 1500 watts
- Argon Flow Rate = 16.5 sccm
- No Axial Heat Conduction
- No Vacuum Tank Back Pressure

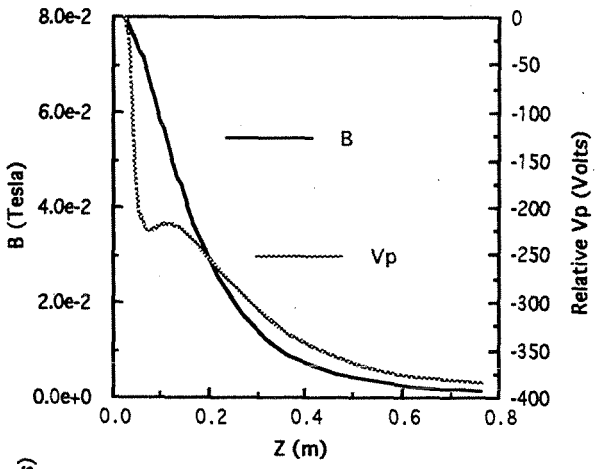

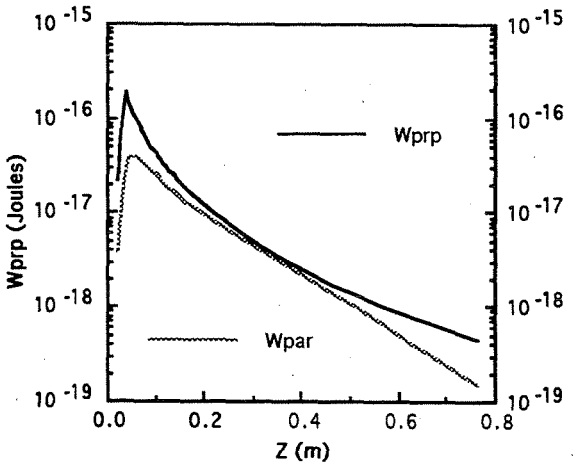

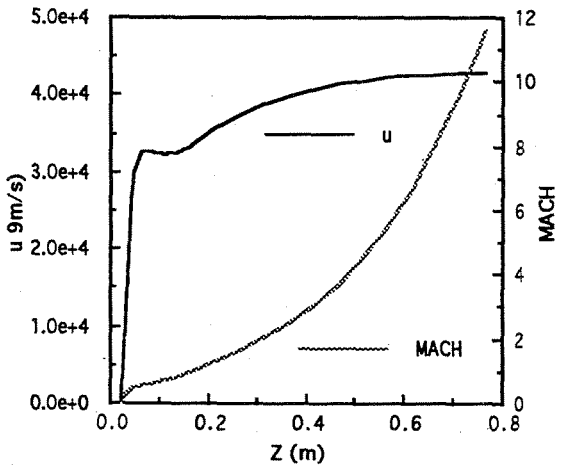

- Coupled ECR Power = 1500 watts
- Argon Flow Rate = 16.5 sccm
- No Axial Heat Conduction
- Finite Vacuum Tank Back Pressure

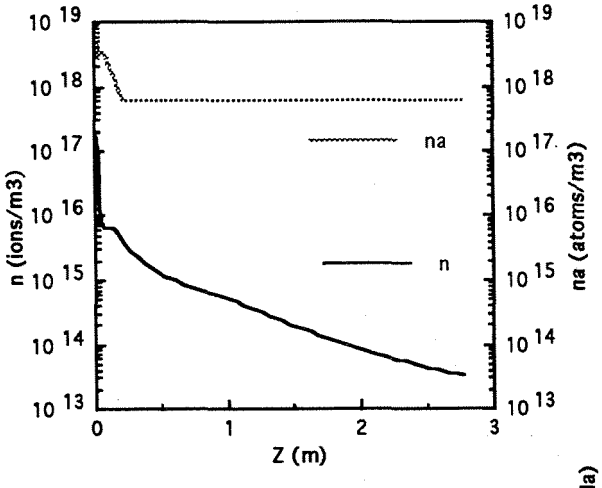

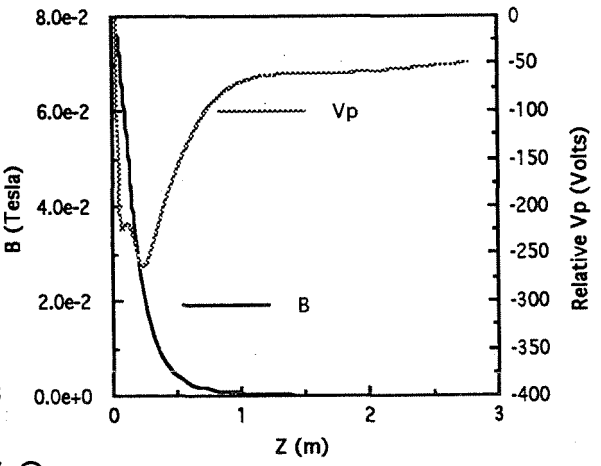

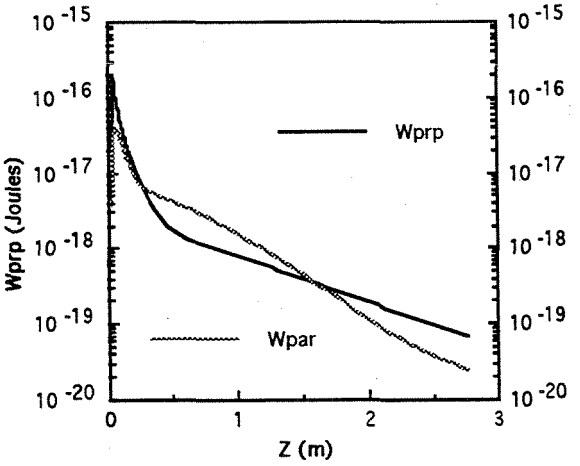

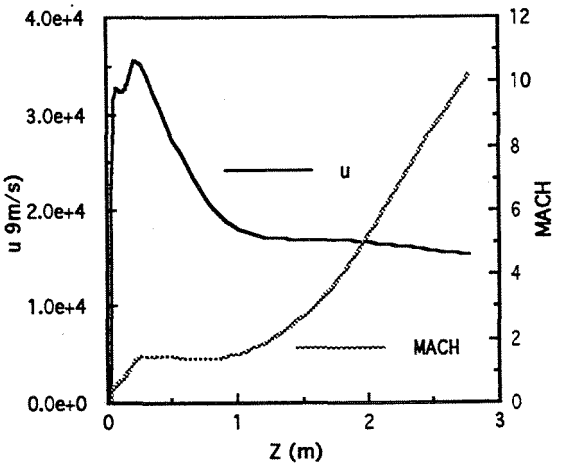

- Coupled ECR Power = 1000 watts
- Argon Flow Rate = 17.5 sccm
- No Axial Heat Conduction
- No Vacuum Tank Back Pressure

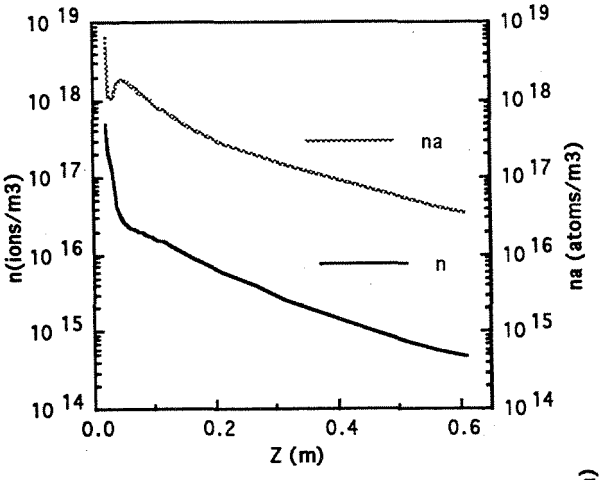

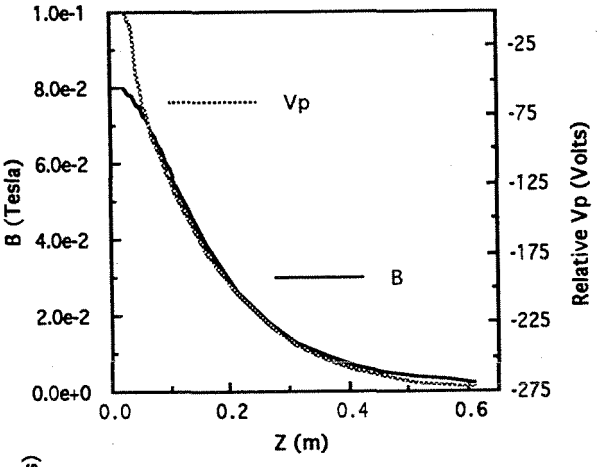

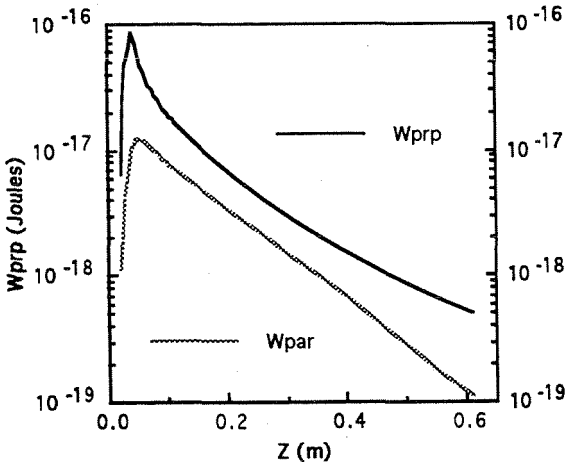

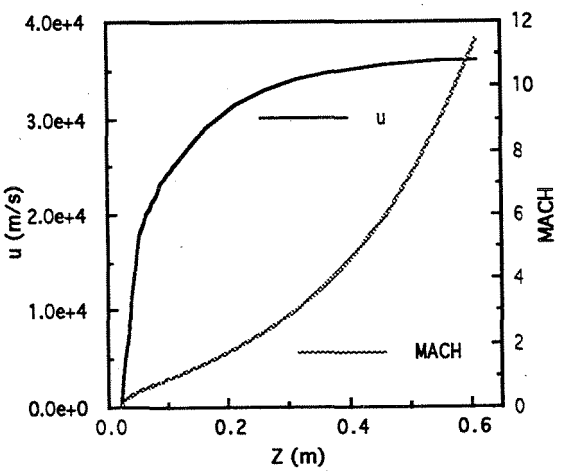

- Coupled ECR Power = 1000 watts
- Argon Flow Rate = 17.5 sccm
- No Axial Heat Conduction
- Finite Vacuum Tank Back Pressure

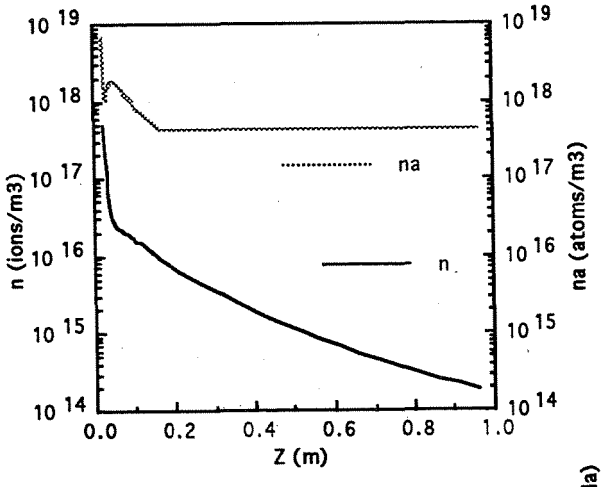

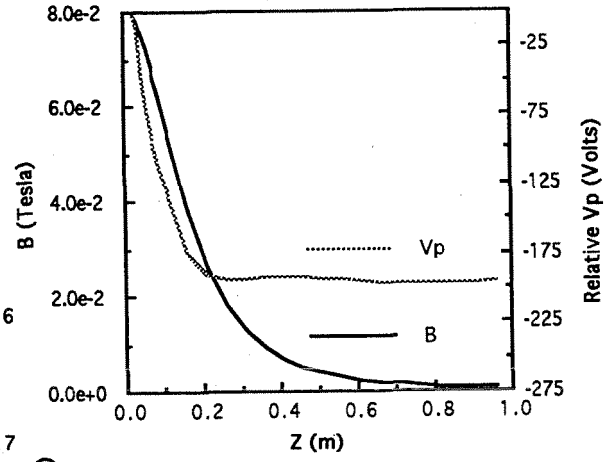

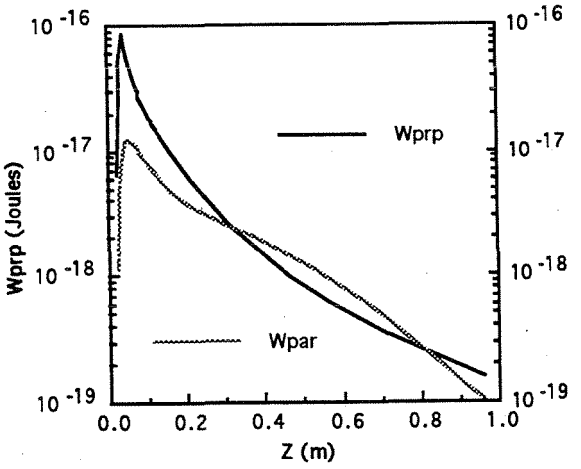

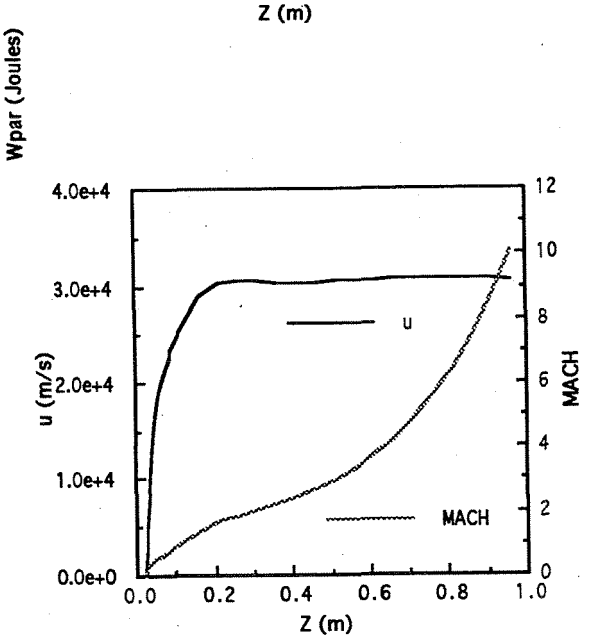

- Coupled ECR Power = 1500 watts
- Argon Flow Rate = 17.5 sccm
- No Axial Heat Conduction
- No Vacuum Tank Back Pressure

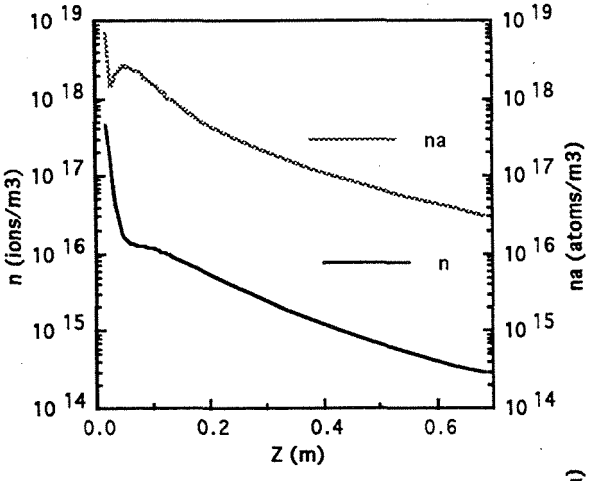

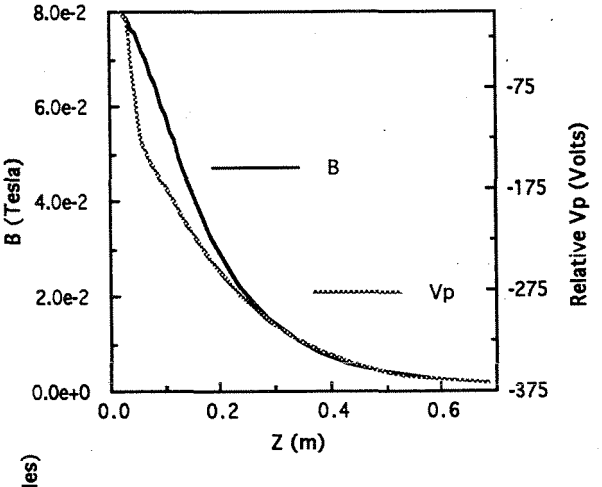

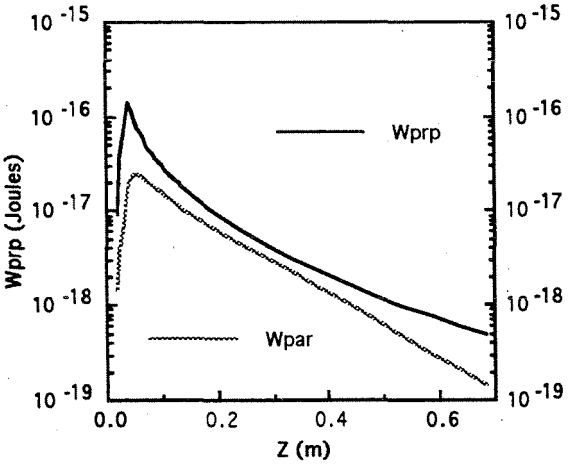

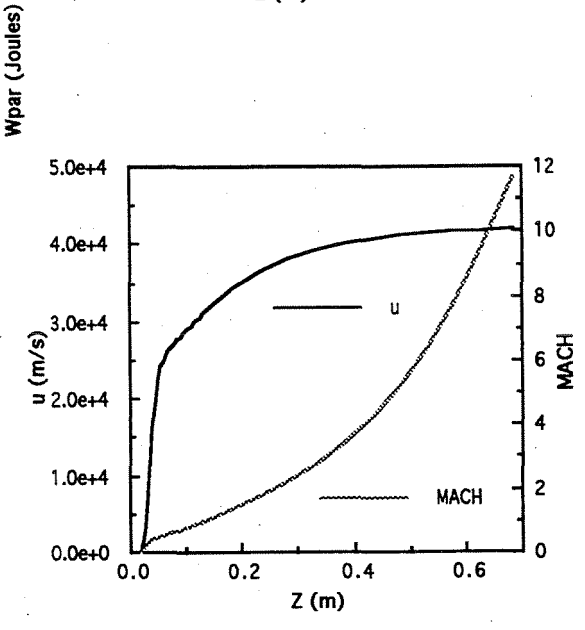

- Coupled ECR Power = 1500 watts
- Argon Flow Rate = 17.5 sccm
- No Axial Heat Conduction
- Finite Vacuum Tank Back Pressure

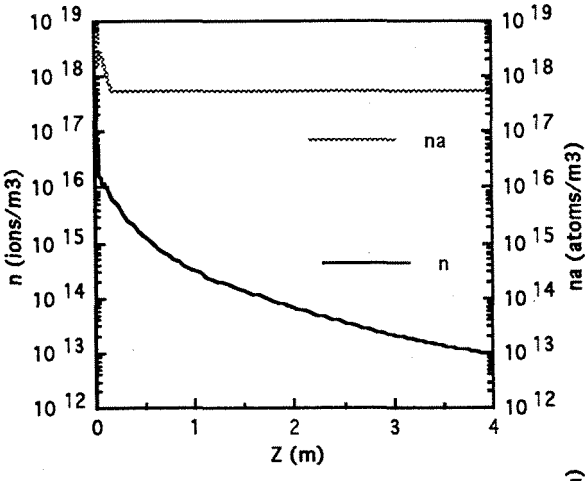

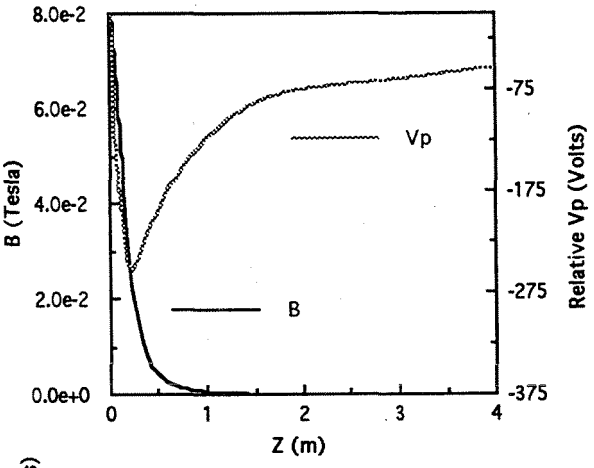

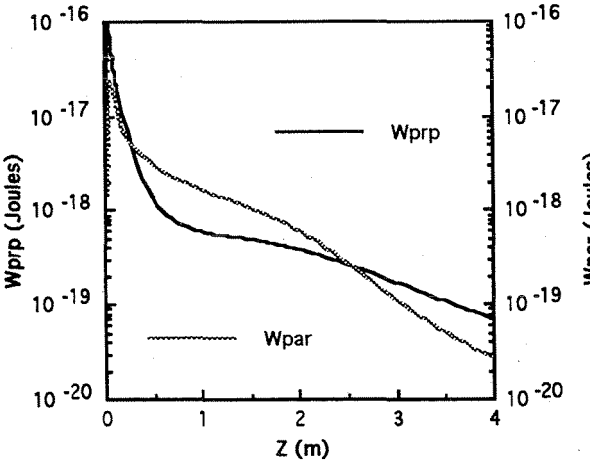

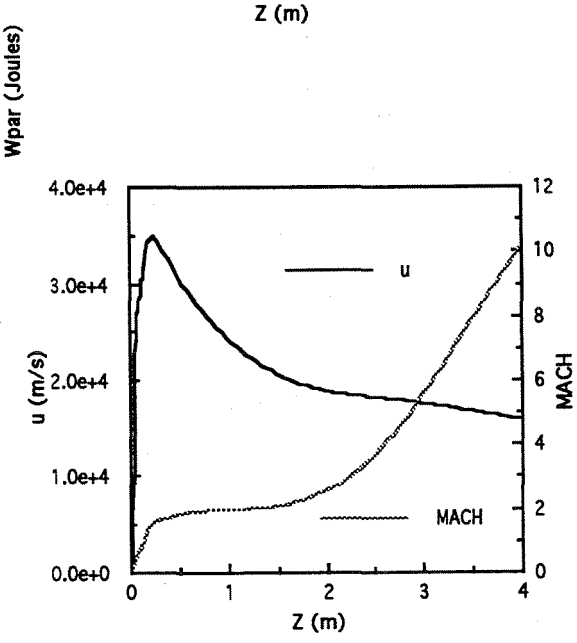

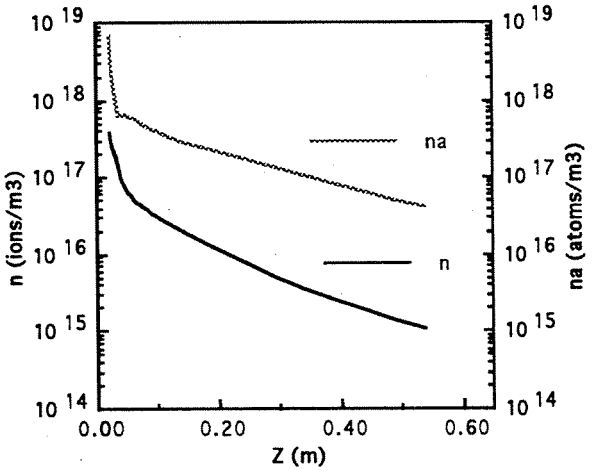

- Coupled ECR Power = 300 watts
- Argon Flow Rate = 17.5 sccm
- No Axial Heat Conduction
- No Vacuum Tank Back Pressure

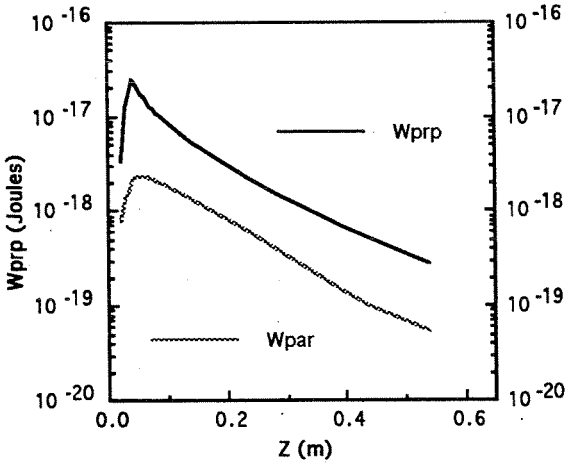

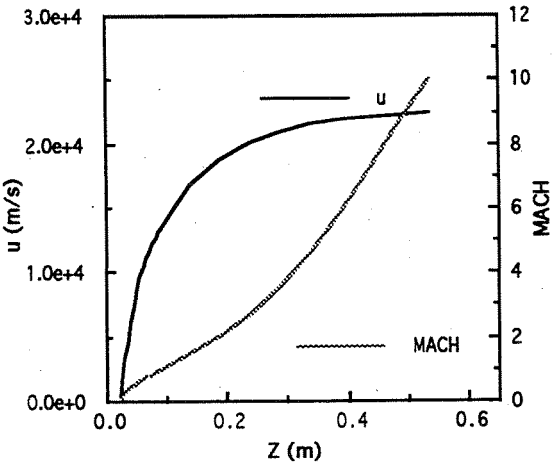

- Coupled ECR Power = 300 watts
- Argon Flow Rate = 17.5 sccm
- No Axial Heat Conduction
- Finite Vacuum Tank Back Pressure

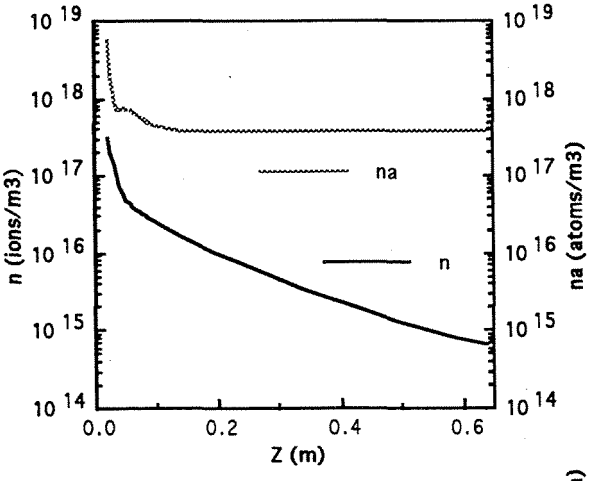

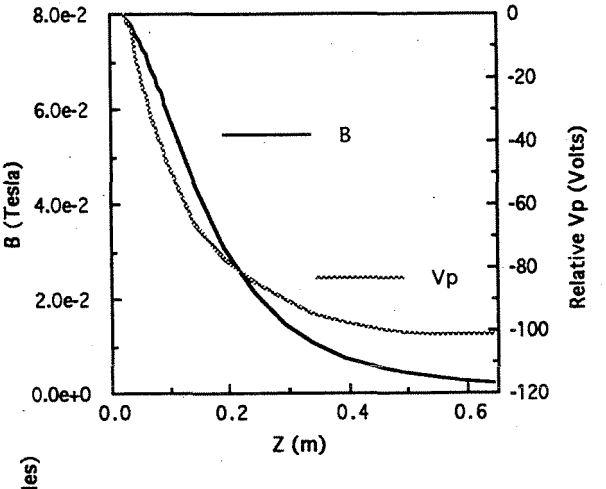

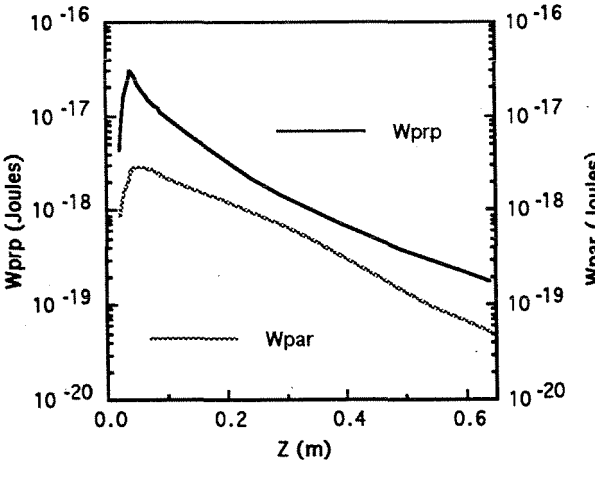

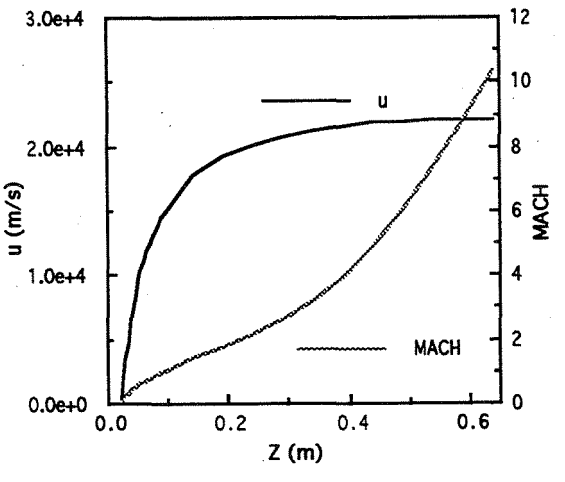

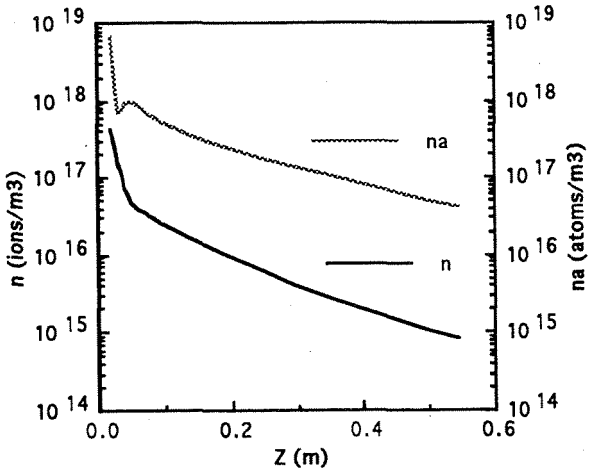

- Coupled ECR Power = 500 watts
- Argon Flow Rate = 17.5 sccm
- No Axial Heat Conduction
- No Vacuum Tank Back Pressure

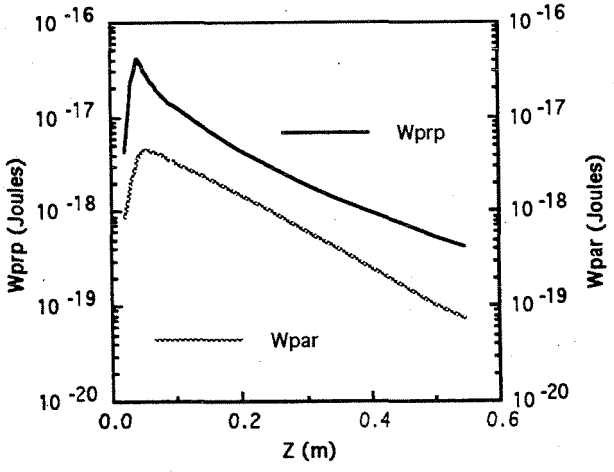

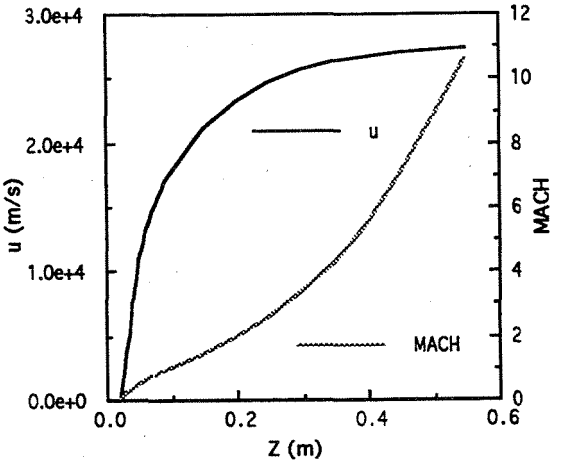

- Coupled ECR Power = 750 watts
- Argon Flow Rate = 17.5 sccm
- No Axial Heat Conduction
- No Vacuum Tank Back Pressure

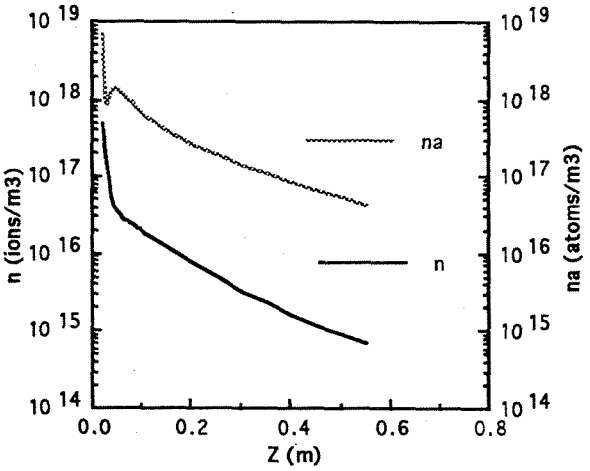

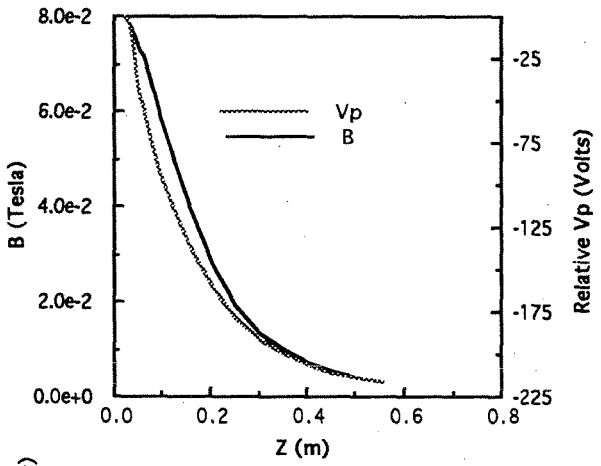

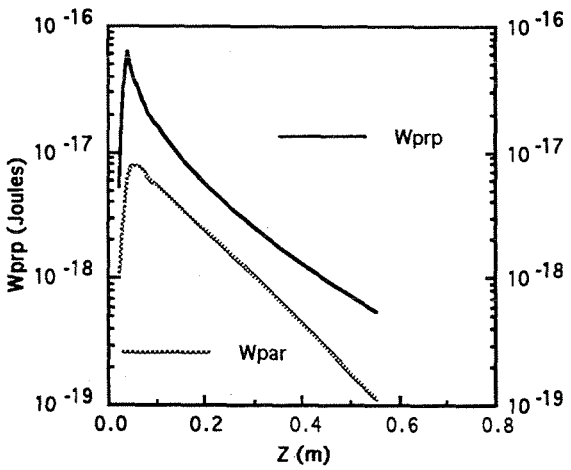

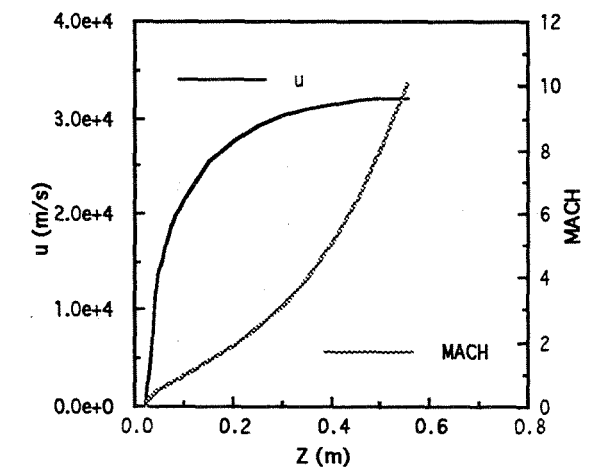

- Coupled ECR Power = 750 watts
- Argon Flow Rate = 17.5 sccm
- No Axial Heat Conduction
- Finite Vacuum Tank Back Pressure

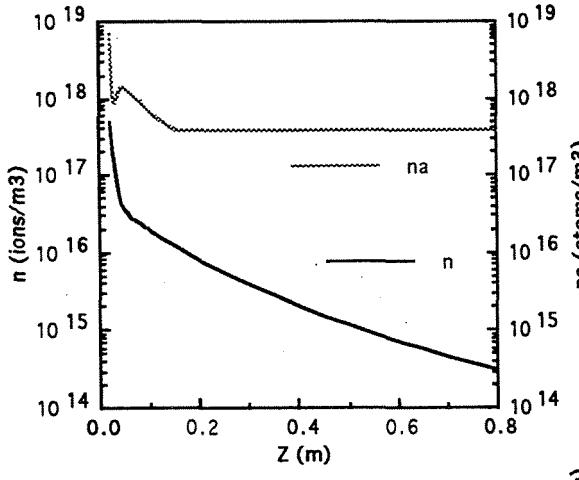

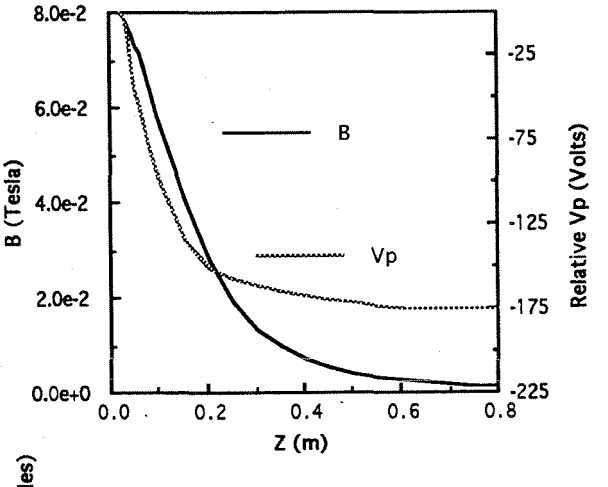

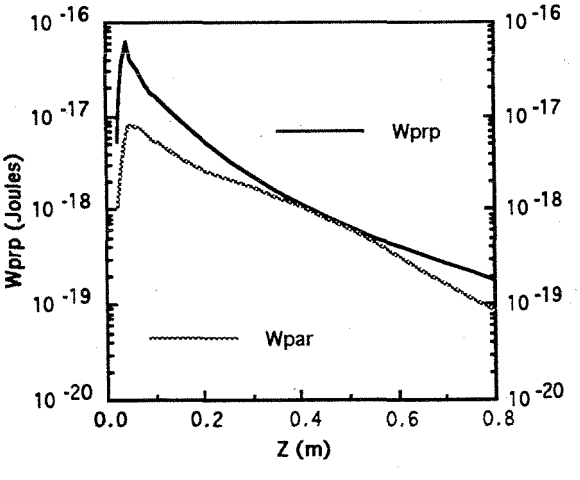

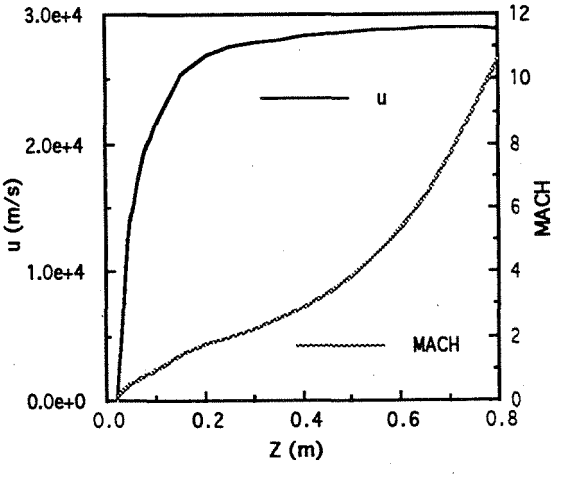

- Coupled ECR Power = 1000 watts
- Argon Flow Rate = 20.0 sccm
- No Axial Heat Conduction
- No Vacuum Tank Back Pressure

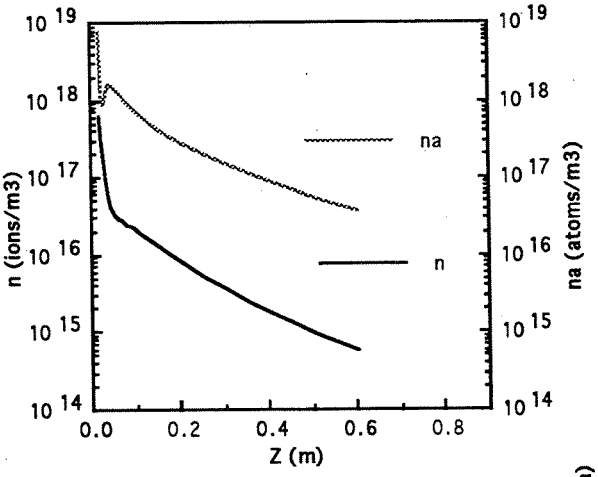

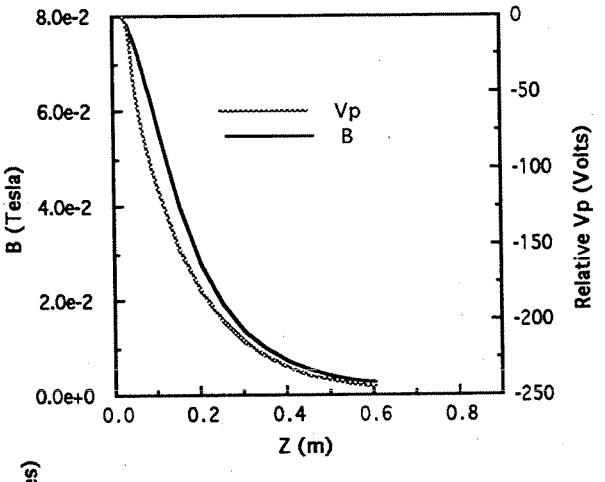

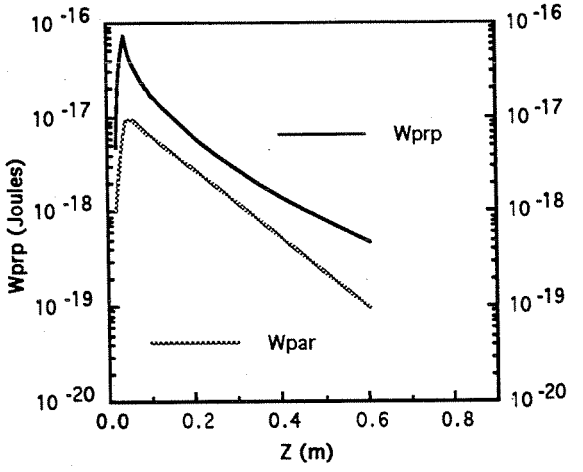

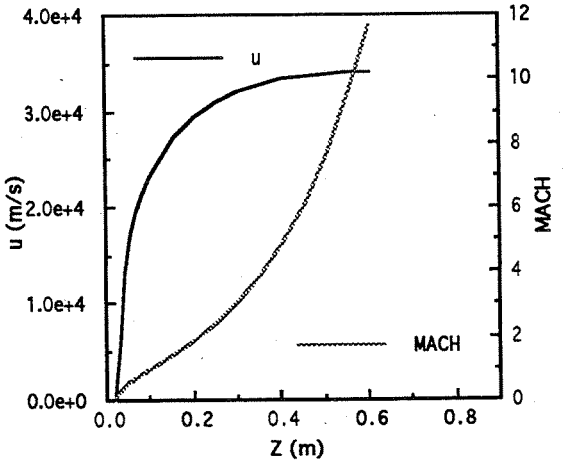

- Coupled ECR Power = 1000 watts
- Argon Flow Rate = 20.0 sccm
- No Axial Heat Conduction
- Finite Vacuum Tank Back Pressure

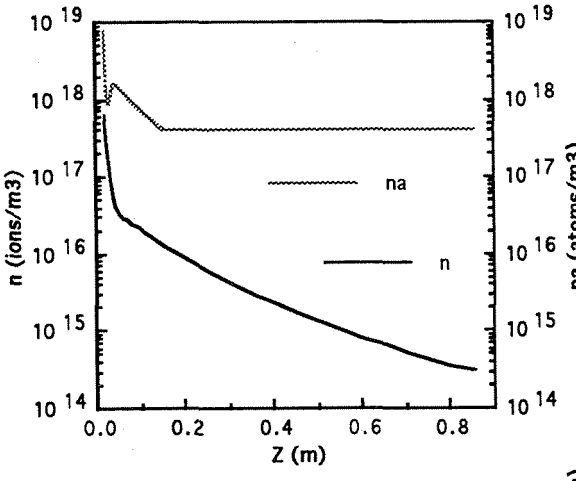

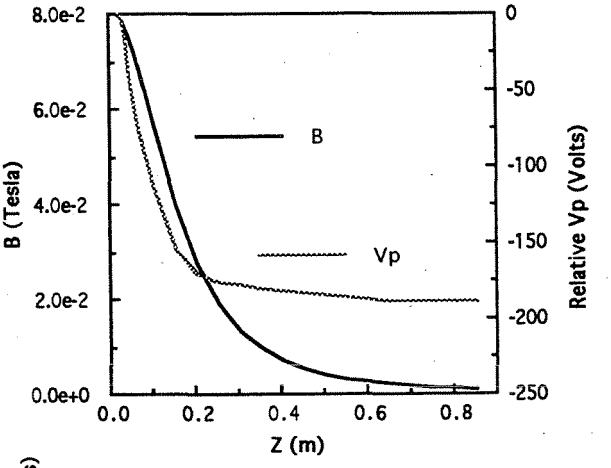

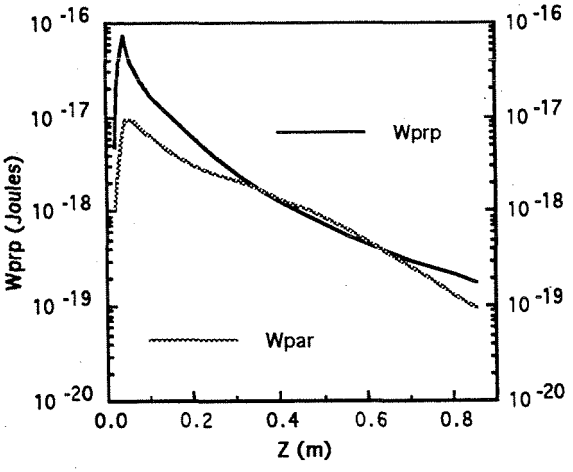

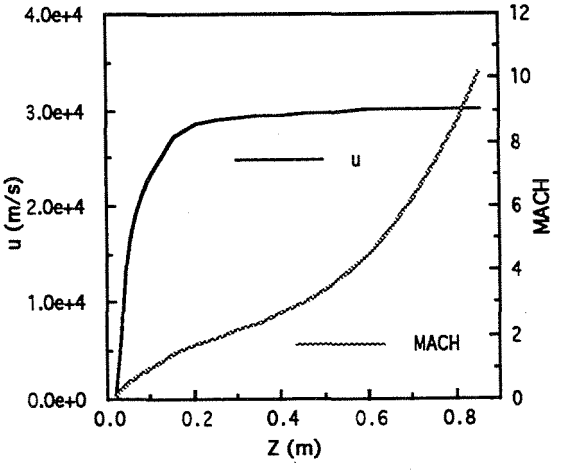

- Coupled ECR Power = 1500 watts
- Argon Flow Rate = 20.0 sccm
- No Axial Heat Conduction
- No Vacuum Tank Back Pressure

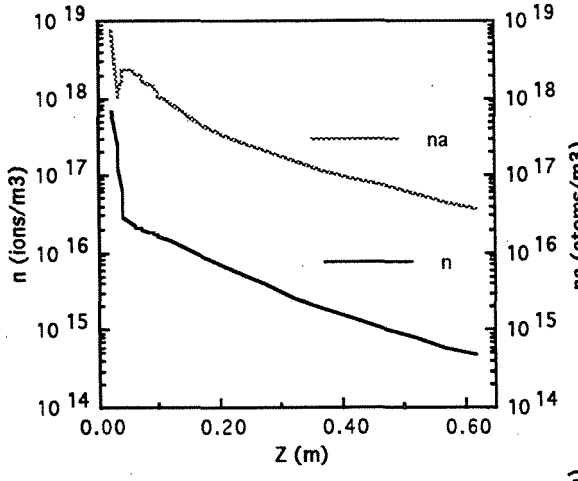

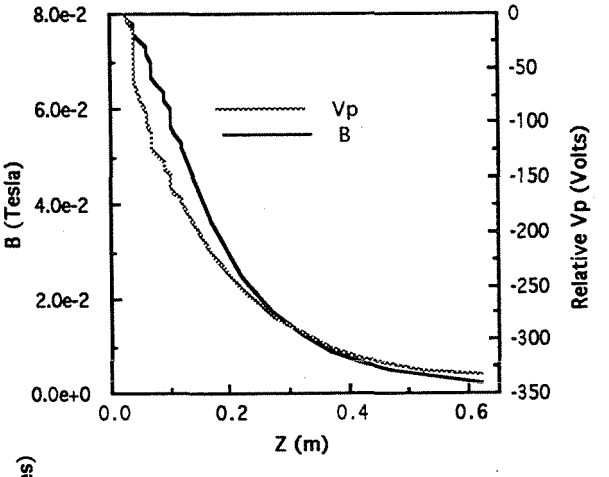

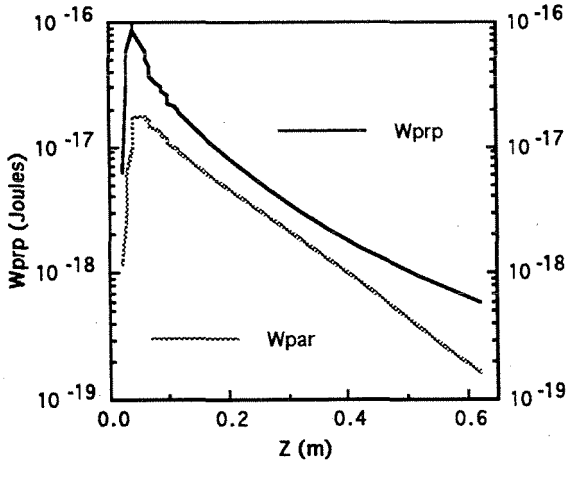

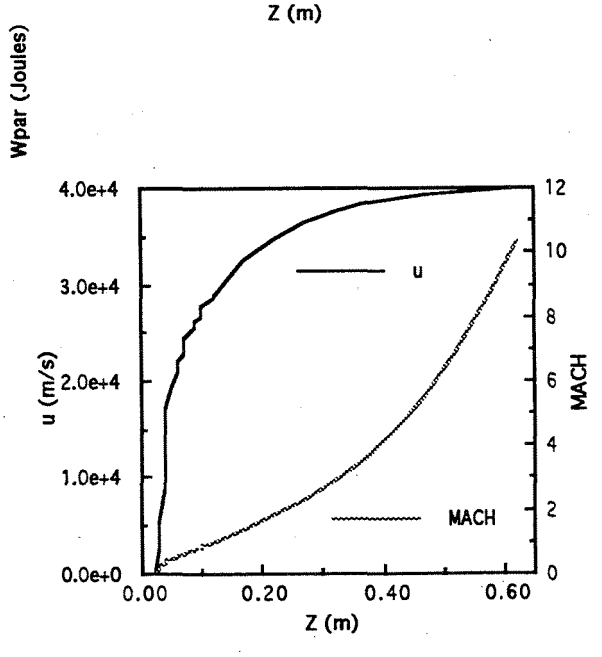

- Coupled ECR Power = 1500 watts
- Argon Flow Rate = 20.0 sccm
- No Axial Heat Conduction
- Finite Vacuum Tank Back Pressure

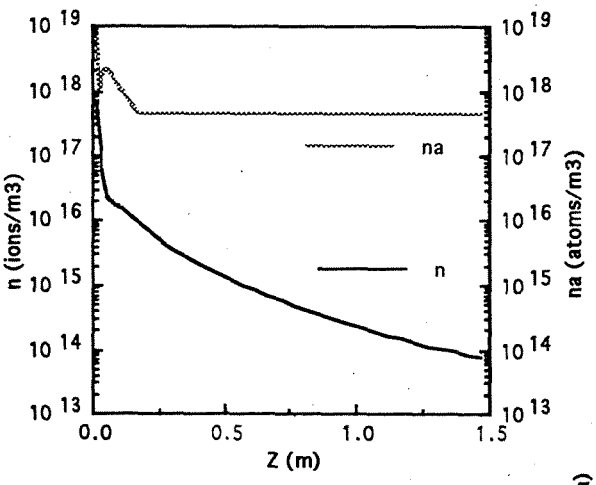

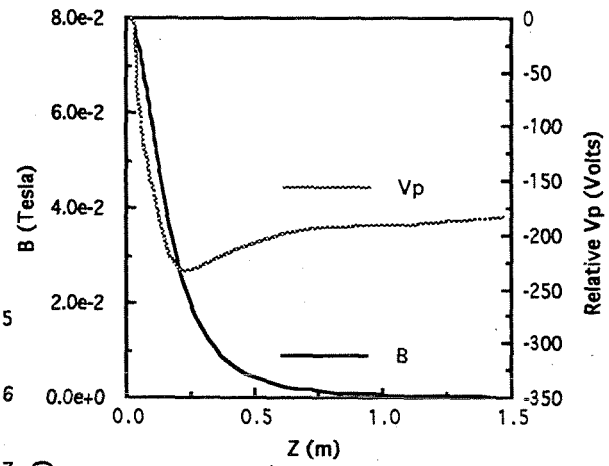

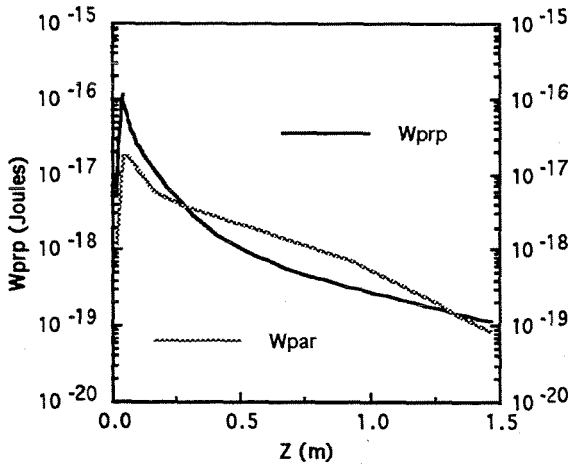

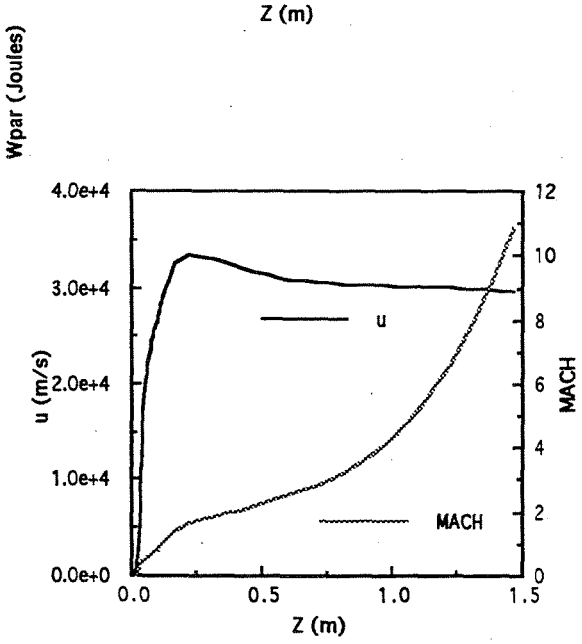

- Coupled ECR Power = 2000 watts
- Argon Flow Rate = 20.0 sccm
- No Axial Heat Conduction
- No Vacuum Tank Back Pressure

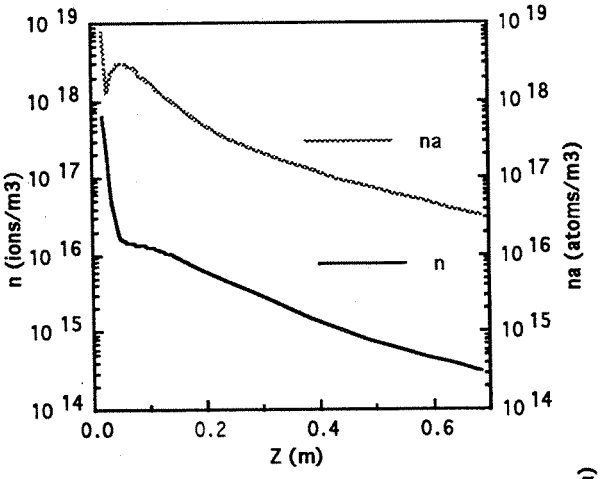

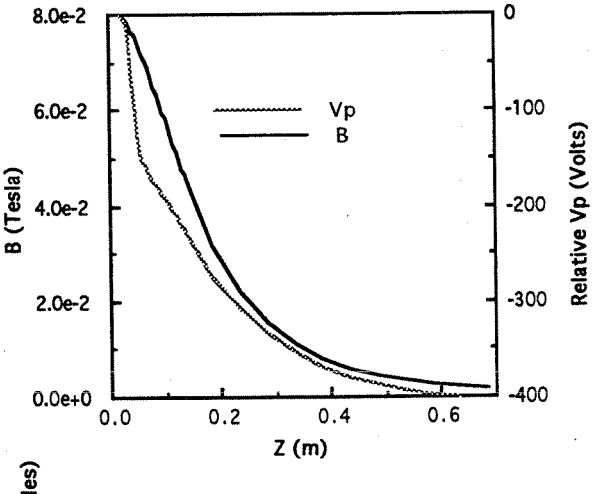

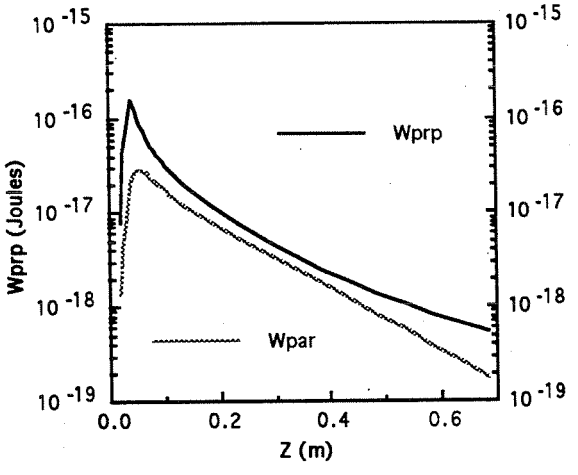

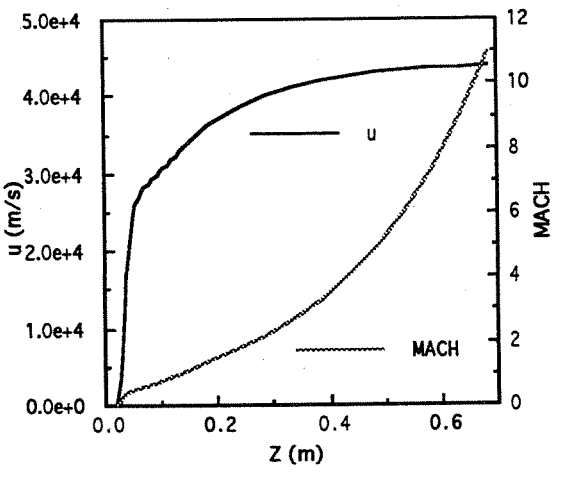

- Coupled ECR Power = 2000 watts
- Argon Flow Rate = 20.0 sccm
- No Axial Heat Conduction
- Finite Vacuum Tank Back Pressure

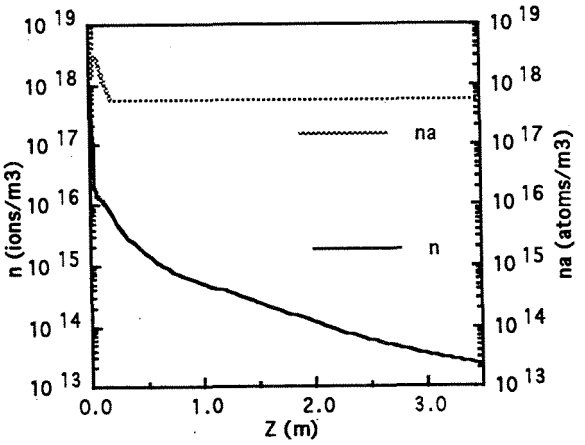

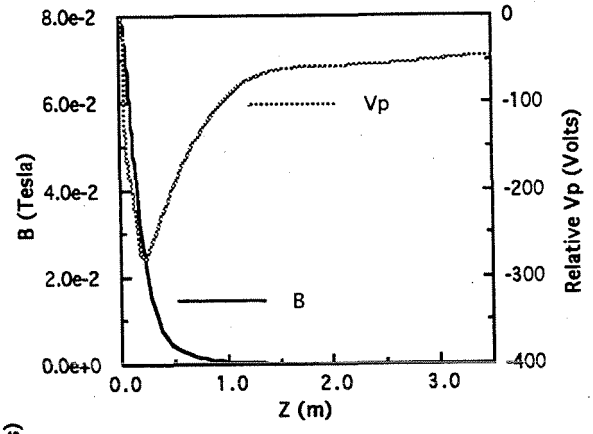

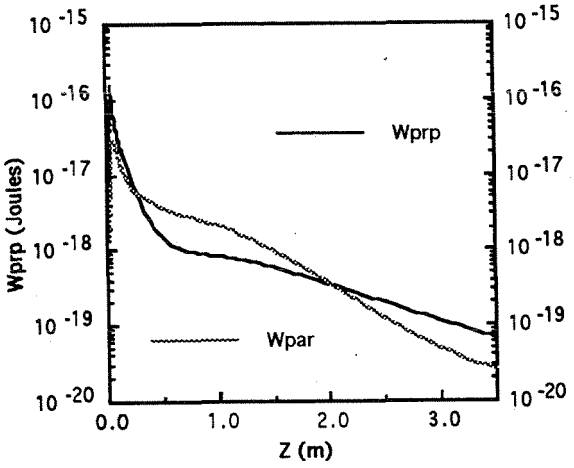

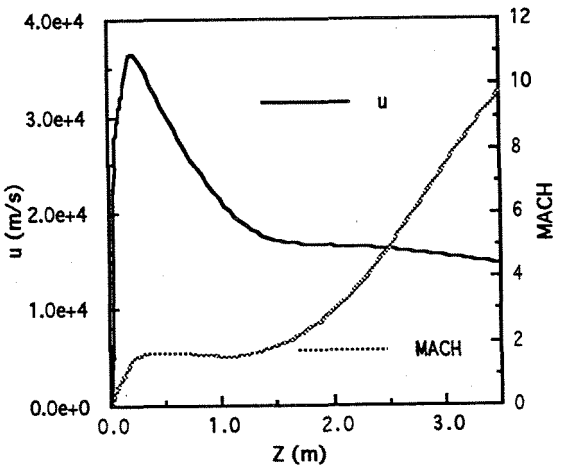

- Coupled ECR Power = 500 watts
- Argon Flow Rate = 20.0 sccm
- No Axial Heat Conduction
- No Vacuum Tank Back Pressure

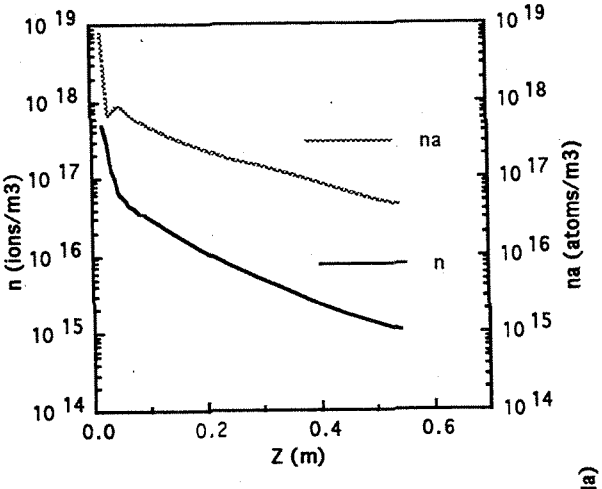

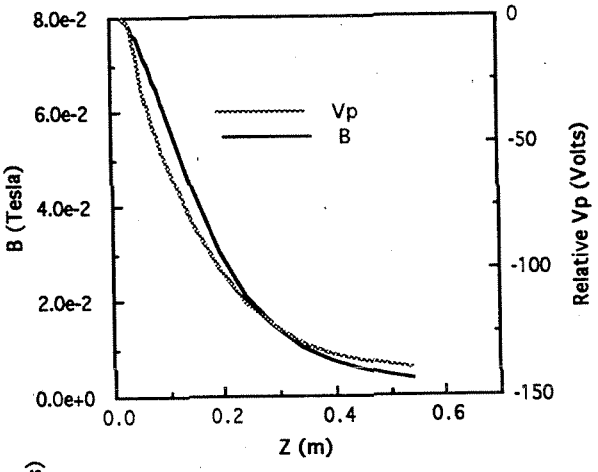

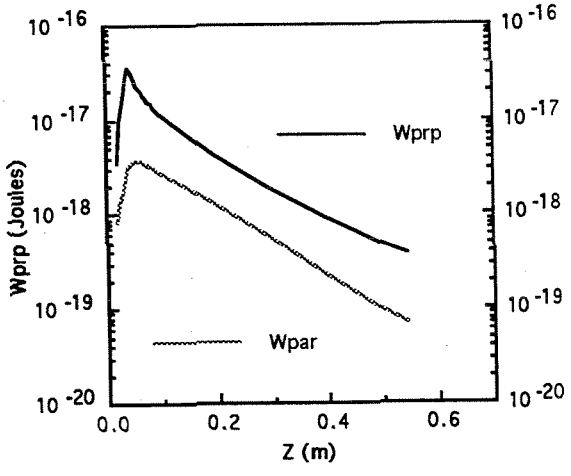

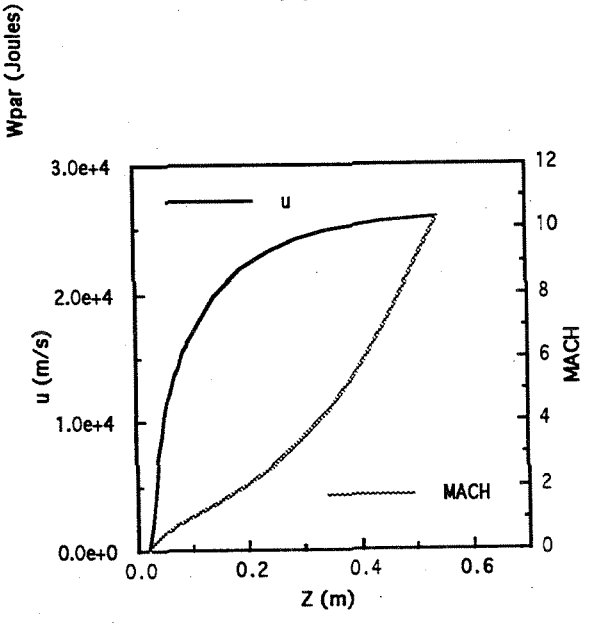

- Coupled ECR Power = 500 watts
- Argon Flow Rate = 20.0 sccm
- No Axial Heat Conduction
- Finite Vacuum Tank Back Pressure

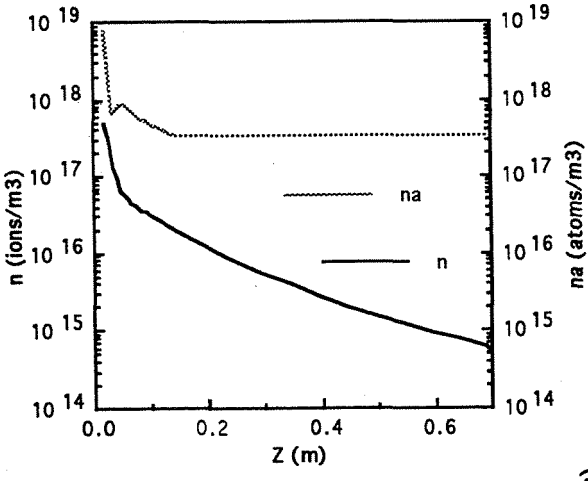

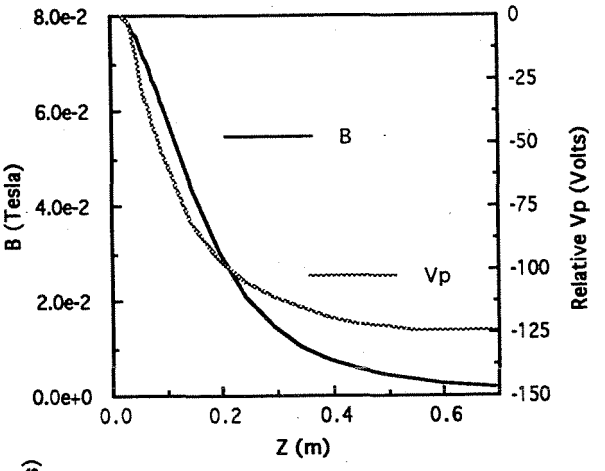

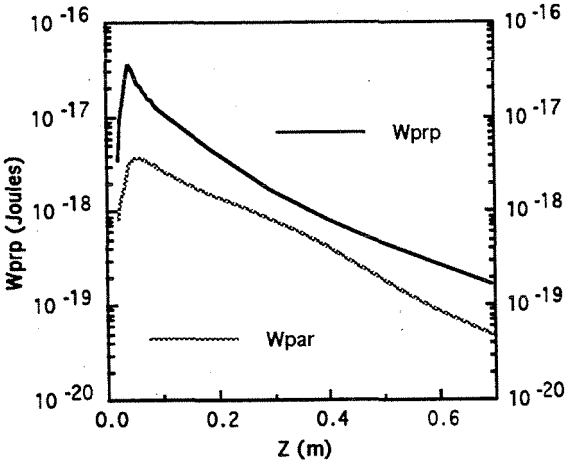

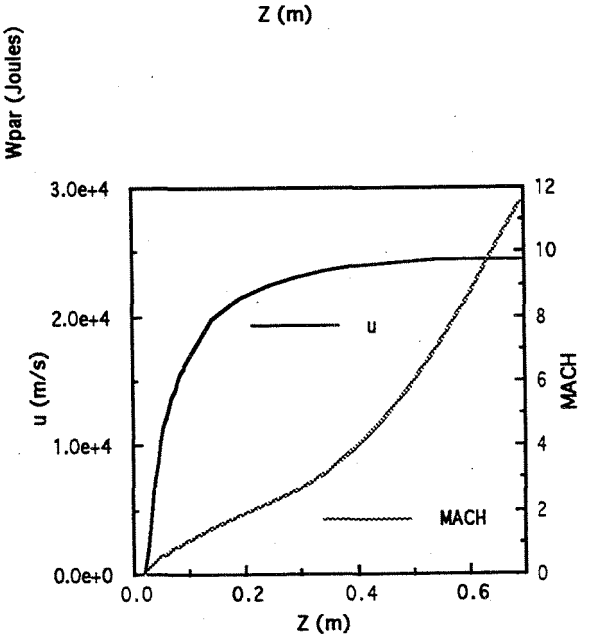

- Coupled ECR Power = 750 watts
- Argon Flow Rate = 20.0 sccm
- No Axial Heat Conduction
- No Vacuum Tank Back Pressure

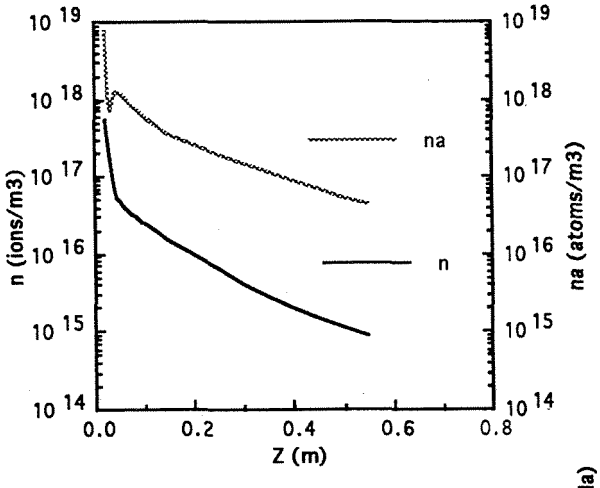

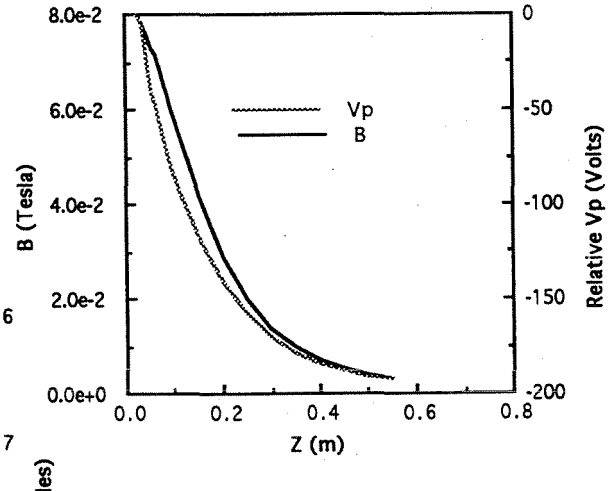

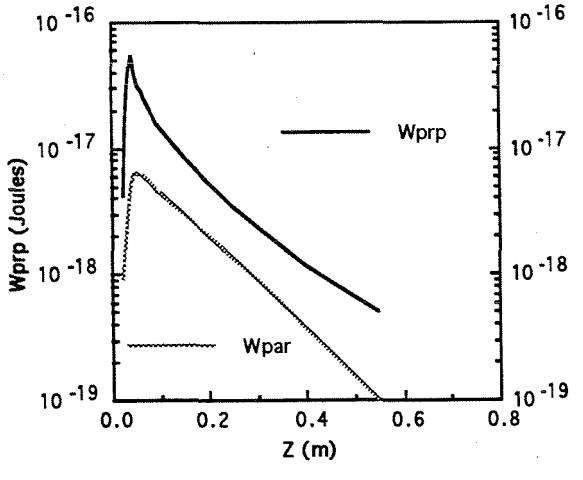

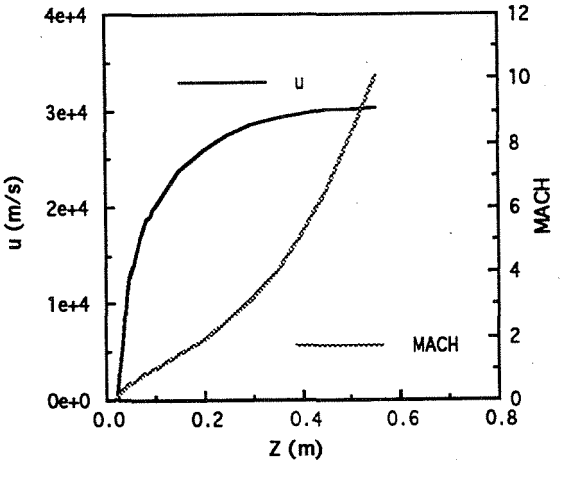

- Coupled ECR Power = 750 watts
- Argon Flow Rate = 20.0 sccm
- No Axial Heat Conduction
- Finite Vacuum Tank Back Pressure

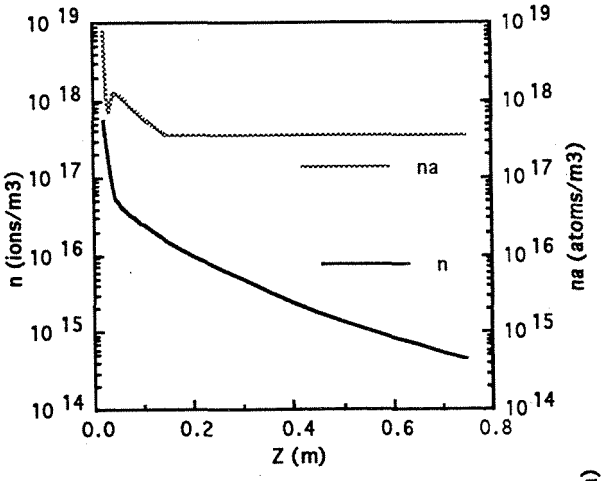

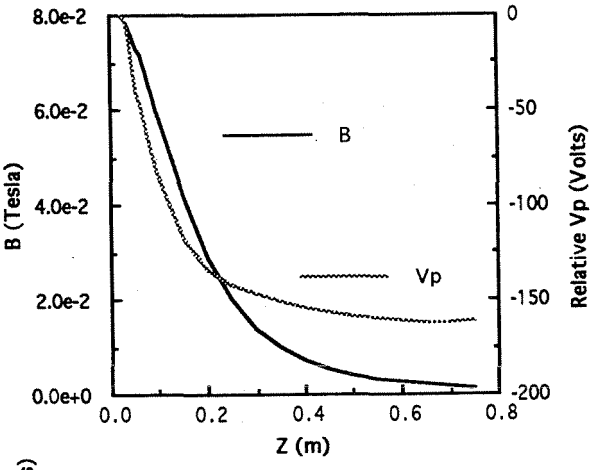

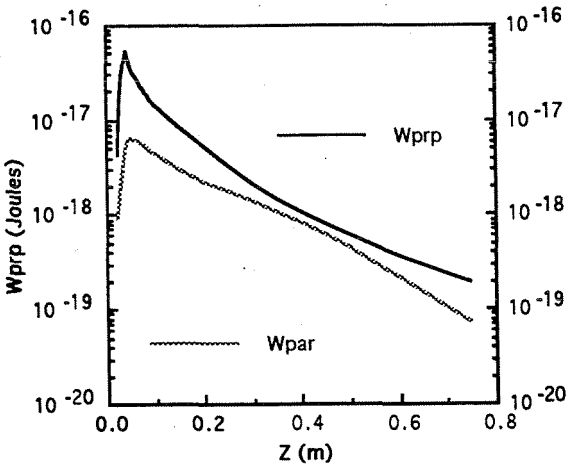

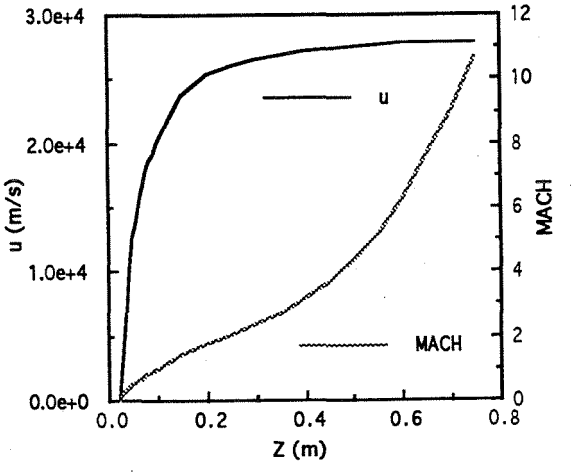

- Coupled ECR Power = 1000 watts
- Argon Flow Rate = 25.0 sccm
- No Axial Heat Conduction
- No Vacuum Tank Back Pressure

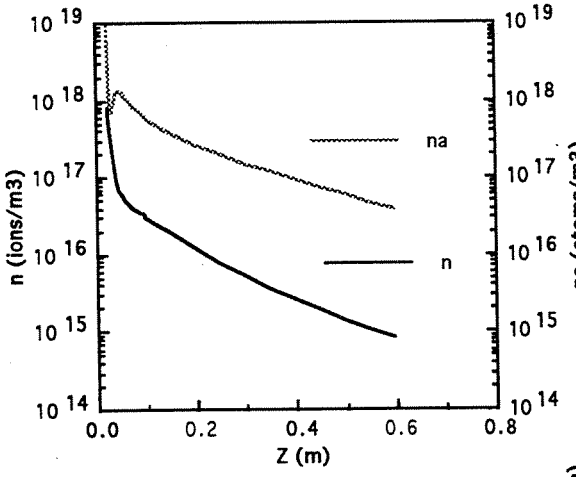

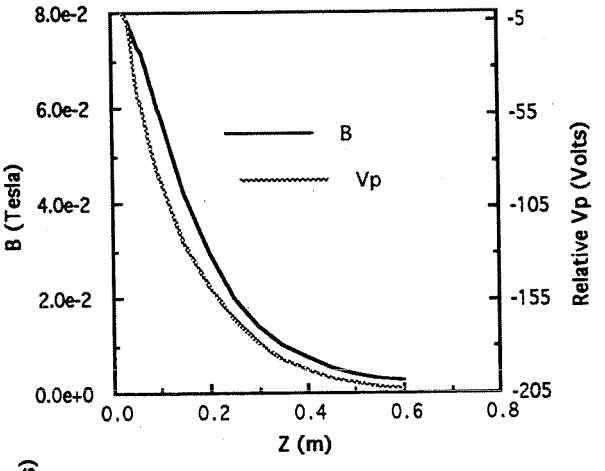

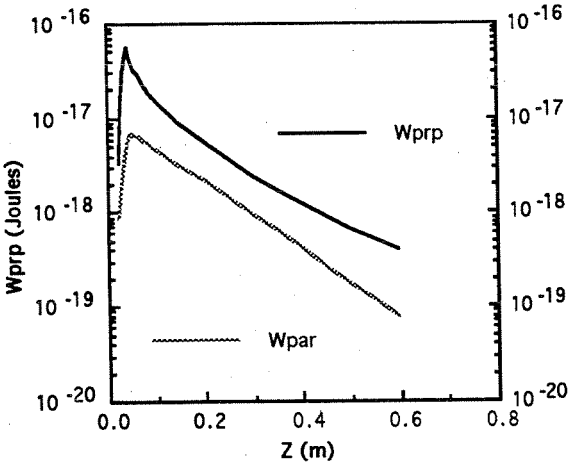

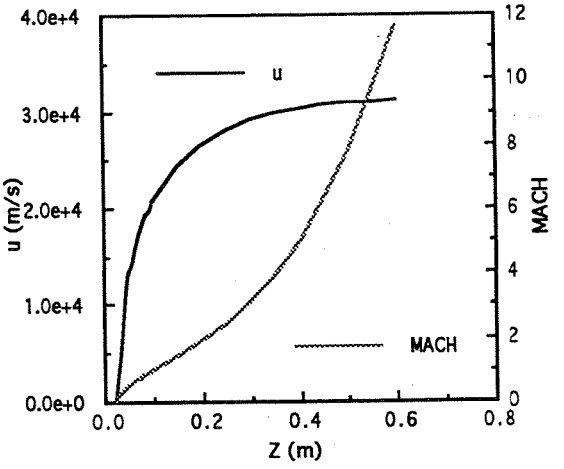

- Coupled ECR Power = 1500 watts
- Argon Flow Rate = 25.0 sccm
- No Axial Heat Conduction
- Finite Vacuum Tank Back Pressure

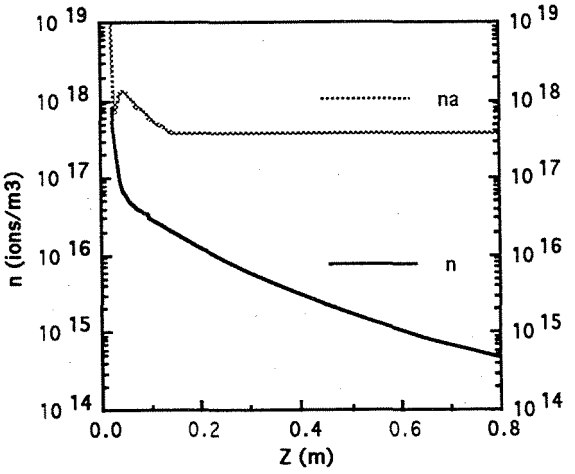

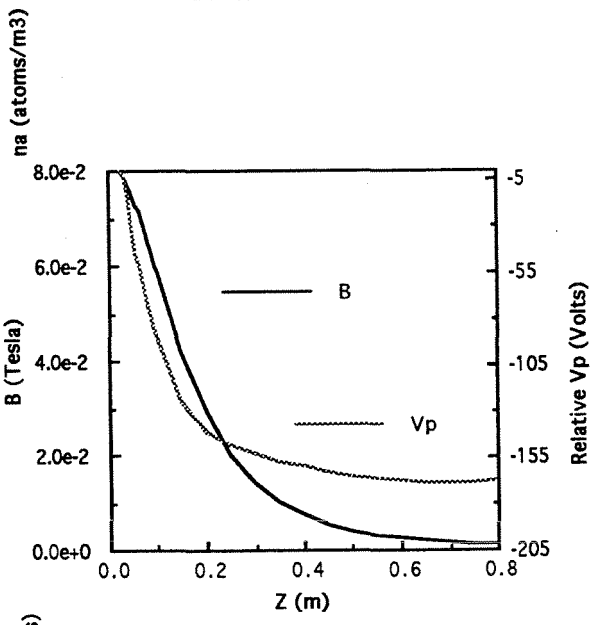

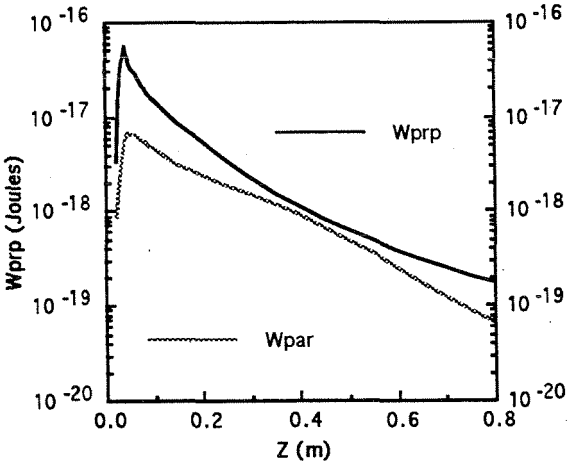

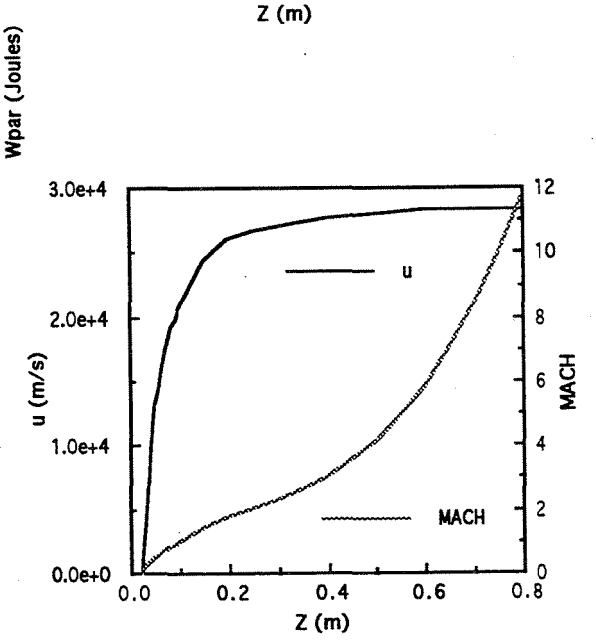

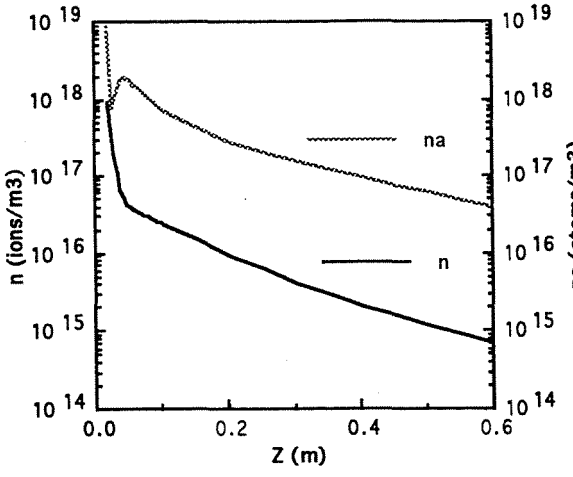

- Coupled ECR Power = 1500 watts
- Argon Flow Rate = 25.0 sccm
- No Axial Heat Conduction
- No Vacuum Tank Back Pressure

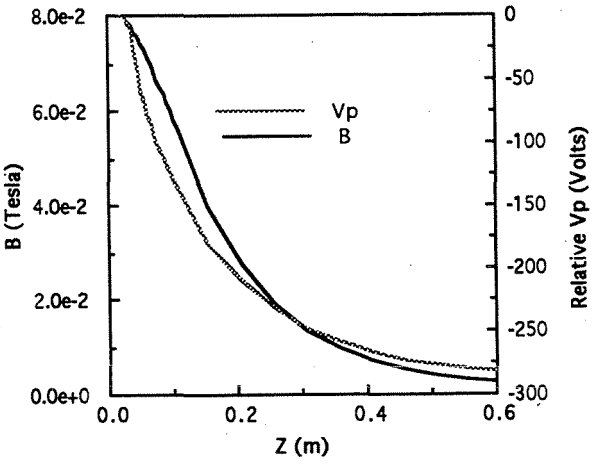

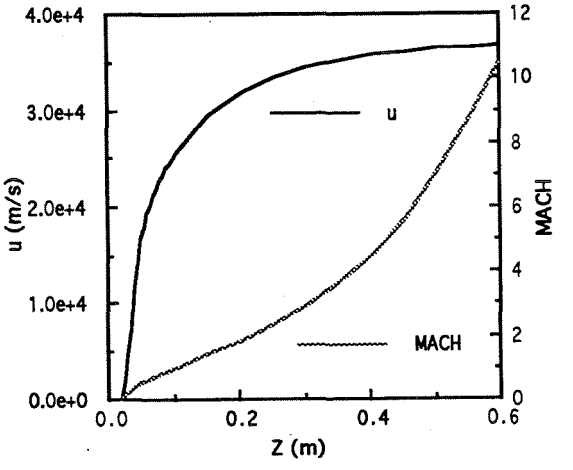

- Coupled ECR Power = 1500 watts
- Argon Flow Rate = 25.0 sccm
- No Axial Heat Conduction
- Finite Vacuum Tank Back Pressure

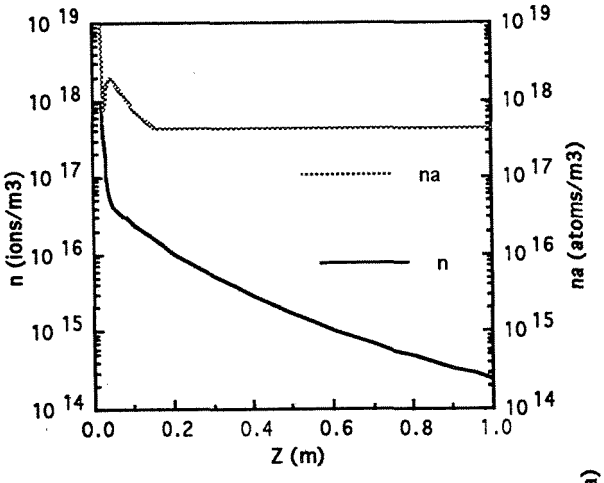

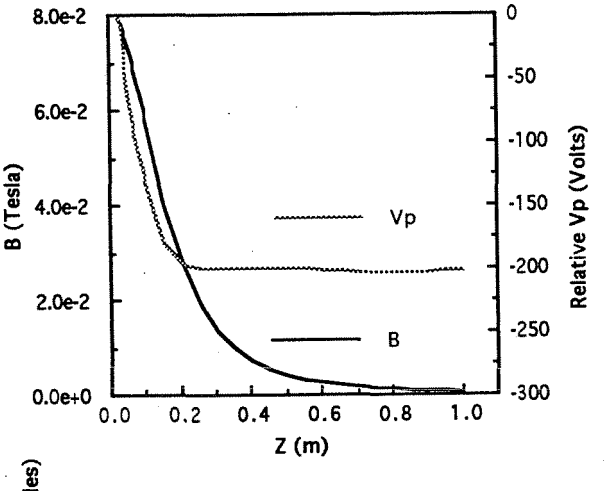

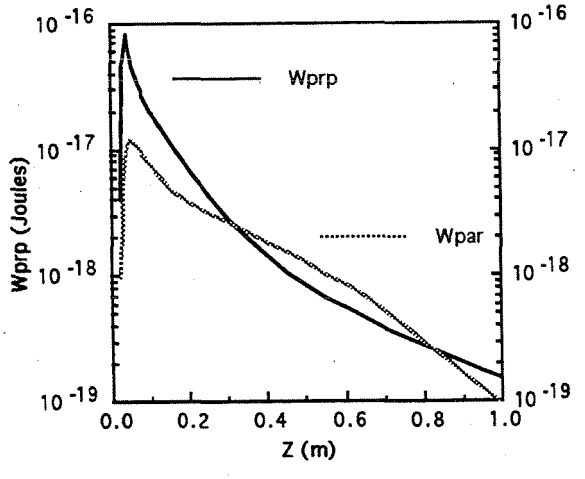

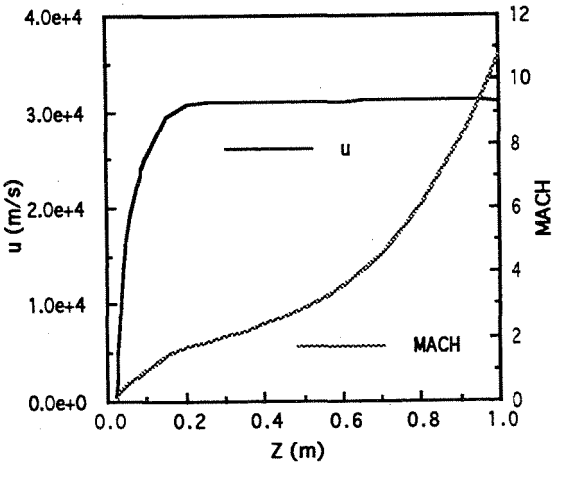

- Coupled ECR Power = 2000 watts
- Argon Flow Rate = 25.0 sccm
- No Axial Heat Conduction
- No Vacuum Tank Back Pressure

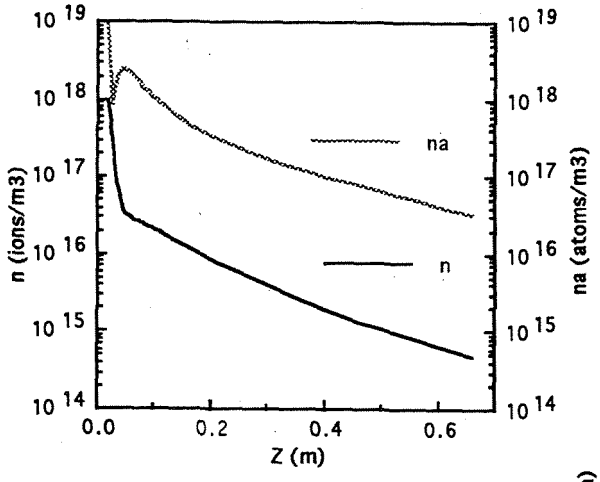

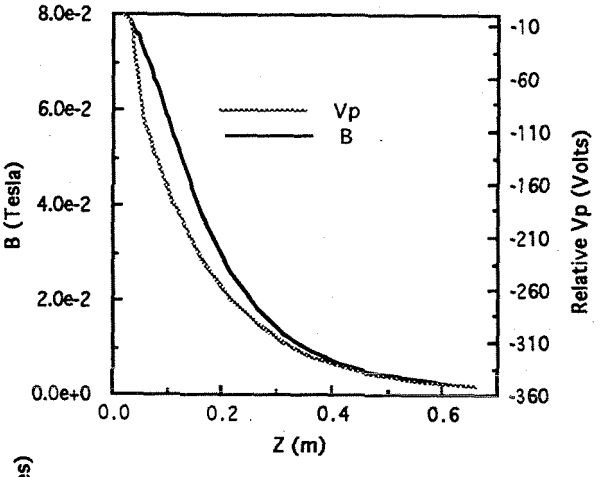

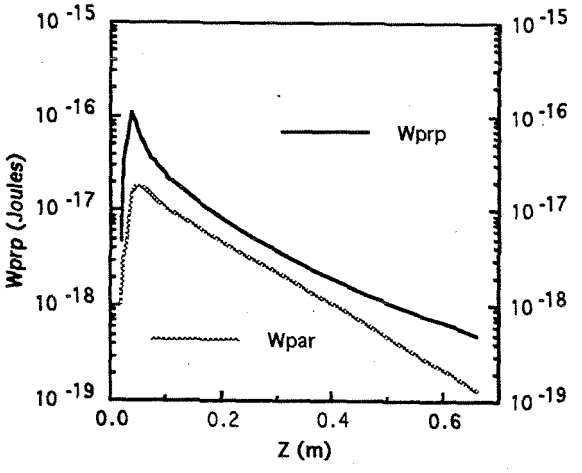

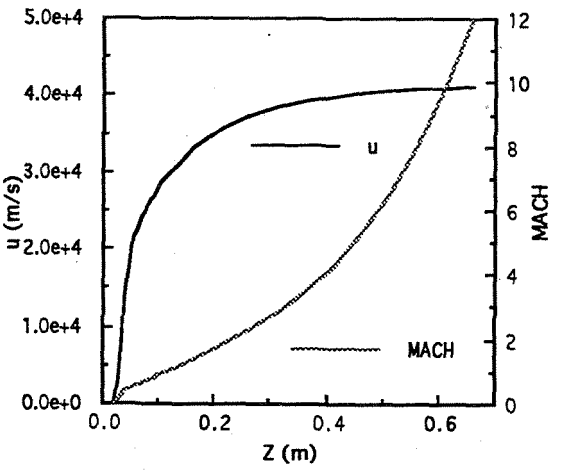

- Coupled ECR Power = 2000 watts
- Argon Flow Rate = 25.0 sccm
- No Axial Heat Conduction
- Finite Vacuum Tank Back Pressure

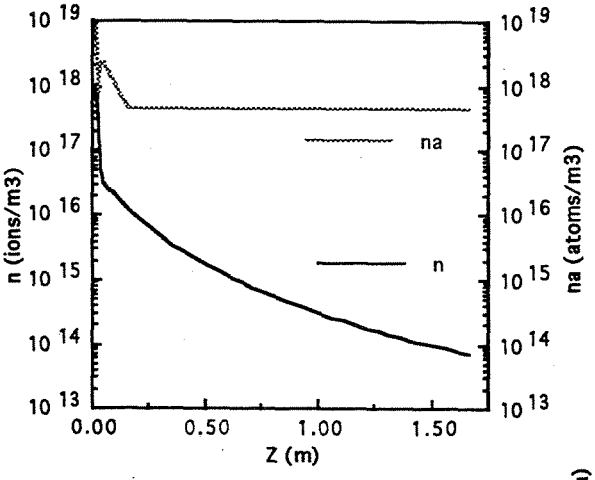

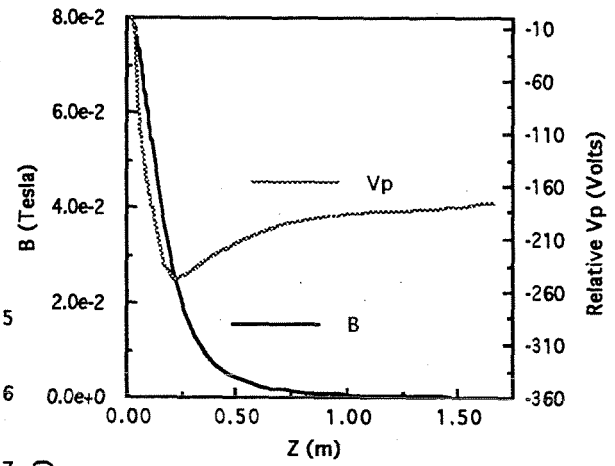

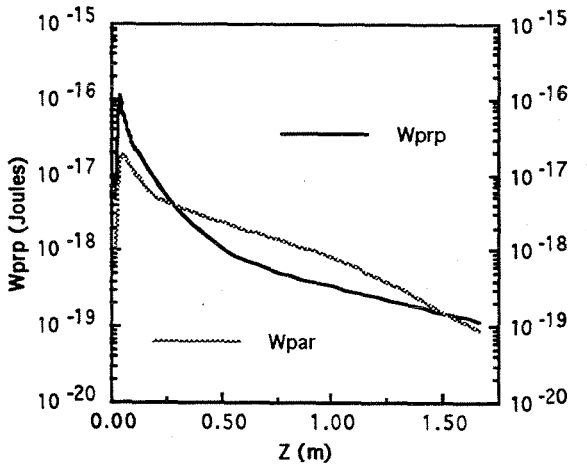

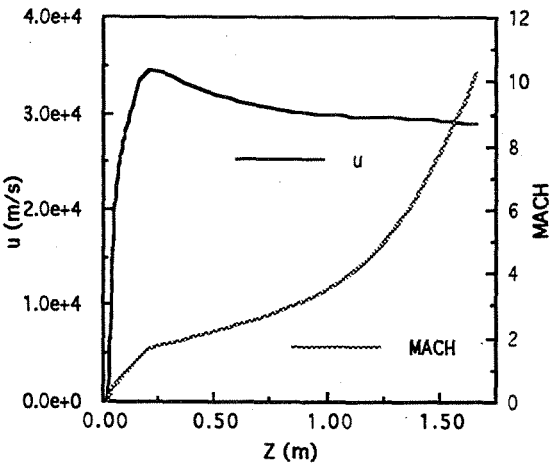

- Coupled ECR Power = 750 watts
- Argon Flow Rate = 25.0 sccm
- No Axial Heat Conduction
- No Vacuum Tank Back Pressure

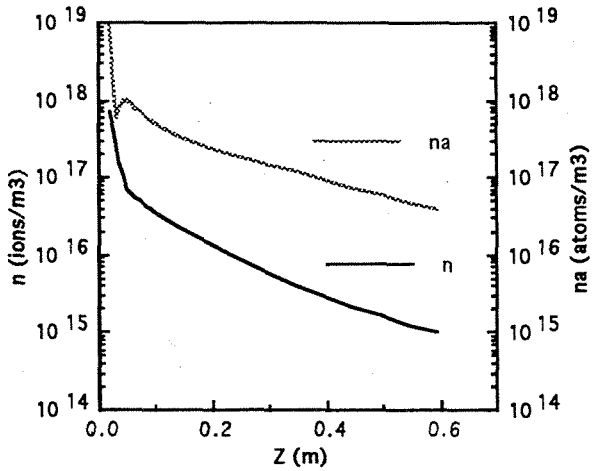

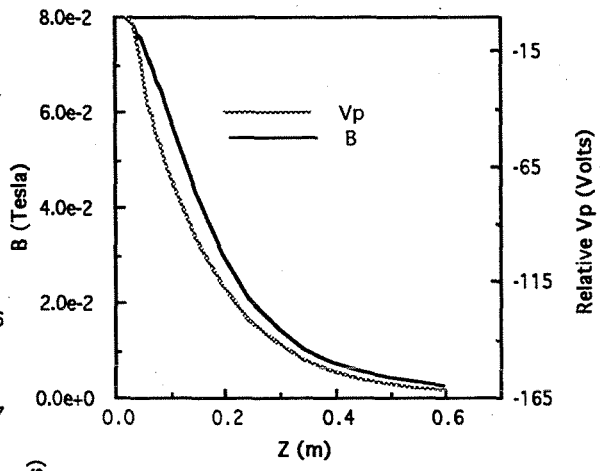

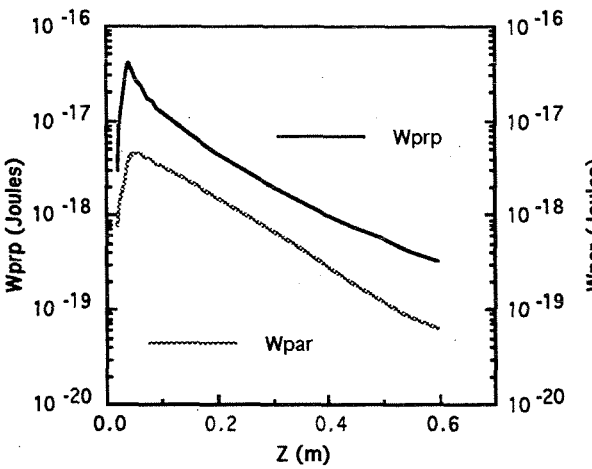

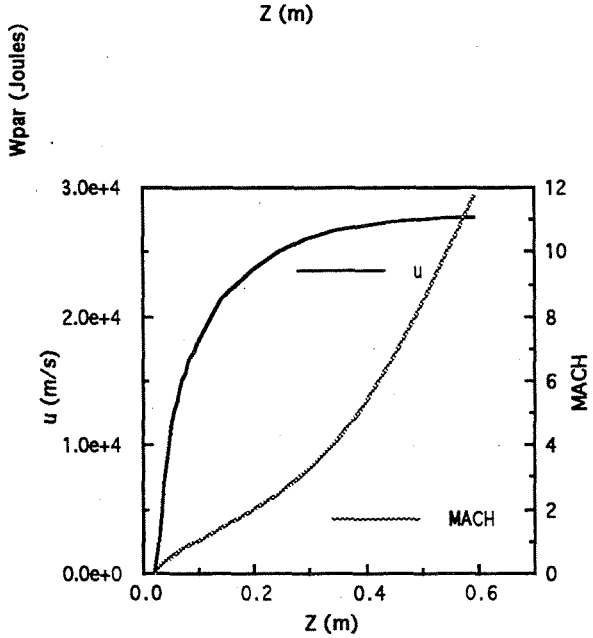

- Coupled ECR Power = 750 watts
- Argon Flow Rate = 25.0 sccm
- No Axial Heat Conduction
- Finite Vacuum Tank Back Pressure

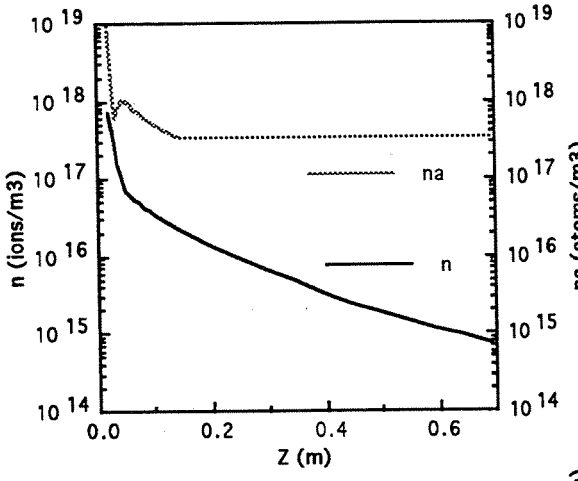

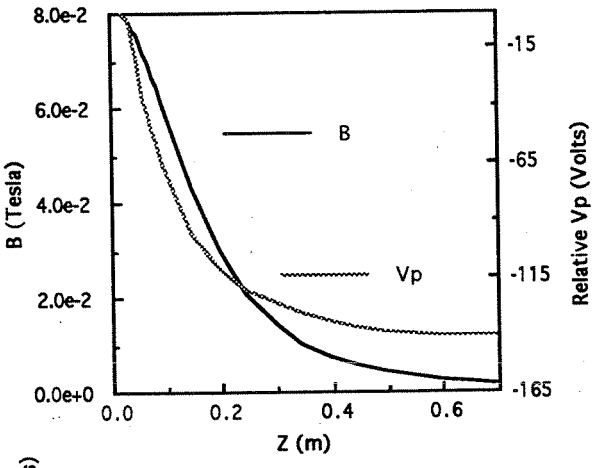

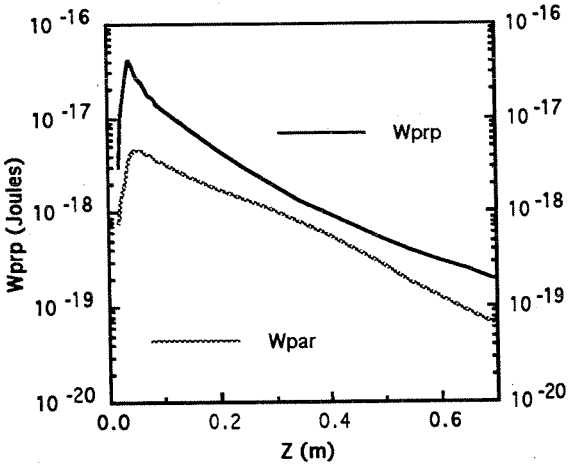

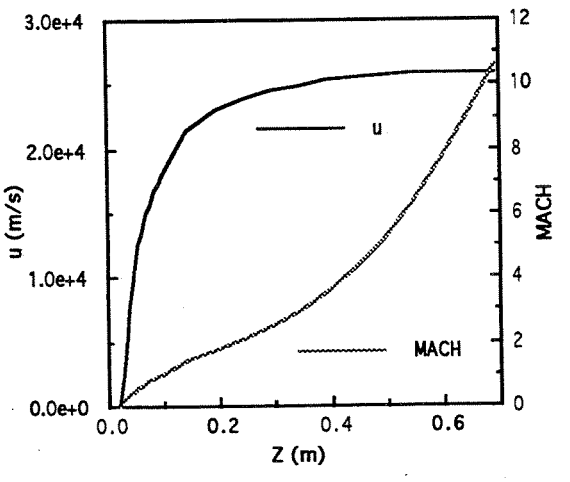

- Coupled ECR Power = 1500 watts
- Argon Flow Rate = 30.0 sccm
- No Axial Heat Conduction
- No Vacuum Tank Back Pressure

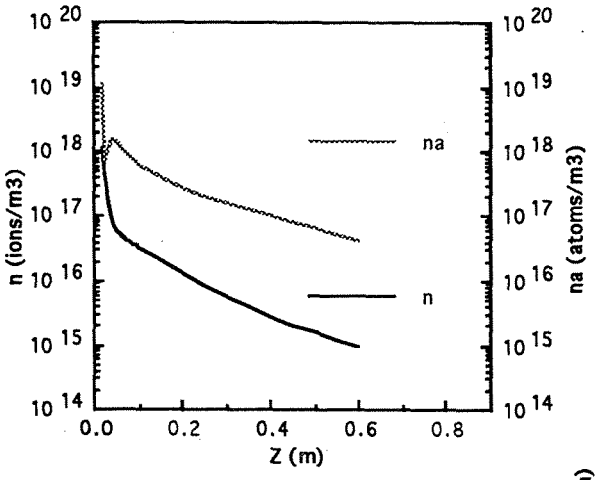

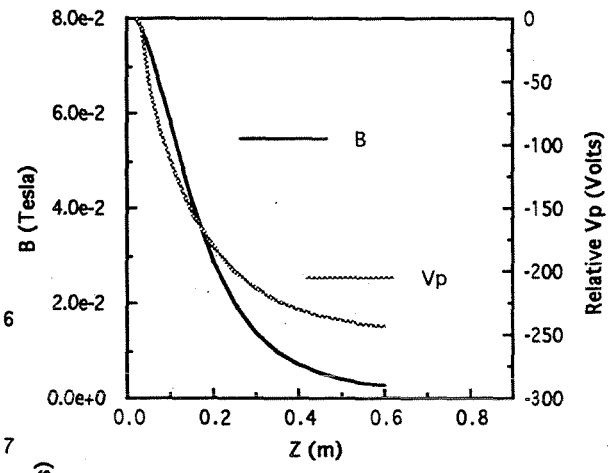

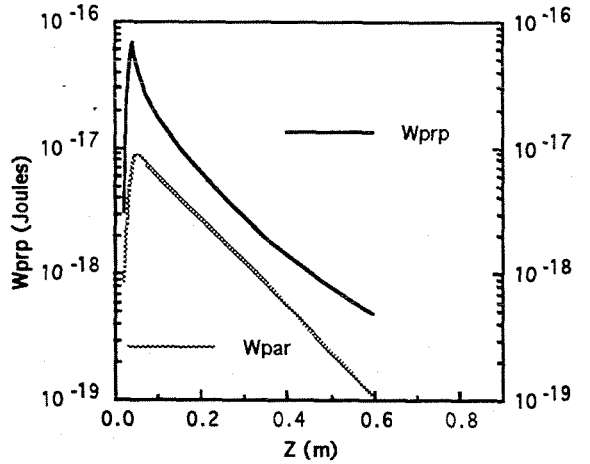

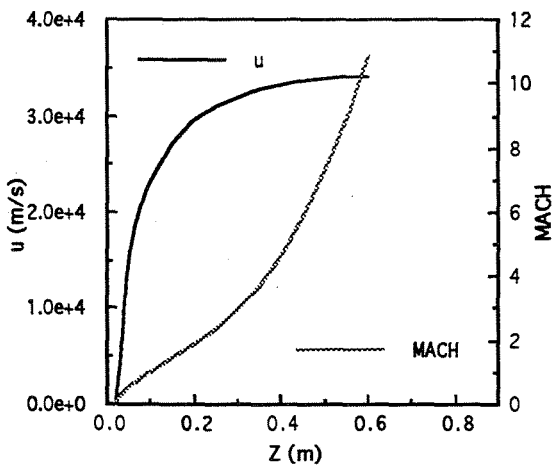

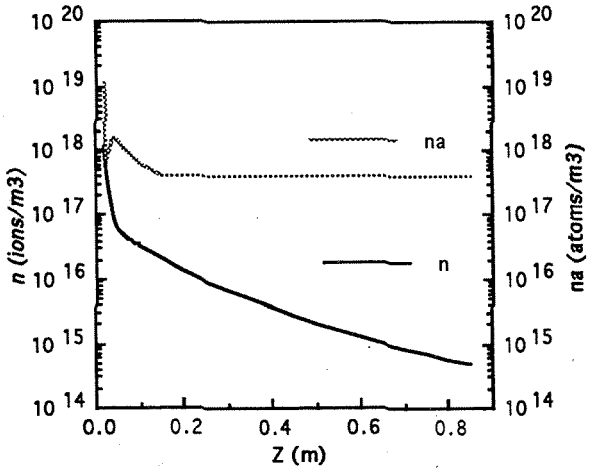

- Coupled ECR Power = 1500 watts
- Argon Flow Rate = 30.0 sccm
- No Axial Heat Conduction
- Finite Vacuum Tank Back Pressure

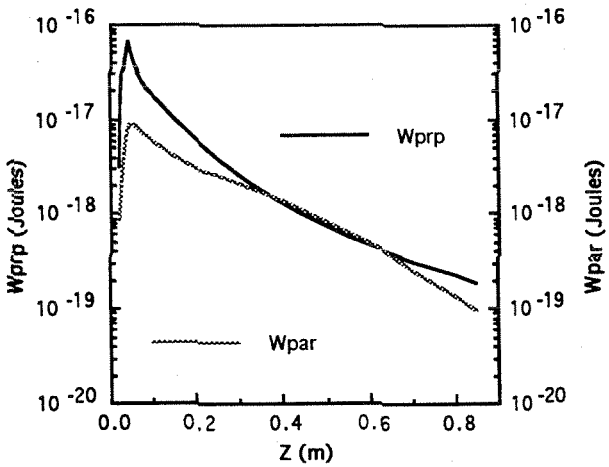

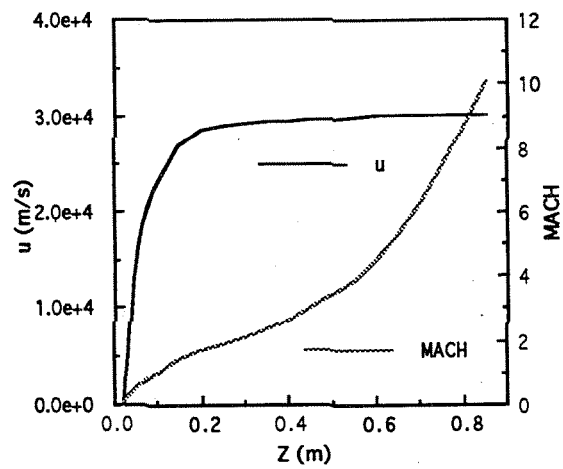

- Coupled ECR Power = 2000 watts
- Argon Flow Rate = 30.0 sccm
- No Axial Heat Conduction
- No Vacuum Tank Back Pressure

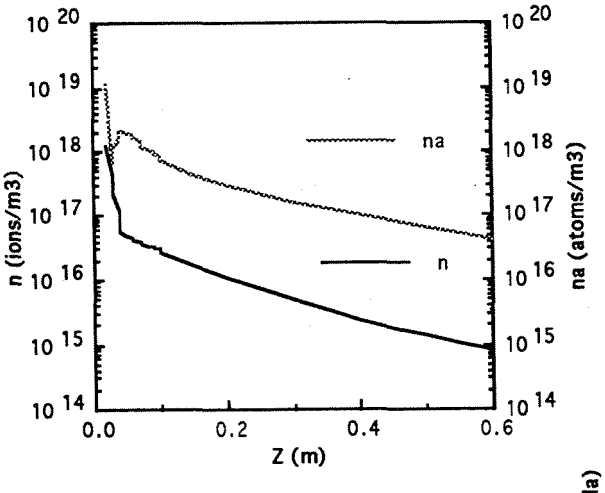

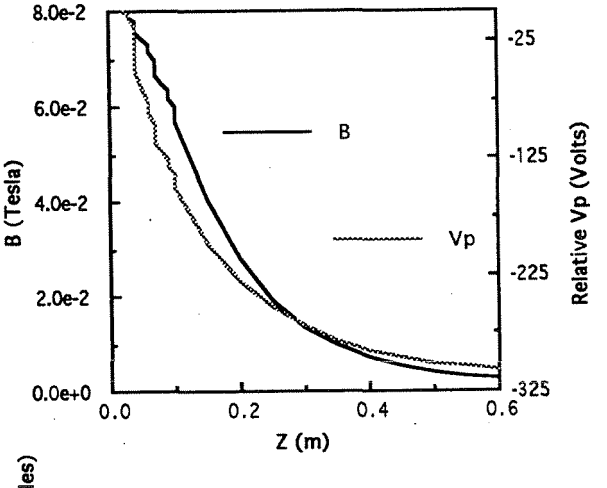

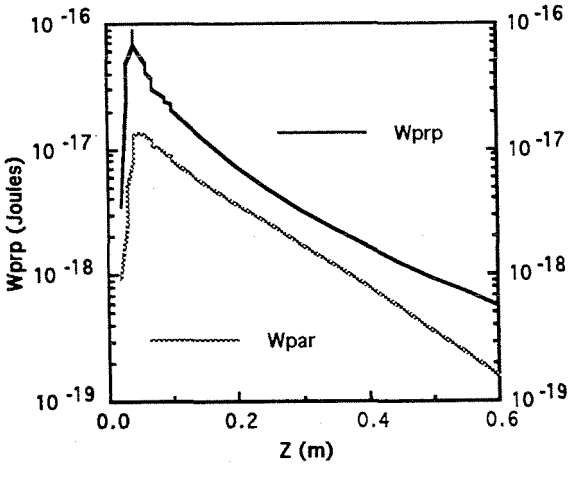

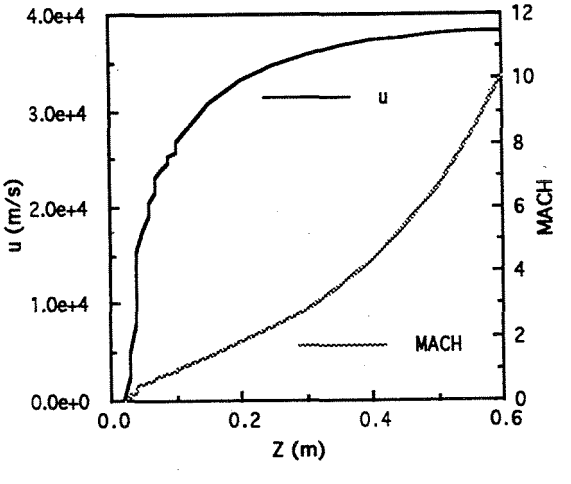

- Coupled ECR Power = 2000 watts
- Argon Flow Rate = 30.0 sccm
- No Axial Heat Conduction
- Finite Vacuum Tank Back Pressure

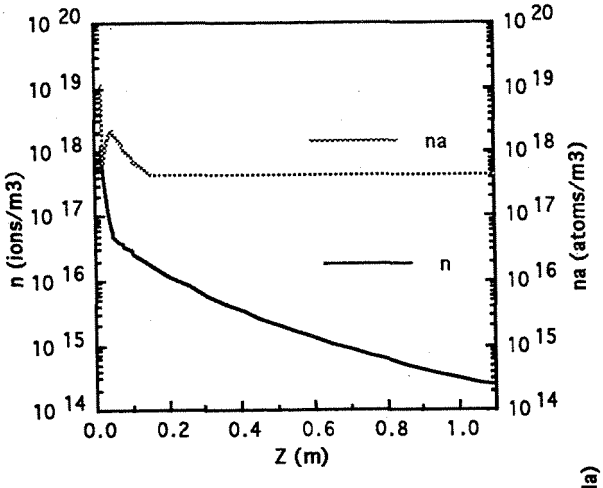

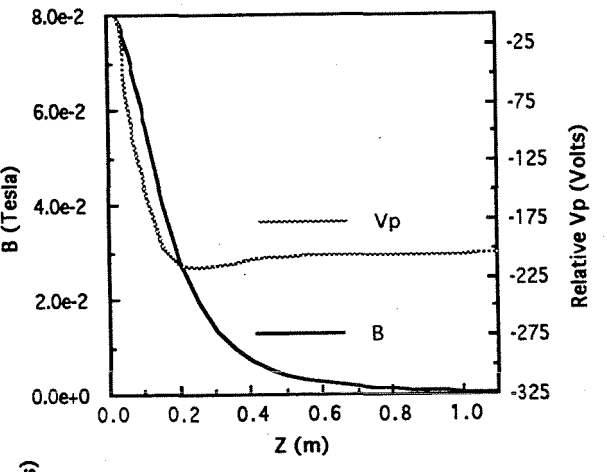

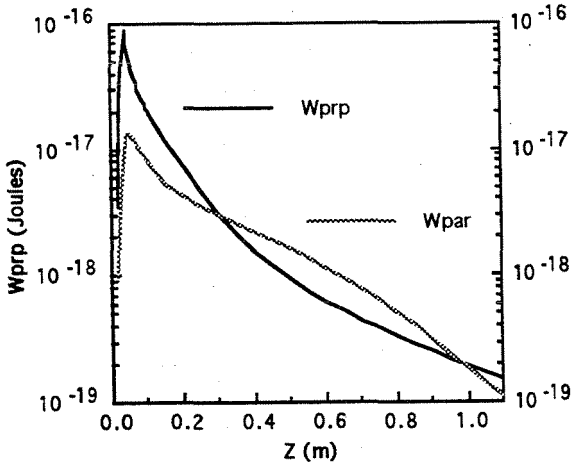

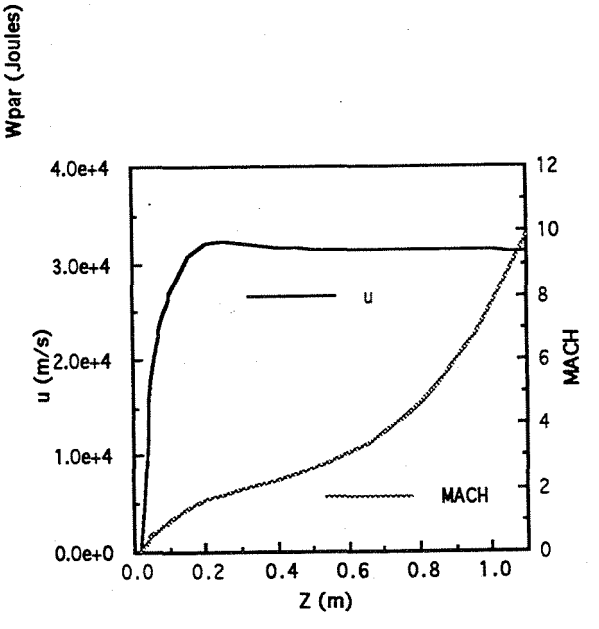

- Coupled ECR Power = 2000 watts
- Argon Flow Rate = 35.0 sccm
- No Axial Heat Conduction
- No Vacuum Tank Back Pressure

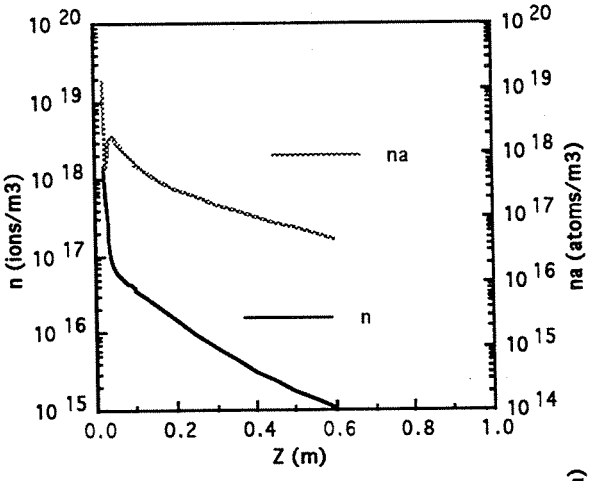

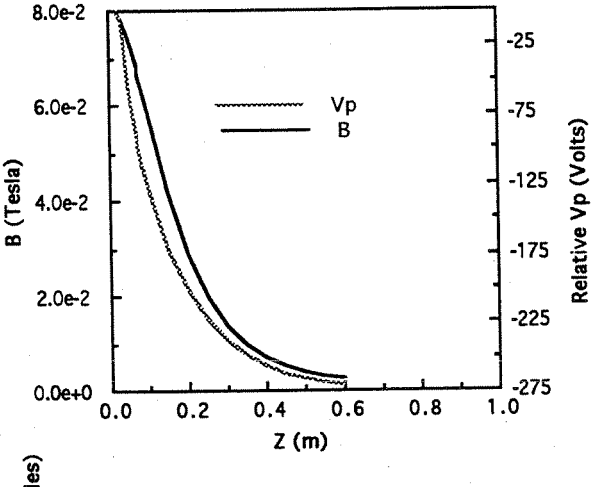

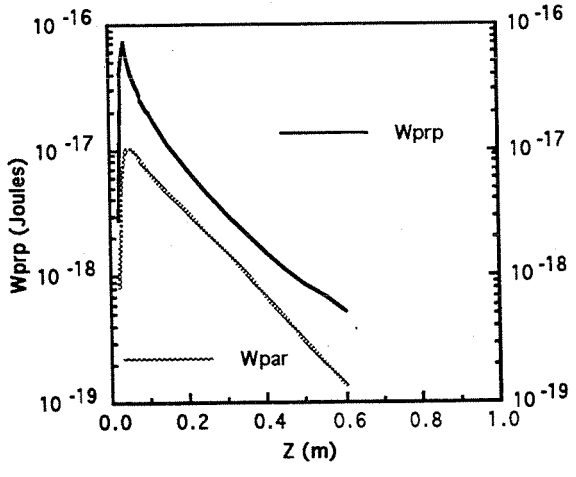

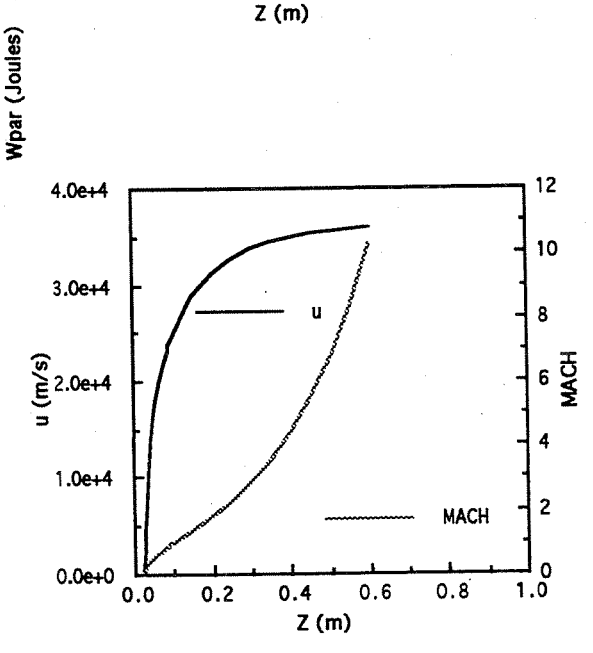

- Coupled ECR Power = 2000 watts
- Argon Flow Rate = 35.0 sccm
- No Axial Heat Conduction
- Finite Vacuum Tank Back Pressure